CYCLIC TESTING AND ASSESSMENT OF SHAPE MEMORY ALLOY RECENTERING SYSTEMS

A Thesis
Presented to
The Academic Faculty

by

Matthew S. Speicher

In Partial Fulfillment
of the Requirements for the Degree
Doctor of Philosophy in the
School of Civil and Environmental Engineering

Georgia Institute of Technology
May 2010

CYCLIC TESTING AND ASSESSMENT OF SHAPE MEMORY ALLOY RECENTERING SYSTEMS

Approved by

Dr. Reginald DesRoches, Advisor
School of Civil and Environmental Engineering
Georgia Institute of Technology

Dr. James Craig
School of Aerospace Engineering
Georgia Institute of Technology

Dr. Roberto T. Leon, Co-Advisor
School of Civil and Environmental Engineering
Georgia Institute of Technology

Dr. Yang Wang
School of Civil and Environmental Engineering
Georgia Institute of Technology

Dr. Laurence Jacobs
School of Civil and Environmental Engineering
Georgia Institute of Technology

Date Approved: December 7, 2009

Engineering is the art of directing the great sources of power in nature for the use and convenience of man – Hardy Cross (1952)

ACKNOWLEDGEMENTS

This work would not have been possible without the contribution of many individuals. The author would like to thank Dr. Reginald DesRoches and Dr. Roberto T. Leon for the support, guidance, and advice that made this research possible.

The author would like to thank Johnson Matthey for donating the stock NiTi material for the tension/compression device experiments and Dr. Darel Hodgson for conceiving and fabricating the tension/compression device and the wire bundles and providing guidance for this research. The author also thanks Mike Sorenson, Andy Udell, and Jeremy Mitchell for the support given in the lab.

Tackling a doctoral thesis is very challenging. The author would like to thank all of the fellow graduate students who made the battle more enjoyable. Specifically, the author thanks Masahiro Kurata for his continued good spirits and guidance in this research and his camaraderie during travels to California, Canada, and China. The author thanks Robert Hurt for getting him into the weight room, helping him develop research ideas, and continually fixing his car. The author thanks his office mates in Mason 522a and other colleagues including Ben Kosbab, Walter Yang, Karthik Ramanathan, Tim Wright, Jieun Hur, Jason McCormick, and Bryant Neilson for making research more enjoyable with daily banter.

Through the highs and lows of graduate research, the author also thanks his beautiful wife Lindsay for the constant encouragement and support. The author thanks his father, mother, brother, and sister for all the support they have given him over the decade he has been in college. Additionally, the author would like to thank Elias

Matthew for his constant reminder of what is important as the author finished the work on this thesis.

Lastly but most importantly, the author would like to thank God and his Son. It is through the author's deep faith in the events laid out in the Bible and his personal experience living in the wake of grace, that the author has unreserved confidence in God's infinite power, love, and wisdom and in the redemption brought through his Son.

TABLE OF CONTENTS

LIST OF TABLES

LIST OF FIGURES

LIST OF SYMBOLS AND ABBREVIATIONS

SYMBOLS

A_f	Austenite finish temperature
A_s	Austenite start temperature
C_d	Deflection amplification factor
K	Stiffness
K_e	Effective Stiffness
M	Moment
M_f	Martensite finish temperature
M_s	Martensite start temperature
M_w	Moment magnitude
R	Strength reduction factor (i.e. Response modification coefficient)
V_{by}	Yield base shear
ζ	Equivalent viscous damping
θ	Rotation
Δ	Deformation (CHAPTER 4), Drift (CHAPTER 5 and 6)
Δ_{res}	Residual drift (CHAPTER 6)
Δ_{max}	Test-target maximum deformation (CHAPTER 4)
Ω_o	System overstrength factor

ABBREVIATIONS

AQ	Articulated quadrilateral
BRB	Buckling restrained brace
DAQ	Data acquisition system

EP	Elastoplastic
EXT	Extensometer
LC	Load Cell
LVDT	Linear variable displacement transducer
MANSIDE	Memory Alloys for New Seismic Isolation and Energy Dissipation Devices
NEHRP	National Earthquake Hazards Reduction Program
NiTi	Nickel-titanium
PARA	Parallel
PR	Partially restrained
PT	Post-tensioned
SDOF	Single-degree-of-freedom
SE	Superelastic effect
SMA	Shape memory alloy
SME	Shape memory effect
SG	Strain gauge
SP	String Potentiometer

SUMMARY

In an effort to mitigate damage caused by earthquakes to the built environment, civil engineers have been commissioned to research, design, and build increasingly robust and resilient structural systems. Innovative means to accomplish this task have emerged, such as integrating Shape Memory Alloys (SMAs) into structural systems. SMAs are a unique class of materials that have the ability to spontaneously recover strain of up to 8%. With proper placement in a structural system, SMAs can act as superelastic “structural fuses”, absorbing large deformations, dissipating energy, and recentering the structure after a loading event. Though few applications have made it into practice, the potential for widespread use has never been better due to improvements in material behavior and reductions in cost.

In this research, a single degree-of-freedom study was first conducted in order to investigate the benefits of recentering compared to energy dissipation. Through this study the following fundamental observation was made: enhanced performance, in terms of maximum displacements, can be obtained from a recentering system by maximizing the hysteretic loop, thus increasing the energy dissipation. This observation, coupled with previous work that has shown that recentering systems are capable of meeting or exceeding the performance level obtained from other advanced systems, has further motivated the experimental work conducted herein.

For the experimental portion of this research, three different structural applications were developed and tested. The first was a tension/compression damper that utilized either nickel titanium (NiTi) helical springs or Belleville washers. These new forms of NiTi were previously untested; therefore the properties were largely unknown.

Nonetheless, the results indicated that unique applications may be possible with both forms. For the second part of the experimental work, a SMA-based partially-restrained interior beam-column connection utilizing NiTi tendons was investigated. The connection was designed to concentrate all of the inelastic deformation into the SMA tendons and then recenter due to the superelasticity of these tendons. The connection proved to have good recentering and ductility even after it was cycled to 5% drift. Finally, for the last part of the experimental work, a special bracing system was developed using an articulated quadrilateral (AQ) arrangement. The AQ arrangement allowed SMA wire bundles to be put in parallel with c-shaped dampers, thus enabling the designer to tailor the amount of damping in the flag-shaped hysteresis. The braced frame experimental results demonstrated that a maximized hysteresis can indeed be obtained while the analytical results demonstrated that one can obtain more evenly distributed deformation demands for an SMA-based system than compared traditional system. This exploratory experimental work highlights the potential for SMA-based structural applications to enhance seismic structural performance and community resilience.

CHAPTER 1

INTRODUCTION

1.1. Problem Description

In 1994 the Northridge earthquake struck Southern California causing $40 billion in direct damage (Eguchi et al., 1998) and exposing previously unknown vulnerabilies of welded moment connections in hundreds of buildings. In 1995 the Kobe earthquake shook central Japan, collapsing elevated highways, destroying numerous buildings, killing over 5000 people, and causing over $130 billion in direct damage (Scawthorn and Yanev, 1995). More recently, on March 12, 2008, a M_w 7.9 earthquake struck Sichuan Province in China killing tens-of-thousands of people, quickly becoming a grim reminder of the consequences of what happens when vulnerable structures are subjected to strong ground shaking.

In an effort to mitigate damage to the built environment caused by earthquakes, civil engineers have been commissioned to research, design, and build increasingly robust and resilient structural systems. Innovative means to accomplish this task have emerged and can be broken down into three basic categories: base isolation, active (and semiactive) control, and passive control. These three categories, combined with new code requirements, promise to enhance modern structures' earthquake performance.

Base Isolation has received considerable attention from the research community over the years and has established itself as the most mature of the three mitigation techniques. Numerous buildings across the world have been designed and/or retrofitted with base isolators (e.g. Istanbul International Airport, San Francisco City Hall, and Oakland City Hall). Base isolators effectively decouple the motion of the ground from

that of the structure and thus greatly reduce damage. However, even with widespread use and excellent performance, base isolation is not always possible or appropriate due to the high premium for such a system. Therefore, other techniques must be explored.

As an alternative to base isolation, active and passive control both deal with inserting special elements within the building in order to modify the response. Active and semi-active control techniques modify response through a combination of energy dissipation and externally-powered force-delivery devices that respond to real-time stimuli. In contrast, passive control techniques modify the response through passively dissipating energy in predetermined elements which, if designed correctly, can eliminate unwanted inelastic behavior in the remainder of the structure and help distribute the deformation demand more evenly over the height of the structure. A variety of structures have been built or retrofitted with passive control techniques, such as the San Francisco State Office Building, Coronado Bay Bridge, and the West Los Angeles Federal Building. Passive control has become a mainstay in the structural engineering toolbox.

In the category of passive control, recentering systems have recently emerged as a viable way to enhance a structure's response. Rather than focusing on energy dissipation, as in typical passive control systems, recentering systems sacrifice damping for the ability to reduce residual deformations after a seismic event. A comparison between an elastoplastic (traditional) system and a recentering (shape memory alloy or SMA) system is shown in Figure 1-1. Recentering can be achieved by using post-tensioned devices/connections (Ricles et al., 2001; Tremblay et al., 2008) or by using superelastic shape memory alloys (Leon et al., 2001; Dolce et al., 2001; McCormick et al., 2007; Sepulveda et al., 2008). Several studies have shown improved structural performance, in terms of maximum and residual drifts, when comparing recentering systems to traditional passive energy dissipation systems (Ricles et al., 2001; Christopoulos and Filiatrault, 2002; Christopoulos et al. 2008; Zhu and Zhang, 2008).

Recently, Eatherton et al. (2009) have begun working on vertically post-tensioned rocking frame systems that incorporate both recentering and energy dissipation elements. With the increasing body of experimental and analytical work being conducted on recentering systems, the balance between recentering and energy dissipation still needs further investigation. Additionally, more practical methods of employing recentering need to be explored.

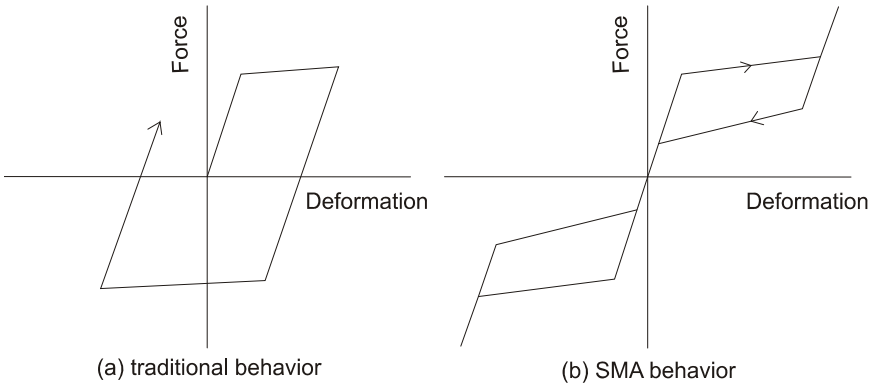

Figure 1-1: Qualitative comparison between (a) a traditional system and (b) a SMA system.

In this research, superelastic nickel-titanium (NiTi) shape memory alloys (SMAs) are investigated as means to accomplish recentering. NiTi SMAs have the distinct ability to spontaneously recover up to 8% strain upon the removal of stress, yet have found limited applications in the civil engineering industry since their discovery over four decades ago. The potential to both provide recentering and supplemental damping is the hallmark of SMAs behavior. It is hypothesized that optimized structural performance can be obtained by appropriately balancing recentering and damping, thus limiting maximum displacements while also reducing residual displacements. To investigate this fundamental idea, a single-degree-of-freedom analytical study is first investigated. Next,

three different SMA-based systems are developed and tested under cyclic loads. With such great potential, the goal of this research is to assess the ability of these new systems to enhance structural performance in order to mitigate earthquake losses.

1.2. Scope of Project

To accomplish the objective of this research, the following tasks were undertaken:

- **TASK 1:** Conduct a preliminary study of a single degree-of-freedom oscillator comparing recentering systems to traditional damped systems. This study examined the response over a range of periods and excitations in order to understand how to best enhance structural performance.
- **TASK 2:** Conduct an exploratory investigation on a novel l tension/compression device. This device subjects new forms of SMAs to compression loading and has potential to be implemented into a bracing system to provide unique force-deformation properties.
- **TASK 3:** Develop and test a recentering beam-column connection using modified and improved detailing from that used by Penar (2005). Modifications included special provisions for preventing local buckling, bolted components to enable interchanging and variation, improved tendon superelasticity, and implementation of SMAs with aluminum in parallel configurations. The ability of a simple finite element model to capture the behavior of the beam-column connection was also assessed.
- **TASK 4:** Develop and test a new type of recentering bracing system based on an articulated quadrilateral (AQ) configuration. This AQ configuration enables SMA wire bundles to be combined in parallel with energy dissipating elements,

thus allowing the engineer to adjust the amount of damping and recentering of the system. The experimental results were used to conduct a case-study on the effectiveness of a SMA braced frame in comparison to traditional and buckling restrained braced frames.

- **TASK 5:** Synthesis and recommendations in order to obtain practice-ready applications of SMA-based systems.

1.3. Thesis Outline

The content of this thesis is organized into the following chapters:

- **CHAPTER 2:** Shape memory alloys are first introduced and their fundamental behavior is reviewed. Next, background on recentering systems is given, including experimental work done on post-tensioned and SMA recentering systems. This review is given to set the context for the rest of the research.
- **CHAPTER 3:** A single degree-of-freedom oscillator is investigated to explore the differences in performance of an elastoplastic system (damping) and a flag-shaped hysteretic system (recentering). Additionally, the balance between recentering and damping is investigated by combining an elastoplastic system in parallel with a recentering system.
- **CHAPTER 4:** Cyclic tests are performed on a tension/compression device that utilizes two new forms of SMAs: helical springs and Belleville washers. Additionally, an investigation into the individual performance of a Belleville washer is presented and potential applications are noted.
- **CHAPTER 5:** Cyclic tests are performed on a half-scale interior beam-column connection that implements SMA tendons. The test results are analyzed in terms

of strength, stiffness, residual drift, and damping. The experimental results are then compared with a simple model implemented into OpenSEES.

- **CHAPTER 6:** An articulated quadrilateral bracing system that utilizes SMA wire bundles in parallel with c-shape dissipators is conceived, developed, tested, and assessed. An analytical study is then conducted to assess the response of a seven-story braced frame that implements SMA-bracing elements.
- **CHAPTER 7:** Overall conclusions are presented with respect to each SMA-based system explored in this work. Recommendations for needed areas of future work and the need for practice-ready applications is discussed.

CHAPTER 2

LITERATURE REVIEW

2.1. Introduction

This chapter presents a summary of the literature relevant to the overall scope of this research. First, a review of shape memory alloys is conducted to provide a better understanding of its behavior. Next, background research on recentering systems (created by post-tensioning or using shape memory alloys) is summarized to support the motivation for this work. Additional background information is given, as necessary, in each subsequent chapter.

2.2. Shape Memory Alloys

2.2.1. SMA overview

Shape memory alloys are a class of metallic alloys with several distinct and advantageous properties. The property that has drawn the most interest is the material's ability to return to its original shape after stress is removed (pseudo- or superelastic effect or SE) or after heat has been applied (shape memory effect or SME). The first recorded observation of the SME was the AuCd alloy in 1932 by Chang and Reid (Otsuka and Wayman, 1998). In 1962, an equal-atomic composition of nickel and titanium was observed to exhibit shape memory characteristics at the U.S. Naval Ordinance Lab, resulting in the name NiTiNOL (Jackson et al., 1972). Several characteristics have made the NiTi alloy the preferred SMA for application in the medical, aerospace, and civil engineering fields. These characteristics include its high

corrosion and fatigue resistance, biocompatibility, stable hysteretic behavior, and large recentering capability (recovers strain of up 8%). Because of these characteristics, NiTi was the alloy used throughout this research.

Even with good promise, applications of SMAs in structural engineering have been limited. This is in part due to the lack of knowledge transfer between the material scientist community developing the SMAs and the civil engineering community trying to implement them (Tyber et al., 2007). It also can be credited to the lack of knowledge of the large-scale performance of the SMAs (McCormick et al., 2007b) and the difficulty in implementing large size SMA elements due to poor machining characteristics (Weinert and Petzoldt, 2004). Despite these challenges, in the last decade knowledge of SMAs' mechanical and material properties has grown dramatically and its potential for applications has never been better. With the call for more resilient, robust, and sustainable structural systems, the use of SMAs in recentering systems needs further investigation to enable implementation of real world applications.

2.2.2. SMA Microstructure

The SMA microstructure is made up of two basic ordered atomic phases which enable it to possess its unique shape memory properties. These two phases are austenite and martensite and their 2D representation is illustrated in Figure 2-1. Austenite is stable at high temperatures and low stresses, is highly symmetric, and has a B2 body-centered atomic structure. Martensite is stable at low temperatures and high stresses, possesses a B19' rhombic geometry, and exists with either twin variants (Figure 2-1b) or a single favored variant (Figure 2-1c) (Wayman and Duerig, 1990). Martensite is softer and has lower strength than its austenite counterpart. The occurrence of the two variant orientations will be explained in the next two sections.

Further detailed information about the microstructure and crystallography of SMAs is readily available in the literature (Duerig et al., 1990; Gall et al., 1999c; Gall et al., 1999d; Hane and Shield, 1999; Otsuka and Shimizu, 1986; Otsuka and Wayman, 1998; Perkins, 1981; Tadaki et al., 1988). Of particular note, Frick et al. (2005) and Tyber et al. (2007) provide a detailed review of the basic material microstructural characterization of NiTi SMAs, the effect of the presence of precipitates in relation to mechanical properties, and an explanation of the role of subphases (R-phase) during the martensitic transformation.

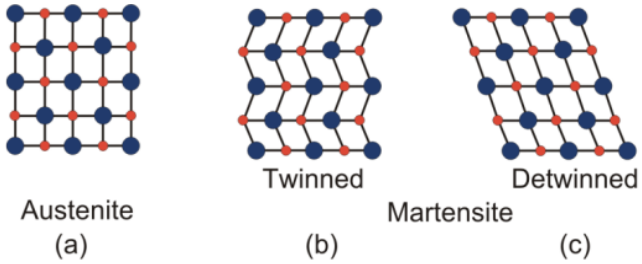

Figure 2-1: 2D representation of the microstructure of SMAs.

2.2.3. Shape Memory Alloy: Fundamental Behaviors

As stated previously, shape memory alloys have two fundamental behaviors: shape memory and superelasticity. These behaviors are dependent on the following characteristic temperatures of the SMA: M_s (temperature at which martensite begins forming), M_f (temperature at which martensite ends forming), A_s (temperature at which austenite begins forming), and A_f (temperature at which austenite ends forming).

2.2.3.1. Shape Memory Effect

The shape memory effect (SME) occurs when the SMA starts in the martensitic phase. The SME behavior is illustrated in a portion of Figure 2-2. Additionally, the typical mechanical behavior is shown in Figure 2-3. The SME begins with martensitic SMA in a twinned orientation. When stress is applied to the material, the twinned structure

reorients into a detwinned single variant in order to accommodate the resulting strains (in traditional metals the strain is accommodated by slip). Upon the removal of the stress, the detwinned structure remains deformed as shown in the bottom right of Figure 2-3. To recover its shape, the metal is heated above its A_f and then cooled back below the M_f. This sequence of heating and cooling causes the martensite crystal structure to revert back into the low symmetry twinned orientation; therefore the shape is fully recovered and the SME is complete.

2.2.3.2. Superelastic Effect

Shape memory alloys exhibit superelastic behavior above the austenite finish temperature, A_f (i.e. austenitic SMA). The top of Figure 2-2 and left side of Figure 2-3 give the qualitative microstructural changes and mechanical behavior. When the SMA is loaded to a certain stress level, the austinite accommodates the strain by transforming into detwinned martensite, creating a loading plateau. After the loading plateau is crossed, the austenite has been fully transformed into stress-induced detwinned martensite.

If the load continues to increase, the SMA will eventually sustain permanent deformations because of the formation of slip planes (as in typical metals). However, if the load is released, the stress will decrease until an unloading plateau is reached, where the detwinned martensite will revert back into austinite and thus full shape recovery will be obtained. The resulting hysteresis gives superelastic SMAs inherent energy dissipation.

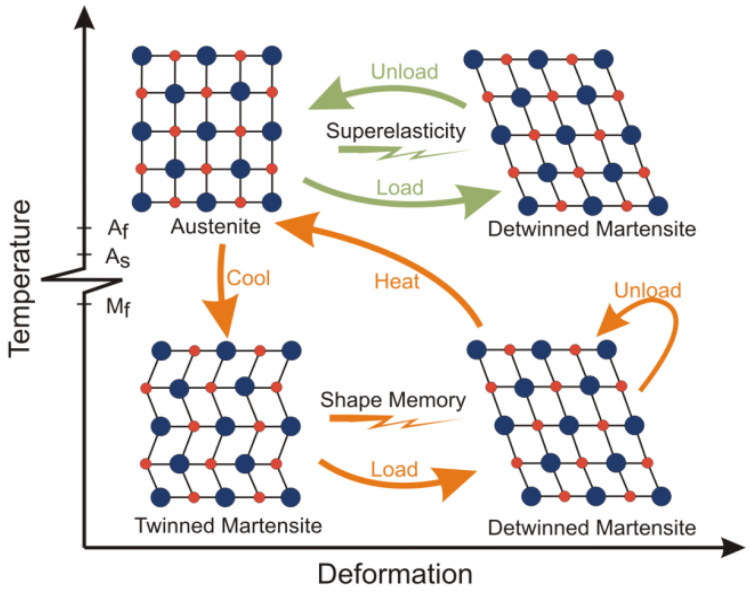

Figure 2-2: 2D microstructure representation of the shape memory effect and superelasticity.

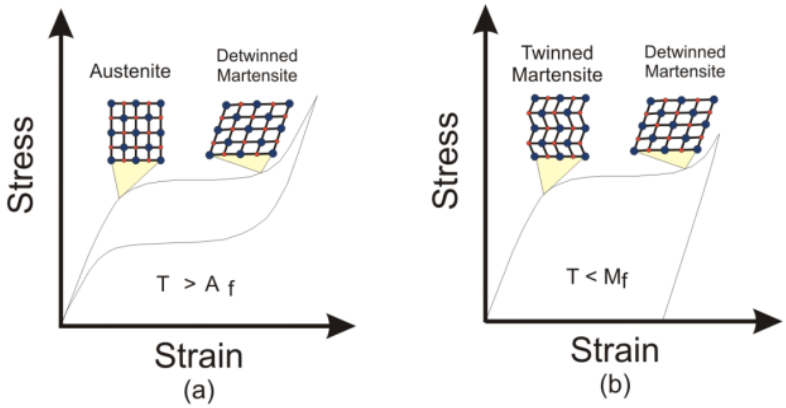

Figure 2-3: Stress-strain relationship for (a) superelastic SMA and (b) shape memory SMA.

2.2.4. NiTi Shape Memory Alloy

NiTi has been established as the alloy of choice for applications in civil engineering because of its fatigue and corrosion resistance, stable hysteresis, and large strain

recoverability. For these reasons, NiTi was the SMA chosen for this research. The following subsections give a review of the state-of-the-knowledge of NiTi.

2.2.4.1. General Properties of NiTi

The mechanical behavior of NiTi has been the subject of numerous studies in the past several decades. Bars, wires, and plates have been tested in multiple shapes and forms. Wires and bars are both of importance to this research because the envisioned applications implement these forms. To better understand the range of behaviors observed in NiTi, a list of NiTi and steel properties are compared in Table 2-1.

Several studies have found that SMA bars have inferior superelastic properties when compared to wires (Dolce and Marnetto, 1999; MANSIDE, 1998). However, recent work has investigated this difference and demonstrated good superelastic (recentering) properties can be obtained from both bars and wires with appropriate chemical composition, heat treatment, and deformation processing (Tyber (McCormick et al., 2007b; Tyber et al., 2007).

Nevertheless, there are still some differences in the properties between bars and wires, some of which come from the additional cold working that wires undergo. One significant difference that has been shown is the equivalent viscous damping (2-4% for bars, 4-8% for wires) (DesRoches et al., 2004). Though the level of equivalent viscous damping in superelastic NiTi does not justify using it for pure damping purposes, it is desirable to maximize performance by balancing the damping and recentering properties. In this research, the difference between the equivalent viscous damping in bars and wires is marginalized by combining other elements in parallel with the SMA elements, thus increasing the overall system damping.

Table 2-1: Typical properties of NiTi compared with structural steel (table adapted from Penar (2005)).

	NiTi		Structural Steel
	Austenite	Martensite	
Physical Properties			
Melting Point	1240-1310°C		1500°C
Density	6.45 g/cm^3		7.85 g/cm^3
Thermal conductivity	0.28 W/cm °C	0.14 W/cm °C	0.65 W/cm °C
Thermal Expansion	11.3 x 10^{-6} /°C	6.6 x 10^{-6} /°C	11.7 x 10^{-6} /°C
Mechanical Properties			
Recoverable Elongation	up to 8%		0.2%
Young's Modulus	30-83 GPa	21-41 GPa	200 GPa
Yield Strength	195-690 MPa	70-140 MPa	248-517 MPa
Ultimate tensile strength	895-1900 MPa		448-827 MPa
Elongation at Failure	5-50% (typically ~25%)		~20%
Poisson's Ratio	0.33		0.27-0.30
Hot Workability	Quite good		Good
Cold Workability	Difficult due to rapid work hardening		Good
Machinability	Difficult, abrasive techniques preferred		Good
Hardness	30-60 R_c		Varies
Weldability	Quite good		Very good
Chemical Properties			
Corrosion performance	Excellent		Fair

2.2.4.2. Cyclic Loading and Fatigue

Since earthquakes induce cyclic loads on a structure, it is clear that there needs to be a firm understanding of NiTi's cyclic behavior. Numerous cyclic tests on superelastic NiTi have been carried out to study the effects of repeated loading and fatigue. These studies have shown cyclic loading causes increased residual strain, decreased loading plateaus, and decreased hysteretic loops (DesRoches et al., 2004; Dolce and Cardone, 2001; Gong et al., 2002; Kawaguchi et al., 1991; Miyazaki et al., 1986; Strnadel et al., 1995a; Strnadel et al., 1995b). To mitigate these trends, several researches have looked at the possibility of training NiTi elements to achieve stabilization. Training generally results in a stabilized hysteresis and enhanced recentering (decreased residuals) (MANSIDE, 1998; McCormick and DesRoches, 2006; Miyazaki et al., 1986; Strnadel et al., 1995a; Wang et al., 2003). An example of this stabilization is shown in Figure 2-4 from a study by Tobushi et al. (1998).

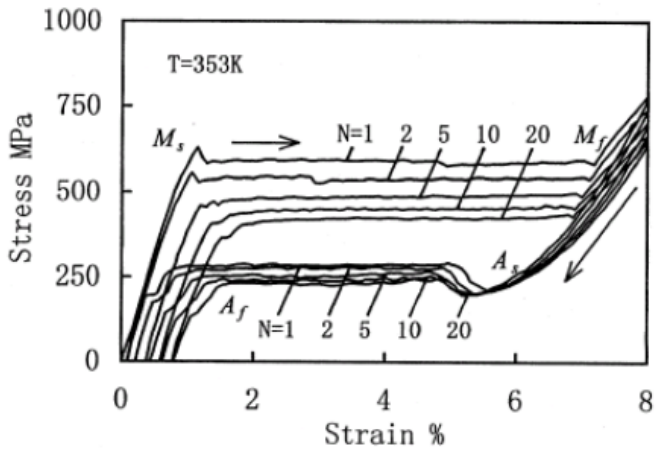

Figure 2-4: Stress-strain curve for superelastic NiTi wire under tension cycling (Tobushi et al., 1998).

2.2.4.3. Thermal Processing

The effects of thermal processing (annealing) also influence the mechanical behavior of NiTi. Annealing causes precipitation of Ni_3Ti_4 within the microstructure which aids in suppressing slip. Suppression of slip results in a suppression of unwanted permanent deformations (Tyber et al., 2007). Additionally, annealing causes a good distributing of dislocations that are introduced if the material is cold worked.

The optimum aging temperature is around 400 °C (Miyazaki, 1990). A protocol for thermal processing of superelastic NiTi is outlined by McCormick et al. (2007b). This protocol was used in the processing of the superelastic NiTi bars for the beam-column connection tested as part of this research. The wires bundles, helical springs, and Belleville washers used in the other parts of this research were processed and heat treated using proprietary knowledge by Nitinol Technology, Inc.

2.2.4.4. Loading Rate

The mechanical behavior of NiTi is influenced by the rate of loading seen in typical civil engineering applications. In general, the dominant frequency range of an earthquake is

0.2 Hz to 4.0 Hz. For NiTi, when the loading frequency (and thus the strain rate) is increased, the loading plateau increases and the amount of hysteretic damping decreases (DesRoches et al., 2004; Dolce and Cardone, 2001; Tobushi et al., 1998). Wu et al. (1996) noted that the true nature of strain rate effects is due to the inability to dissipate heat rather than any internal time dependant phenomena. They conducted cyclic strain rate tests in a liquid environment and found that the increase in loading plateau stress and decrease in unloading plateau stress is a function of self-heating and self-cooling of the specimen rather than strain rate. Thus, larger diameter bars will generally have increased strain rate dependence, though the effect of this on a structural system needs further study. The tests conducted in this research were quasi-static, thus the effects of loading rate were not considered.

2.2.4.5. Deformation Processing

Most NiTi is cold-worked to produce the desired shape. In metals, cold working generally produces higher strength and fatigue resistance due to increased dislocation densities (Callister, 2000). Since dislocations, on average, are repulsive, and increased dislocation density helps stop plastic flow and results in a stronger and, in the case of NiTi, a more superelastic material. However, hot-rolled NiTi has also recently been shown to have good superelasticity. This is due to the presence of Ti_3Ni_4 precipitates which hinder plastic flow (Frick et al., 2005; McCormick et al., 2007b; Tyber et al., 2007). Since hot-rolled NiTi costs only a fraction of its cold-worked counterpart, hot-rolled NiTi is an attractive option for bars.

2.2.5. Applications of SMAs

2.2.5.1. Non-Structural Applications

Shape memory alloys have been used in a wide range of non-structural applications. The majority of these applications are in the medical, commercial, and aerospace fields.

Applications in the medical field include arterial stents, catheters, orthodontic braces, and orthopedic prostheses (Duerig et al., 1990). Commercial applications have taken advantage of the superelastic properties of SMAs and include eyeglass frames, cellular telephone antennas, golf clubs, and brasserie underwires (Asai and Suzuki, 2000; Hsu et al., 2000). Additionally, the aerospace industry has looked at SMAs in adaptive aircraft wings and smart helicopter blades in order to reduce noise and vibrations (Beauchamp et al., 1992; Chandra, 2001).

2.2.5.2. Structural Applications

The unique mechanical behavior of SMAs has continued to drive an interest in investigating potential applications in structural systems (discussed further in Section 2.3.3). Though applications are not widespread, several historic structures in Italy have been seismically retrofitted with SMA devices. These buildings include the St. Giorgio Church bell tower in Rio, St. Feliciano Cathedral in Foligno, and St. Frances Basilica in Assisi (Castellano et al., 2001; Indirli et al., 2001).

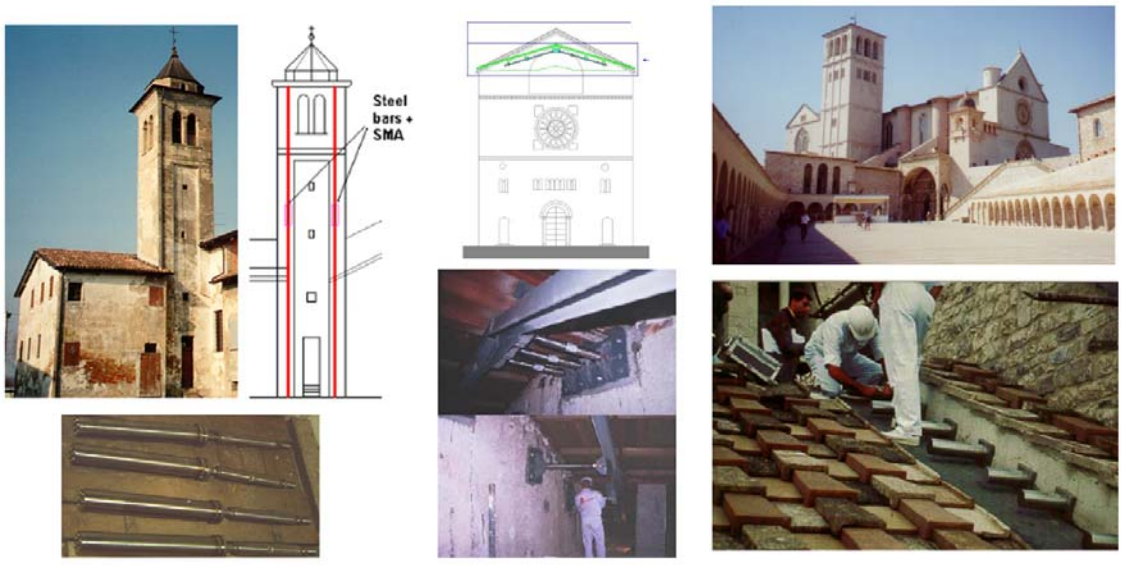

a) St. Giorgio (b) St. Feliciano (d) St. Frances

Figure 2-5: SMA seismic retrofit in Italy. (Castellano et al., 2001; Indirli et al., 2001).

2.3. Recentering Systems

Recentering systems are a form of passive control that enables a structure to eliminate (full recentering) or greatly reduce (partial recentering) residual deformations after a loading event. Recentering is accomplished through the application of a recentering force originating from a mechanism (post-tensioning) or a material property (SMA). Recentering can result in enhanced structural performance, as has been shown in recent studies (Christopoulos et al., 2002a; Wang and Filiatrault, 2008). In contrast to recentering, traditional passive control schemes focus on energy dissipation as the means of improving structural response. The following section gives a brief summary of the current state-of-knowledge of recentering systems (as they apply to structural engineering).

2.3.1. Single Degree-of-Freedom (SDOF) Studies

The study of a simple single degree-of-freedom (SDOF) oscillator can be a useful tool in gaining a better understanding of the governing characteristics of a recentering system. Several researchers have taken this approach and investigated the response of a SDOF system with recentering behavior. Christopoulos et al. (2002a) looked at the response of a system with self centering flag-shaped hysteretic behavior modeled after a post-tensioned (PT) energy dissipating connection. The recentering response was compared to traditional elastoplastic (EP) systems as shown in Figure 2-6. The SDOF oscillator was subjected to a suite of ground motions from California with a probability of exceedance of 10% in 50 years. The study showed the following:

- For every EP system there is at least one flag-shaped recentering system with similar period and strength that resulted in smaller or equal maximum displacements.

- Maximum accelerations were similar for small flag-shaped loading plateau slopes.
- Dissipated energy is generally much larger for the EP system.
- Increasing the slope of the flag-shaped loading plateau for short period and low strength systems was most effective at decreasing the displacement demand.
- Conversely, for long period systems with high strength, increasing the hysteretic area is more effective then increasing the slope of the loading plateau

This study provides a broad overview of how a SDOF system is affected by a PT-based recentering behavior. One of the main highlights of such a system is the ability to eliminate residual deformations.

Following up on this research, Wang and Filiatrault (2008) undertook an even more rigorous investigation into the behavior of a SDOF recentering system. Their work, published in an extensive MCEER technical report, investigated a SDOF recentering system over a variety of parameters and over an expanded set of ground motions. Numerous charts were produced with the purpose of providing a direct design aid for recentering systems. The findings affirmed and expanded on the study by Christopoulos et al. (2002a), including the observation that a recentering system can be used to reduce maximum and residual displacements. Furthermore, the design charts provide a tool for developing a methodology for the design of a recentering system (discussed further in the next section).

In contrast to PT-based systems, other studies have investigated the response of SMA-based SDOF recentering systems. Duval et al. (2000) used random vibrations to analyze the response of a helical SMA spring. Masuda et al. (2002) investigated the effect that the shape of the hysteretic loop has on the dynamic performance. Additionally, Seelecke (2000) investigated the response of a rigid mass suspended by a tube and subjected to torsional loadings. None of these studies, which used SMA as the

backbone of the recentering model, evaluated the performance of the SDOF oscillator subjected to earthquake ground motions. Additionally, they did not present the trends over a range of periods and other structural properties, which would be useful in assessing the applicability of SMA-based devices in earthquake applications. For this reason, a brief SDOF study was conducted in the next chapter of this research to see if additional insight can be gleaned.

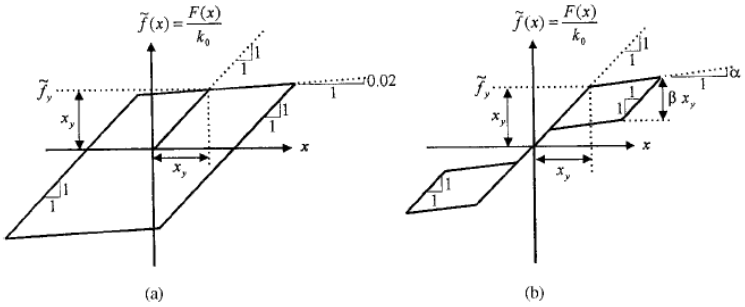

Figure 2-6: (a) elastoplastic and (b) recentering systems (Christopoulos et al., 2002a).

2.3.2. Posttensioned Systems

Several researches have experimentally and analytically investigated PT recentering framing systems. Choek and Lew (1990; 1991) and Cheok et al. (1993) experimentally investigated one-third-scale post-tensioned (PT) precast concrete connections. They found that the PT assemblies, in comparison to cast-in-place monolithic assemblages, increased ductility, decreased damage, and decreased residual drift. Priestley and MacRae (1996) tested PT concrete connections and a 60% scale five-story building as part of the Precast Seismic Structural Systems (PRESSS) initiative. Excellent performance was again reported for the system.

Ricles et al. (2001) expanded the idea of PT connections by investigating their use in steel moment-resisting frames. The connection investigated is shown in Figure

2-6a. The qualitative flag-shaped recentering moment-rotation relationship is shown in Figure 2-6b. This flag-shaped recentering behavior is produced from the synergy between the post-tensioning and the dissipating angles.

In parallel with Ricles' work, Christopoulos et al. (2002b) also extended the post-tensioning concept with several studies. A typical layout of the recentering connection scheme and the details of the PT connection are shown in Figure 2-7a-b, respectively. Energy dissipating bars are used in lieu of angles to create improved damping behavior. The connection was investigated analytically and experimentally. The results showed that the connection had a large amount of ductility, good damping, and excellent recentering.

As a continuation of the SDOF study mentioned in the previous section, Wang and Filiatrault (2008) reported on the shaketable testing of a three-story PT steel frame. A detailed design procedure was outlined for the design of the multi-degree-of-freedom (MDOF) recentering system approximated as a SDOF system. The design procedure used a set of SDOF charts that plot a performance index versus structural period over varying levels of strength factors (yield strength/weight of structure), post-yield stiffnesses, and hysteretic energy dissipation levels. The analytical and experimental results demonstrated that improved performance can be reached with a recentering system.

Yet another system using PT elements has been recently proposed and experimentally evaluated by Christopoulos et al. (2008). Instead of creating a recentering beam-column connection, a self-centering energy dissipating (SCED) bracing system was conceived. This special brace has post-tensioned elements combined with friction energy dissipators in order to produce flag-shaped recentering behavior. The device consists of a HSS tube sliding inside of another HSS tube with a

series of aramid tensioning elements providing a PT force and friction pads creating energy dissipation. Schematics of the SCED system are shown in Figure 2-9.

Tremblay et al. (2008) performed an analytical study of a 2-, 4-, 8-, 12-, and 16-story braced steel frames to further investigate the potential of the SCED device. The SCED braces were compared to buckling restrained braces (BRB) over three suites of ground motions. The SCED system performed very well in comparison to the BRB system; reducing peak story drifts and eliminating residual deformations. However, the analysis did indicate higher maximum accelerations for the SCED system, which was in agreement with the findings of the recentering SDOF studies (Wang and Filiatrault, 2008).

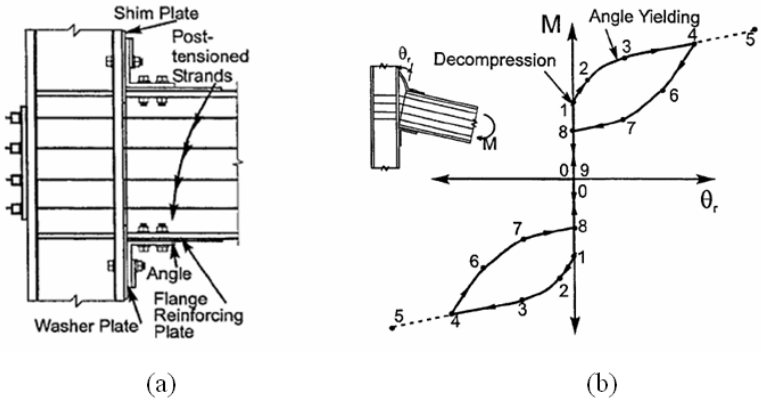

Figure 2-7: (a) Post-tensioned connection with dissipating angles and (b) corresponding moment-rotation relationship (Ricles et al., 2001)

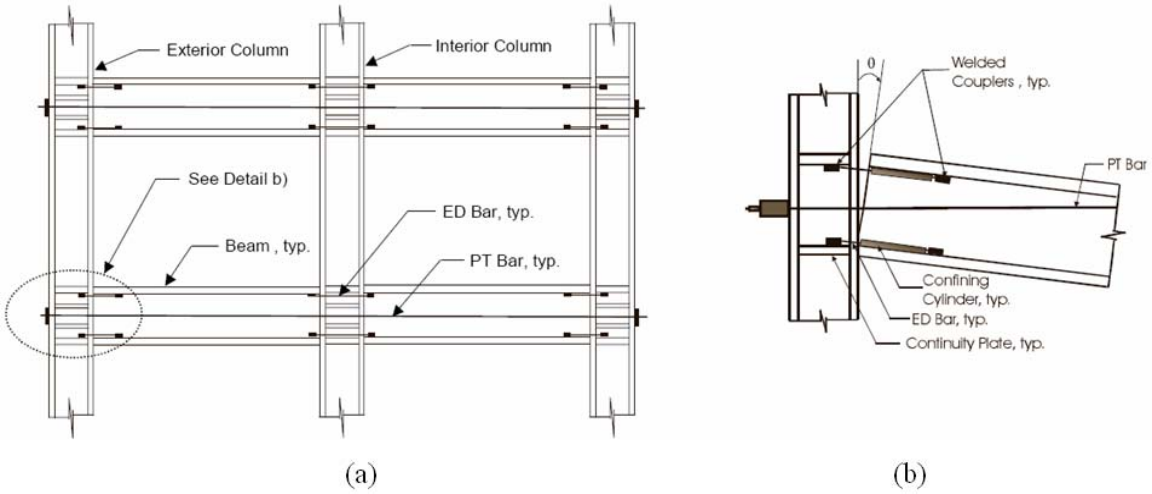

Figure 2-8: (a) Post-tensioned energy dissipating layout and (b) connection (Christopoulos et al., 2002b)

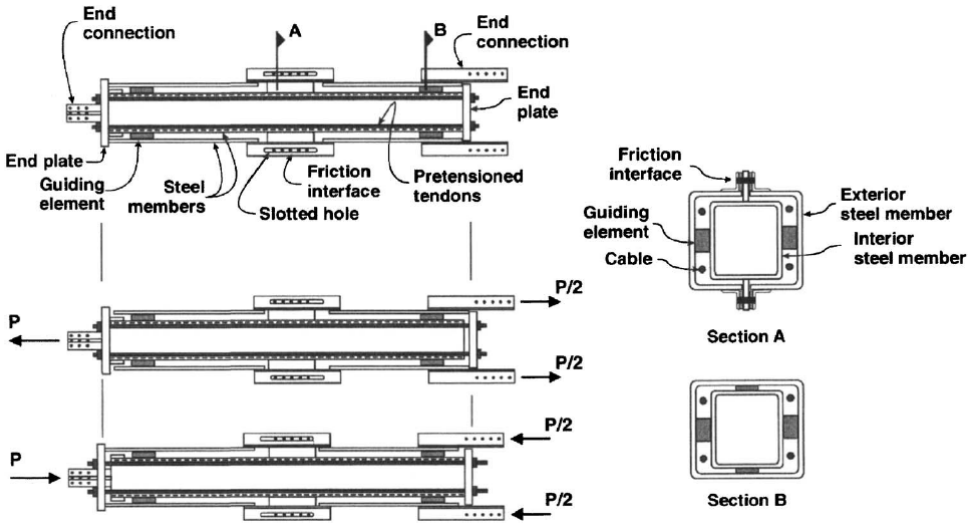

Figure 2-9: SCED device (Christopoulos et al., 2008).

2.3.3. SMA-Based Systems

SMAs have drawn considerable attention in the civil engineering community over the past two decades because of their unique stress-strain behavior. In the 1990's the European Commission launched a research initiative, known as the MANSIDE (Memory Alloy for New Structural Isolation Devises) project to investigate and implement SMAs

into civil engineering structures (MANSIDE, 1998). From this project, several retrofit schemes were investigated and/or developed using SMA wires and bars (Dolce and Cardone, 2006; Dolce et al., 2000; 2001; 2004; 2005; Dolce and Marnetto, 1999). The functioning scheme of one such recentering device is shown in Figure 2-10. The device showed good energy dissipation and excellent recentering. The self-centering friction damped brace (SFDB) developed by Zhu and Zhang (2008) is another SMA-base recentering device. This device is very similar in response to the SCED described in the last section, with the recentering driven by NiTi wires rather aramid fibers (schematic shown in Figure 2-11. The energy dissipation is derived from the sliding friction between the adjacent steel members. A typical force-deformation response for the device is shown in Figure 2-12. Three- and six-story braced frames were used to compare the SFDB vs. BRB vs. SFDB-frictionless. The results show that the SFDB effectively eliminates residual deformations and, on average, reduces maximum inter-story drifts when compared to the BRB.

SMA beam-column connections have also been investigated in the literature. Ocel et al. (2004) investigated the use of SMAs in an exterior connection. They used martensitic (SME) NiTi tendons as the primary moment-resisting elements. In order to recover shape spontaneously, Penar (2005) investigated the use of superelastic NiTi tendons in an interior connection. However, due to unwanted local buckling and poor superelasticity in the NiTi tendons, the connection displayed very little recentering ability.

Analytical work has also been done on SMA beam-column connections. Taftali (2007) presented an extensive study on the probabilistic seismic demand of SMA connections in steel frames. Superelastic SMA connections were shown to be most beneficial in reducing or eliminating residual deformations. This study demonstrated that neither recentering nor energy dissipation produces the optimal response over a range of hazard levels. Rather, Taftali concluded that it may be beneficial to incorporate both

recentering and energy dissipation elements into the same system to optimize the performance while understanding that increased recentering results in reduced system residual deformations.

Recently, Sepulveda et al. (2008) tested a beam-column connection with superelastic CuAlBe SMAs. CuAlBe is a much more cost-effective form of SMA, but has been shown to have inferior (only superelastic until 2.3% strain) behavior when compared to NiTi. Their initial evaluation showed that the SMA connection did not improve the response due to poor performance of the CuAlBe material.

Various other SMA-based systems have been investigated analytically and experimentally. This includes investigations of NiTi bracing systems or devices (Aiken et al., 1993; Cardone and Dolce, 2009; Clark et al., 1995; Dolce et al., 2005; Higashino et al., 1996; Lafortune et al., 2007; McCormick et al., 2007a; Yan et al., 2007; Zhang and Zhu, 2008), investigations of NiTi bridge restrainers (Adachi and Unjoh, 1999; Andrawes and DesRoches, 2005; DesRoches and Delemont, 2002), and investigations of NiTi base isolators for both bridges (Wilde, 2000) and buildings (Dolce et al., 2001; Graesser and Cozzarelli, 1991). Additionally, strategies for seismic retrofit are outlined in work done by Di Sarno and Elnashai (2003).

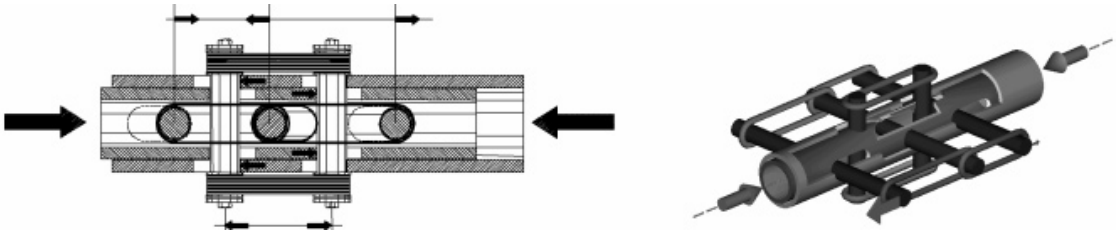

Figure 2-10: Recentering device with superelastic SMAs (Dolce et al., 2000).

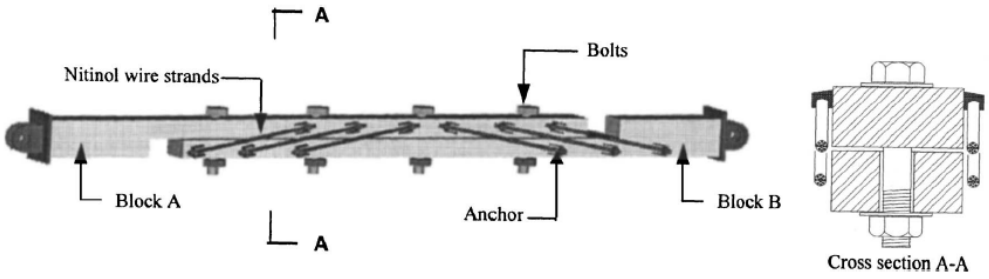

Figure 2-11: Details of self-centering friction damper with NiTi wires (Zhu and Zhang, 2008).

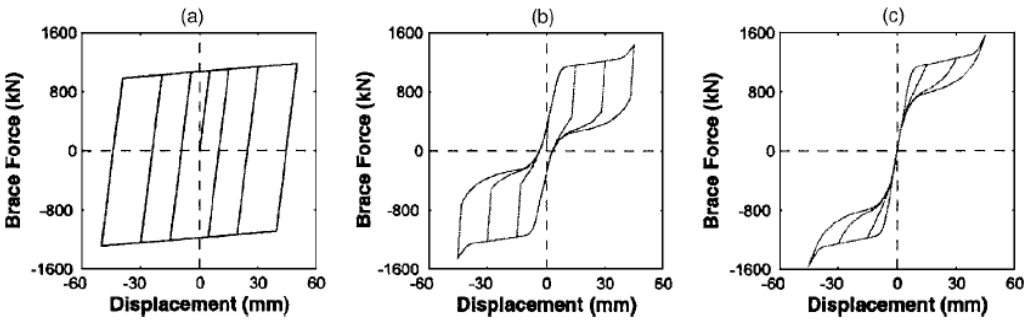

Figure 2-12: Force deformation of (a) friction only, (b) friction + SMA, (c) SMA only (Zhu and Zhang, 2008).

CHAPTER 3

SINGLE DEGREE OF FREEDOM STUDY

3.1. Introduction

This chapter investigates the influence of the superelastic hysteresis on the response of a single degree-of- freedom (SDOF) oscillator. In general, buildings have at least 80% of their modal participation coming from the first mode. Therefore, it is reasonable to approximate a structure as a SDOF oscillator in order to investigate overall response. Several SDOF studies investigating the effects of recentering systems have been conducted by other researchers (as mentioned in Chapter 2). This study approaches the topic from a slightly different angle by doing the following:

- Modeling the flag-shaped hysteresis after NiTi mechanical behavior
- Conducting the analysis over a range of strength reduction factors
- Comparing elements with the same initial stiffness and yield strength
- Varying the flag-shaped hysteresis based on optimum parallel system behavior

The parameters of this SDOF study were selected to help determine the important factors that govern a SMA-based recentering system's response, which in-turn motivated the experimental portion of this research.

3.2. Approach

With SMA's ability to recover large strains, the effects of this unique stress-strain behavior on displacement and acceleration demands were investigated under code-level earthquakes. This was done in the following ways:

- First, the differences in the response (displacement and acceleration) of a normal elastoplastic (EP) and a generic recentering (SMA) system were investigated. Both of these systems were given zero post-yield (or transformation for the SMA) stiffness.
- Second, the level of hysteretic damping in the recentering system was increased to determine if improved behavior could be obtained. Previous research has noted that SMAs have varying hysteretic damping properties depending on thermomechanical processing and physical dimensions (DesRoches et al., 2004). An SMA system was given nearly optimum energy dissipation and then the performance was compared to the other systems.
- Third, the effect of the loading plateau stiffness was investigated by comparing two new SMA and EP systems with equivalent loading plateau stiffnesses. Since the mechanical behavior of large-scale SMA specimens generally show moderate loading plateau stiffnesses, this is a more realistic approximation.
- Fourth, the effect of including the stress-induced martensite's stiffness was investigated. Since SMAs begin to stiffen at 6-8% strain, a true SMA-based system would have this inherent stiffening effect. Once the plateau is crossed, it is expected that improved behavior will be observed.
- Finally, a case study was investigated in order to study the effects of using a parallel system consisting of an SMA and an EP element. The parallel system was created as a practical way to increase the energy dissipation of the superelastic hysteretic loop while still maintaining a high level of recentering. Though it depends on the exact system composition, in this example, adding an EP element in parallel with an SMA element increased the energy dissipation by approximately 300% (compared to the equivalent SMA-only system).

3.3. Analytical Setup

The SDOF system was idealized as a mass, *m*, attached to a spring with stiffness, *k*, and a dashpot with damping coefficient, *c*. In all of the analysis, *c* was held constant by defining ζ, the damping ratio, to be 5%. This value is commonly assumed in analytical studies and should not be construed as a property of these recentering systems. The damping coefficient is defined as:

$$c = 2m\omega_n\zeta \tag{3.1}$$

The general force-displacement relationships for the SMA and EP systems are shown in the top of Figure 3-1. The parameters that define the SMA system are $\gamma_{1\text{-}4}$ (normalized force levels of SMA hysteresis), β (loading plateau width), and *k* (stiffness). The parameters that define the EP system are γ_1 (normalized yield force), α (hardening value), and *k* (stiffness).

A total of six different systems were created (*SMA1-4*, *EP1-2*) as shown in Figure 3-2. These systems were compared to investigate the effects of loading plateau stiffness (strain hardening for EP), recentering, and energy dissipation. *SMA1* was modeled after an idealized SMA response with zero transformation plateau stiffness and no deformation limit to this plateau. *SMA2* was modeled the same as *SMA1* but with a larger hysteretic loop. *SMA3* was modeled after SMA experimental test response with a typical stress plateau slope (DesRoches et al., 2004). The deformation limit of the plateau was again extended to prevent the stiffening effect that occurs in the martensite phase. *SMA4* was modeled after SMA experimental test response with a normal-sloped loading plateau and the martensite stiffening included (this is intended to be the most realistic model in this study). For the non-recentering systems, *EP1* and *EP2* were modeled after an elastic-perfectly-plastic system and an elastic-plastic system with strain hardening (equivalent to the loading plateau slope in the *SMA3-4* models), respectively.

The finite element program used for analysis was OpenSEES (McKenna and Fenves, 2004). The SMA constitutive model used was a modified one-dimensional model (Fugazza, 2003) first proposed by Auricchio and Sacco (1997). This behavior is shown in the left part of Figure 3-1 with two trigger-lines controlling the behavior around the hysteretic loop. The model implicitly assumed the SMA has no strength degradation and no residual strain accumulation. This is a reasonable assumption when SMAs are mechanically trained (McCormick et al., 2005) and was determined sufficient for this study.

One suite of ground motions from the Los Angeles (LA) area was taken from the FEMA/SAC building study (Somerville et al., 1997). The suite consisted of 20 records with a 10% probability of exceedance in 50 years (LA1-20). In order to assist in the comparison of results, each ground motion record was scaled to the suite's average spectral acceleration at the corresponding period that was being analyzed.

The analysis was run over a range of periods and strength reduction factors from 0.1 to 2.1 sec. at an interval of 0.2 sec. This period range covers the typical range expected for single-story through small high-rise buildings. The strength reduction factor, R, was assigned to be 2, 4, or 8. Since it is generally desirable to have larger strength reduction factors (in order to decrease the forces and resulting member sizes in a structure), special attention was paid to the structures with the higher strength reduction factor.

The fundamental issue investigated in this study was whether there are any noticeable trends in which recentering was more advantageous then damping. In order to probe this question, the performance parameters that were assessed are the maximum displacement (a measure of structural damage) and maximum acceleration (a measure of serviceability). The residual displacement was not considered during the majority of this study because the SMA-based systems all have zero residual (by

definition). However, a brief case study at the end of this chapter highlights the difference in residual displacement, which is arguably the most important benefit of using a recentering system.

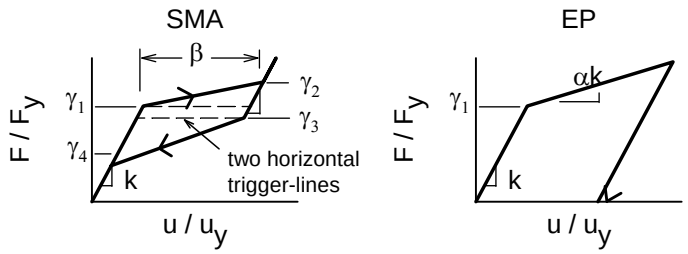

Figure 3-1: Definition of the SMA and EP force-displacement relationships.

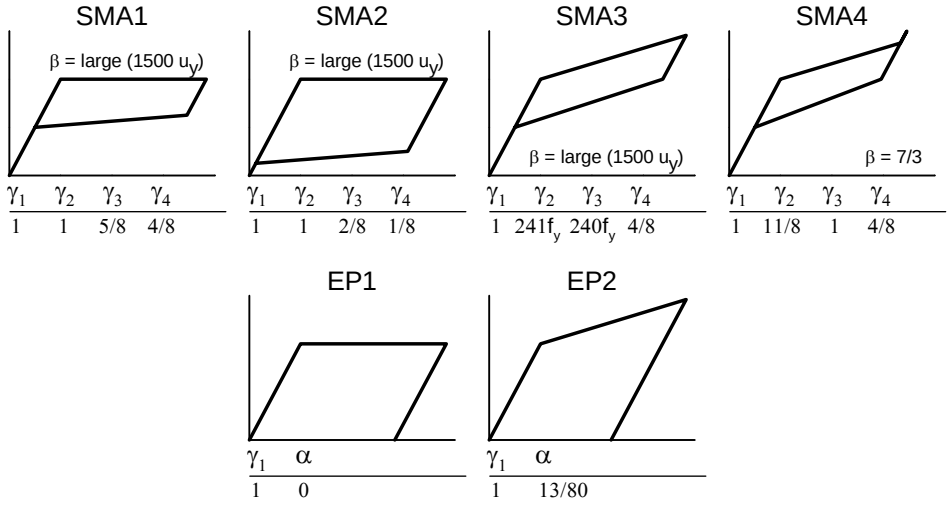

Figure 3-2: Force-displacement relationships of the four SMA (*SMA1-4*) and two EP (*EP1-2*) systems.

3.4. Results and Discussion

3.4.1. General Behavior

To illustrate the general trends seen in this study, an example displacement-time-history and force-displacement responses are shown in Figure 3-3. These results were from systems with a period of 0.5 sec. and strength reduction factor of 2 subjected to the LA1 record. In general, the SMA-based systems had larger maximum displacements than the equivalent EP system. However, the residual displacements of the SMA-based system were always zero compared to varying levels of residual in the EP systems. The larger maximum displacements can be attributed to the SMA system not dissipating as much energy compared to its EP counterpart. This undissipated energy resulted in the SMA system incurring larger displacement demands.

For the entire range of results, the performance of the recentering system was assessed by dividing the SMA system by the EP system. This term will be referred to as the normalized displacement. A normalized displacement less than unity indicates that the SMA system outperformed the EP system. Conversely, a normalized displacement greater than unity indicates the EP system outperformed the SMA system. Additionally, error bars of plus/minus one standard deviation were plotted to give a representation of the data spread.

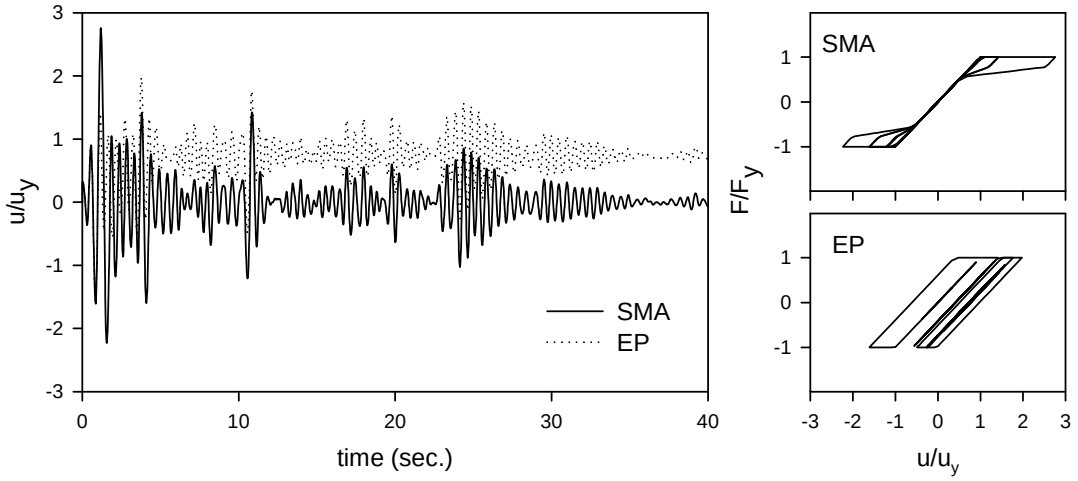

Figure 3-3: Displacement time history of SMA and EP systems for T=0.5 sec. and R=2.

3.4.2. Displacement and Acceleration Demands

3.4.2.1. SMA1 vs. EP1

SMA1 and *EP1* were the first two systems compared. Both of these systems have zero load plateau stiffnesses and unlimited ductility (β = large ($1500u_y$) for the SMA). By comparing these two systems, the benefits of damping were being weighed against that of recentering. The results of this comparison are shown in row (a) of Figure 3-4 (displacement) and Figure 3-5 (acceleration).

In general, the maximum displacement of the SMA approached that of the EP system for increasing period and decreasing R. An exception to this trend was seen at small periods (T < 0.5 sec.) where increasing R results in improved SMA performance. However, in this same small period range, the behavior of SMA was poor in comparison to the EP system. These results support the idea that recentering systems (which, by definition, have less hysteretic damping than an EP system) generally perform better for longer (larger) period systems. Conversely, for shorter (smaller) period systems, damping was expected to be more effective. This explains why the EP system was greatly outperforming the SMA system at shorter periods.

In terms of the acceleration demands, the performance of the SMA system approached that of the EP system as the period increased. For periods greater than 1.0 sec., the difference in acceleration demand between the two systems was negligible. Additionally, the acceleration demands did not seem to be sensitive to a change in R, especially at longer periods (T > 1.0 sec.).

3.4.2.2. SMA2 vs. EP1

In order to investigate the benefit of increased damping in a recentering system, the *SMA2* system was compared to the *EP1* system. *SMA2* had approximately 50% more energy dissipation in its hysteresis in comparison to *SMA1*. The results of this increase are shown in row (b) of Figure 3-4 (displacement) and Figure 3-5 (acceleration).

The trends observed in this comparison were nearly identical to that seen in the previous comparison (*SMA1* vs. *EP1*) for both maximum displacement and acceleration demand. However, when comparing the results of *SMA1* to *SMA2* (row (a) to row (b)), there was a clear improvement of behavior in the *SMA2* system. The displacement demand for the *SMA2* system was reduced across the entire range of T and R. However, the EP system still consistently outperformed the SMA system with regards to displacement demand. In contrast, the SMA system's acceleration demand was nearly equivalent to that of the EP system for medium to long period levels, which was consistent with the *SMA1* performance.

3.4.2.3. SMA3 vs. EP2

For *SMA3* and *EP2*, stiffness was introduced into the loading plateaus. *SMA3* and *EP2* both had the same loading plateau slopes (slope = 0.16). The slope was determined from mechanical test results of a 12.7 mm (0.5 in.) diameter NiTi bar (McCormick and DesRoches, 2004). The results of this comparison are shown in row (c) of Figure 3-4 (displacement) and Figure 3-5 (acceleration).

The displacement demands were similar to that seen in the comparison between *SMA1* vs. *EP1*. An exception to this similarity was seen in the short period range, where *SMA3* (with loading plateau stiffness) performed better then *SMA1* (without loading plateau stiffness). In terms of acceleration demands, no significant differences were observed between *SMA1* and *SMA3*, indicating little sensitivity to the loading plateau stiffness.

3.4.2.4. SMA4 vs. EP2

In order to investigate the effect of the stiffening seen in SMA after the loading plateau has been crossed, *SMA4* was compared with *EP2*. The loading plateau length was set to 7/3 u_y (an approximation from mechanical tests by DesRoches et al. (2004)). The results of this comparison are shown in row (d) of Figure 3-4 (displacement) and Figure 3-5 (acceleration).

In terms of displacement demand at short periods, *SMA4* dramatically reduced the response in comparison to *SMA3*. Additionally, *SMA4* had improved performance vs. *EP1* as the R increased, with a dramatic improvement observed at short periods. The improved performance was the direct result of *SMA4's* stiffness after the loading plateau, preventing further displacements at the expense of attracting increased loads. This effect was especially dominant at short periods and larger R values. The resulting effect on a MDOF system is anticipated to be positive because this behavior will help prevent the formation of soft-stories and force a more uniform drift demand along the entire height of a structure.

In terms of acceleration demand, *SMA4's* response was essentially identical for the R of 2. However, acceleration demands increased for R values of 4 and 8, with the most significant increase in the period range of 0.3 to 1.1 sec. This result indicates that acceleration demands will be increased in a real SMA-based system due to the stiffness increase after the SMA has been fully transformed from austenite to martensite.

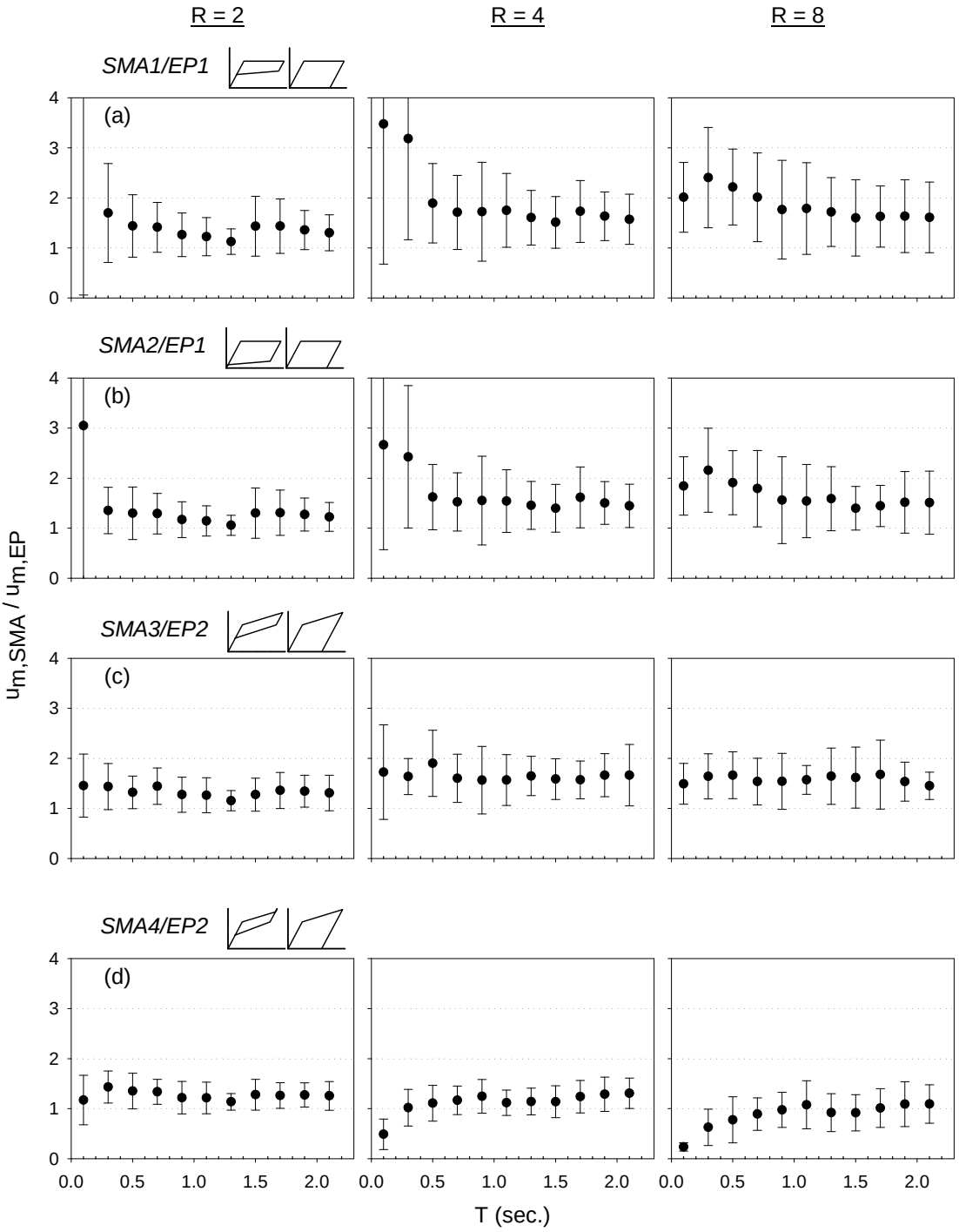

Figure 3-4: Maxiumum average displacement of SMA divided by the maximum displacement of EP over a range of periods subjected to LA1-20. Row (a) is SMA1/EP1, (b) is SMA2/EP1, (c) is SMA3/EP2, and (d) is SMA4/ EP2.

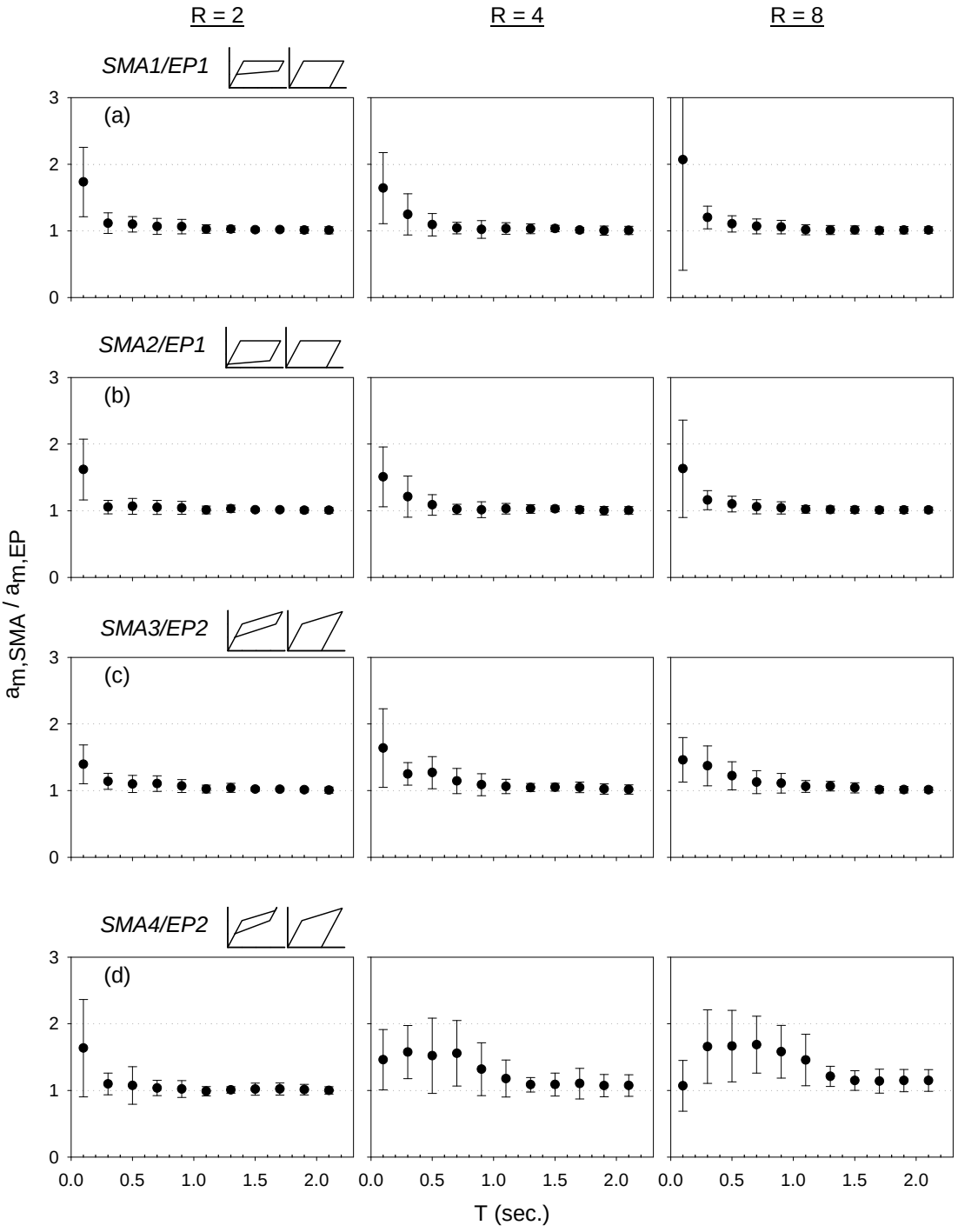

Figure 3-5: Maxiumum average acceleration of SMA divided by the maximum acceleration of EP over a range of periods subjected to LA1-20. Row (a) is SMA1/EP1, (b) is SMA2/EP1, (c) is SMA3/EP1, and (d) is SMA4/ EP2.

3.4.3. Case Study: SMA4 vs. EP1 vs. PARA1

The beneficial effects of increased hysteretic damping and post-plateau stiffness were shown in the previous sections. In order to create a system with maximized energy dissipation and minimized residual accumulation, *PARA1* system was created with SMA and EP elements in parallel. The system selected has the force-deformation as show in Figure 3-6, where T=1.1 sec. and R=4. The hysteretic damping is 3.4 times that found in an SMA-only system. The *SMA4* was used as the SMA model.

The PARA system was subjected to the scaled LA1 ground motion. The resulting force-deformation responses and displacement time histories are shown in Figure 3-7. The normalized maximum and residual displacements (u_m/u_y, u_r/u_y) for the *SMA4*, *PARA1*, and *EP1* systems were (5.9, 0.0), (5.6, 0.1), and (6.4, 4.7), respectively. The *PARA1* and *SMA4* system have 5-10% smaller displacement demands compared to the *EP1* system in this case, giving these systems a slight advantage. However, there is a clear advantage when comparing the residual deformations, in which the *PARA1* system returned to approximately 1.8% of its maximum deformation compared to the EP system returning to 73% of its maximum deformation. This indicated there is potential in the improved damping provided by a parallel-type system, as was supported by the investigation of the increased damping system of *SMA2*. If the SMA's restoring force is properly balanced with the yielding force of the EP element to ensure a good balance of energy dissipation and recentering ability, the response can be improved while simultaneously limiting unwanted residual damage.

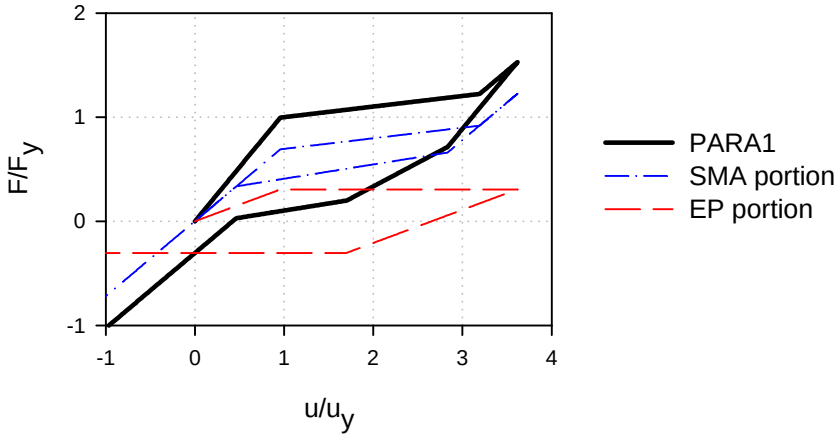

Figure 3-6: Force-deformation of parallel system created for the case study.

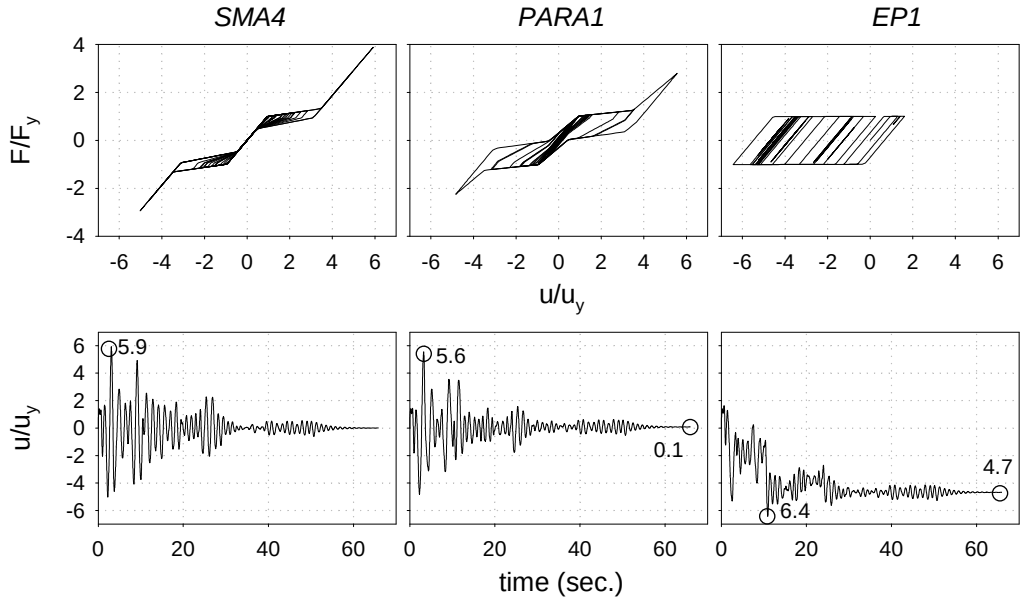

Figure 3-7: Force-deformation and displacement time histories for *SMA4*, *PARA1*, and *EP1* systems.

3.4.4. Summary

A new look was taken into the performance of a superelastic SDOF system when subjected to a suite of ground motions. This was specifically done in the light of NiTi SMA characteristics that have been documented in numerous studies. In general, SMAs become more effective in reducing the response of a system in the longer period range when compared to traditional elastoplastic systems. However, unlike elastoplastic systems, SDOF systems with SMAs have limited residual deformations. The effect of increasing the size of the recentering hysteretic loop was examined.

The results showed that the increased hysteretic loop adds a positive effect on the performance, reducing displacements without noticeably affecting acceleration demands and residual displacements. Additionally, the benefit of accounting for the post-plateau stiffness in an SMA was demonstrated. This post-plateau stiffness reduced displacement demands over a broad range of periods, though the side-effect was an increase in force demands. However, it is expected that this behavior will have a beneficial effect on a multiple degree-of-freedom system, spreading ductility demand more uniformly throughout the system. Lastly, a practical way to increase the hysteretic damping was proposed by using a parallel system. A case study showed a parallel system can moderately decrease displacement demands when compared with a SMA-only system while maintaining small residual displacements when compared with an elastoplastic system.

In summary, it should be noted that this was a preliminary study into the wide range of parameters that affect a SDOF recentering system. Though some information was gleaned, further analysis need to be conducted to understand the circumstances (e.g. period range, ground motion characteristics) in which damping, recentering, or a mix of both is most effective in reducing structural response parameters.

CHAPTER 4

TENSION/COMPRESSION DEVICE

4.1. Introduction

Engineers continue to look for creative new ways to use SMAs in hopes of enhancing structural performance during extreme events. This chapter investigates the behavior of a new tension/compression device developed for bracing applications in buildings. The device is designed to allow various forms of NiTi SMA, such as helical springs or Belleville washers, to be used in compression. The device allows both overall extension (tension) and contraction (compression) while subjecting the NiTi to a compression deformation mode. It is possible, due to the versatility of the design, to adjust the force and stroke of the device without changing the overall configuration. This new device was subjected to a cyclic loading protocol that tests the NiTi element's ability to recover large deformations. The effect of different NiTi configurations was evaluated in the study. The results for the helical spring show good recentering and damping. However, the Belleville washer results call for further investigation and development.

4.2. Background

As mentioned in the literature review of CHAPTER 2, a variety of research initiatives have looked at the viability of using SMAs as structural recentering and/or damping elements in both bridges and buildings (Wilson and Wesolowsky, 2005). Dolce et al. (2000) devised several types of recentering systems using SMA wires and bars as part of the European Commission sponsored MANSIDE Project (1998). Experimental testing of their devices showed predictable behavior, good energy dissipations, and excellent

recentering. However, the concepts and devices gleaned from Dolce's research have found limited application. Additionally, other SMA-based systems have been investigated without wide implementation, including a self-centering friction damped brace by Zhu and Zhang (2008) and beam-column connections by Ocel et al. (2004), Penar (2005), and Sepulveda (2008).

The inherent advantage of using an SMA-based system is that it can be designed 1) to significantly reduce the residual deformations after an earthquake and 2) to have the ductility and energy dissipation to prevent collapse. This research presents the development and initial testing of a new device that facilitates the use of two new forms of NiTi SMA: helical springs and Belleville washers. Whether the device is in tension or compression, the SMA elements are compressed. To the author's knowledge, there is no published research on the investigation of SMA helical springs or Belleville washers for structural applications (besides that published as part of this work (Speicher et al., 2009)).

4.3. Device Description

The tension/compression (TC) device is a cylindrical shaped damper that can accommodate a variety of SMA elements. The body and the shaft of the device were made out of standard 304 stainless steel cylinders. Schematic drawings of the device with a helical spring and a Belleville washer stack are shown in Figure 4-1. The device is approximately 50 cm (19.7 in.) in length and 6.4 cm (2.5 in.) in diameter. The stroke capacity of the damper is dependent on the active element that is inserted, with values in the range of 2-5 cm (0.8-2.0 in.) for the arrangements presented in this study. The damper was fitted with either helical springs or Belleville washers. Different strength and stiffness properties can be easily obtained by using different combinations of active

elements. Additionally, this device setup is scalable to accommodate a wide range of force and stroke capacities.

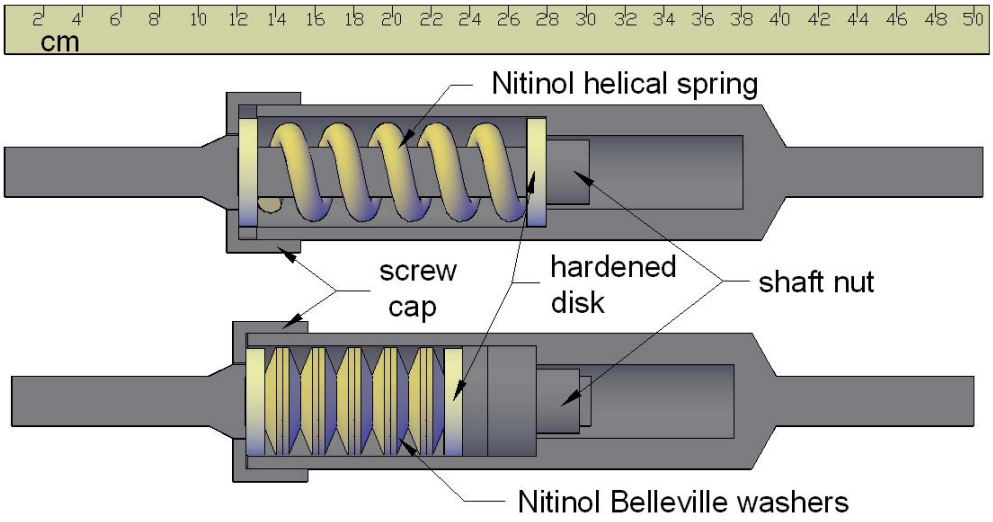

Figure 4-1: Internal view of tension/compression device.

4.4. Active Element Description

Two different types of active elements were used in the testing of the device: NiTi helical springs and NiTi Belleville washers. This section briefly describes each element.

4.4.1. Helical Springs

Two springs were used in this study: a hollow spring and a solid spring. The springs were made from NiTi 508 (50.8% atomic % Nickel). The hollow NiTi spring has a diameter of 3.8 cm (1.5 in.), an initial length of 14.2 cm (5.6 in.), and a deformation capacity of 8.0 cm (3.1 in.) (undeformed vs. fully compressed). The hollow spring was made from tubing with an outside and inside diameter of 12.5 mm (0.5 in.) and 9.5 mm (0.37 in.), respectively. The solid NiTi spring has a diameter of 3.8 cm (1.5 in.), an initial

length of 13.0 cm (5.1 in.), and a deformation capacity of 4.6 cm (1.8 in.) and was made from solid stock with a 12.5 mm (0.5 in.) diameter.

Both springs were made by heating small sequential sections of the stock with a small torch just to the point of initial softening (very low red heat, approx. 650-700 °C). The softened metal was then bent around a mandrel to produce a helix. The finished coils were given a final heat treatment to achieve uniform properties and good superelasticity. Full details of this process are proprietary information of Nitinol Technology Inc.

4.4.2. Belleville (Spring) Washers

The NiTi Belleville washers were 5.5 cm (2.2 in.) wide, 0.64 cm (0.25 in.) tall, and 0.31 cm (0.12 in.) thick. The washers were cut with a waterjet from a hot-rolled sheet of standard NiTi 508. Two phases of testing were conducted on the washers. In *Phase I* (the first set), the conical shape was made using a 30° angled cone. This yielded washers with a cone angle of 23-25°. A set of 12 washers was used for all the testing in this phase, including the individual and stacked washer tests. For *Phase II* (the second set), the *Phase I* washers were reformed to have an increased cone angle of 27-30°. This time a set of 8 washers were used for a single stacked test. Additionally, several individual cyclic tests were conducted in *Phase I* and *Phase II* to investigate various questions that surfaced during other tests.

4.5. Experimental Setup

A 250 kN (55 kip) MTS Universal Testing Machine (shown in Figure 4-2a) was used for the tests. The MTS machine was fitted with hydraulic vee-notched wedge grips which could accommodate a rod diameter up to 1.9 cm (0.75 in.). Stainless steel coupler elements were used to transfer the force from the 2.5 cm (1 in.) diameter rods of the

damper to 1.9 cm (0.75 in.) diameter rods gripped by the MTS machine. The MTS machine was controlled by a Teststar controller running Testware software. The tests were conducted in displacement control using the built-in LVDT attached to the bottom grip.

A far field loading protocol, modeled after the protocol used in the SAC Steel Project (SAC, 1997), was selected for the experiments. The loading protocol, shown in Figure 4-2b, uses the testing machine's stroke as the deformation parameter. For each specimen arrangement, the maximum deformation was calculated and then 90% of this value was set as the test-target maximum (Δ_{max}). This was done to prevent overloading of the device. A quasi-static loading rate was set at 0.13 cm/sec (0.05 in./sec) to eliminate dynamic effects. Though SMA's behavior is not completely rate-independent, loading rate effects were ignored for this study. Additionally, all experiments were carried out under ambient temperatures in the range of 26-28 °C. Self-heating was not recorded because of the difficulty in monitoring the heat in the confined device and it was not expected to greatly impact the tests due to the quasi-static protocol implemented.

As mentioned before, the tension/compression device was fabricated to facilitate the ability to implement different types of active elements. In this investigation, the following six different tests were conducted:

- ***Test A***: Hollow NiTi helical spring
- ***Test B***: Solid NiTi helical spring
- ***Test C***: 10 NiTi Belleville washers, single-stacked
- ***Test D***: 12 NiTi Belleville washers, double-stacked
- ***Test E***: 12 NiTi Belleville washers, triple-stacked
- ***Test F***: 8 NiTi Belleville washers, triple-stacked, increased depth, spherical spacer

Additionally, element level tests were conducted on the individual washers.

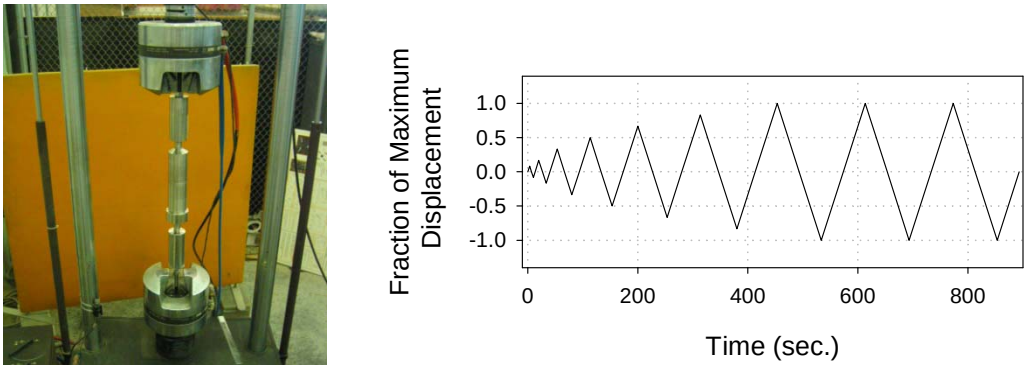

Figure 4-2: Tension/compression device (a) test machine setup and (b) example loading protocol.

4.6. Results and Discussion – Helical Spring Tests

4.6.1. Results – Hollow Helical Spring

Test A was performed using the hollow NiTi spring as the active element. The spring was inserted into the device and the shaft nut was tightened to give the spring 4.1 cm (1.6 in.) of precompression (shown in Figure 4-3). This was done to increase the initial stiffness of the device. The length of the spring (in the precompressed state) was 10.1 cm (4.0 in.). The fully compressed length was approximately 5.8 cm (2.3 in.). This resulted in a maximum device stroke of 4.2 cm (1.7 in.).

The test-target maximum deformation, Δ_{max}, was set to 3.8 cm (1.5 in.) for this test. Using the previously described protocol, the resulting force-deformation plot was obtained as shown in Figure 4-4. The 1/3, 2/3, and full Δ_{max} cycles are highlighted to show the progressive behavior. The precompressed helical spring provided high initial stiffness and recentering over the entire cyclic protocol.

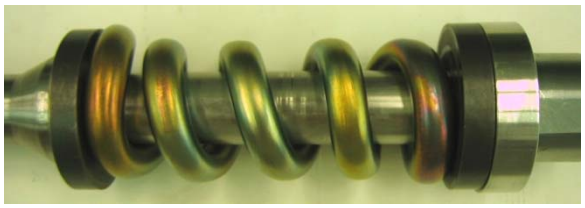

Figure 4-3: Nitinol spring loaded on center shaft (*Test A* and *B*).

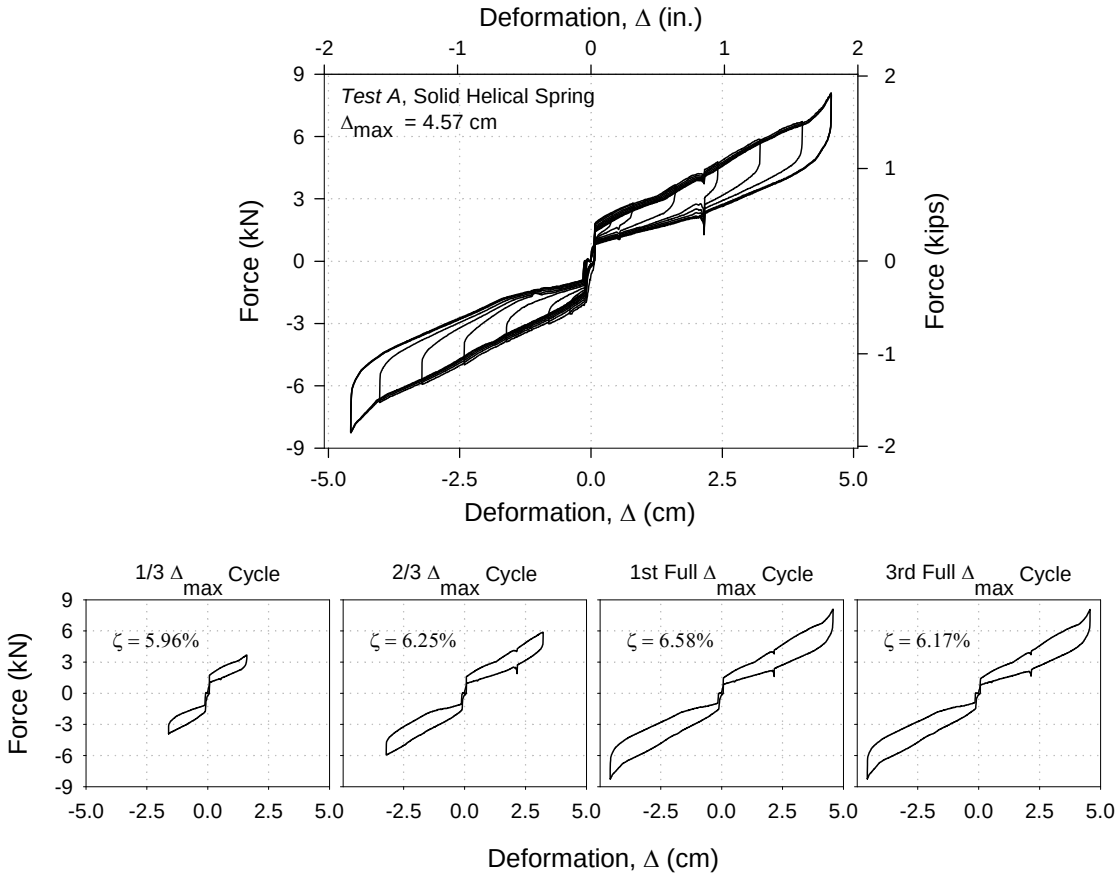

Figure 4-4: Force-deformation response of hollow Nitinol spring in device (*Test A*).

4.6.2. Results – Solid Helical Spring

Test B was performed using the solid NiTi spring as the active element. Again the spring was inserted into the device and the shaft nut was tightened to give the spring 1.2 cm (0.45 in.) of precompression. The spring was only precompressed this amount

because of how the spring fit on the shaft. The length of the spring (in the precompressed state) was 11.8 cm (4.7 in.) and the fully compressed length was estimated at 6.8 cm (2.7 in.). This resulted in a maximum device stroke of 5.1 cm (2 in.); in which 90% of this value, 4.6 cm (1.8 in.), was used for the test-target maximum. The force-deformation for *Test B* is shown in Figure 4-5. The qualitative behavior was similar to that seen in *Test A*.

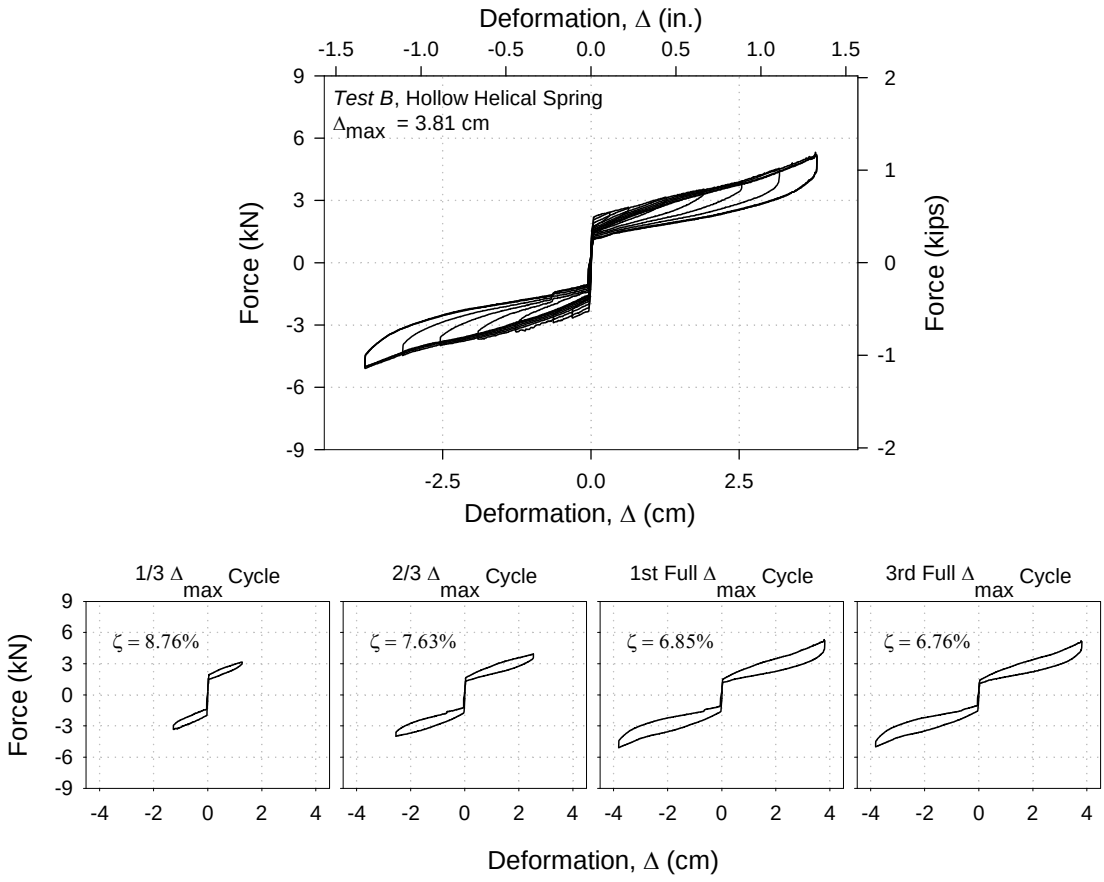

Figure 4-5: Force-deformation response solid Nitinol spring in device (*Test B).*

4.6.3. Discussion - Helical Spring Tests

The force-deformation relationships for both *Tests A* and *B* demonstrate good hysteretic damping, limited strength degradation, and excellent repeatability. In assessing the performance of a damper, the equivalent viscous damping level and the consistency of force levels are two important issues. The equivalent viscous damping is defined as:

$$\zeta = E_D/(4\pi E_{so})$$

where, E_D is the energy dissipated in one cycle and E_{so} is the energy absorbed by an equivalent linear elastic system loaded to the same maximum force and displacement level as used in E_D. In structural engineering, typical values of ζ are around 5-10%.

For this study, the “yield” force was defined as the force level in which the overall device breaks from its initial stiffness; which is the “kinked” point in the bilinear loading response. Also, the yield force is defined at the positive (tension) stroke of the device. Ideally this should not matter, but in practice there were some small differences between the positive and negative behavior.

The superelasticity combined with precompression of the spring resulted in a slender flag-shaped hysteric loop that accounted for ζ ranging from 6-11%, with the majority of the values between 6-7% for the hollow spring and 7-9% for the solid spring. In Figure 4-6a, the trend of ζ as a function of deformation is presented. In comparison to the solid spring, the hollow spring tended to have more stable levels of damping over the entire cyclic range.

When interpreting the behavior of the force levels in *Tests A* and *B*, it should be noted that the precompression given to the hollow spring was almost 4 times that given to the solid spring. As a result, the hollow spring setup had a higher yield force then the solid spring, which at first glance is counterintuitive. However, the stiffness of the sloped loading plateau is clearly larger for the solid spring.

The yield forces for the hollow and solid springs are shown vs. the fraction of Δ_{max} in Figure 4-6b. Both springs have the same trend; the yield force decreases as the loading cycles increase. The hollow spring yield force decreases faster than that of its solid counterpart. This can be contributed to the hollow spring having a larger precompression. When the cyclic loading is applied, the hollow spring is presumably pushed further into its superelastic range which results in an accumulation of residual deformations. This accumulation presets stress in the material causing a reduction in the yield force. Finally, it noted that further investigation should be conducted to investigate how much of the superelasticity of the NiTi is being exploited.

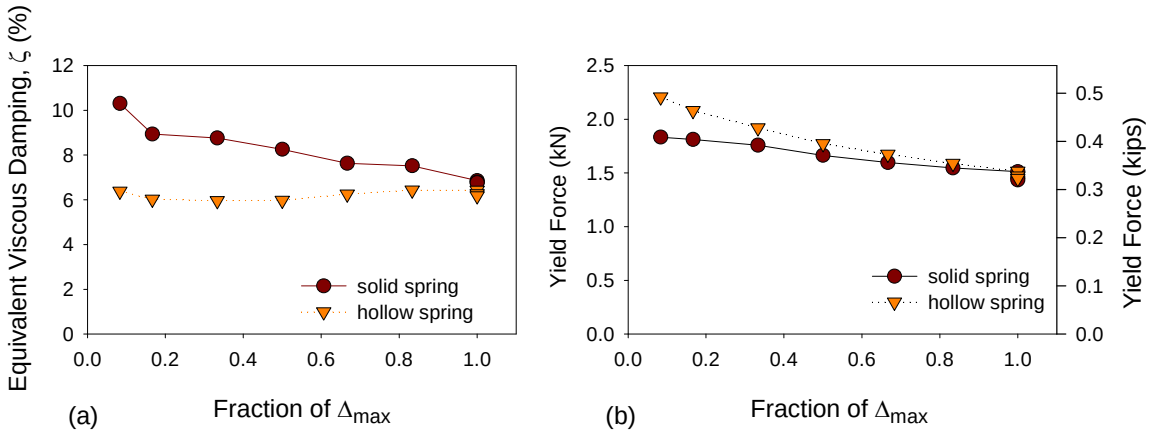

Figure 4-6: Helical spring tests (a) equivalent viscous damping and (b) yield forces over a range of deformations.

4.7. Results and Discussion – NiTi Belleville Washer Tests: *Phase I*

For *Phase I* testing, the NiTi washers had a cone angle of approximately 23-25°. A series of individual (monotonic) and stacked (cyclic) tests were carried out to assess the behavior.

4.7.1. Individual

Three washers were randomly selected for compression testing from the set of 12 used in this phase of testing. These tests were performed using the MTS machine as shown in Figure 4-7. Each individual Belleville washer was placed between two 1.3 cm (0.5 in.) hardened disks and compressed until just short of flat. The resulting duck-head-shaped force-deformation curves are shown in Figure 4-8. The washers had good initial stiffness and strength, but at a deformation of approximately 0.15 cm (0.06 in.) the force carrying capacity peaks and there is a significant load drop-off until the imposed deformation is released at 0.61 cm (0.24 in.).

The trends for all three individual washers were the same but there were varying levels of strength, stiffness, and residual deformations. The large initial stiffness followed by a peaking and dropping-off of load carrying capacity can be explained when looking at the geometry of the washer. A handbook (Fromm and Kleiner, 2003) produced by Schnorr Corporation thoroughly details the behavior of Belleville washers made from Hookian elastic materials. Washers with similar geometry to those used in these tests show a response characteristic similar to Figure 4-8, excluding the superelastic recovery seen during the release of the deformation.

The effect of the superelasticity of the washer is not fully understood and more investigation is needed. However, when the washers were loaded to the flat position, some had the tendency to pass through a region of bifurcation and buckle (invert) into another stable configuration. After recovering the shape with a wooden mallet, little-to-no residual deformations were observed. Generally in structural engineering, it is desired to have materials that retain load carrying capacity when subjected to large deformations, which is not the case here. A strategy to correct this behavior and prevent inverting is proposed in the *Phase II* testing.

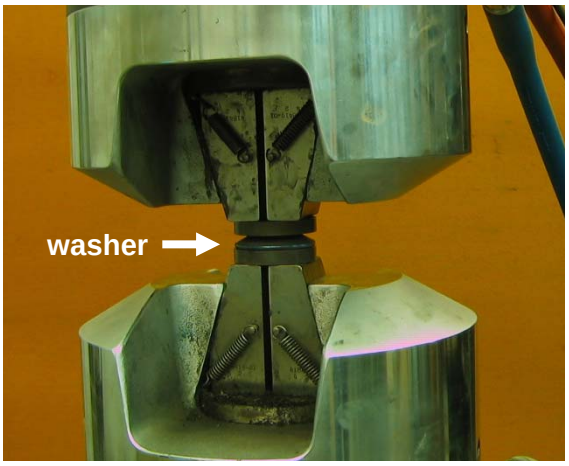

Figure 4-7: Test setup for individual washer test.

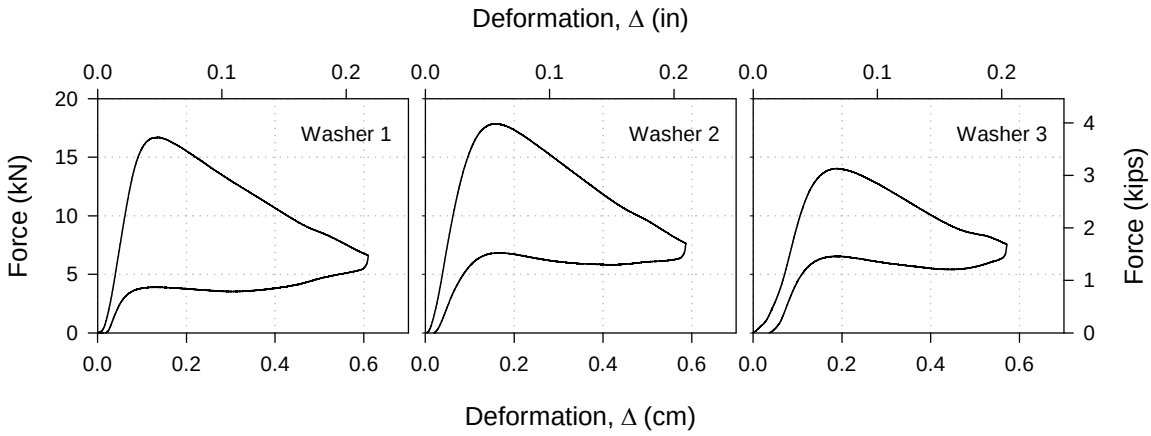

Figure 4-8: Response of individual NiTi Belleville washers under compression (*Phase I*).

4.7.2. Single-Stacked

Test C was conducted on a washer stack with the most flexible configuration of 10 single-stacked washers as shown in Figure 4-9. Flat steel washers of 0.2 cm (0.08 in.) thickness were inserted between each SMA washer in an attempt to prevent the SMA washers from inverting as seen in preliminary tests. As stated in the specimen

description section, the SMA washers used in this test were not virgin; they had been used in preliminary tests.

The initial length of the washer configuration was 10.4 cm (4.1 in.) after the shaft was hand-tightened. The Δ_{max} was 5.1 cm (2.0 in.). The cyclic force-deformation curves are shown in Figure 4-10. The washer stack gave semi-sporadic loading and unloading plateau paths, but these paths were repeatable and consistent at smaller deformation levels.

Residual deformations were observed as the device was subjected to larger deformations. After the test was complete and the damper was disassembled, it was observed that one of the washers had inverted. The flat washers did not completely prevent the SMA washers from inverting. To recover its original shape, the washer was hit with a wooden mallet against a hard surface. The washer promptly snapped back.

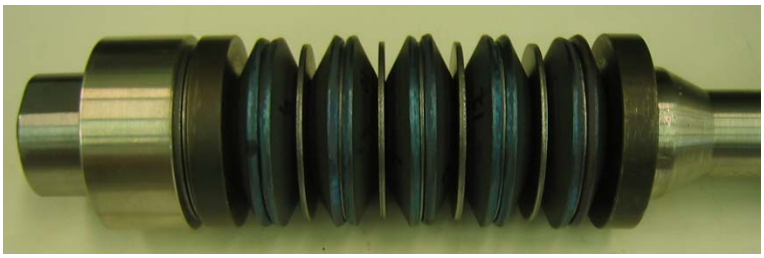

Figure 4-9: Washer configuration for *Test C.*

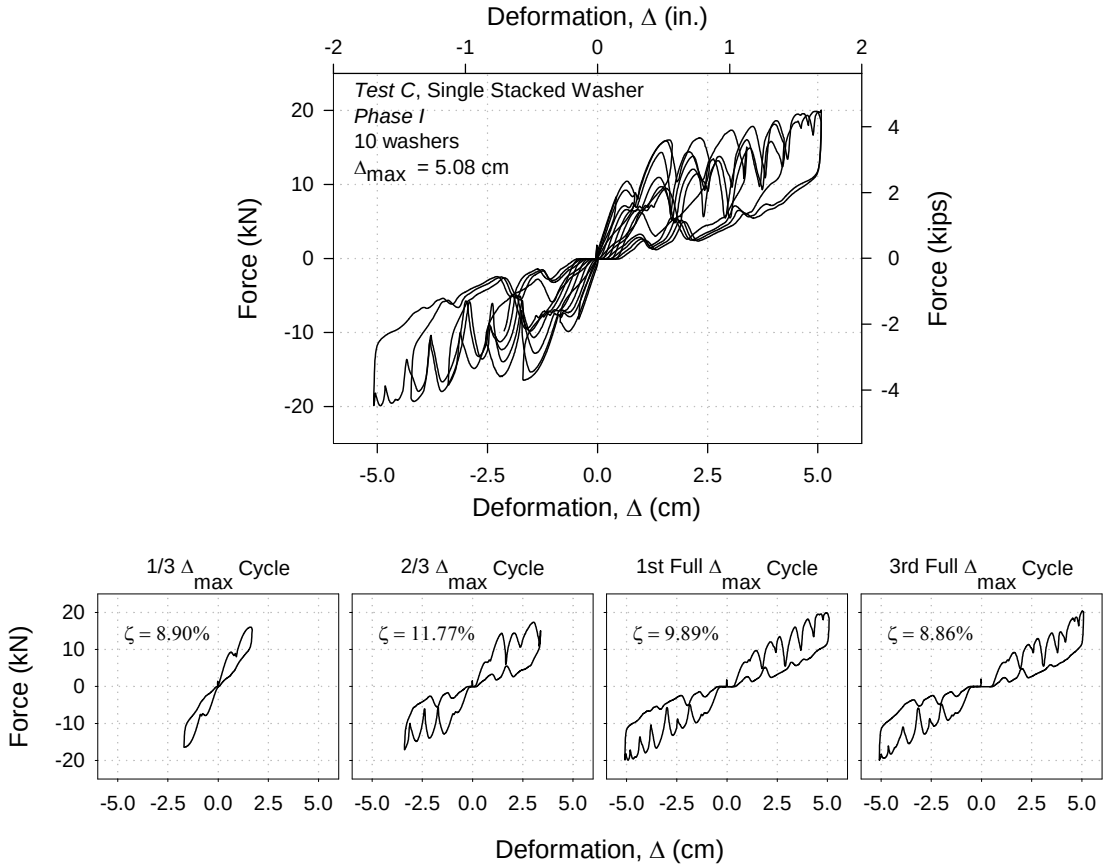

Figure 4-10: Force-deformation response of single-stacked washer configuration (*Test C*).

4.7.3. Double-Stacked

Test D was performed using a double-stacked 12-washer configuration (show in Figure 4-11). This configuration gave increased stiffness and strength in comparison to the single-stacked test. Unlike the previous test, flat washers were not added since they were determined ineffective in the previous test. Additionally, it was expected that the double-washer arrangement would naturally prevent individual washers from inverting. To fill the gap on the device center shaft, additional stainless steel cylinders were added between the shaft nut and the hardened disk. The shaft nut was hand tightened and the cylinder was slid into position.

The initial length and Δ_{max} of the washer configuration were 7.9 cm (3.1 in.) and 3.3 cm (1.3 in.), respectively. The resulting force-deformation is shown in Figure 4-11. A semi-sporadic response was observed, but this time fewer humps were noticed. After the test was complete and the damper was disassembled, one washer was found to be inverted. This washer was not the same one which inverted in the single-stacked test (*Test C*).

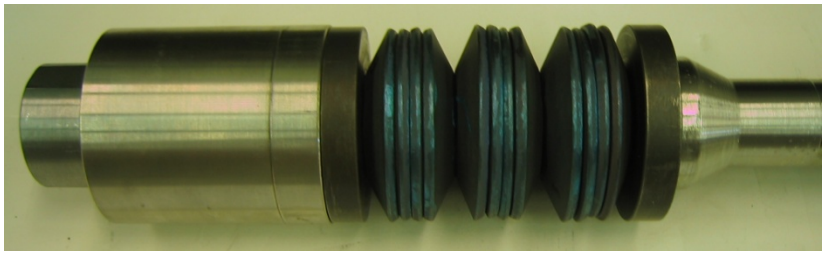

Figure 4-11: Washer configuration for *Test D.*

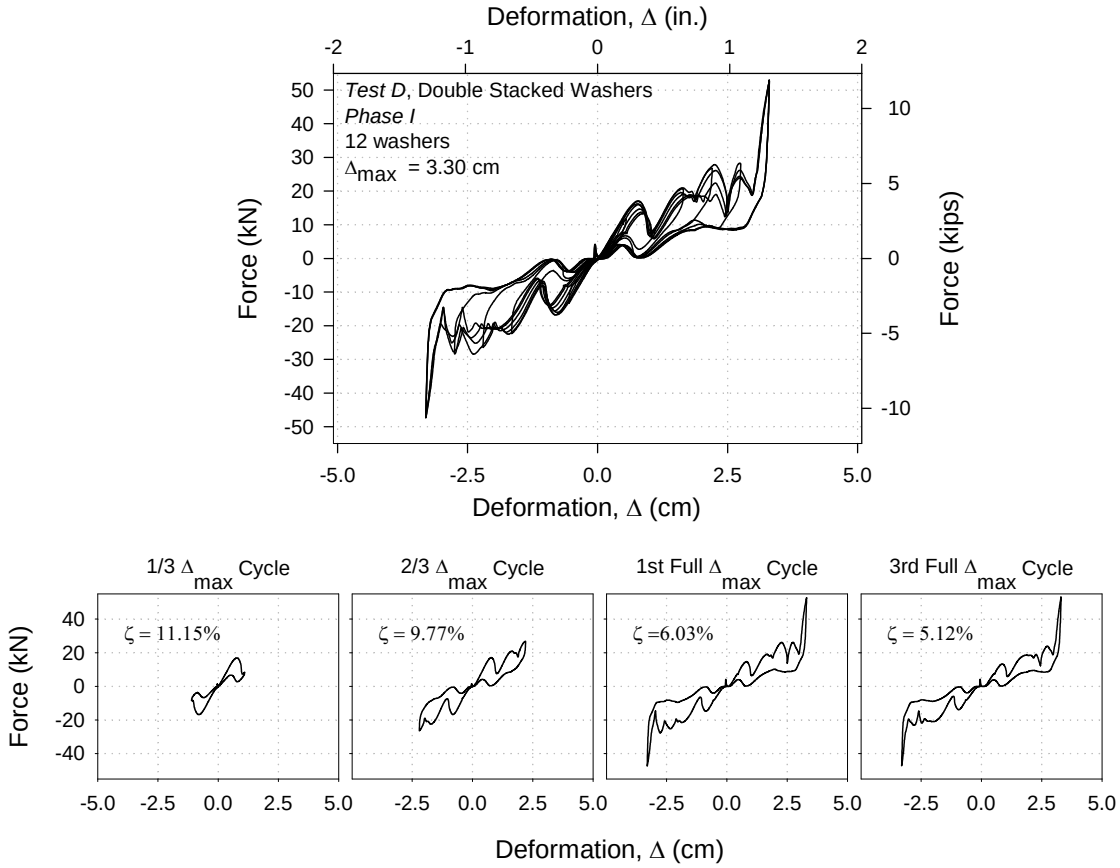

Figure 4-12: Force-deformation response of double-stacked washer configuration (*Test D*).

4.7.4. Triple-Stacked

The final test of *Phase I, Test E,* was done using a triple-stacked 12-washer configuration (Figure 4-13), giving even more stiffness and strength in comparison to the double-stacked test. Flat washers were again added in a second attempt to prevent the inverting observed in the previous tests. Additional stainless steel cylinders were added as fillers between the shaft nut and the hardened disk. Again the shaft nut was hand tightened and the cylinder was slid into position.

The initial length and Δ_{max} of the washer configuration were 6.8 cm (2.7 in.) and 2.0 cm (0.8 in.), respectively. The resulting force-deformation is shown in Figure 4-14.

This time a less sporadic load path was observed. The force-deformation curve had two distinct humps with a minor intermediate hump. After the test was complete and the damper was disassembled, no washers were found to be inverted.

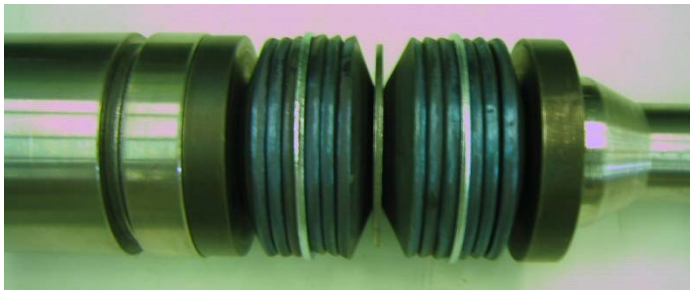

Figure 4-13: Washer configuration for *Test E*.

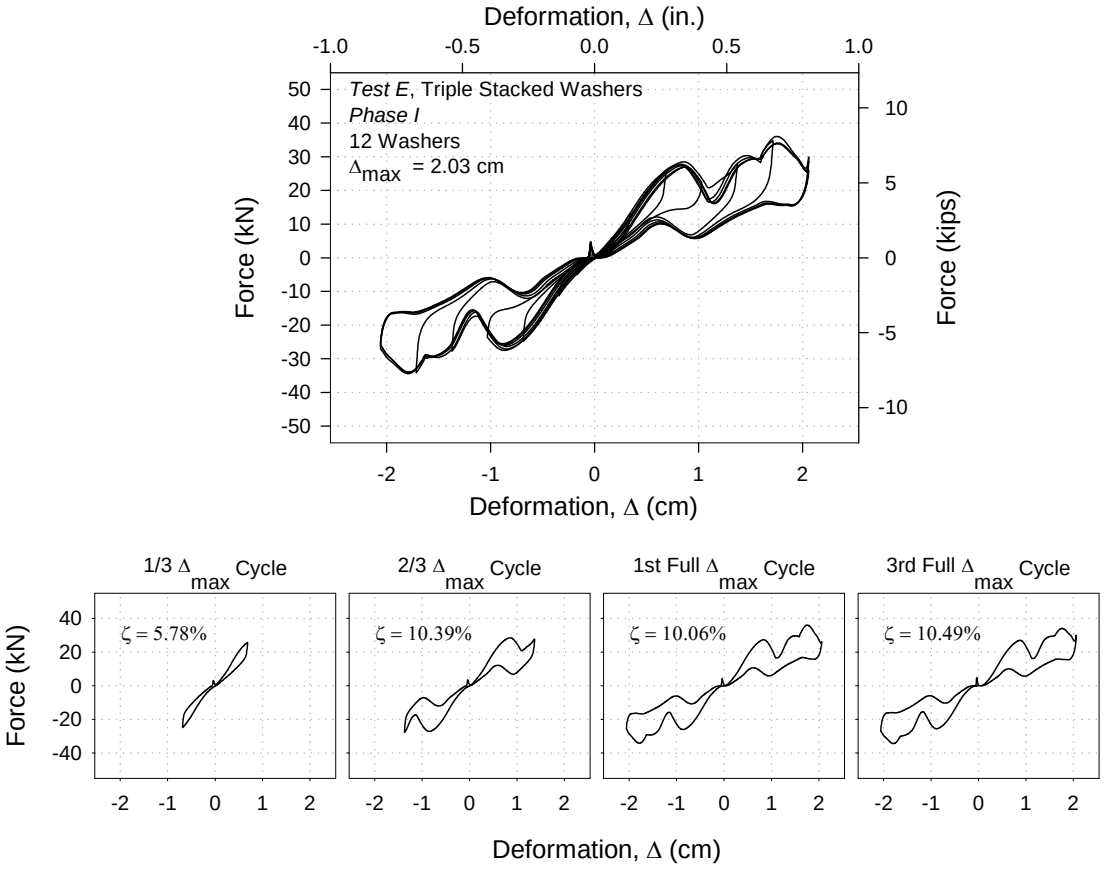

Figure 4-14: Force-deformation response of triple-stacked washer configuration (*Test E*).

4.7.5. Discussion – Single, Double, and Triple-Stacked Washers

The behavior of the single-stacked configuration was governed by the tendency of individual washers to lose their load carrying capacity as they were deformed beyond a certain limit. This was the direct result of the duck-head-shaped behavior observed in the individual washer tests. Since it can be assumed that each SMA Belleville washer has different peak strengths, the response of the single-stacked washer configuration was governed by the weakest link. As soon as the weakest washer was deformed to approximately 0.15 cm (0.06 in.), this washer began to lose its strength and thus take on the deformations of the other washers. This was reflected in the device's force-deformation humps. Once the displacement was increased enough to flatten the weakest washer, the remaining washers began to acquire more deformation. This cycle was repeated until the either the entire group of washers had flattened or the device deformation was decreased.

Upon the release of the imposed deformation, the flattened Belleville washers sprang back causing the force in the device to increase sporadically even while the deformation was decreasing (see the unloading path in Figure 4-10, Figure 4-12, and Figure 4-14). Residual deformations of each setup began to noticeably accumulate during the 2/3 Δ_{max} cycle. Upon the completion of the 3rd full Δ_{max} cycle, the bulk of the residual deformation could be attributed to a Belleville washer completely inverting (as noted in the results section).

The double and triple-stacked configurations had progressively less sporadic loading paths. Beyond the initial softness observed due to some of the washers settling into their positions, the stiffness increased as more washers were nested together. This initial stiffness, defined at a point half-way up the first hump, was 1.74, 2.45, and 3.93 kN/mm (9.94, 13.99, and 22.44 kip/in.) for the single, double, and triple-stacked

configurations, respectively. By adding more washers to each nest, fewer humps were able to form because there were fewer nests to allow this to occur.

The equivalent viscous damping, ζ, of the stacked washer configurations is shown in Figure 4-15 for each stacked washer test. The ζ ranged from approximately 4-13%. The E_{so} was calculated using the maximum deformation and the maximum force of each respective cycle (not necessarily the same point). The damping values were dependent on the location that each deformation cycle fell with respect to the humped response. The triple-stacked configuration showed increased damping at increased deformation. It was expected that as more washers were nested together, additional damping would result from the friction action between the nested surfaces. However, the damping caused by each washer's mechanical hysteresis seemed to be dominant in comparison to this friction action.

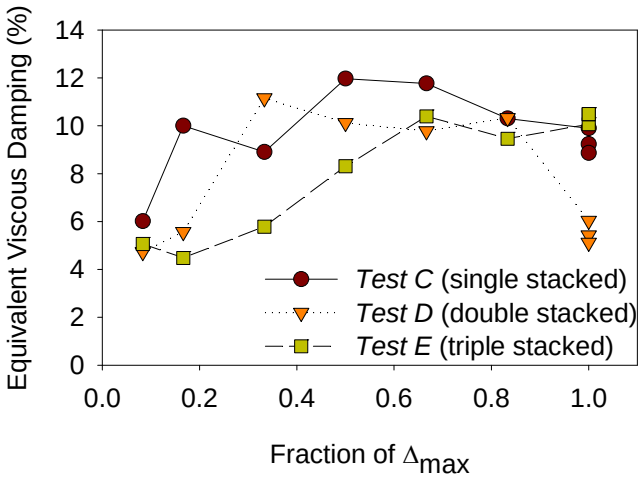

Figure 4-15: Comparison of equivalent viscous damping ratios for the stacked washer tests (*Phase I*).

4.8. Results and Discussion – NiTi Belleville Washer Tests: *Phase II*

For *Phase II* testing, the shape of the original set of NiTi washers was reset to have a 27-30° cone angle and then re-heat treated to ensure superelasticity at room temperature. A series of individual (monotonic and cyclic) and stacked (cyclic) tests were then carried out to assess the new behavior.

4.8.1. Individual

As in *Phase I*, individual washer tests were performed using the MTS machine. The resulting duck-head-shaped force-deformation curves are show in Figure 4-16. The washers had good initial stiffness and strength, but at a deformation of approximately 0.15-0.20 cm (0.06-0.08 in.) the force carrying capacity peaked and there was a significant drop-off in load. The drop-off in load was especially noticeable for *Washer 2*, in which a sharper peak was obtained (attributed to an increased cone angle compared to *Washer 1*). When the imposed deformation was released at 0.60-0.75 cm (0.24-0.30 in.), an unloading plateau was formed and the majority of the deformation was spontaneously recovered. As for *Washer 3*, a smaller deformation level was imposed to assess the effects of limiting the deformation.

In Figure 4-17, the cyclic behavior of two different washers was investigated (*Washer 4* and *5*). First *Washer 4* was cycled three times to almost flat (Figure 4-17a). The response began to somewhat stabilize, but further cycles were not carried out to determine the extent of this stabilization. Therefore, *Washer 5* was cycled ten times to 50% of its flat deformation (Figure 4-17b). The response of *Washer 5* clearly began to stabilize as the cycling progressed. Residual deformations began to decrease from one cycle to the next and the stress plateau began to flatten, thus eliminating the load drop-

off tendency (see the comparison in Figure 4-17c). This preliminary investigation shows that NiTi Belleville washers can be trained to have improved force-deformation behavior and opens the door to a wide range of potential applications. Though further applications are not studied, the potential for the superelastic Belleville washer use in bolted connections could be one area of future research.

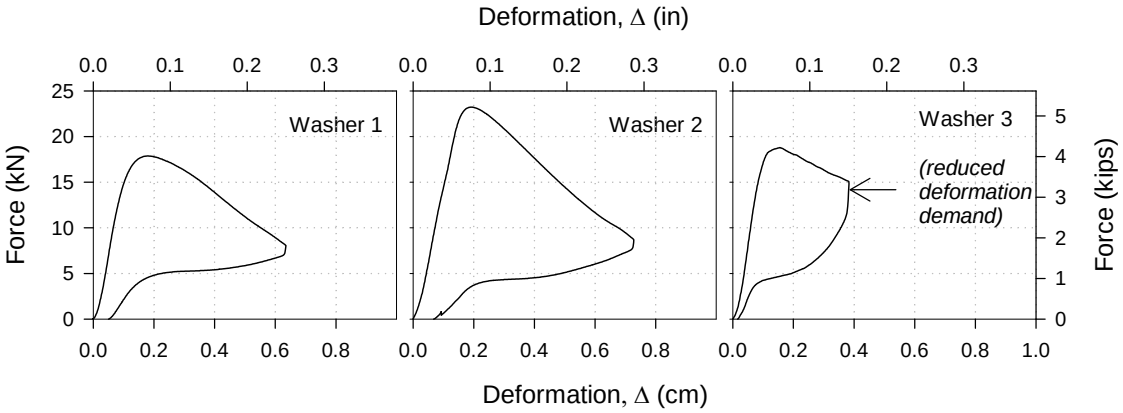

Figure 4-16: Response of individual NiTi Belleville washers under compression (Phase II).

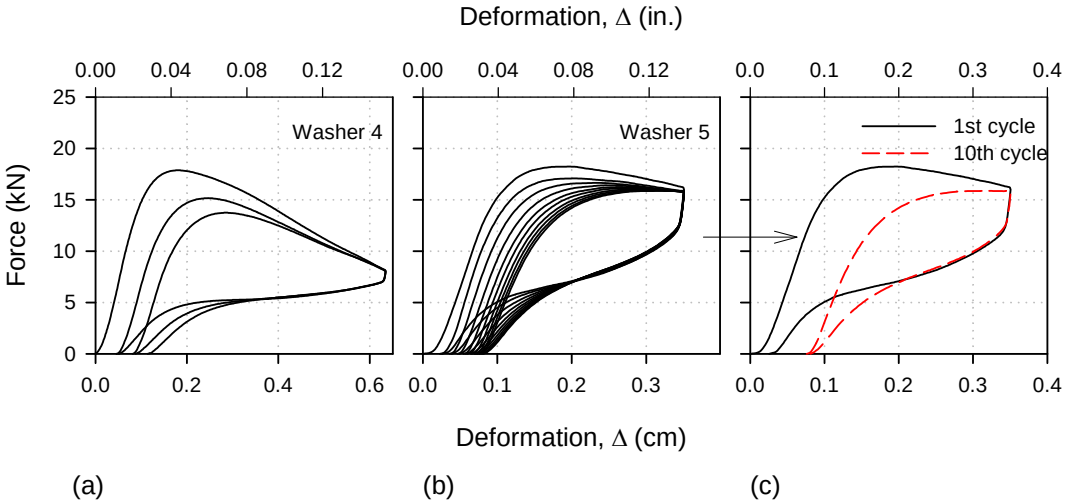

Figure 4-17: Response of individual NiTi Belleville washers (*Washer 4* and *5*) under cyclic compression. Plot (a) shows washer 1 cycled three times, (b) shows washer 2 cycled ten times, and (c) shows the first and tenth cycle of *Washer 5*.

4.8.2. Single-Stacked

One of the issues with the testing in *Phase I* was the tendency of some of the washers to invert. This resulted in sporadic behavior of a stacked assembly. Flat-washer spacers were added in an attempt to prevent the washer from inverting, but this was not successful. For the *Phase II Test F*, spherical washers (see Figure 4-18) were used as spacers to prevent the washers from inverting and also limit the range of imposed deformation. The spherical washers had a 3.0 cm (1.2 in.) inside diameter and a 5.7 cm (2.25 in.) outside diameter.

The final test of *Phase II* (*Test F)* was done using a single-stacked 8-washer configuration (Figure 4-19). Since thick spherical washers were used as spacers, the deformation capacity of this configuration was only 4.1 cm (1.6 in.). The resulting force-deformation behavior is shown in Figure 4-20. The recentering behavior of this stack was good through the 1/3 Δ_{max} cycle. However, beyond this the recentering became poor because of accumulating residual deformations in each individual washer. The energy dissipation also decreased as cycling continued, which was a direct result of the residual accumulation. After the testing was completed, the assembly was examined and there were no inverted washers.

To create an assembly with improved performance, it is suggested to train each individual washer (as done in the individual test) and prevent the washers from buckling by whatever means is deemed appropriate. The training showed that behavior degradation can be stabilized and the load drop-off effect can be reduced or eliminated.

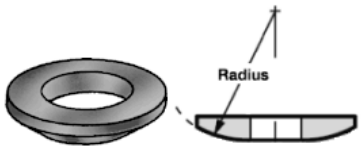

Figure 4-18: Spherical washer used in *Test F* (McMaster-Carr, 2009).

Figure 4-19: Washer configuration for *Test F.*

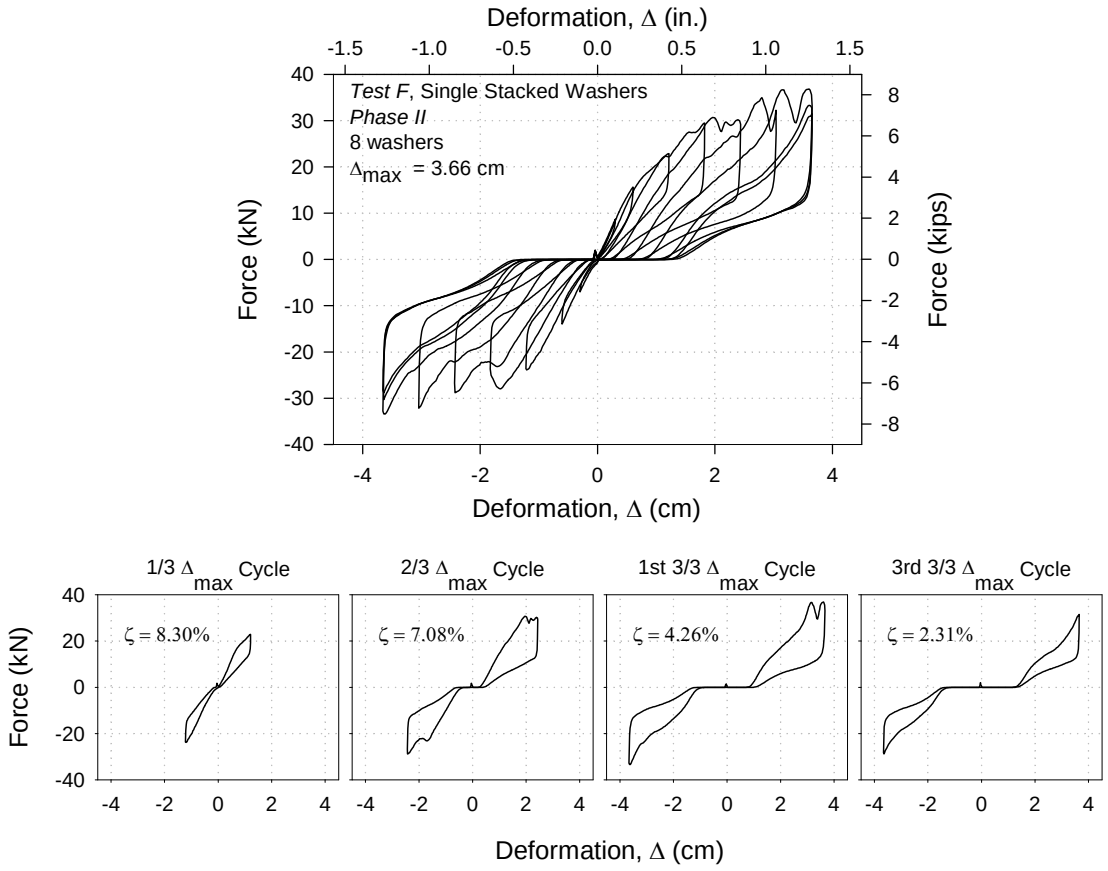

Figure 4-20: Force-deformation response of single-stacked washer configuration (*Test F*).

4.9. Conclusions

A SMA-based tension/compression device was investigated with two new forms of NiTi. The results of this exploratory investigation showed promise, but clearly further work is required. Particularly, the response of the NiTi helical springs was promising because of the good superelasticity (as noted by the recentering), damping, and repeatability. However, more research needs to be done to understand the stress levels in the spring material and to determine if the springs can achieve full-scale load and stiffness levels. Additional work needs to be done to better understand the effect of several design parameters (coil diameter, pitch, and thickness) on the resulting strength values.

With regards to the NiTi Belleville washers, they behaved in a unique manner that is traditionally undesirable in structural engineering (the load dropped off with increased deformation). However, the prospect of improving this behavior was demonstrated through cyclic training and deformation demand reduction. A key attraction to using Belleville washers is the ability to stack them in numerous arrangements to achieve a wide variety of force-deformation responses. However, work needs to be done to improve the behavior of individual washers and verify the benefits of training illustrated in this study. Furthermore, other applications should be explored, such as implementing into a bolted beam-column connection.

CHAPTER 5

INVESTIGATION OF A RECENTERING BEAM-COLUMN CONNECTION

5.1. Introduction

In this chapter the conception, design, proof-of-concept testing, performance, and behavior of a SMA-based recentering beam-column connection is presented. Since the 1994 Northridge earthquake, many different research initiatives have been undertaken to create connections that have more robust performance under seismic loads. Numerous vulnerabilities in fully restrained connections have resulted in the re-evaluation of their partially restrained counterpart (i.e. bolted connections). This re-evaluation has shown that properly detailed partially restrained connections have good seismic performance (Murray, 1988; Ocel et al., 2004; Penar, 2005; Swanson and Leon, 2000). A SMA-based partially restrained connection is proposed in this research. The connection is designed to have excellent ductility, yet maintain the ability to recenter after large drift demands.

The experimental testing and results from five beam-column connection tests are presented in the work herein. The connection was a modified version of the connection previously tested by Penar (2005) at Georgia Tech. Several enhancements to the previous connection were made in order to ensure that all the inelastic deformations were concentrated in the NiTi tendons. The performance of the connection is assessed in terms of strength, stiffness, recentering, and damping. Additionally, the experimental results are compared with analytical predictions from a simple model incorporating a material object previously developed in OpenSEES by Fugazza (2003).

5.2. Experimental Program

In this section a summary of the experimental procedures used to carry out the recentering beam-column tests is presented. This includes details of the component testing results, of the loading scheme, and of the instrumentation and data acquisition plan. A sketch of the connection is shown in Figure 5-1. The critical elements are the following:

a) Shear tabs welded to the column flange and bolted to the beam web

b) L-shape anchor brackets

c) HSS transfer elements

d) SMA tendon elements

Further details of the connection are discussed in Section 5.3.

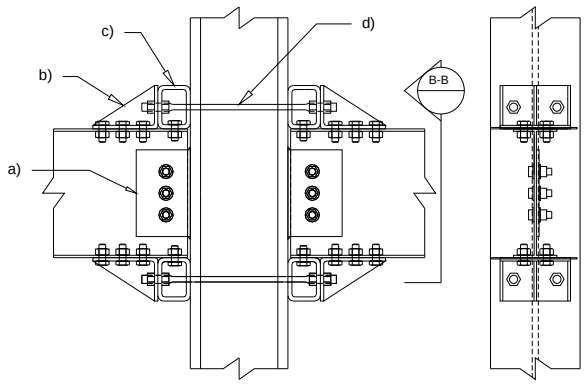

(a) front view (b) side view, section B-B

Figure 5-1: An overview of the SMA beam-column connection.

5.2.1. Component Testing

Various mechanical tests were performed to provide an understanding of the material behavior of the elements that make up the connection. The mechanical test results for the NiTi dogbone are shown in Figure 5-2a while the dogbone dimensions are shown in

Figure 5-2b. After being cycled to 6% strain, the NiTi specimen displayed good superelasticity with residual deformations of only 0.6%. The elastic modulus and the yield stress (of the initial large cycles) was approximately 23.0 GPa (3340 ksi) and 325 MPa (47.0 ksi), respectively.

Mechanical test were also conducted on the steel and aluminum dogbones as well as on two beam coupons. For these mechanical tests, the important quantities (yield strength, elastic modulus, and the ultimate strain) were gleaned and the resulting values are summarized in Table 5-1. No coupons were tested from the column specimen because of its sufficient overstrength. Beyond simple monotonic tests, several cyclic tests were run in order to observe each materials cyclic behavior. For further information on the mechanical tests, see APPENDIX B.

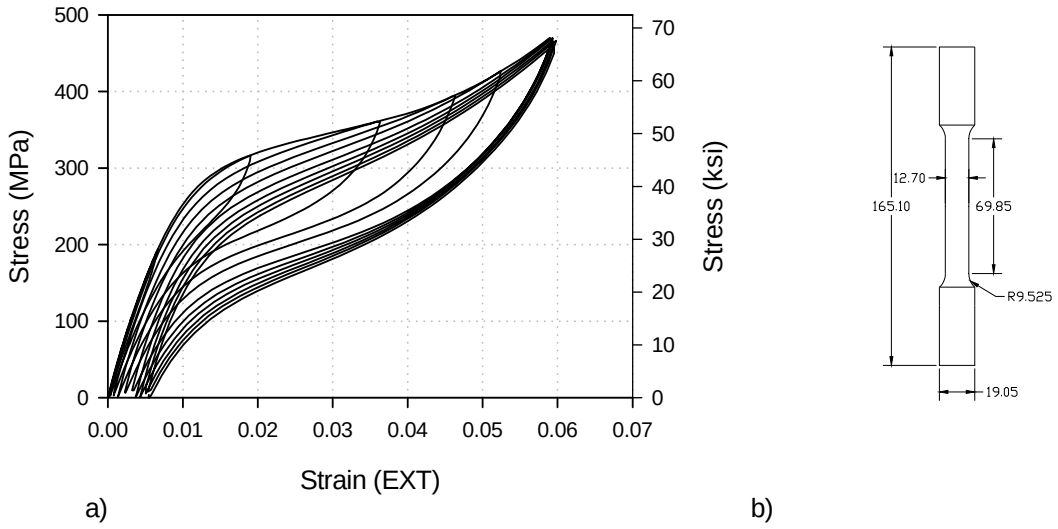

a) b)

Figure 5-2: The (a) stress-strain relationship of the NiTi dogbone and (b) the corresponding dogbone dimensions (mm).

Table 5-1: Summary of the component mechanical tests.

Component Specimen	Beam-Column Test	A, cm^2 (in^2)	σ_y, MPa (ksi)	E, GPa (ksi)	ε_{ult} (%)
beam flange coupon	*A-E*	0.824 (0.128)	376 (54.5)	197 (28600)	32
beam web coupon	*A-E*	0.834 (0.130)	386 (56.0)	197 (28600)	25
steel tendon dogbone	*A*	1.27 (0.196)	325 (47.1)	197 (28600)	32
steel tendon dogbone	*B*	1.27 (0.196)	325 (47.0)	197 (28600)	-
NiTi tendon dogbone	*D-E*	1.27 (0.196)	350 (50.8)	32.5 (3340)	-
AL tendon dogbone	*E*	1.27 (0.196)	117 (17.0)	32.4 (4700)	-

5.2.2. Loading Scheme

5.2.2.1. Loading Frame

The loading frame described in APPENDIX A was used as the platform for testing the beam-column connection. The frame, with the SMA connection specimen, is shown in Figure 5-3. This frame was designed by fellow researcher Masahiro Kurata and constructed by Kurata and the author. It was designed to be a flexible apparatus in which numerous lateral-load-resisting systems could be tested. Further details of the loading frame and a discussion of the frame-specimen interaction can be found in APPENDIX A and APPENDIX B, respectively.

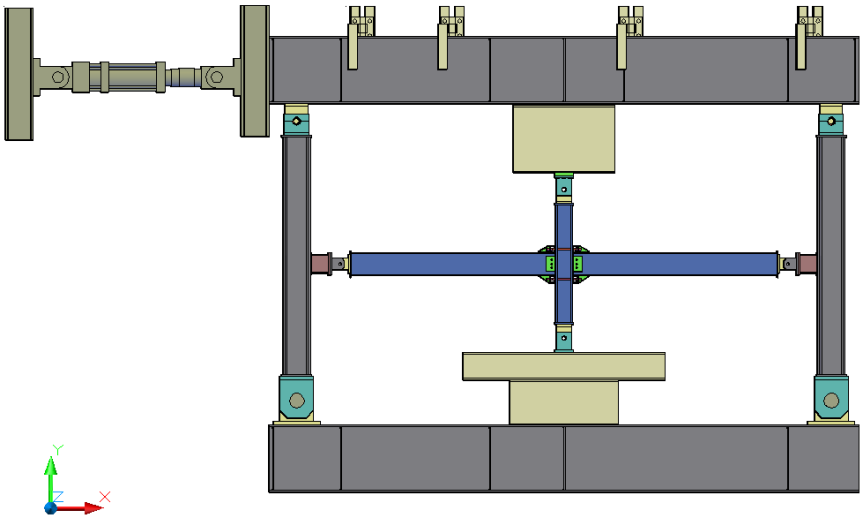

Figure 5-3: Loading frame schematic.

5.2.2.2. Loading Protocol

The connection was tested using the loading protocol from the SAC Steel Project as shown in Figure 5-4 (SAC, 1997). The loading protocol consisted of 6 cycles at 0.375%, 0.50%, and 0.75% drift, followed by four cycles of 1% drift, and finished with two cycles of 1.5%, 2%, 3%, and 4% drift. For *Test B-E* an additional two cycles at 5% drift were performed. The SAC protocol was originally developed after the 1994 Northridge Earthquake to investigate the behavior of fully-restrained welded moment connections, and has since become a standard protocol for cyclic connection testing.

The drift angle was selected as the governing parameter for this protocol. The load was applied in a quasi-static manner, at a rate of 51 mm (2.0 in.) per minute. This protocol was implemented by manually inputting points into the ramp generator of the MTS 407b controller, giving the operator step-by-step control of the loading.

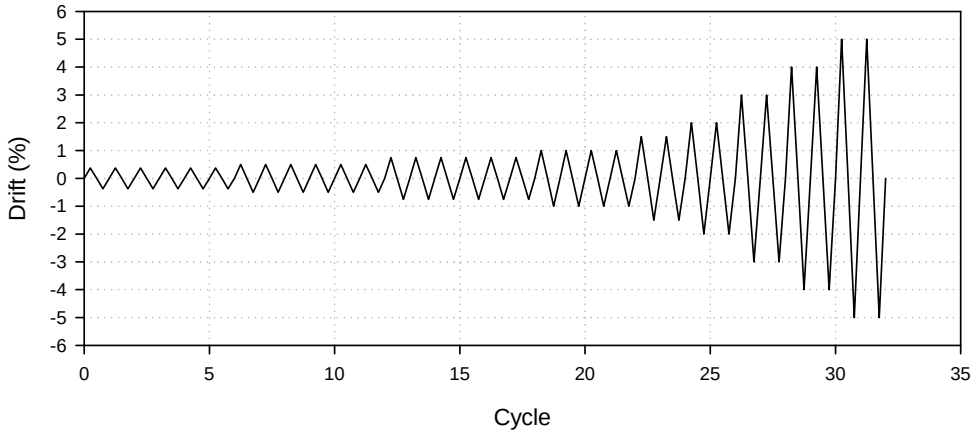

Figure 5-4: The SAC loading protocol.

5.2.3. Instrumentation and Data Acquisition Plan

In order to properly assess the performance of the beam-column connection, a variety of sensors were utilized. These sensors included load cells (LC), linear variable displacement transducers (LVDT), string potentiometers (SP), extensometers (EXT), and strain gauges (SG). A detailed layout of the instrumentation scheme is shown in Figure 5-5 and Figure 5-6 . For a complete detailed schedule of the sensors employed, see Table B-1 in APPENDIX B.

Data from the appropriate sensors was collected using a National Instruments system connected to a Dell computer. The data was recorded every 0.9 seconds due to limitations of the setup. Further details of the data acquisition system can also be found in APPENDIX B.

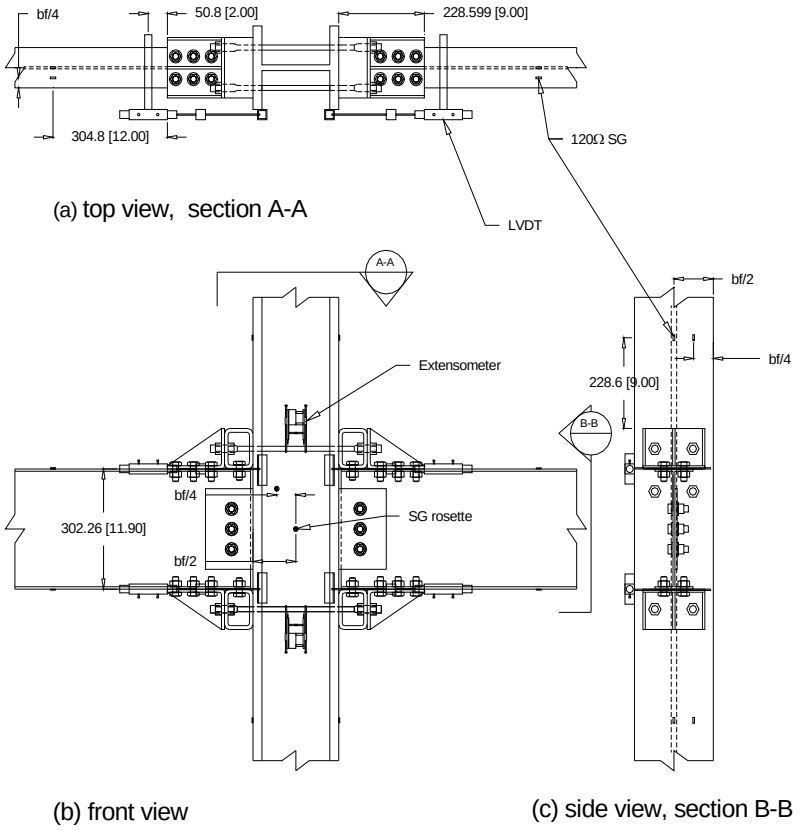

Figure 5-5: Instrumentation of specimen connection. Units in mm(in.).

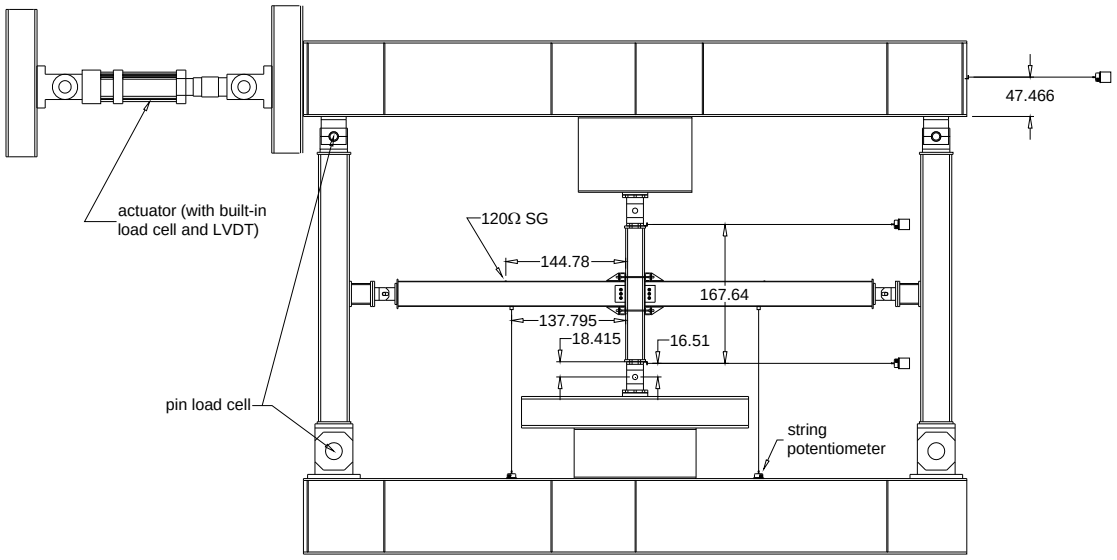

Figure 5-6: Instrumentation of loading frame and specimen. Units in cm.

5.3. Connection Details

The beam-column connection was designed to concentrate the inelastic deformation into tendon “fuse” elements, while the rest of the connection remained elastic. It should be noted that this was a proof-of-concept connection test; this connection was not intended to be representative of a real connection that would be installed in a building. Issues such as ease of installation and floor slab interference were ignored.

5.3.1. Beams, Column, and Bracket Elements

Members left over from an investigation by Penar (2005) were used in this experimental investigation. The beams and the column were W356x21 (W12x14) and W203x100 (W8x67) sections, respectively, and were made of A572 Grade 50 steel. The connection was designed to fulfill the weak-beam strong-column requirements of the AISC seismic provisions (AISC, 2005a). Additionally, the connection was designed to facilitate easy modifications for future tests.

A picture of the connection is shown in Figure 5-7 and the details are given in Figure 5-8. This connection is designed to transfer moment primarily through the coupled forces resulting from the HSS element bearing against the column face (compression) and the tendons pulling against the stiffened bracket (tension). The anchor bracket and transfer element were made from a stiffened 152x102x9.23 mm (6x4x3/8 in.) L-shape and a 102x76.2x6.35 mm (4x3x1/4 in.) HSS section. The L-shape was stiffened with three 9.2 mm (3/8 in.) triangular plates, one in the middle and one on each side.

The HSS was inserted to help transfer force from the L-shape bracket to the column face and to increase the moment arm of the force couple. In previous work done by Penar (2005) on a similar connection, the beam flange experienced local buckling because of the large compression force transferred through the flange. The HSS added

stiffness to the beam flange, which effectively prevented the beam flange from buckling. Additionally, after *Test A* was completed, the HSS was stiffened with a custom-fit 25.4 mm (1.0 in.) thick plate in order to prevent it from becoming inelastic. This plate was hammered into position at the center of the HSS member's length. Ultimately, the addition of the HSS element resulted in a stiffer and stronger beam connection.

The L-shape bracket and HSS transfer element were connected to the flange of the beam by A325 15.9 mm (5/8 in.) bolts and pretensioned per the turn-of-the-nut method from the AISC 2005 Specification (AISC, 2005b). The bracket-beam connection was designed as slip critical. The controlling moment (tension rupture at the bolt holes) was found to be 73.9 kN-mm (654 kip-in). To ensure elastic performance in the beam, the moment caused by the tendon-bearing couple was kept below this controlling moment.

The connection details for the five tests (with the progressive changes in each test noted) are shown in Figure 5-9. The bolts holding the HSS and L-shape elements were left out for clarity. An additional set of brackets were attached to the inside of the beam flanges to accommodate the additional tendons used in *Test E*. These brackets were attached after *Test A* using the same bolts as the other brackets, as illustrated in Figure 5-10.

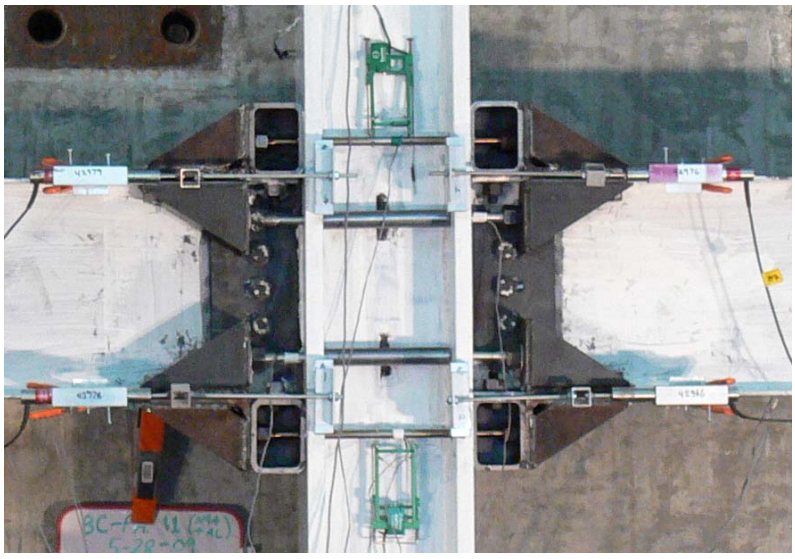

Figure 5-7: Connection profile view.

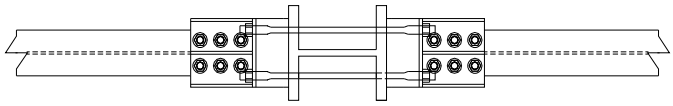

(a) top view, section A-A

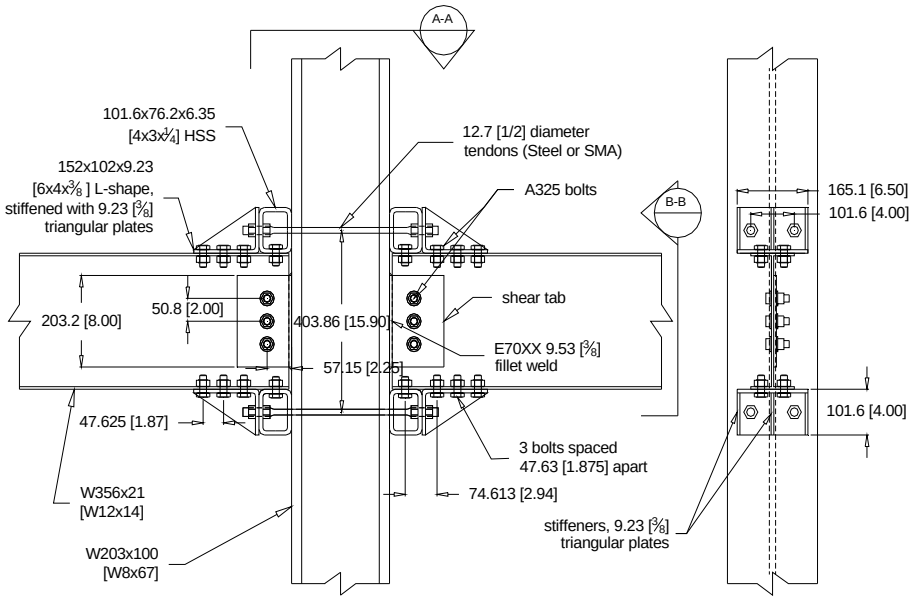

(b) front view

(c) side view, section B-B

Figure 5-8: Connection details and dimensions. Units in mm (in).

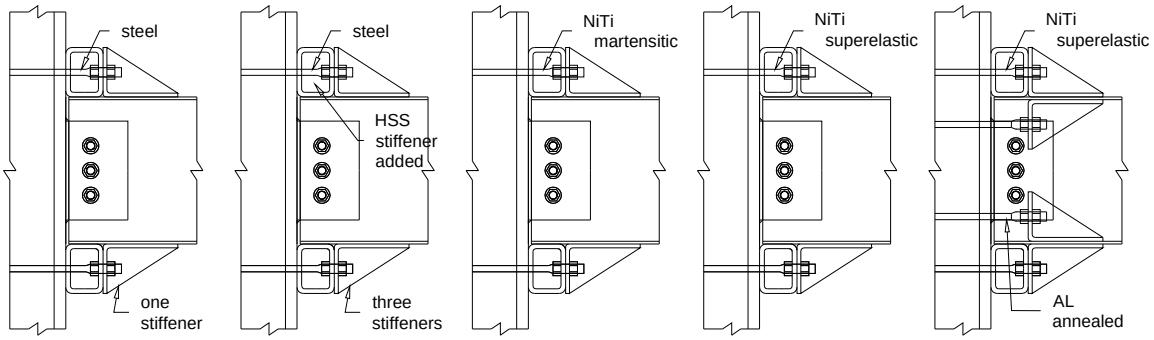

(a) Test A (b) Test B (c) Test C (d) Test D (e) Test E

Figure 5-9: Connection details with highlighted differences over the progression of testing.

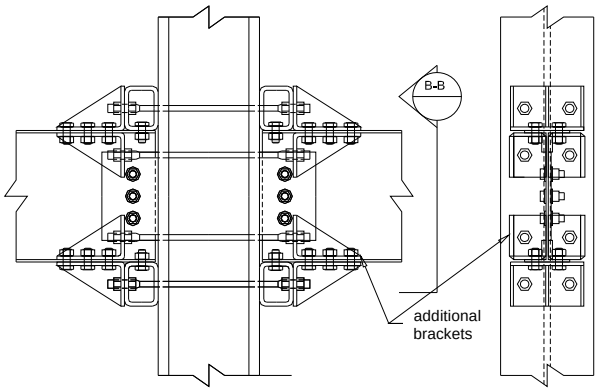

(a) front view (b) side view, section B-B

Figure 5-10: Additional connection brackets for *Test E.*

5.3.2. Shear Tab

A 203x127x6.35 mm (8x5x0.25 in.) plate was welded to both sides of the column face using 9.5 mm (3/8 in.) beveled groove welds with E7018 electrodes to effectively transfer the shear to the column. The shear tab had 17.5 mm (11/16 in.) holes slotted 25.4 mm (1.0 in.) to accommodate the relative rotation expected between the beam and the column. The beam was connected to the shear tab with three 16 mm (5/8 in.) bolts tightened using a torque wrench to 135, 81, 81, 68 N-m (100, 60, 60, and 50 ft-lbs) for

Tests B, *C*, *D*, and *E*, respectively. For *Test A*, the bolts were hand tightened using a 250 mm (10 in.) long wrench, which provided a torque less than the lowest reading of 69 N-m (50 ft-lbs) on the torque wrench.

To assess the moment contribution of the shear tab connection and better predict the experimental response of the entire setup, the connection was first tested without tendons attached (shear-tab-only). This was done at various shear tab bolt torque levels and the results are presented in Figure 5-11. The shear tab friction provides a significant contribution to the strength, stiffness, and energy dissipation in the positive drift direction. However, once the beam was forced away from the column face and there was nothing to pull it back (i.e. no superelastic tendons), the contribution of the shear tab to the strength and stiffness was significantly decreased.

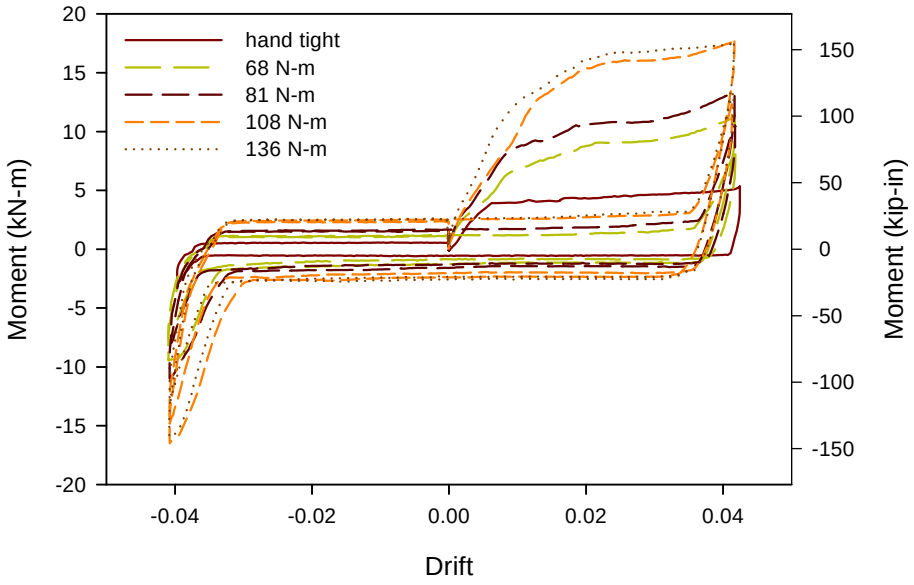

Figure 5-11: Tests ran on the connection with the shear tab bolts tightened to various torque levels per a torque wrench. No tendons were installed.

5.3.3. Tendon "Fuse" Elements

The tendon "fuse" elements were made from 19.1 mm (0.75 in.) diameter bar. Each bar was machined, as shown in Figure 5-12, to concentrate the deformations in the reduced section. The tendons were made from the following:

a) Unrated threaded steel rod, 19.05 mm (0.75 in) with 0.394 threads per mm (10 threads per in), *Test A*

b) A36 steel, 19.05 mm (0.75 in) with 0.394 threads per mm (10 threads per in), *Test B*

c) NiTi, martensitic (shape memory effect), 19.05 mm (0.75 in) with 0.63 threads per mm (16 threads per in), *Test C*

d) NiTi, austenitic (superelastic), 19.05 mm (0.75 in) with 0.63 threads per mm (16 threads per in), *Test D* and reused in *Test E*. Heat treatment: (1) 350 °C for 0.5 hrs then air-cooled. (2) Machined per drawing. (3) 300 °C for 1.5 hrs then immediately water-quenched.

e) 6061-T6 aluminum, annealed to achieve low strength, 19.05 mm (0.75 in) with 0.394 threads per mm (10 threads per in), *Test E*

Mechanical testing was performed on each type of material to determine the material properties prior to implementing in the connection (as previously described in the component testing section).

The tendon elements were each pretensioned after being inserted into the connection. For the steel tendons in *Test A* and *B*, pretensioning was achieved by cranking a torque wrench to 90 ft-lbs. This sufficiently snugged up the connection and ensured there was good initial stiffness. For the NiTi tendons in *Test C*, *D*, and *E*, the tendons were pretensioned to approximately 0.5% strain (as measured by high

elongation strain gauges). Further pretensioning was attempted but was not successful due the tendency of the NiTi tendon to twist rather than allowing the nut to turn on the threads.

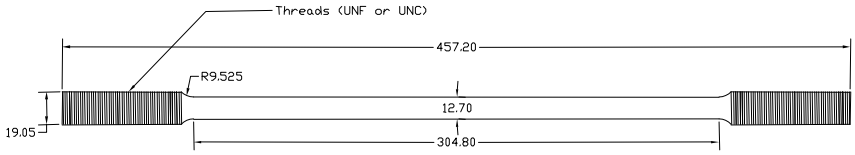

Figure 5-12: Tendon details with threads 19.05-0.63 (3/4-16) UNF for the SMA tendon and 19.05-0.394 (3/4-10) UNC for the steel and aluminum tendons. Units in mm (in.).

5.4. Experimental Results

The results of the experimental tests are presented in this section. Additional figures and information can be found in the supporting appendices. The equations and methodology used for data reduction can be found in APPENDIX C. Validation of the results is detailed in APPENDIX D. For each test, the moment-rotation curves were shifted in order to have the origin at the approximate center of the curves. This shifting was done in an effort to further "zero" the connection data. The shifted amounts were in the range of 1-2% of the data maximum. Complete data sets for all tests are given in APPENDIX E. Only selected results are used for illustrative purposes in the following discussions.

5.4.1. Test A – Steel 1

In *Test A*, an unstiffened HSS transfer element and singly-stiffened L-shape anchor brackets were used (refer to Figure 5-9). The tendon elements were made from 19.1 mm (0.75 in.) diameter threaded rod machined per Figure 5-12. The shear tab bolts

were tightened by hand with a standard wrench (denoted “hand-tight” in Figure 5-11). *Test A* was carried out in order to investigate the overall setup and to assess whether any modifications needed to be made to the connection brackets before the NiTi tests were performed. In addition, this test (along with *Test B*) provided benchmark data for comparison purposes.

The left beam’s moment vs. concentrated rotation (hereafter moment-rotation) relationship is presented in Figure 5-13. Similar response was seen in the right beam and is shown in Figure E-4 of APPENDIX E. The connection remained elastic during the 0.375% drift cycles, but then began to show signs of yielding at the 0.5% drift level. Low stiffness at small rotations and a hysteresis in the moment-rotation relationship were observed.

Increasing the drift level resulted in a decrease in stiffness at small rotations and an increase in hysteretic damping. These effects were due to yielding and friction in the connection. Yielding occurred both in the tendon elements and in the connection HSS and L-shape bracket members. The final residual strain in each steel tendon was 1.7, 1.7, 2.2, and 2.1% for the top-front (T1), top-back (T2), bottom-front (T3), and bottom-back tendon (T4), respectively (Figure 5-14). The stiffener in the L-shape bracket experienced yielding and the HSS was noticeably deformed after the test was complete. This was the result of the high level of compression transferred from the tendon attachment point to the column flange face. Since the bracket yielding was not desired, stronger brackets were fabricated for *Tests B-E*.

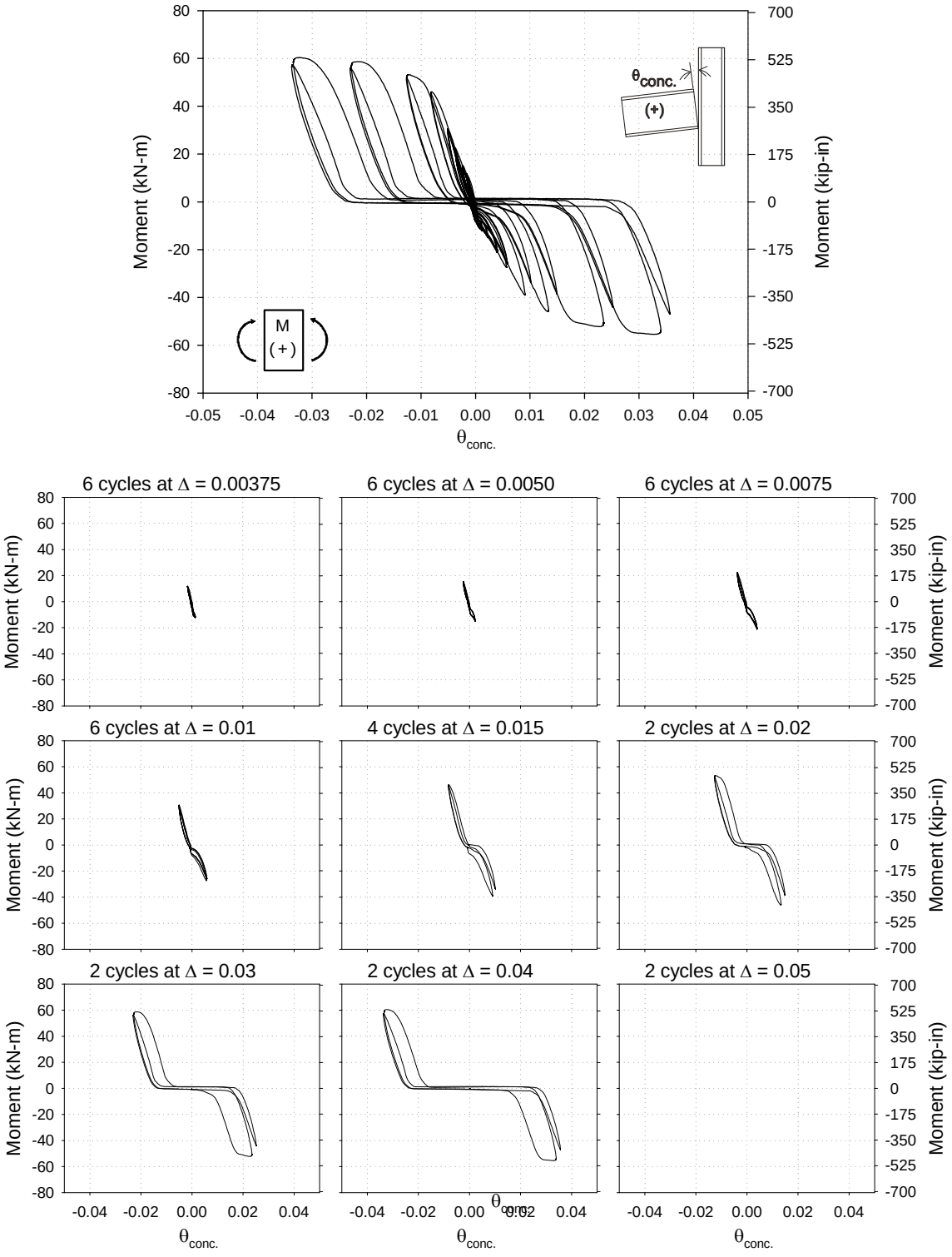

Figure 5-13: Moment vs. concentrated rotation for the left beam in *Test A.*

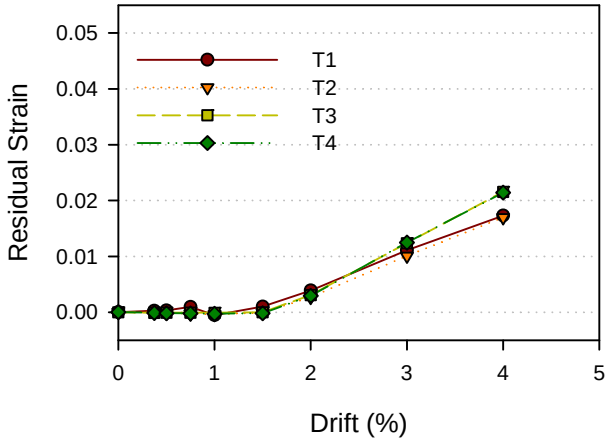

Figure 5-14: Residual strain (EXT) in tendons at end of each drift level for *Test B.*

5.4.2. Test B – Steel 2

After the conclusion of *Test A*, the beams were removed and the connection brackets were modified in order to correct the observed deficiencies. New brackets were fabricated with the intent of ensuring elastic behavior. The new HSS pieces were stiffened with a custom fit 25.4 mm (1 in.) thick steel plate, which virtually eliminated any potential yielding in the HSS section. New L-shape brackets were stiffened with three triangular stiffeners in lieu of the single stiffener used in *Test A*. Additionally, the shear tab bolts were tightened to 135 N-m (100 ft-lbs) with a torque wrench.

These modifications were done to prevent the anchor brackets from becoming inelastic during the test, but are in no way suggestive of the most economical or efficient connection design. Further comments on realistic connection design are made later in this chapter in Section 5.5.6.

As with *Test A*, *Test B* was another “test-run” for the NiTi tests. A36 steel bars were used as the tendon elements. Before presenting the results, it should be noted that after the test was completed it was observed that the bolts connecting the right beam to the pin-clevis-assembly end were only loosely tightened. This oversight

resulted in unexpected performance from the right beam (and consequently the connection), so the data should be interpreted in context of this error.

The connection remained elastic through the 0.75% drift cycles. During the reverse stroke of the first 1.0% drift cycle, tendon T3 began to yield, resulting in approximately 0.4% residual strain in the tendon, as shown in Figure 5-16. However, while this took place, the connection's global performance remained mostly elastic with only a slight hysteresis in the moment-rotation curve. Once further cycles were imposed at 1.0% drift, the tendon's residual strain increased, reaching approximately 0.7% after the final 1.0% cycle. A small, but increasing, hysteretic loop was observed in the moment-rotation curve indicating some influence of a small amount of tendon yielding and the inherently present friction in the shear tab connection. The stiffness of the connection remained constant at approximately 10 kN-m/rad (89 kip-in/rad).

During the forward stoke of the first cycle at 1.5% drift, tendon T4 began yielding, resulting in approximately 0.8% residual tendon strain. Tendon T3 also experienced further yielding during this step, resulting in approximately 1.3% residual strain. Additionally, tendon T1 yielded both in the forward and reverse steps; resulting in approximately 0.3% residual drift after the first cycle was completed. This resulted in a large hysteretic loop being formed during the forward portion of the first cycle at 1.5% drift and smaller hysteretic loops being formed during the rest of the 1.5% cycles.

Reduced stiffness was observed in the first cycle's backward loading due to the gap developed between the beam and the column face. This softening can be attributed to the gap opening caused by the yielded tendons' tendency to force the beams away from the face of the column. This gap effectively prevented moment from being transferred by the tendon-bearing couple until the beam end brackets contacted the column face at a sufficiently high drift level. Since the connection was designed with the expectation that the tendons would pull the beams back into contact with the column

face (via superelastic tendons), this gap opening was an expected phenomena for the steel tendon tests (*Test A-B*).

Upon the application of the first forward cycle at 2.0% drift, all of the tendons yielded in nearly equal amounts. On the reverse cycle, more yielded was induced in each bar. This first cycle of 2.0% drift added approximately 1.0% residual strain in each tendon. The yielding further softened the connection by increasing the gap between the beam end and the column face. The increase connection softness began to expose the friction based hysteretic loop that was formed around the x-axis (caused by the bolted shear tab).

Further cycling resulted in a similar pattern of yielding tendons and reduced connection stiffness. During the 4.0% drift level, the connection had negligible stiffness until the concentrated rotation reached approximately 2%. The hysteretic loops in the moment-rotation plots for the left beam tended to be larger in the second quadrant (negative moment, positive rotation) because the forward loading cycle induces the bulk of the tendon yielding. After the 4% drift cycles were completed the test was stopped.

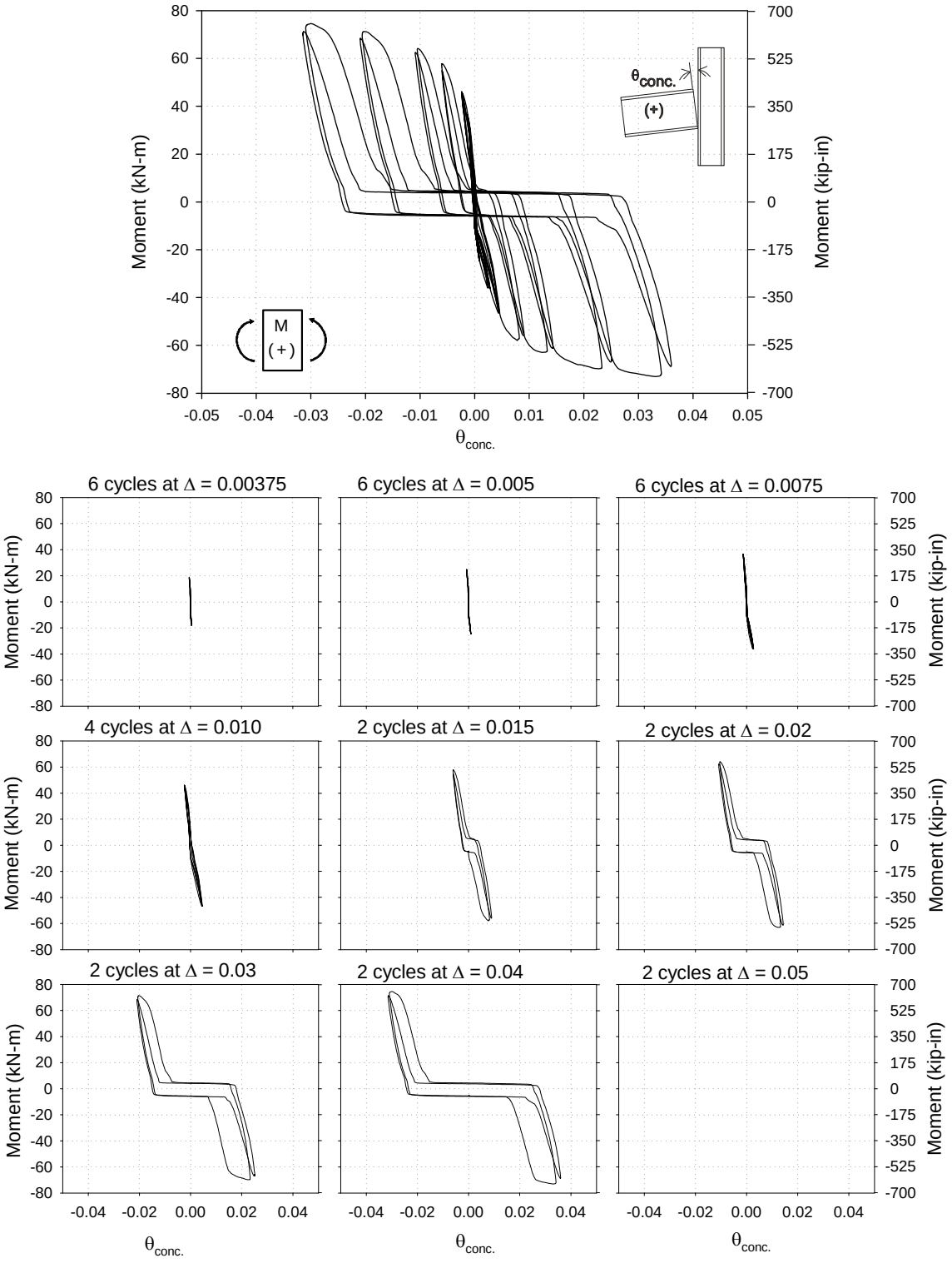

Figure 5-15: Moment vs. concentrated rotation for the left beam in *Test B.*

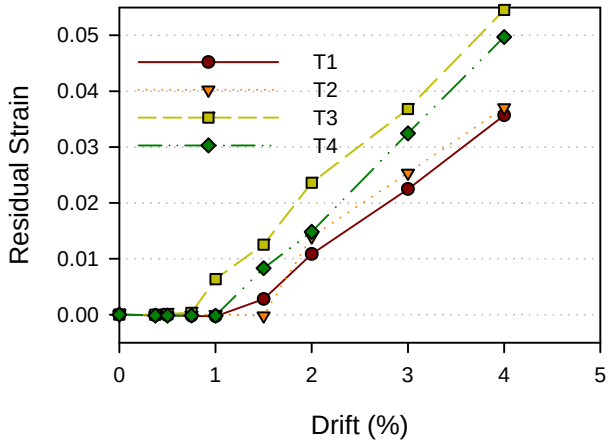

Figure 5-16: Residual strain (EXT) in tendons at end of each drift level for *Test B.*

5.4.3. Test C – SMA 1

Test B demonstrated that the modifications from *Test A* produced a connection that concentrated the inelastic deformations solely into the tendons. After the conclusion of *Test B*, the steel tendons were removed and NiTi tendons were installed. These tendons were once again from previous connection testing done by Penar. The exact processing and properties of the bars were unknown. It was unknown whether the bars were superelastic due to the previous research's inability to strain the tendons into the phase transformation range. As the results of *Test C* confirmed, the NiTi tendons were in the martensitic form (SME), rather than having superelastic behavior.

Nevertheless, the assumption was made before the test that the tendons were superelastic. To encourage recentering and ensure good initial stiffness, each bar was pretensioned to 0.5% strain as measured by the installed high elongation strain gauges. Additionally, the shear tab bolts were tightened to 81 N-m (60 ft-lbs) per a torque wrench.

The connection remained elastic until the first cycle of 0.5% drift load step in which all tendons had residual strains up to approximately 0.1%. As seen in the previous two

tests, this caused some slight loss of stiffness in the moment-rotation response and a slight hysteresis was formed in both the forward and reverse loading directions. Significant loss of stiffness was not observed until the 0.75% load, in which the stiffness went from 4.1 (36) to 3.6 kN-m/rad (32 kip-in/rad) for the last cycle at 0.5% to the first 0.75% cycle, respectively. This stiffness degradation was due to the continued unrecovered strains in the tendons.

It should be noted that the residual tendon strain was not due to yielding, as in ordinary metals, but rather due to one of the following two phenomena: 1) the superelastic NiTi's crystal structure transforms from austenite to martensite and then, due to lack of superelasticity, the strain is not automatically recovered or 2) the martensitic NiTi's crystal structure transforms from twinned martensite to detwinned martensite and retains this residual strain until heated to a specified temperature. Since the assumption was that the tendons were superelastic, heat was not applied to the tendons until the testing protocol was completed.

Further loading continued to result in residual strain accumulation in the NiTi tendons at varying degrees. The residual accumulation trend for each tendon is shown in Figure 5-18. The final residual strains in the tendons were 0.038, 0.035, 0.044, and 0.035 for tendons T1, T2, T3, and T4, respectively. This accumulation of residual strain shifted the beam away from the column face, resulting in initial softness in the connection until the beam rotated sufficiently to bear against the column face (similar trend seen in *Test A* and B).

Upon completion of the loading protocol, the left and right beams had shifted away from the face of the column creating a gap of approximately 6.4 mm (0.25 in) and 5.9 mm (0.23 in). To investigate the NiTi shape memory properties, a heat gun was used to recover the strain in the presumed detwinned martensite. After heating all the tendons for approximately 30 seconds, both the left and right gaps closed significantly,

resulting in a 1.6 mm (0.125 in) gap on both sides. As stated previously, the connection was designed for superelastic tendons therefore further testing was not carried out even though the majority of the residual strain was recovered. During *Tests B* and *C*, the residual elongation of the tendons produced softening in the connection rather than added damping. If the connection was designed to force the tendons into both tension and compression, added damping would have occurred.

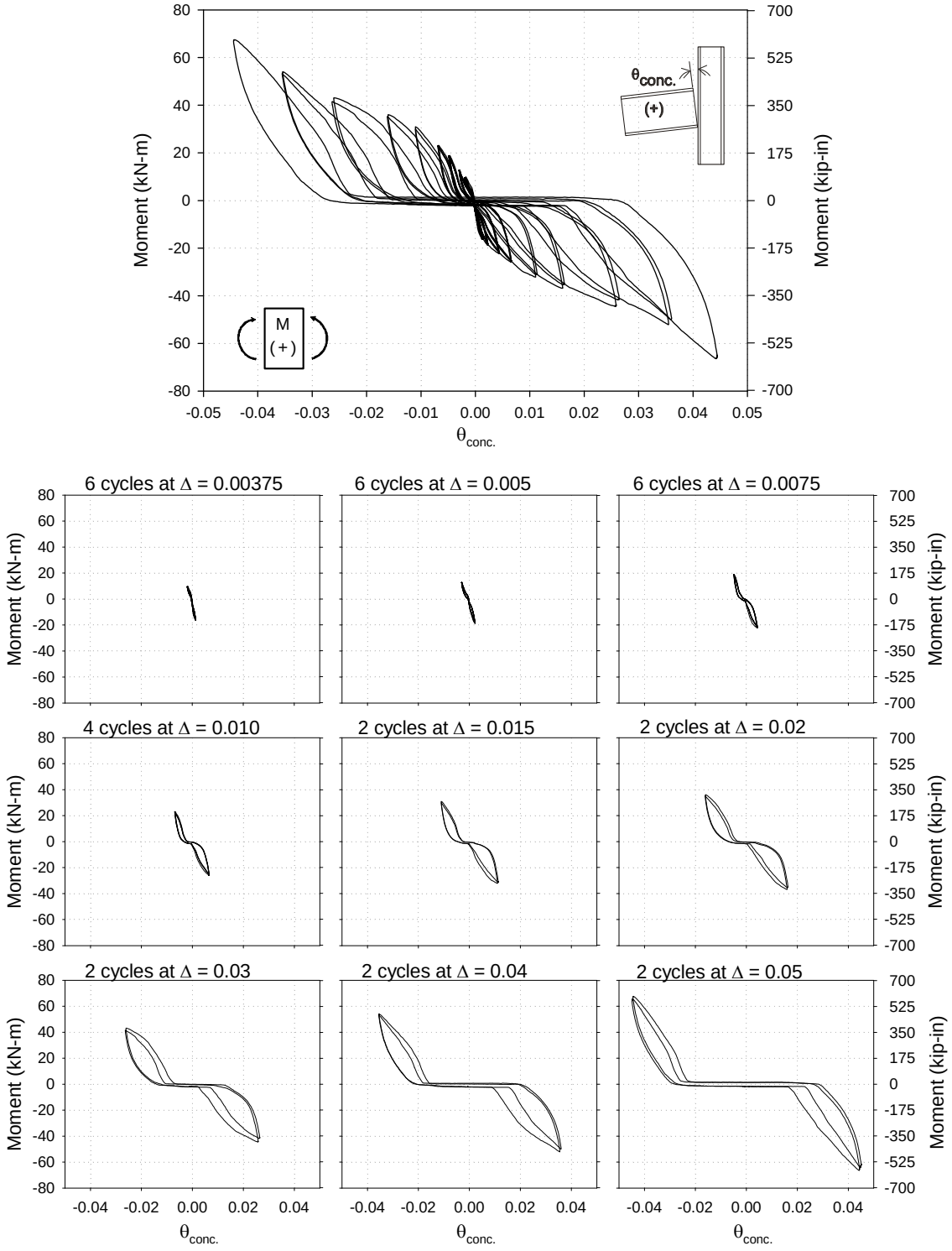

Figure 5-17: Moment vs. concentrated rotation for the left beam in *Test C.*

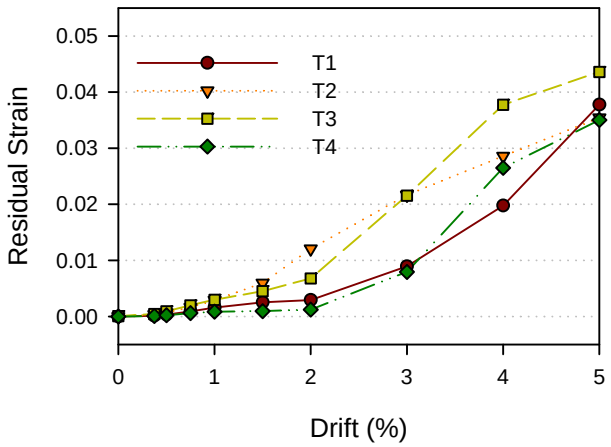

Figure 5-18: Residual strain (EXT) in tendons at end of each drift level for *Test C.*

5.4.4. Test D – SMA 2

Since the NiTi tendons of *Test C* did not exhibit superelastic behavior, new bars were machined and heat treated as per the protocol recommended by McCormick (2006). The NiTi bars were first heat treated to 350 °C for 30 min. and air cooled, then machined to the appropriate tendon size (see Figure 5-12), and finally heat treated again to 300 °C for 1.5 hrs. and immediately water quenched. The NiTi dogbone specimen shown in Figure 5-2 also used this protocol. The new tendons were installed and prestrained to approximately 0.5% (as measured by the mounted strain gauges).

The connection remained elastic through the 0.5% drift level. After the forward stroke of the first 0.75% drift cycle, a small amount of residual deformation was recorded in tendon T2 (top-back) while the other tendons exhibited full recentering. Additionally, small hysteretic loops were observed in the beam-column moment-rotation during this drift step.

Initial stiffness remained steady through the 0.75% drift level for the left beam. However, the initial stiffness for the right beam displayed some softness even during the small 0.375 and 0.5% drift levels. This phenomenon became especially noticeable

during the 0.75% drift cycles, in which the NiTi tendons were reaching strains of up to 0.28%. As shown in Figure 5-20, the residual strains in the tendons remained negligible.

During the 1.0% and 1.5% drift cycles, the left beam had good recentering, moderate hysteretic loops, and little-to-no softening in its moment-rotation response. In contrast, the right beam continued lag in performance compared to the left beam, perhaps due to the loading sequence (push to the right, then to the left). The right beam's initial moment-rotation softness and residual rotation continued to slowly grow.

Upon loading into the 2.0% drift level, the connection began to display a more recognizable flag-shaped hysteretic loop characteristic of superelastic NiTi. The strains induced in the tendons were between 1.25% and 1.50%, which indicated that the initial part of the phase transformation had been reached.

Once the 3.0% drift level was imposed, the tendons were strained up to 3.25%, which was well into the phase transformation range. The flag-shaped hysteresis of the moment-rotation behavior became more pronounced and recentering was still fully achieved in the left beam. Residual rotations (and thus initial softness) continued to increase slowly in the right beam's response. Furthermore, there was slight stiffness and strength degradation in the connection, most assuredly due to the degradation of NiTi's mechanical behavior as seen in mechanical tests.

During the 4.0% drift level, the tendons were strained up to approximately 5.0%, which was approaching the zone where all the austenite has transformed to martensite. From this stage and beyond, it was expected that there would be increased residual rotation accumulation based on the tendency of deformations to be accommodated by plastic strains (dislocation movements) in lieu of phase transformation at high strain levels. As expected, the residual accumulation contributed to the flag-shaped hysteresis continuing to enlarge. At this point, some slight initial softness was finally observed in the left beam moment-rotation while the right beam moment-rotation continued to have

increased initial softness. Additionally, continued strength degradation was observed as a result of the NiTi tendons mechanical characteristics.

The final 5.0% drift cycles induced on the connection were performed to push the tendons further along their stress plateaus. Both beams moment-rotation response showed increased initial softness. For the left beam, a very small stiffness was recorded for approximately +/- 0.00125 radians (2.8% of the total). Upon returning to the zero position, the tendons exerted a recentering force until 0.0025 radians (5.6% of the total). For the right beam, a very low stiffness was observed for approximately +/- 0.005 radians of rotation (10% of the total). Upon returning to the zero position, the tendons kept the recentering force until 0.009 radians (20 % of the total). After the testing was completed, there was no gap between the left beam and the column face. In contrast, there was a 3.0 mm (0.125 in.) gap between the right beam and the column face, which was expected due to the loss of initial stiffness observed during the test.

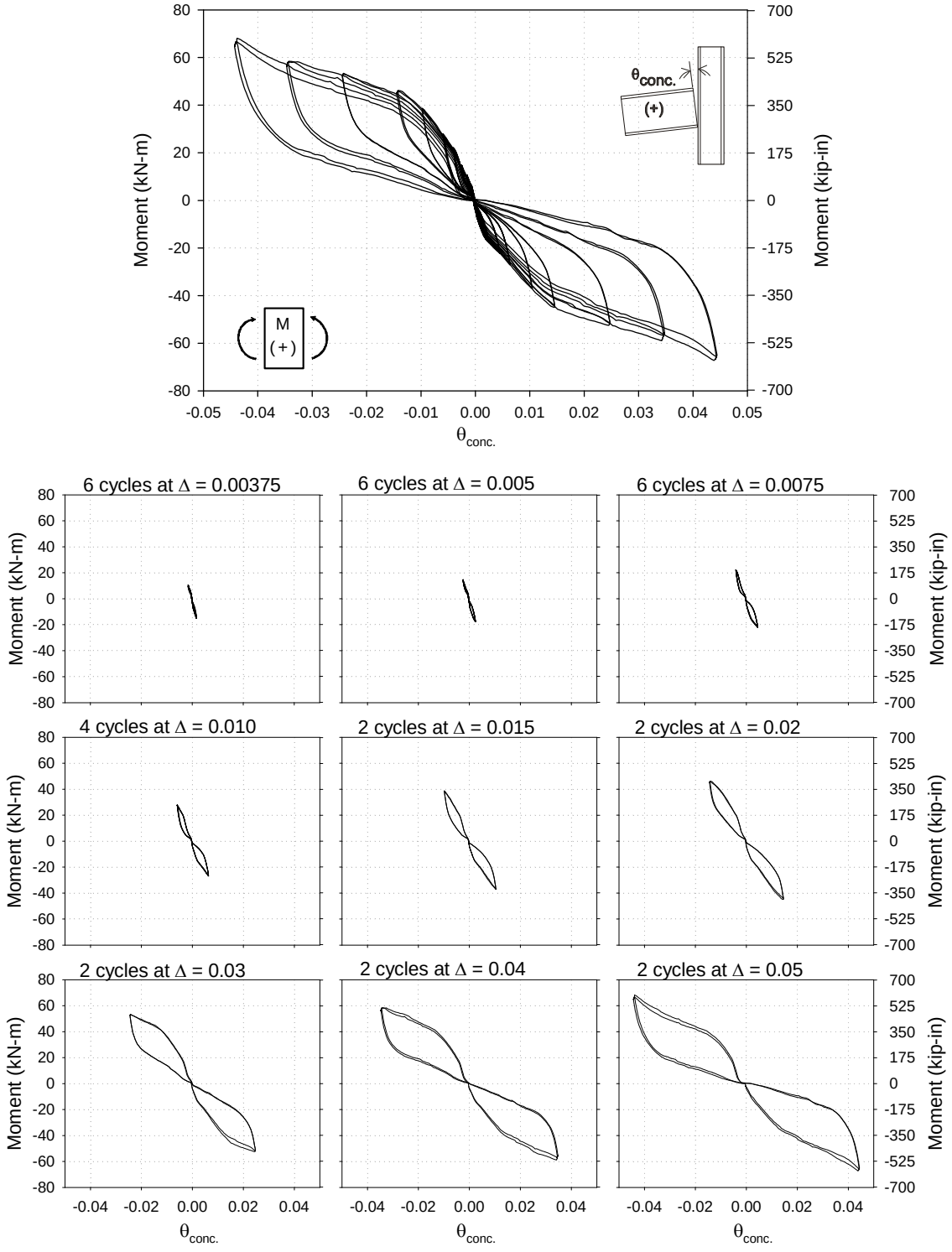

Figure 5-19: Moment vs. concentrated rotation for the left beam in *Test D.*

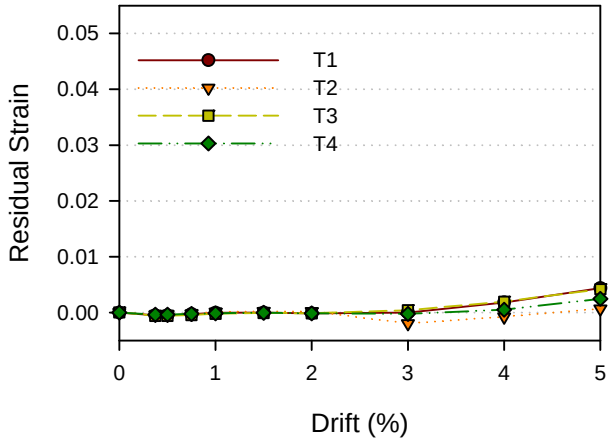

Figure 5-20: Residual strain (EXT) in tendons at end of each drift level for *Test D.*

5.4.5. Test E – SMA 2 + AL (PARA)

With the positive results from *Test D*, the effect of adding an additional element in parallel with the NiTi tendons was pursued. The intent was to provide additional energy dissipation without losing the recentering capability. This was done by adding low strength aluminum (AL) tendons to interior connection anchor brackets. These AL bars were encased with a 19.1 mm (0.75 in.) interior diameter steel tube in order to limit buckling.

The connection remained elastic through the 0.50% drift cycles, as with *Test D*. After the first cycle at 0.75% drift, both the NiTi tendons and the AL tendons displayed slight residual strains according. Small hysteretic loops were observed in the moment-rotation curves for both beams. The initial stiffness remained stable with full recentering occurring after each cycle.

During the 1.0% drift level, the AL tendons reached a strain of up to 0.42%, well above the yield strain of 0.36%. Upon returning to the zero position, the AL tendons were forced into compression due the NiTi tendons' superelastic restoring force. Due to the AL tendons small moment of inertia, the bars easily buckled until they were inhibited

by both the steel tube encasing and the column flange holes. This led to double curvature buckling at both ends of the tendons and unknown buckling inside the steel tube. Even with this phenomenon taking place, the connection continued to display good stiffness and recentering which indicated that the NiTi tendons were retaining good superelasticity.

During the first and second 1.5% drift cycles, the connection began to lose stiffness at small drift levels. This softening effect can be attributed to the increased yielding and buckling of the AL tendons and the residual strain accumulation in the NiTi tendons. At the end of the second 1.5% drift cycle, the residual strains in the NiTi tendons were 0.02, 0.05, 0.03, and 0.05% for the T1, T2, T3, and T4 tendons, respectively. These small values indicate the connection still had a large amount of recentering capability.

Further loading cycles resulted in a continued increase in the hysteretic loop area and continued softening in both beam moment-rotation relationships. The residual strain in the tendons had its first noticeable increase during the 3.0% drift level. During the 4 and 5.0% drift cycles, the residual strains continued to increase in tendon T3, but decreased in the other three tendons.

During the 5.0% drift cycles, both beams had reduced stiffness near the origin (as seen in Figure 5-21). For the left beam, a small stiffness was observed for approximately +/- 0.0035 radians (7.8% of the total). Upon returning to the zero position, the tendons exerted a recentering force until 0.006 radians (13% of the total). For the right beam, a small stiffness was observed for approximately +/- 0.005 radians (10% of the total). Upon returning to the zero position, the tendons kept the recentering force until 0.0075 radians (17% of the total). After the testing was completed, no gap was present between the left beam and the column face. In contrast, there was a 3.0 mm

(0.125 in.) gap between the right beam and the column face, which was exactly what was seen in *Test D*.

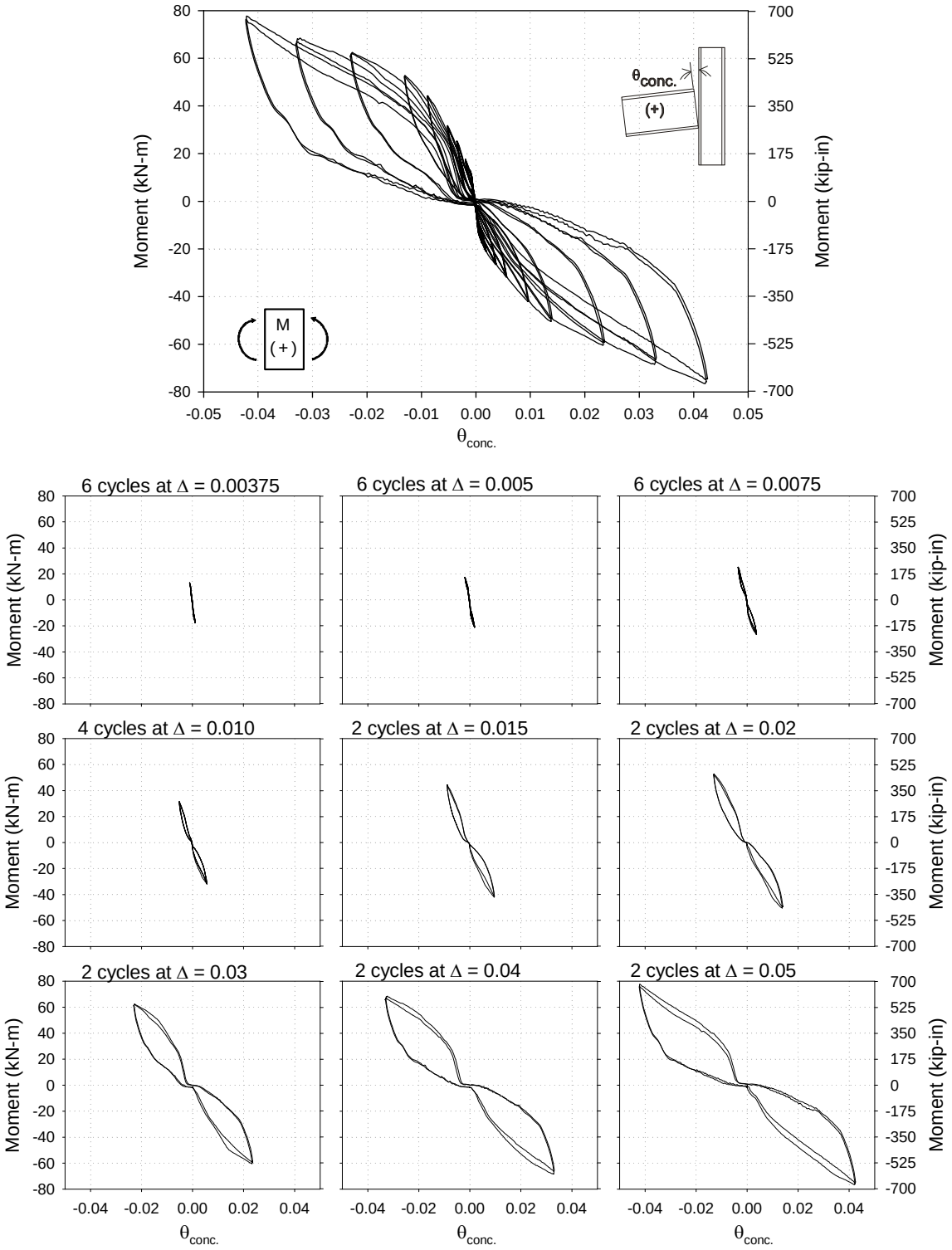

Figure 5-21: Moment vs. concentrated rotation for the left beam in *Test E.*

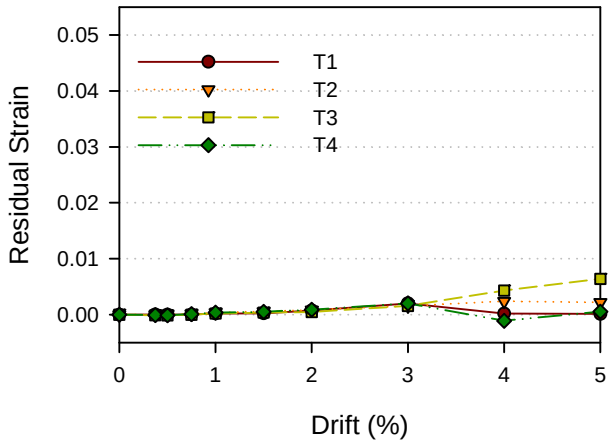

Figure 5-22: Residual strain (EXT) in tendons at end of each drift level for *Test E.*

5.5. Discussion of Results

5.5.1. General Behavior

While the previous section presented the performance of the five beam-column tests, this section takes an in-depth look into these results and tries to explain the underlying behavior. Comparisons between the tests are made in order to demonstrate the ability of the superelastic NiTi to provide the restoring force for the recentering system. While the ultimate goal is to produce and validate a model that corresponds well with the experimental results, many different trends are explored along the way. These trends include changes in stiffness, strength, energy dissipation, and recentering.

5.5.1.1. Average Response

In order to simplify the discussion, the average of the left and right beam's moment-rotation was taken. This average was obtained by the following equations:

$$M_{AVG} = \frac{(M_R - M_L)}{2} \tag{5.1}$$

$$\theta_{AVG} = \frac{(\theta_R + \theta_L)}{2} \tag{5.2}$$

The average moment was obtained by switching the sign of the left beam in order to obtain a sign convention in which the average moment is positive when the frame is moved to the right of center. This averaged moment-rotation relationship and the sign convention are shown in the upper left of Figure 5-23. Since the left and right beams were not independent of each other due to the shared tendon configuration, the average moment-rotation is a reasonable representation of the overall connection behavior. In addition, the overall connection response can be easily found by doubling the average moment values.

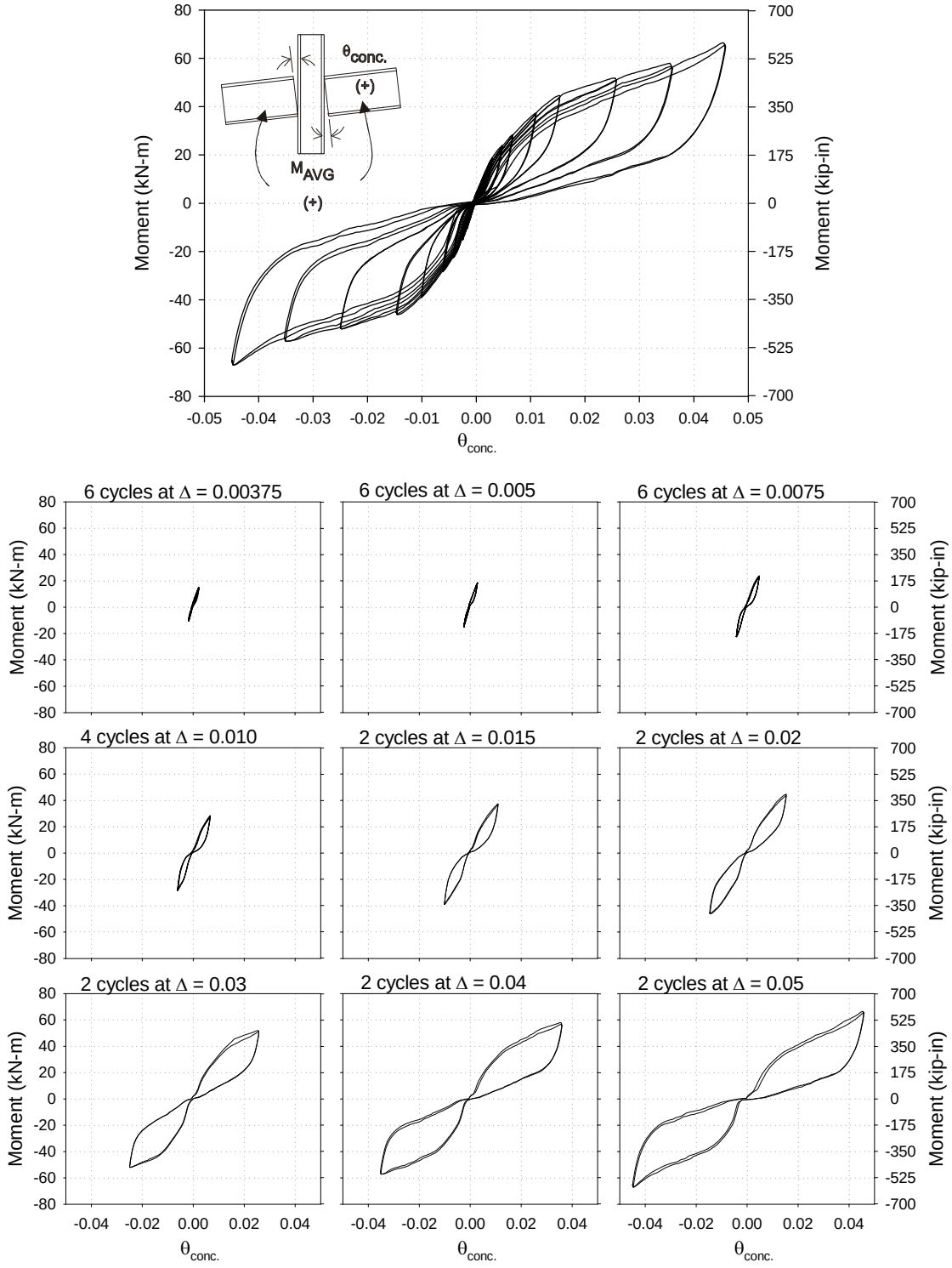

Figure 5-23: The averaged connection moment vs. concentrated rotation for *Test D.*

5.5.1.2. Response Path

Before the response parameters are examined, it is helpful to look at an individual moment-rotation curve for the NiTi tendon tests. Figure 5-24 shows the moment-rotation curve for the first 5% drift cycle for the superelastic SMA test (*Test D*). This test was selected because it exhibited all of the different transition points. The transition points (*a* through *g*) are plotted to help delineate the different phenomena that were occurring as the connection was cycled.

During small rotations levels of the loading portion, the connection was prone to stiffness degradation due to the accumulating residual strains in the tendons, as denoted from points *a* to *a'* in Figure 5-24. From point *a'* to *b*, the combined tension in the tendons and the friction in the shear tab resulted in an approximate linear moment-rotation stiffness. Once point *b* was reached, the NiTi began to transition into its phase transformation region. At point *c*, the SMA had presumably reached the stress in which the austinite began to transform into detwinned martensite, which allowed the increased accommodation of strain with smaller changes in stress. At point *d*, the austinite had almost fully transformed to martensite, and there was some indication of the stiffer martensitic behavior being displayed.

For the unloading portion, the tendons remained in the detwinned martensite phase until the transition started to happen at point *e* and was completed at point *f*. At point *f*, the detwinned martensite began to fall back into the austinite phase, because it was more stable at the lower stress levels. From point *f* to *g'*, the NiTi tendons attempted to pull back the connection because of the reverse phase transformation. Because of the resistance caused by the shear tab friction and the trend of residual accumulation in the NiTi, point *g'* fell somewhere to the right of point *g*. This distance is defined as the residual rotation in the connection. Further cycling resulted in this path being followed all over again, with the previous cycle affecting the current cycle.

It should be noted that if both points *a-a'* and *g-g'* are at the same coordinates, then full recentering would be obtained. Additionally, when the frame was loaded and unloaded in the opposite direction (frame moves to the left for the loading), the resulting behavior was similar.

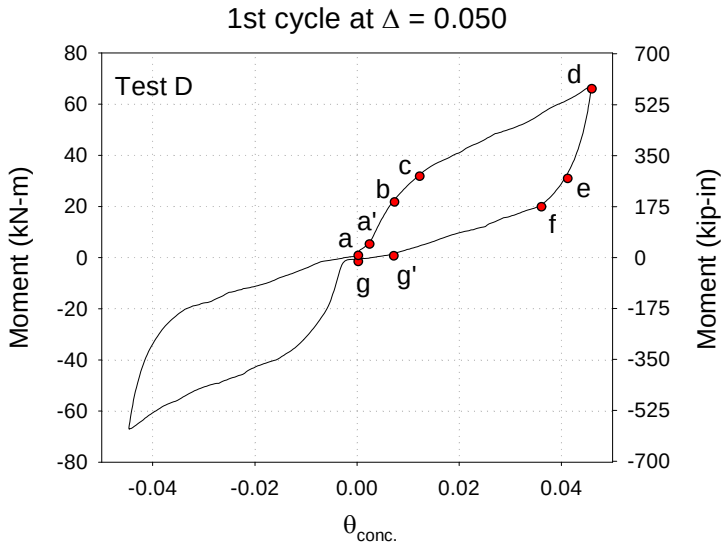

Figure 5-24: Example moment-rotation response for *Test D.*

5.5.2. Yield Moment and Effective Stiffness

The cyclic curves for the first cycle at 2.0% and 5.0% drift are shown in Figure 5-25. Straight lines were overlaid in order to approximate the effective stiffness, K_{eff}, and "yielding" moment, M_y, of the connection (where "yielding" is really phase transformation for the SMA). The line for determining the stiffness was drawn asymptotically to the forward and reverse loading curves and runs approximately through the origin as depicted in Figure 5-25. In order to determine the "yielding" plateau, another line was drawn. For the smaller drift cycle (2.0% and below), the "yield" plateau was difficult to determine. Using Figure 5-23 as a gauge, it was determined that a "yielding" plateau

was not reached for drift levels at and below 1.5%. This observation is supported by the strain levels observed in the tendons (Figure E-55 through Figure E-58).

For each cycle, the K_e and M_y were determined using the described methodology. The change in M_y over the range of drift is shown in Figure 5-26 for Tests B, D, and E. The M_y for *Test C* is not reported because of an indistinguishable yielding point (however, it is clear that the connection yielded by looking at the residual accumulation in both the tendons and overall connection). For tests *B*, *D*, and *E*, M_y was not fully reached for drift levels below 1.5%. Conversely, for drift levels at and above 1.5%, the M_y for *Test B* increased steadily while that of *Test D* and *E* remained fairly constant. The increase in M_y for *Test B* is justified by the strain hardening that occurred in the A36 tendons. The relatively constant trend of M_y vs. drift level for *Tests D* and *E* is attributed to the NiTi and AL tendons' stable hysteretic behavior.

The change in K_e is shown in Figure 5-27 for *Tests B-E*. All connections lost stiffness at larger drift levels due to the accumulation of residuals in the setup. For *Test B*, K_e dropped from 2.0e4 kN-m/rad (1.77e5 kip-in/rad) to 2.8e3 kN-m/rad (2.48e4 kip-in/rad) over the drift range. This dramatic decrease was due to the yielding of the steel tendons, resulting in the K_e being governed by the initial softness of the connection rather than the tendon material stiffness. *Test C* had a similar trend to that of *Test B*, but with lower values due to the smaller elastic modulus of NiTi compared to that of steel. For *Test D*, the stiffness during the 5.0% drift level was more than half of the stiffness during the initial drift levels due to the superelastic behavior of the NiTi tendons. This behavior was the result of reduced residual deformations. Finally, for *Test E*, the initial stiffness of the connection was greater than that of *Test D* due to the additional AL tendons. The AL tendons yielded during the 0.0375% and 0.5% drift levels which resulted in reduced connection stiffness. For drift levels greater the 0.5%, the trend of the K_e for *Test E* was comparable to that seen in *Test D*. During the repeated cycling of

the connection, the AL tendons were forced into compression buckling by the superelastic NiTi tendons. This buckling limited the effectiveness of the AL tendons at low drift levels which explains the similarity between *Test D* and *E*'s K_e trends. However, once the AL tendons became fully engaged the resulting parallel action of the AL and NiTi tendons produced a slightly stronger connection, which can be seen when comparing Figure 5-19 to Figure 5-21.

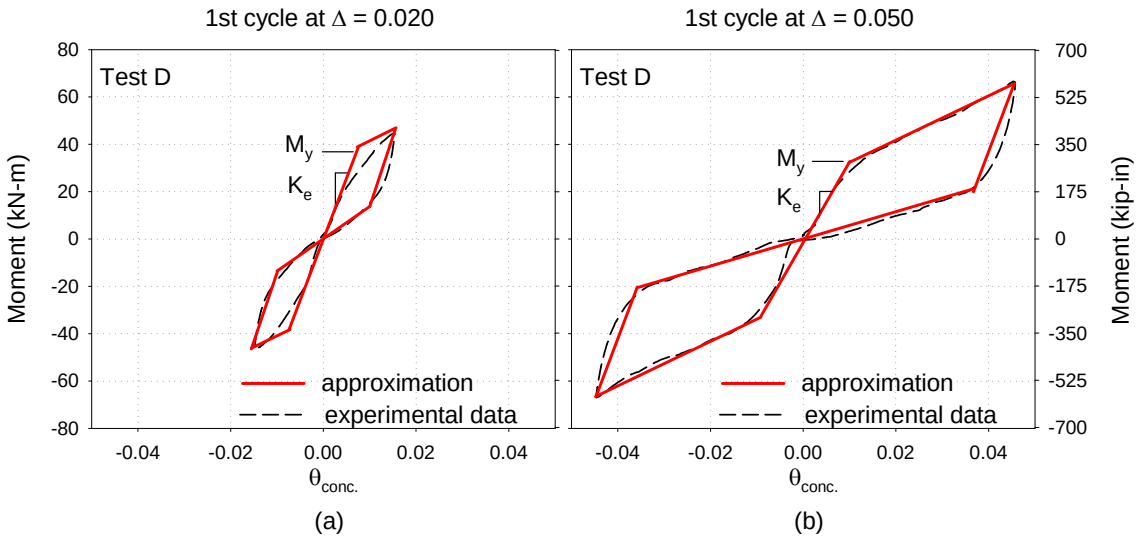

Figure 5-25: Straight line approximation of the M-θ response to get M_y and K_e.

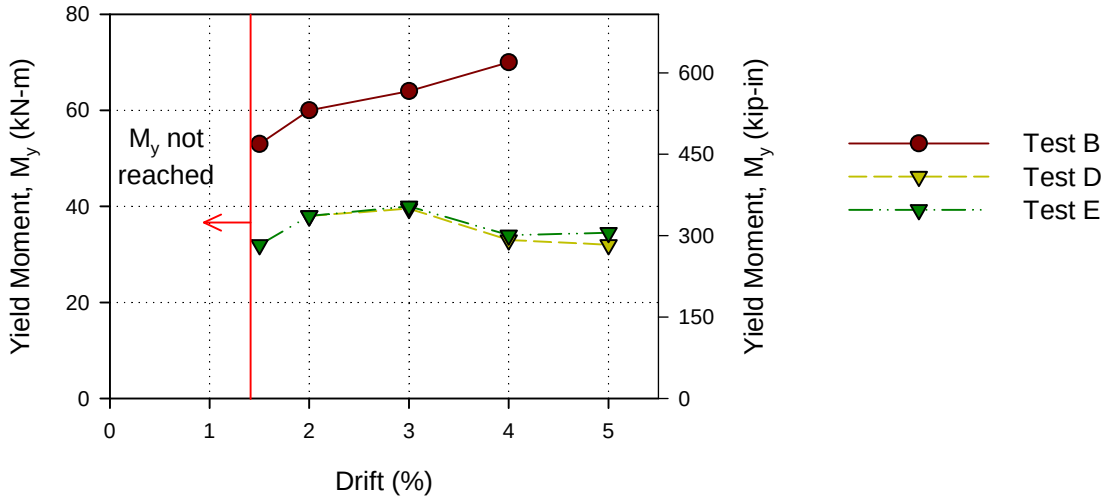

Figure 5-26: M_y over a range of drift levels for *Tests B*, *D*, and *E*.

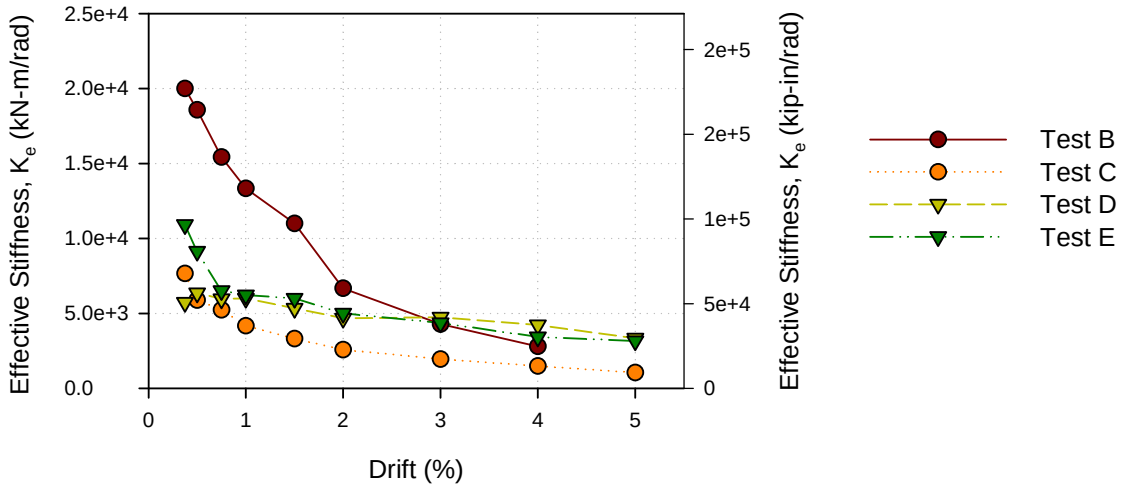

Figure 5-27: Effective stiffness, K_e, over a range of drift levels for *Tests B-E*.

5.5.3. Residual Rotation

The change in stiffness in the connection was mainly due to the accumulation of residuals in the respective steel, AL, or NiTi tendons and each tendon's inability to completely overcome the forces resisting recentering. The connection residual was defined as the point in which the slope changes on the unloading curve as shown in

Figure 5-28. This point was manually approximated for each cycle and the trend is shown in Figure 5-29. For *Test B*, the residual rotation, θ_{res}, began accumulating during the 1.5% drift level and linearly increased to 0.025 rad at 4% drift (recall *Test B* was not cycled to 5%). For *Test C*, θ_{res} began to accumulate at an earlier 0.75% drift and then increased linearly to 0.028 rad at 5.0% drift. This earlier accumulation was the result of the smaller NiTi elastic modulus which enabled the connection to strain the tendons more at smaller drift levels.

The superelastic NiTi connection tests resulted in a clear reduction in residuals (as expected). For *Test D*, θ_{res} accumulation was not observed until the 1.0% drift level, and then increased in a semi-linear fashion to 0.006 rad at 5.0% drift. For *Test E*, θ_{res} accumulation was not observed until the 1.5% drift level and then increased in a semi-linear fashion to 0.007 rad at 5.0% drift. The larger residual accumulation observed later in *Test E* compared to *Test D* was most likely due to the training that the NiTi tendons had already been through since the same physical tendons were used for both *Test D* and *Test E*.

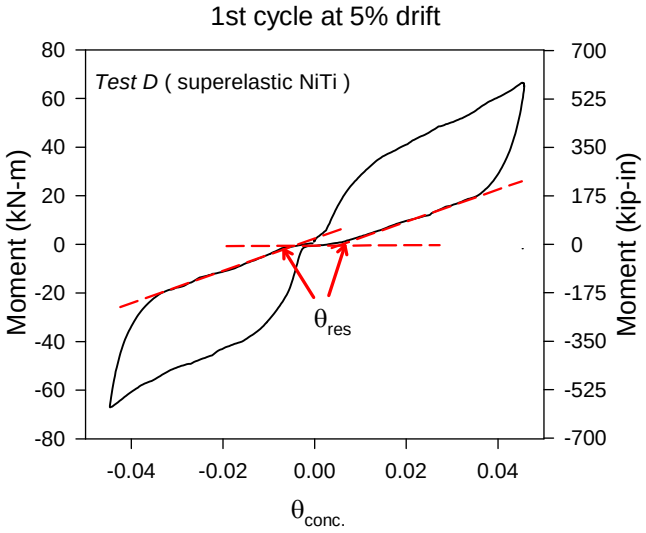

Figure 5-28: Definition of residual rotation, θ_{res}.

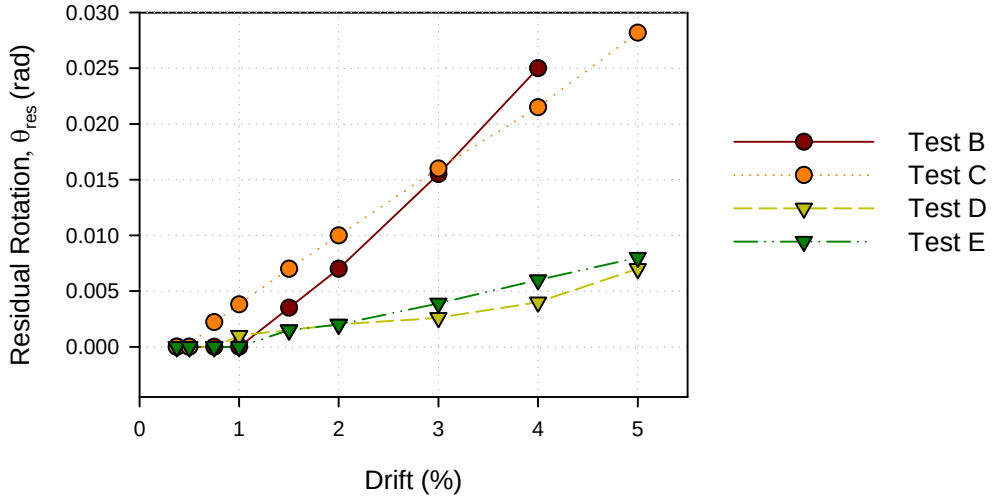

Figure 5-29: Residual Rotation, θ_r, over a range of drift levels for *Tests B-E*.

5.5.4. Energy Dissipation

During a seismic event, the earth imparts a certain amount of energy into a structure that must be either dissipated through inelastic action and damping or stored and released elastically. Energy dissipation provided by a connection generally has beneficial effects on the performance of the structure. As investigated in CHAPTER 3 of this thesis, it has been found that the right combination of energy dissipation and recentering creates a system that has reduced maximum deformations and limited residual strains. However, recentering has also been found to generally create increased acceleration demands in comparison to an equivalent elastoplastic system (Wang and Filiatrault, 2008). Therefore, the properties of a recentering system need to be properly balanced in order to produce a good performing system.

The energy dissipation for the first cycle at each drift level is shown in Figure 5-30. The cumulative energy dissipation for the first cycle at each drift level is shown in Figure 5-31: Cumlative hysteretic energy dissipated for the 1st cycle of each drift step vs. drift level for *Test B-E*.Figure 5-31. At first glance, it is surprising that the energy

dissipation in *Test B* was greater than or equal to that of the other tests at drift levels up to the 4%. However, recall the effects of the shear tab bolt tightening shown in Figure 5-11. These different torques explain the larger than expected energy dissipation for *Test B* and *C*.

In structural engineering it is customary for damping to be quantified by calculating the equivalent viscous damping ,ζ, as shown in Figure 5-32 (first cycle) and Figure 5-33 (second cycle). The ζ varied from 2-14%, with the first cycle generally greater than that of the second cycle. *Test A* and *B* had the most notable drop in ζ from cycle 1 to 2, with values dropping 75% at some drift levels. *Test D* (superelastic SMA) and *Test E* maintained ζ of 5-13% over the entire range, with ζ values increasing as drift levels increased.

Energy dissipation can be generally associated with improving structural response by decreasing drifts and accelerations. However, several studies have come to different conclusions on the need for energy dissipation in recentering systems. As pointed out in the literature review (CHAPTER 2), the research performed on PT recentering systems and corresponding SDOF systems indicate that recentering systems can produce response on par with systems focused on dissipating energy. The SDOF study done as part of this research (CHAPTER 3), demonstrated that there can be improvement in response by increasing the hysteretic area of a recentering system. However, the results of this SDOF suggest that recentering is the driving factor in the response; therefore energy dissipation is only an added secondary benefit. Furthermore, a fairly extensive analysis of partially-restrained moment frames performed by Taftali (2007) demonstrated that neither recentering nor energy dissipation produces the optimal response over a range of hazard levels. Rather, Taftali concluded that it may be beneficial to incorporate both recentering and energy dissipation elements into

the same system to optimize the performance while understanding that increased recentering results in reduced system residual deformations.

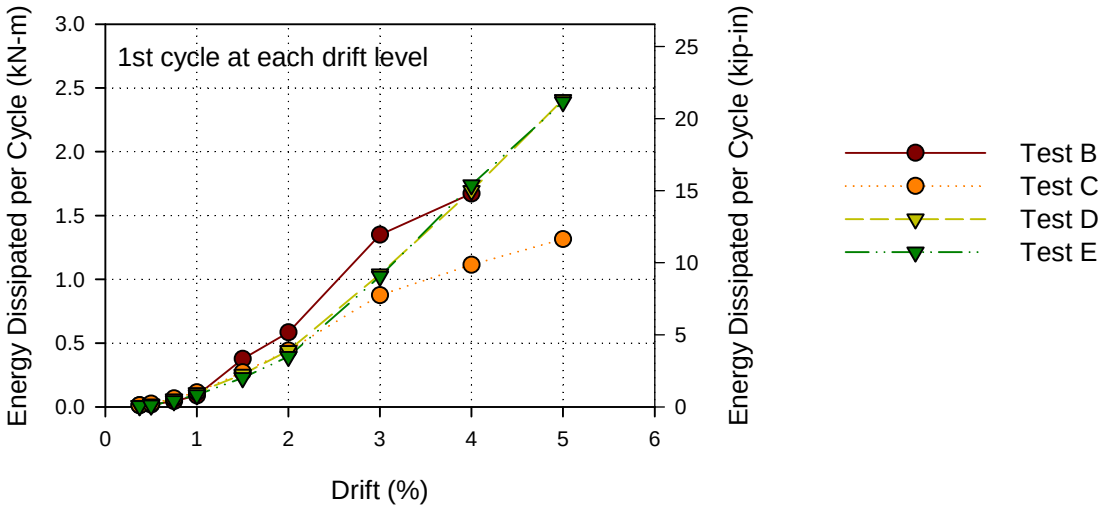

Figure 5-30: Hysteretic energy dissipated for the first cycle of each drift step vs. drift level for *Test B-E*.

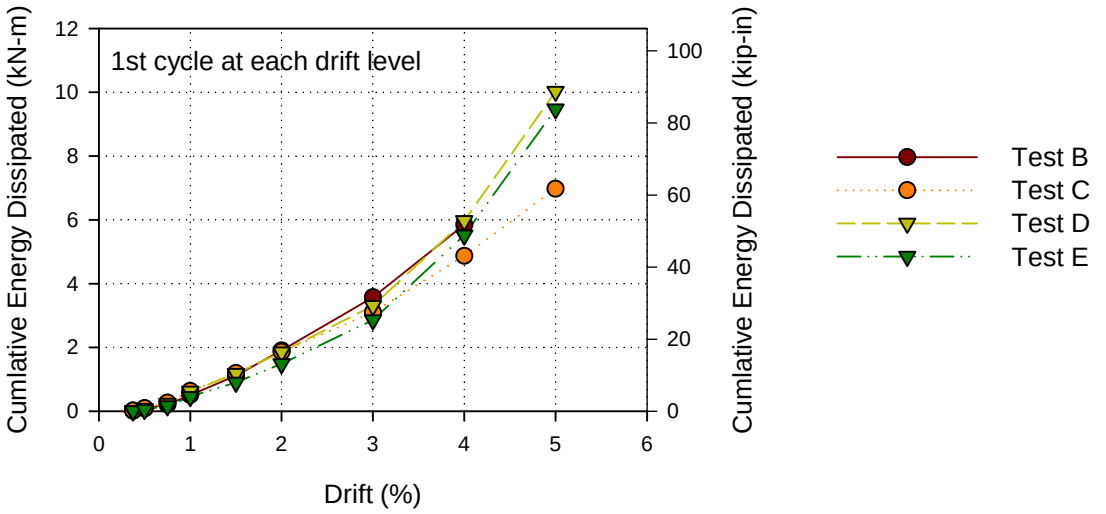

Figure 5-31: Cumlative hysteretic energy dissipated for the 1st cycle of each drift step vs. drift level for *Test B-E*.

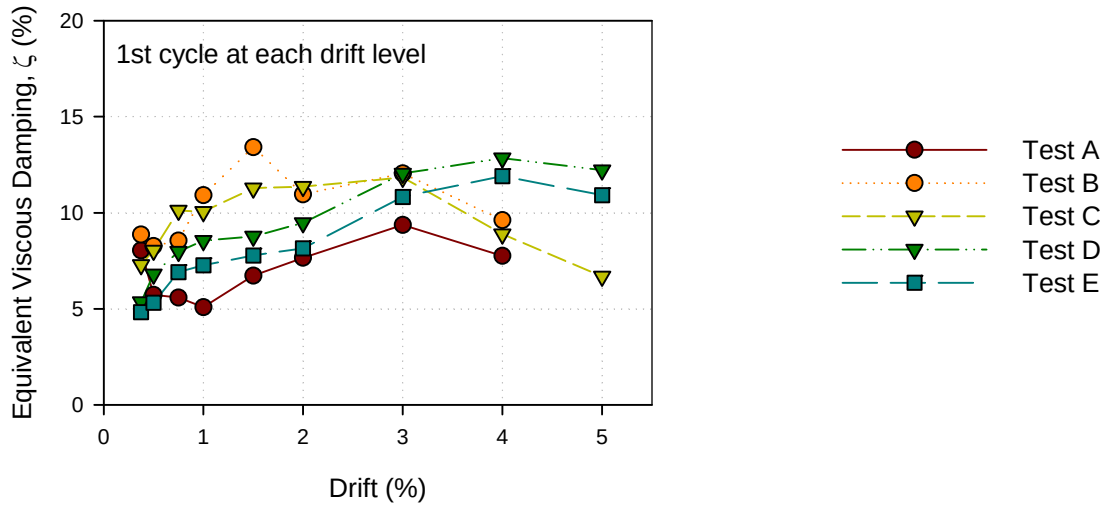

Figure 5-32: Equivalent viscous damping of the first cycle at each drift level for each test.

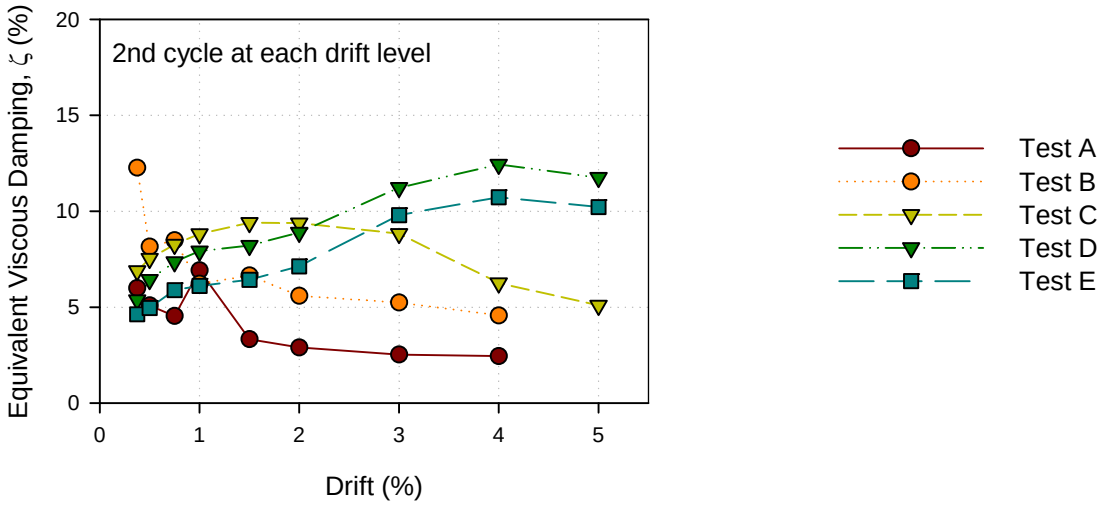

Figure 5-33: Equivalent viscous damping of the second cycle at each drift level for each test.

5.5.5. Connection Modeling

5.5.5.1. Predicted Behavior Comparison

The response of the beam-column connection was governed by three parameters: (1) the mechanical properties of the tendons, (2) the location and behavior of the pivoting

surface, (3) and the friction resistance of the shear tab. Assuming that the pivoting surface behavior is known and the bracket elements do not slip and remain effectively rigid, the contribution from the tendons and the shear tab are of most interest. In order to understand the response of the shear tab, some cyclic tests were carried out without tendons in place (as shown previously in Figure 5-11). These shear-tab-only tests were used to calibrate the shear tab elements in the connection model. Correspondingly, the mechanical tests on each material type (steel, NiTi, and AL) were used to calibrate the behavior of each tendon in the connection model.

The overall response of the beam-column connection was predicted quite well by a relatively simple model developed in OpenSEES. The model, shown in Figure 5-34, incorporated the various actions of the connection by using an appropriate combination of elements. The full loading frame was modeled because of its kinematic contribution to the connection response. The tendons were modeled as truss members with either *Steel02* or *SMA* material properties. The shear tab was modeled by connecting two nodes and an elastic no-tension (ENT) element. This ENT element was calibrated to give the corresponding stiffness and yield moment as observed in the shear-tab-only tests (Figure 5-11).

The predicted response is plotted along with the experimental response for *Test D* in Figure 5-35. The model captured the basic trends (reduced yield moment and residual accumulation) as seen in the experiment. The hysteretic damping was less in the model then in the experimental results. Two of main differences between the model and the experiment are noted in Figure 5-36. The model predicts a sharper transition zone near the loading plateau and also fails to predict the hardening experienced in the experiment for larger drift levels (which tended to decrease the concentrated rotation for equivalent drift levels).

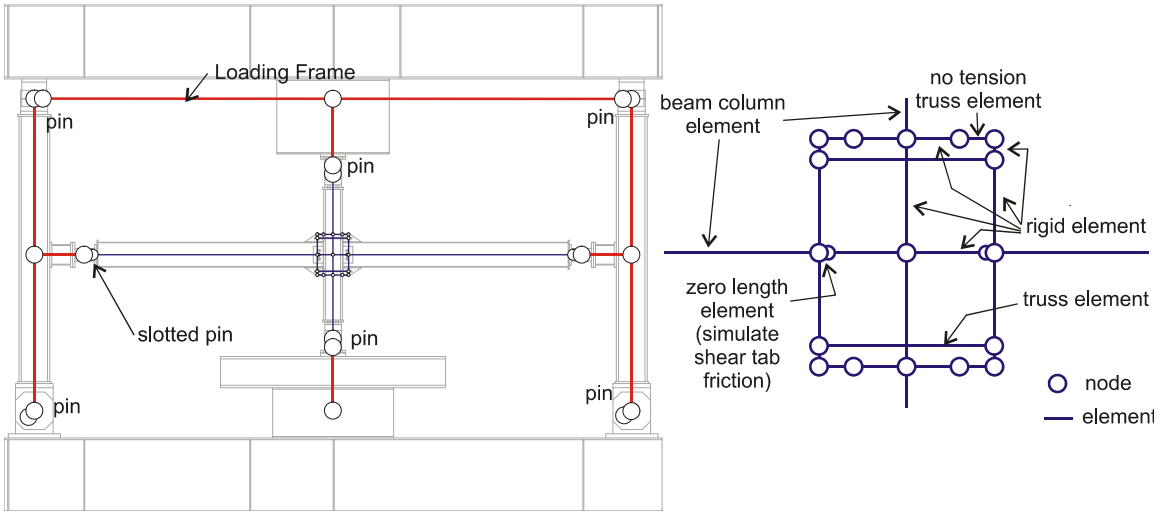

Figure 5-34: Modeling details for the prediction analysis of the beam-column connection.

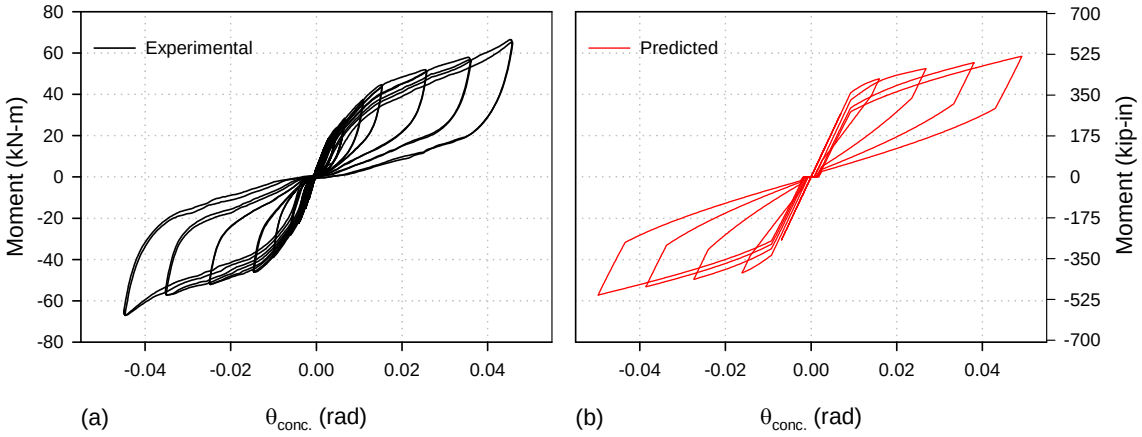

Figure 5-35: (a) Averaged experimental moment-rotation response for *Test D* vs. (b) the predicted moment-rotation response using OpenSEES

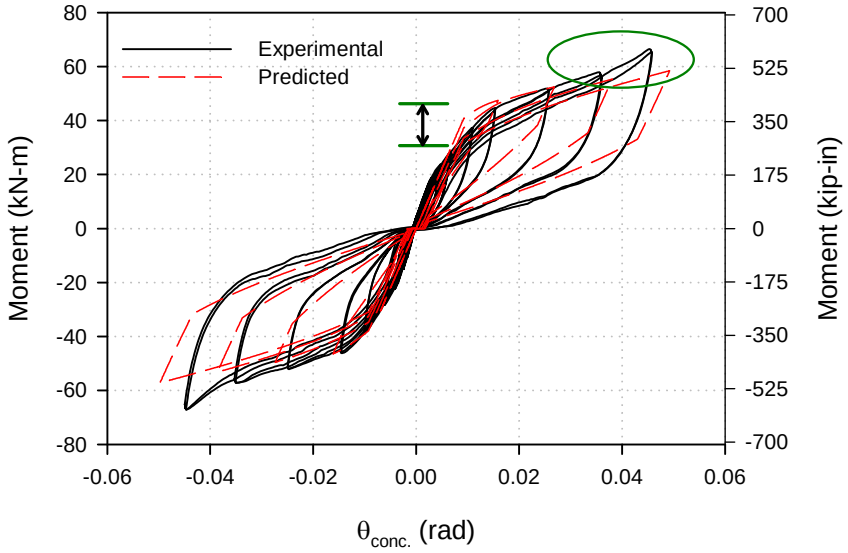

Figure 5-36: Experimental vs predicted reponse for *Test D* with some differences highlighted.

5.5.5.2. Simplified Connection Model

In order to create a model that can be more efficiently implemented into analysis of a building, a simplified model is needed. A simplified model was easily created by using a zero-length element (*zeroLengthSection*) available in OpenSEES. First, a *uniaxialMaterial* object was defined in order to describe the force-deformation (or in this case the moment-rotation) response of the section. The *uniaxialMaterial* chosen was a SMA material model developed and implemented into OpenSEES by Fugazza (2003). This is the same material model used in all the analysis of SMAs in this research. With the moment-rotation described, a *Uniaxial* section object was created with the *uniaxialMaterial* assigned to the moment resistance, M_z. Next, a *zeroLengthSection* element was created to join the beam end node to the column node (these nodes were given the same coordinates), in which the *Uniaxial* section object was used. Finally, a

multipoint constraint object (*equalDOF*) was created to constrain the translational degrees of freedom, simulating the shear tab. Although there are other ways one can create a simplified model in OpenSEES, other research suggests this is the most computationally efficient (Taftali, 2007). The simplified connection is shown in Figure 5-37.

The simplified connection model was calibrated with the experimental data and the response is shown Figure 5-38a-b. The simplified model is much more efficient than the model used for the prediction (3 nodes vs. 19 nodes per connection). However, the cost of the increased efficiency is the models inability to accumulate residuals show degradation in strength. To correct this deficiency in the simplified model, there is a need for a more advanced *uniaxialMaterial* object to be developed in OpenSEES that incorporates residual accumulation and strength reduction. With the current OpenSEES toolkit, it is recommended that the simplified model be used, but a thorough parametric assessment would need to be undertaken to back this judgment.

Investigating further, a simple way to create a model with residual accumulation is to add a hysteretic material in parallel with the SMA. This was done by using the *uniaxialMaterial Steel02* in OpenSEES and then creating a parallel material with the *uniaxialMaterial Parallel* command. The results of this change are shown in Figure 5-38c-d. For this example, the *Steel02* and *SMA* materials were given 20% and 80% of the stiffness and strength of the original simple model (Figure 5-38c-d), respectively. A comparison between the experimental results and this model is shown in Table 5-2.

In terms of maximum moment and maximum concentrated rotation, the model does a good job of capturing the response, especially for drift levels above 1.0%. Below 1.0% the model's inability to capture the smooth/rounded transition zone tends to result in an over-prediction of the moment and an under-prediction of the rotation. This over- and under-prediction also affected the model's equivalent viscous damping. For small drift

levels (1.0% and below), the model had minimal ζ, while the experiment had values of 5-8%. The author feels that the effect would be minimal because the model captures other behaviors successfully and the lower damping in the model is conservative in terms of performance results (maximum drift and acceleration). Nonetheless, additional analytical studies should be carried out to determine the effect of this difference on frame performance.

As for the residual accumulation, the model under-predicts the residual rotation in the connection for small and large rotation but accurately predicts the residual rotation at the intermediate 3.0% drift level. This is an improvement from the simple model, where, by definition, no residuals are accumulated. Moreover, other researchers have found that small levels of residual have minor effects on the overall response of a structure (Andrawes and DesRoches, 2008). Nonetheless, because of the ease of implementing the residual accumulations and the fact that a more refined model could be calibrated, the model with the residual accumulation is recommended (or a model of similar/improved behavior).

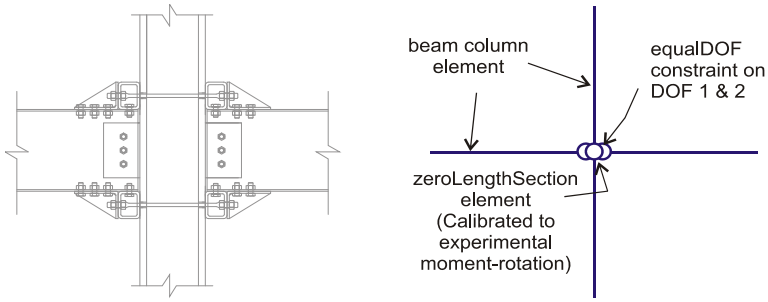

Figure 5-37: Simplified connection model.

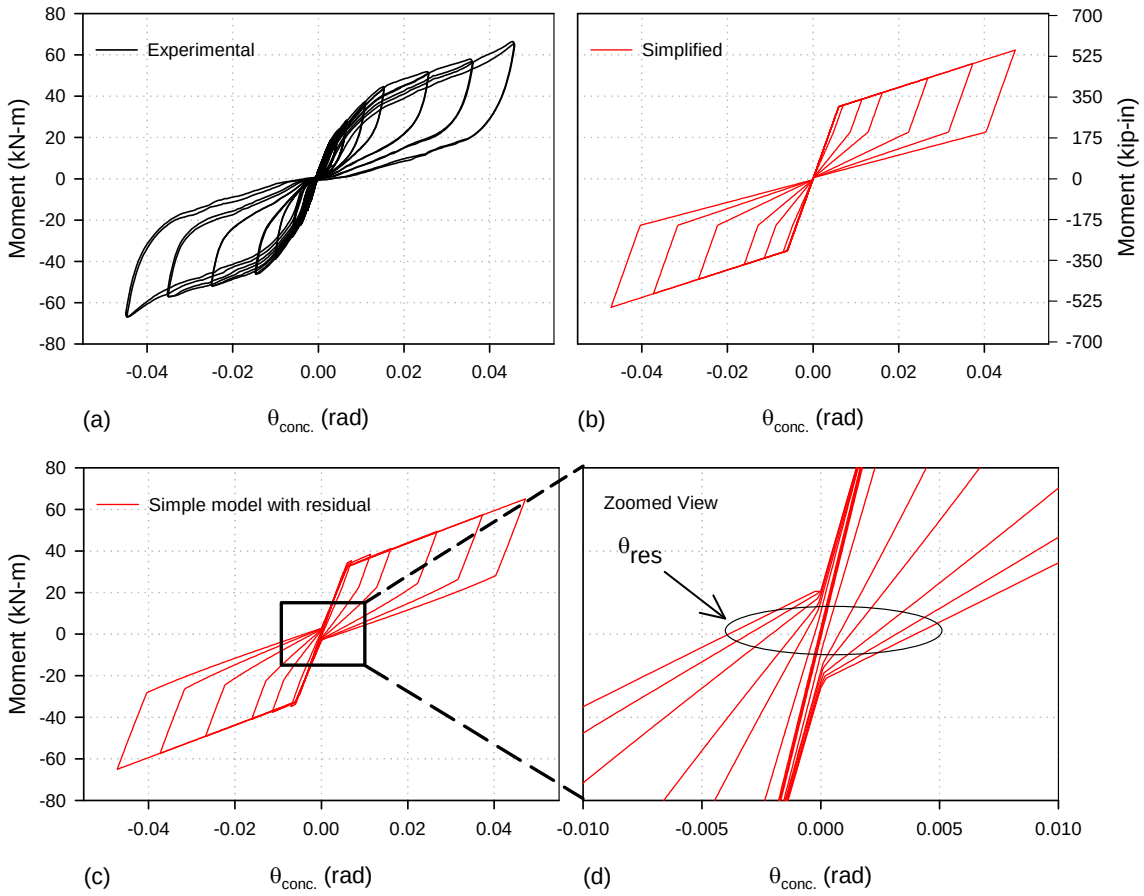

Figure 5-38: Moment-rotation response of (a) experiment (averaged left and right beam from *Test D*), (b) simplified model, (c) simplified model with residual accumulation, and (d) zoomed view of the simplified model with residual accumulation.

Table 5-2: Comparison of the experimental results (*Test D*) versus the model with residual accumulation in terms of the maximum concentrated rotation, maximum moment, residual rotation, and equivalent viscous damping.

Experimental = Exp, Model with Residual Accumulation = Mod								
	Exp	Mod	Exp	Mod	Exp	Mod	Exp	Mod
Drift, %	Max Conc. Rotation, rad		Max Moment, kN-mm (kip-in)		Residual Rotation θ_{res}, rad		Equiv. Viscous Damping ζ, %	
0.375	0.0023	0.0026	13930 (123)	15460 (137)	-	-	5.4	0
0.5	0.0027	0.0032	18060 (160)	18950 (168)	-	-	6.8	0.02
0.75	0.0048	0.0051	23890 (211)	29510 (261)	-	-	8.0	0.3
1.0	0.0067	0.0070	28310 (251)	35230 (312)	0.0010	0.0003	8.5	3.6
1.5	0.0109	0.0114	37380 (331)	38360 (340)	0.0015	0.0008	8.8	9.4
2.0	0.0154	0.0161	44580 (395)	41150 (364)	0.0020	0.0013	9.5	11.9
3.0	0.0256	0.0268	51620 (457)	49400 (437)	0.0026	0.0023	12.1	13.4
4.0	0.0357	0.0373	57620 (510)	57340 (508)	0.0040	0.0032	12.9	13.7
5.0	0.0455	0.0472	66320 (587)	64980 (575)	0.0070	0.0040	12.2	13.7

5.5.6. From Research to Practice: Potential Applications

As mentioned previously, the design details of this connection were not intended to represent a connection that would be appropriate for application in the construction practice. Rather, these connection tests were performed in order to demonstrate that one can predict the behavior of some of the "spring" elements in the connection (in this case the NiTi tendons). The other "rigid" element (anchor brackets, etc.) can be modified as needed with the goal of creating a connection that could be practically implemented into real-world construction.

One potential path in which NiTi tendons could be implemented into a connection is by integrating them into a Kaiser bolted bracket (KBB) connection (Adan and Gibb, 2008). The Kaiser bolted bracket was originally created after the 1994 Northridge and 1995 Kobe earthquakes as a way to rehabilitate damaged fully-restrained connections. The creators also saw potential in the economic and performance benefits for the

implementation of these brackets in new construction. Currently, the KBB is prequalified and is an extremely viable option for various construction projects.

The KBB connection shifts the beam's inelastic rotation away from the column face, thus creating a very ductile system. However, the extensive damage to the beams during a large earthquake would inevitable require demolition or extensive repair of the structure. To elevate this performance to a higher level, it is proposed that NiTi tendons be integrated into the system. Rather than the beam yielding, the NiTi could provide a "fuse" in order to absorb the deformations and limit force transfer. This type of system would provide another layer of protection to a structure and have potential to greatly enhance the performance. Additional solutions, such as the welded T-stubs being developed by Swanson and Leon (2000), could also be investigated.

5.5.7. Analytical Study

Though a formal analytical study was not conducted in this research, Taftali (2007) presented an extensive study on the probabilistic seismic demand of SMA connections in steel frames. Superelastic SMA connections were shown to be most beneficial in reducing or eliminating residual deformations. Taftali demonstrated that neither recentering nor energy dissipation produced the optimal response over a complete range of hazard levels. Rather, Taftali concluded that it may be beneficial to incorporate both recentering and energy dissipation elements into the same system to optimize the performance while understanding that increased recentering results in reduced system residual deformations.

5.6. Summary

Five tests were conducted on a beam-column connection in order to assess the viability of creating a recentering connection using superelastic NiTi tendons. *Test A* and *B* were preliminary tests ran to ensure that all of the inelastic action would be concentrated into the tendon "fuse" elements. Modifications were made to the anchor brackets after *Test A* and the adequacy of these modifications were verified in *Test B*. *Test C* was the first attempt at obtaining recentering connection behavior; however, the NiTi tendons proved to be martensitic, resulting in strain recovery only after the application of heat. Recentering response was obtained in *Test D* after new superelastic NiTi tendons were created and installed. This recentering action could be predicted accurately by a detailed finite element model in OpenSEES. However, in order to create a model that could be implemented efficiently into a full structural analysis, a simplified model was created and the adequacy of this model was verified. Finally, in *Test E*, aluminum tendons were installed in parallel with the NiTi tendons used in *Test D*. Once again the connection had good recentering behavior and demonstrated that NiTi tendons can exert significant force during their shape recovery. The connection in *Test E* had increased strength, stiffness, and energy dissipation. However, the lack of effective buckling restraint on the aluminum bars decreased the complete benefits of this parallel system.

The results of these five tests demonstrated that a NiTi SMA-based connection can be developed to have excellent ductility, energy dissipation, and recentering. The following conclusions and significant observations are:

- NiTi tendons possess significant superelastic properties which were able fully recenter a connection at drift levels below 1.0% and adequately recenter a connection at drift levels above 1.0%. Additionally, the connection was able to recover 85% of its drift at the 5.0% drift level.

- The NiTi connection had equivalent viscous damping that varied from approximately 6 to 13% as drift levels increased from 0.375 to 5.0%. The energy dissipation in the connection was a direct result of NiTi's hysteretic mechanical behavior and friction in the shear tab connection.
- The equivalent viscous damping in the superelastic NiTi (*Test D*) connection was greater than that of the parallel (*Test E*) connection. This surprising result is explained by the following observations: 1) the same physical tendons were used in both tests, resulting in reduced material hysteresis for *Test E* (as was observed in the mechanical test conducted herein and other training studies); and 2) the AL tendons buckled in compression resulting in a minimal increase in hysteretic area at larger drift levels.
- For the test connection layout, a 0.5% prestrain was applied to all NiTi tendons. Prestraining of the NiTi tendons was effective in increasing the recentering capability, and the overall behavior of the connection.
- A simple model in OpenSEES provided a good fit to the experimental data. However, this model tended to overestimate the strength and stiffness at small drift levels due to its inability to capture the behavior at the transition zones. A simple model with residual accumulation accurately predicted the equivalent viscous damping and forward stress plateau of the connection. Both simple models enable the NiTi connection to be efficiently implemented into further analytical studies.

The next step for such a connection is to create a prototype that is designed with realistic, efficient, and cost effective construction details. Such a connection could involve integrating NiTi tendons into other promising connection types currently being

developed, such as the Kaiser Bolted Bracket connection (Adan and Gibb, 2008) or the welded T-stub (Kasai and Xu, 2002a; Kasai and Xu, 2002b) connection.

CHAPTER 6

INVESTIGATION OF A RECENTERING ARTICULATED QUADRILATERAL BRACING SYSTEM

6.1. Introduction

This chapter presents the conception, design, and proof-of-concept testing of a SMA-based recentering articulated quadrilateral bracing system. Braced frames have received renewed interest since the 1994 Northridge and 1995 Kobe earthquakes because of the unexpected damage found in a large amount of welded moment frames. This poor performance under moderate earthquakes has resulted in a reevaluation of steel moment resisting frames. Researchers have thus begun to revisit other lateral load resisting systems, giving the engineering community new options to obtain earthquake resilience.

Braced frames are one of the main viable alternatives to moment resisting systems. To obtain good ductility, and therefore enable higher strength reduction factors, traditional bracing systems have to be designed with special attention to the connections. However, even with special measures, traditional braces are characterized by a loss of load carrying capacity due to compression buckling and degrading behavior after repeated cycling. To improve this behavior, newer systems, such as the buckling restrained brace (BRB), have become an excellent option when a high level of performance is needed. The BRB performance is characterized by an elastoplastic-type response with good energy dissipation, controlled strength, and large ductility.

As an alternative to an elastoplastic system, several researchers have investigated the benefits of recentering systems. Analytical and experimental studies

have shown that recentering systems are a viable alternative to both traditional and advanced systems, especially when residual deformations need to be limited.

In this chapter a SMA-based recentering system is proposed, developed, and tested. The system is based on a unique articulated quadrilateral geometry and implements SMA wire bundles that can either act alone or be placed in parallel with c-shaped conventional steel energy dissipators. The details of the AQ are first outlined and then the experimental results from three braced frame tests are presented and summarized. The behavior is then assessed in terms of strength, stiffness, recentering ability, and energy dissipation. Lastly, an analytical case study is conducted to investigate the potential benefits of such a system.

6.2. Background

Quadrilateral arrangements of the type proposed in this research have been investigated before. Pall and Marsh (1982) investigated the use of a special arrangement of members to create a friction damped bracing system as shown in Figure 6-1a. Renzi et al. (2004) referred to this arrangement as an *articulated quadrilateral* (hereafter AQ). One key advantage of an AQ arrangement is that both tension and compression can occur in the inside elements, while all other elements experience only tension. The link members of the AQ force the contraction of one diagonal when the opposite diagonal is being extended. Since yielding elements require both tension and compression to cycle about the origin, this configuration provides a convenient way to create hysteretic damping without the need for buckling restraint in a global brace member. Additionally, due to the kinematics of the AQ, if the adjacent bracing members are sufficiently stiff, these bracing members will be forced to stay in tension.

Other researchers have investigated similar types of geometry with friction or yielding as the energy dissipation mechanism (Ciampi et al., 1995; Tyler, 1983; 1985a; 1985b). More recently, Renzi et al. (2007; 2004) used an AQ setup with c-shaped energy dissipators, as shown in Figure 6-1b. The concept is similar to that devised by Pall and Marsh, but friction dissipation is replaced with flexural yielding dissipation. When the c-shape is loaded, a constant moment (at small displacements) is developed along its body, resulting in a theoretically uniform plastic moment along the c-shaped length. The results from Renzi's experimental tests showed the c-shaped dissipator produced good dissipating behavior.

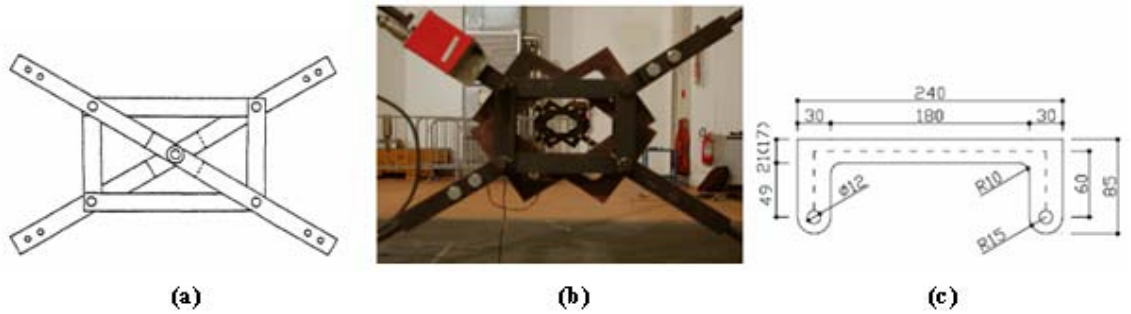

Figure 6-1: (a) Pall friction AQ (Aiken et al., 1993) and (b-c) c-shape dissipator in AQ (Renzi et al., 2007).

6.3. Test Setup

6.3.1. General AQ

The general setup of the AQ is shown in Figure 6-2 with both the SMA and c-shape dissipators. The dimensions of the AQ were governed by the dimensions of the loading frame (length-to-width ratio) and the length of the available SMA bundles. The SMA bundles were 711 mm (28 in.) long. Figure 6-3 shows the resulting dimensions that were selected for the AQ. The AQ links were made from 12.7 mm (0.5 in.) thick, 50.8 mm (2.0 in.) wide A36 flat bar. The joints were pinned with A490 22.2 mm (0.875 in.) bolts. The anchor blocks, made from A572 grade 50 steel, served to transfer the load from the cable assembly to the SMA wire bundles via two 12.7 mm (0.5 in.) grade 8 coarse-threaded rods connected to a 19.1 mm (0.75 in.) square bar combined with a 19.1 mm (0.75 in.) stainless steel half-round (not shown). The c-shape was attached to the anchor block on the outside of the AQ links via the joint bolts.

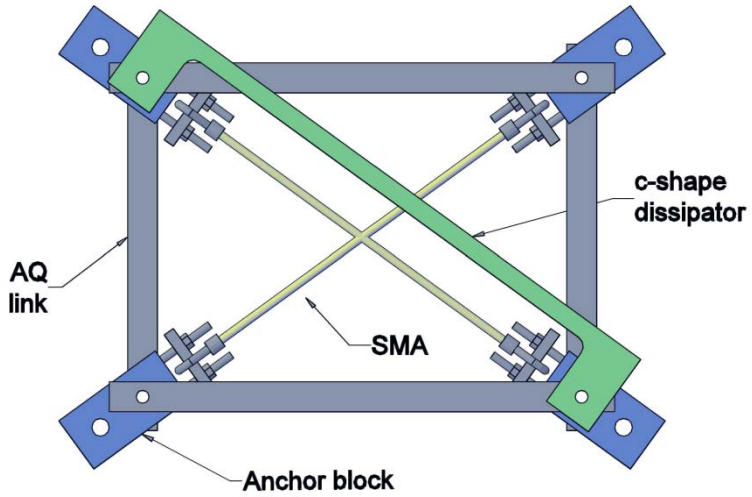

Figure 6-2: General articulated quadrilateral (AQ) setup with c-shapes and SMA wire bundles.

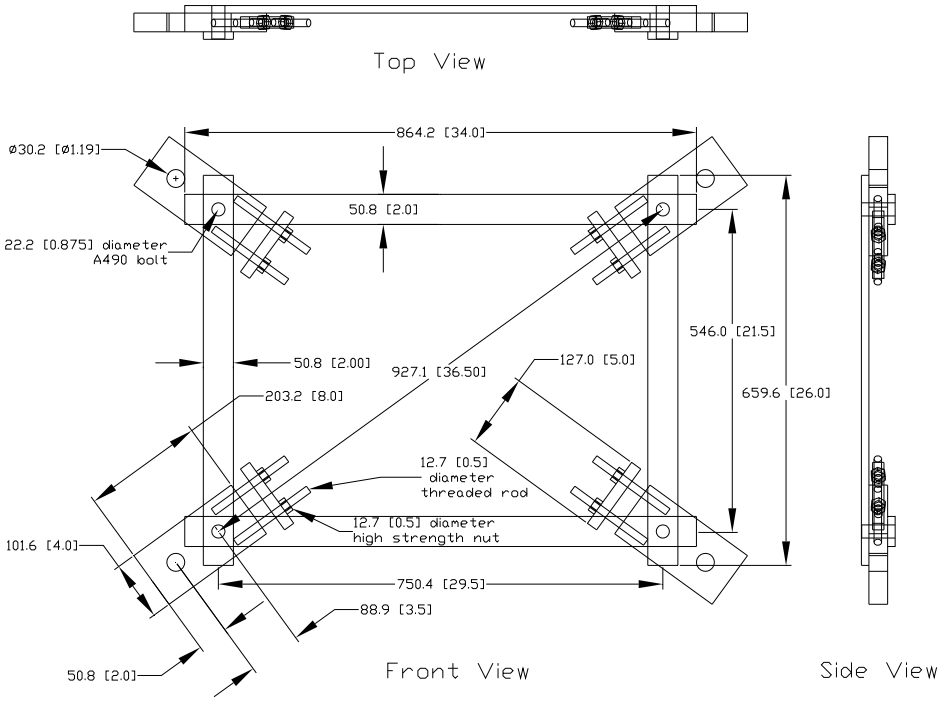

Figure 6-3: Dimension of AQ without c-shapes and SMA. Units in mm (in.).

6.3.2. Cable Assembly

The following components were used to create the cable assemblies that formed the remaining balance of the brace:

- A 25.4 mm (1.0 in.) 18-7 bright wire cable with thimbles and swag sleeves installed at each end, giving the cables 95% of its rated 222 kN (50 kips) breaking strength.
- A 25.4 mm (1.0 in.) 457 mm (18 in.) take-up turnbuckle with jaw-jaw ends and a breaking strength of 222 kN (50 kips).
- A 22.2 mm (0.875 in.) Crosby shackle with breaking strength of 454 kN (104 kips)
- A tensile load cell created from 25.4 mm (1.0 in.) grade 8 coarse-threaded rod.
- A padeye anchor attached to the testing frame with four 7/8 in. A325 bolts. The padeye anchors were fabricated from 31.8 mm (1.25 in.) thick A572 grade 50 steel. The dimensions are shown in Figure 6-5.

The entire bracing system is shown in Figure 6-4 with the cable assembly labeled.

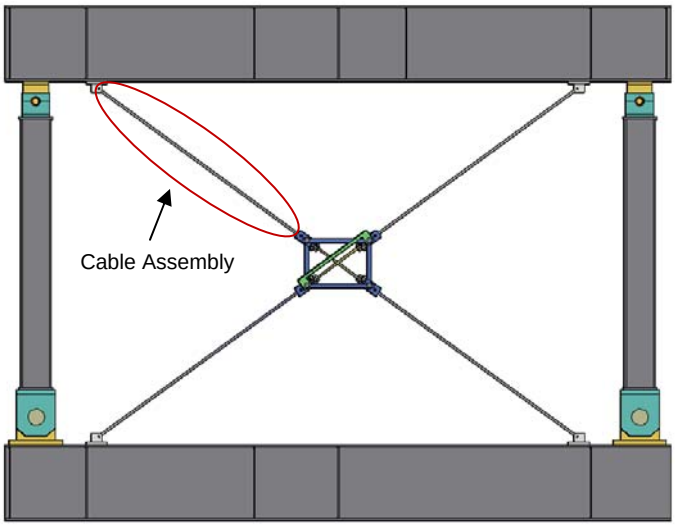

Figure 6-4: AQ brace system in loading frame.

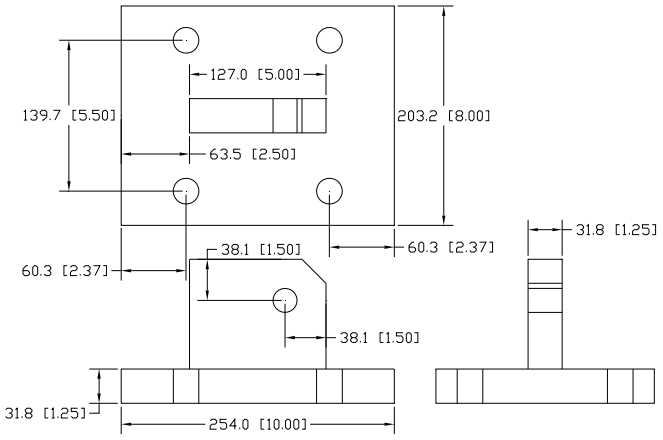

Figure 6-5: Padeye dimensions for AQ tests. Units in mm (in.).

6.3.3. Test A: SMA-only

Test A was conducted using SMA wire bundles as shown in Figure 6-6. The details of the wire bundles are described in the component test section (Section 6.5.1). The SMA bundles were prestrained approximately 2.5 mm (0.1 in.) in order to give the device some initial stiffness. Further prestraining was not possible due to the AQ links buckling in compression. After the SMAs were prestrained, the AQ was inserted into the test frame and the cable assemblies were tightened in a sequential manner to give each cable approximately 6.7 kN (1.5 kips) of tension. Lastly, the nuts on the SMA attachments were further tightened 1/3 turn to increase the pretension in the SMA wires. The test was performed at 26 °C.

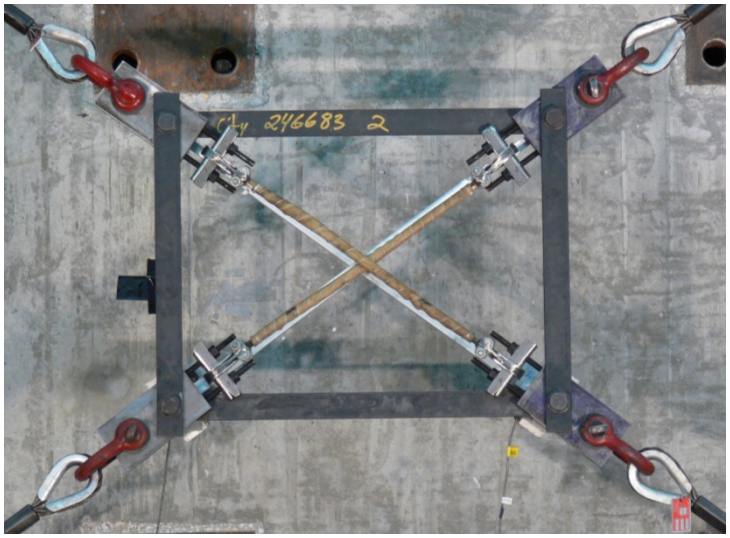

Figure 6-6: AQ setup for the SMA-only test, *Test A*.

6.3.4. Test B: C-shape-only

Test B was performed with two c-shapes installed in the AQ. The c-shapes were put in the same direction and braced to one another in order to increase their out-of-plane buckling resistance. The dimensions of the c-shapes are shown in Figure 6-7. They were fabricated from 203 mm (8.0 in.) wide, 12.7 mm (0.5 in.) thick A36 flat bar. A plasma cutter was used to cut the shape and then the edges were finished with a grinder and a mill file. The AQ specimen is shown in Figure 6-8. The cables were again pre-tensioned to 6.7 kN (1.5 kips). The test was performed at 27 °C.

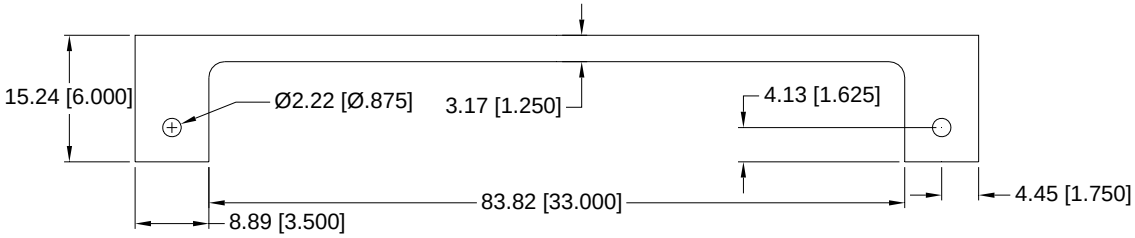

Figure 6-7: C-shape dimensions for *Test B*, t = 12.7 mm (0.5 in.). Units in mm (in.).

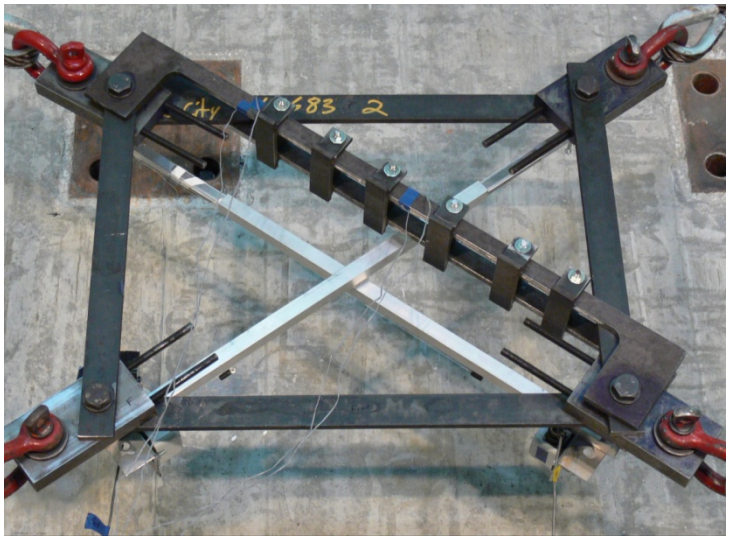

Figure 6-8: AQ setup for the c-shape-only test, *Test B*.

6.3.5. Test C: Parallel System (SMA + c-shape)

Test C was performed with SMA bundles installed in parallel with two c-shape dissipators. The same size c-shapes were used as those in *Test B*, with one modification; the holes were slotted 19.1 mm (0.75 in.). This was done to alleviate some of the kinematic stiffening seen in the c-shape (see APPENDIX G for further discussion). The c-shapes were again put in the same direction, but were only tied together at two points rather than six. The c-shape dimensions are shown in Figure 6-9. The specimen is shown in Figure 6-10. The cables were pretention to 6.7 kN (1.5 kips) and the test was performed at 24 °C.

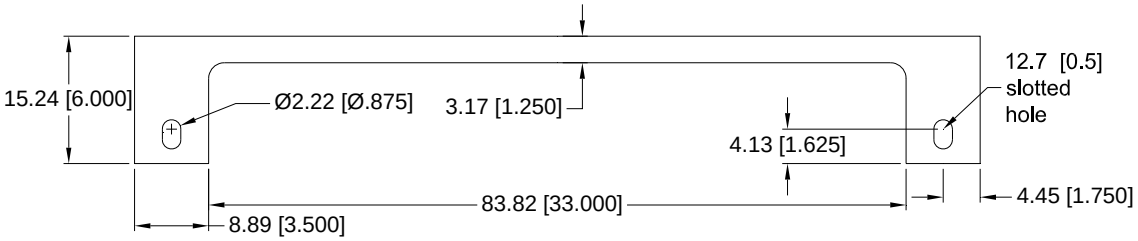

Figure 6-9: C-shape dimensions for *Test C*, t = 12.7 mm (0.5 in.). Units in mm [in.].

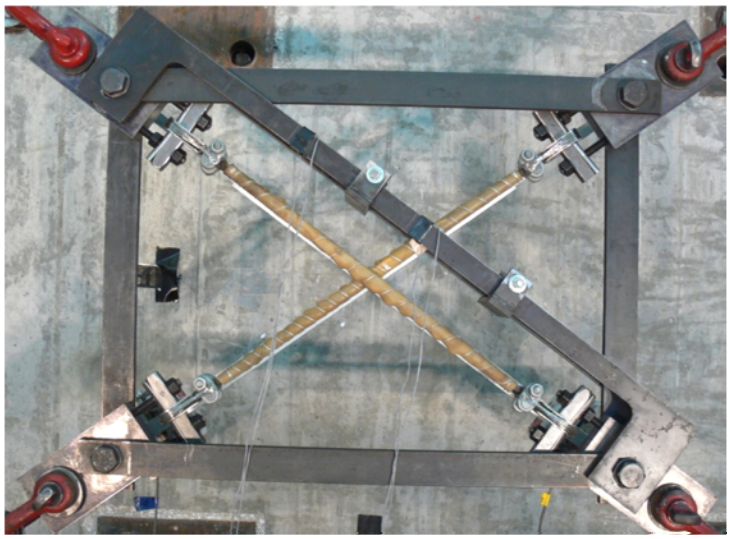

Figure 6-10: AQ setup for the c-shape-only test, *Test C*.

6.4. Testing Scheme

This section describes the testing scheme used for the experimental portion of this study. The same loading frame described in CHAPTER 5 was used for this experimental investigation. Further details of this loading frame can be found in APPENDIX A.

6.4.1. Instrumentation

The instrumentation for the experimental testing plan is shown in Figure 6-11. The cable loads were monitored by custom-made cable load cells. A 25.4 mm (1.0 in.) high-strength threaded rod was milled to create a section that was 18 mm (0.7 in.) square and 50 mm (2.0 in.) long. FLA-3-11 TML 120-ohm strain gauges were attached to each flat-milled surface in alternating longitudinal and transverse directions. These four gauges were then wired together to form a Wheatstone Bridge. The resulting output voltage was linearly related to the applied load. The load cells were calibrated to 145 kN (32.5 kips) and the sensitivity values for a 10 V excitation are shown in Table 6-1.

To obtain the AQ diagonal deformations, stringpots were mounted to 6.4 mm (0.25 in.) bolts that were screwed into threaded holes at the ends of the joint bolts. These stringpots were guided by a sliding aluminum tube assembly (Figure 6-12). Another stringpot was used to obtain the lateral displacement of the testing frame. Additionally, the actuator load cell and LVDT were monitored in order to obtain redundant measurements of base shear and lateral drift of the bracing system. To verify that the padeyes were not slipping at the end of the cable assemblies, LVDTs were mounted between the padeyes and the loading frame beams. Finally, for the tests incorporating the c-shape dissipators, four strain gauges were installed at quarter-points along the length (noted in Figure 6-13).

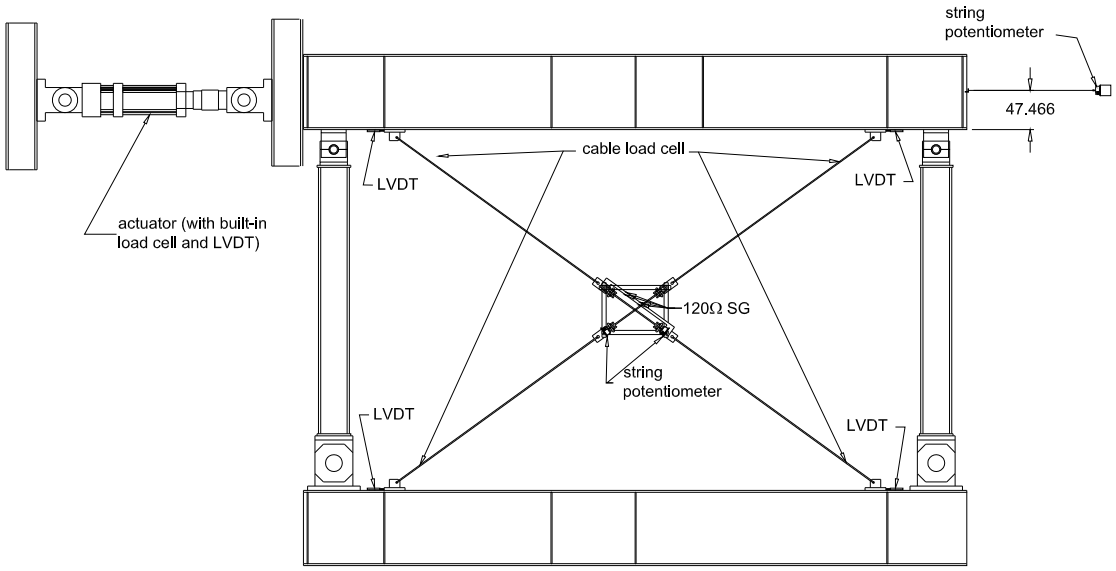

Figure 6-11: Instrumentation scheme for AQ testing.

Table 6-1: Tensile load cell calibration values with 10V excitation.

Load Cell	Sensitivity (kN/mV)
LC1	4.650
LC2	4.499
LC3	4.716
LC4	4.560

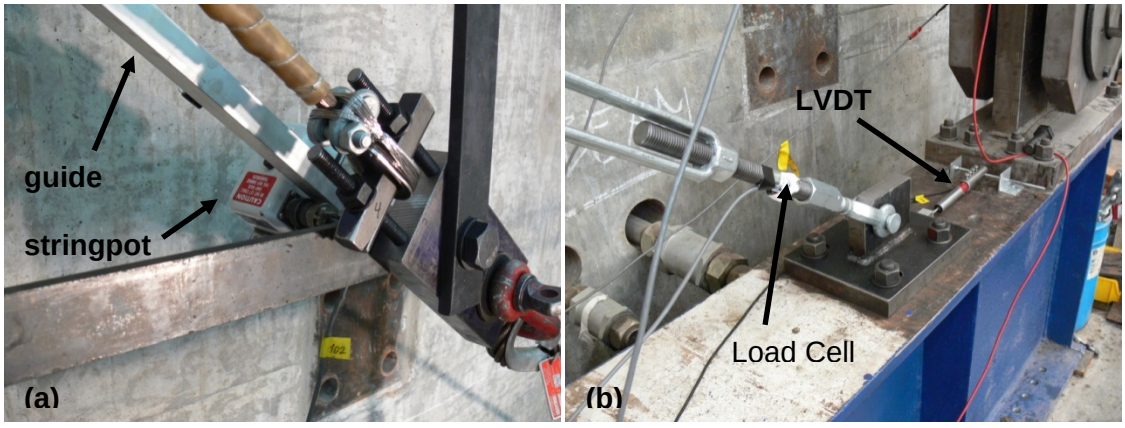

Figure 6-12: Instrumation details for (a) the AQ and (b) the cable assembly.

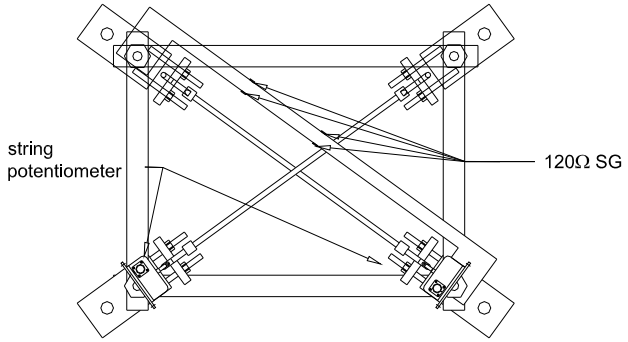

Figure 6-13: Close-up view of instrumentation scheme for AQ testing.

6.4.2. Loading Protocol

The loading protocol used for these tests was the same as that used for the beam-column connection test in CHAPTER 5, except for a few deviations that are noted in the test results section. The interstory drift was selected as the controlling parameter, based on a 437 cm (172 in.) story height. The testing protocol was implemented using a MTS 407b controller.

6.5. Pretests

6.5.1. Component Test: Wire Bundle

The SMA wire bundle was first tested in a 250 kN (55 kip) MTS Universal Testing frame. The force-deformation behavior is shown in Figure 6-14. The SMA bundle had a cross-section of 320 0.71 mm (0.028 in.) diameter superelastic NiTi wires. To create this cross-section, a NiTi wire was wound 160 times around 9.6 mm (0.375 in.) thimbles and then fixed with a 9.6 mm (0.375 in.) double-saddle cable clip. The cross-sectional area of the SMA bundle was 130 mm^2 (0.20 in^2). The effective length, defined as the distance from clamp-to-clamp, was 559 mm (22 in.). The length from bearing-to-bearing was 711 mm (28 in.).

The bundle had great ductility and limited residual deformations. The transformation stress was approx. 550 MPa (80 ksi), compared to 325 (47.0 ksi) found in the bar (see Section 5.2.1). This stress increase was most likely due to cold working. Additionally, the hysteretic area is larger for the wire bundle than that displayed in the bar, which is also a result of cold working and has been noted in previous work (DesRoches et al., 2004).

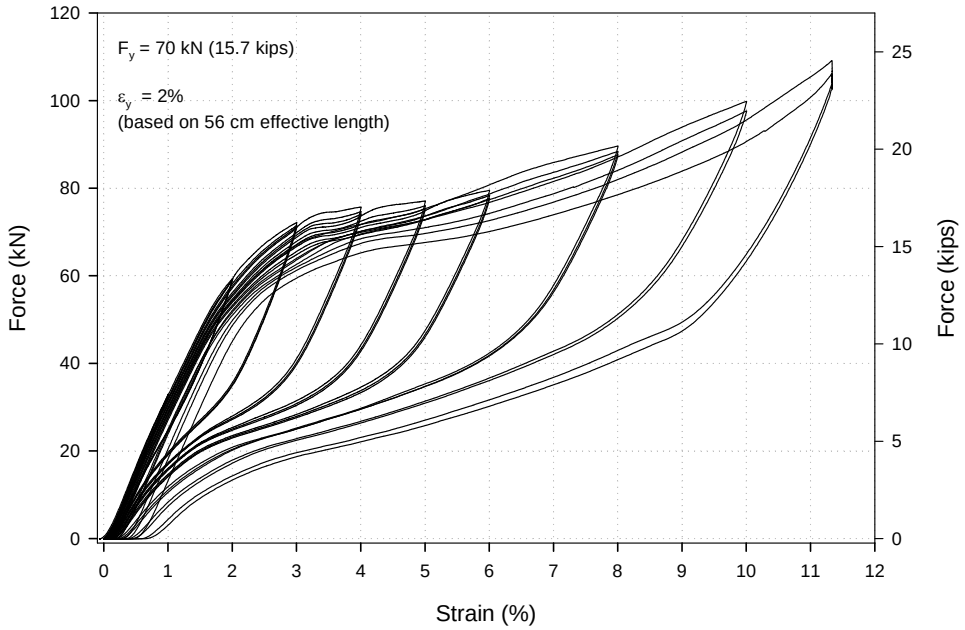

Figure 6-14: Cyclic force-strain relationship of 129 mm^2 (0.2 in^2) SMA wire bundle.

6.5.2. Shakedown Test

A “shakedown” test was carried out in order to get rid of some of the cable assemblies’ expected inelastic deformations. This test consisted of installing two extra SMA wire bundles and systematically cycling the frame, tightening the turnbuckles, and then cycling the frame until the cable load cells reach 133 kN (30 kips). The majority of the inelastic deformation came from the cable thimbles collapsing and the accompanying thimble bearing service flatting out. This shakedown effectively locked-in the deformations into the cable-assembly elements.

6.6. Experimental Results

6.6.1. Test A

In *Test A*, SMA wire bundles were the only elements installed in the AQ. The actuator displacement time history is shown in Figure 6-15. The resulting base shear vs. story drift is shown in Figure 6-16, assuming the story height to be 437 cm (172 in.). The brace remained elastic through the 1.0 % drift cycles, with full recentering at the end of each cycle.

During the 1.5% cycle, the SMA wire bundles reached their transformation stress, as is evident by the load plateau in Figure 6-16. Figure 6-17 plots the cable force (averaged from the two load cells on each diagonal) vs. the AQ deformation. This plot is essentially the force-deformation plot of the SMA element. Additionally, the cable force vs. drift is plotted in Figure 6-18.

During the 2% drift cycle, the SMA was pushed further along its loading plateau but not completely into its martensitic phase. The brace showed little strength degradation and little stiffness degradation. To finish the test, the frame was cycled six times to 3% drift. The brace began to have some strength degradation and some residual accumulation (and therefore effective stiffness degradation). However, the response stabilized after several cycles.

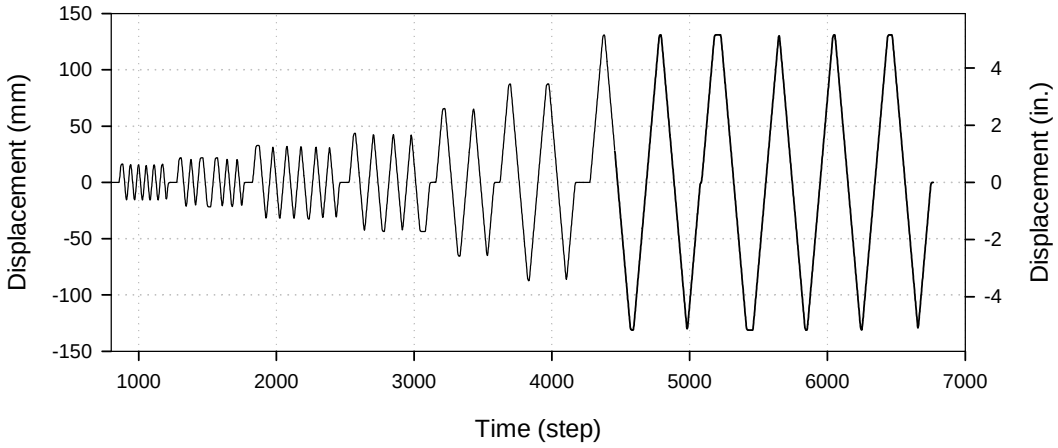

Figure 6-15: Actuator displacement time history for *Test A*.

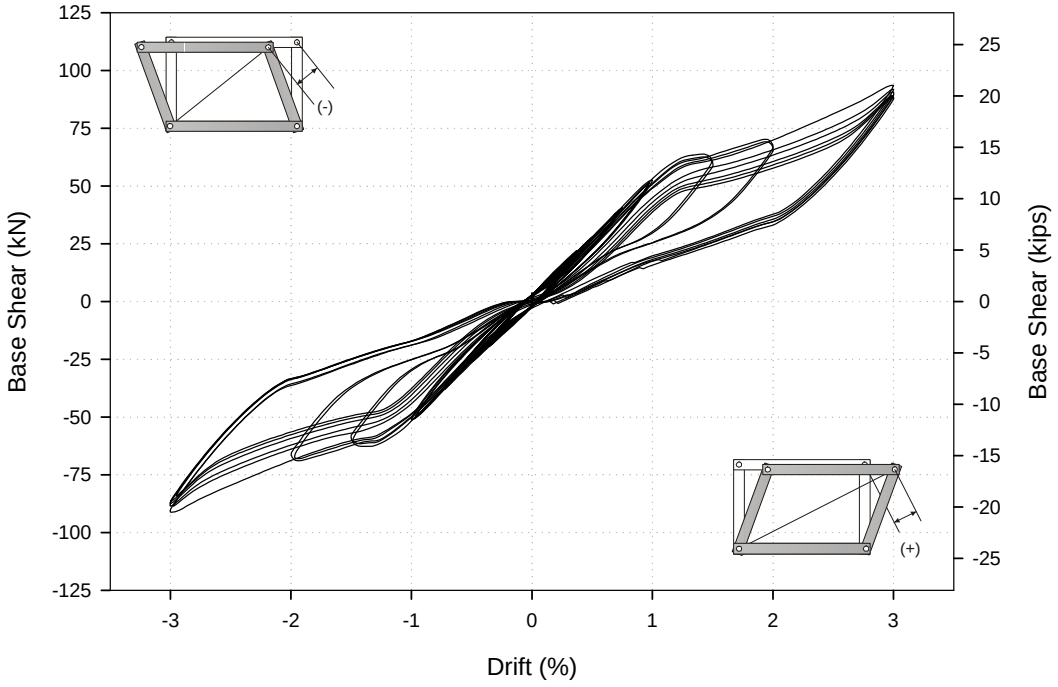

Figure 6-16: Base shear vs. story drift for *Test A*.

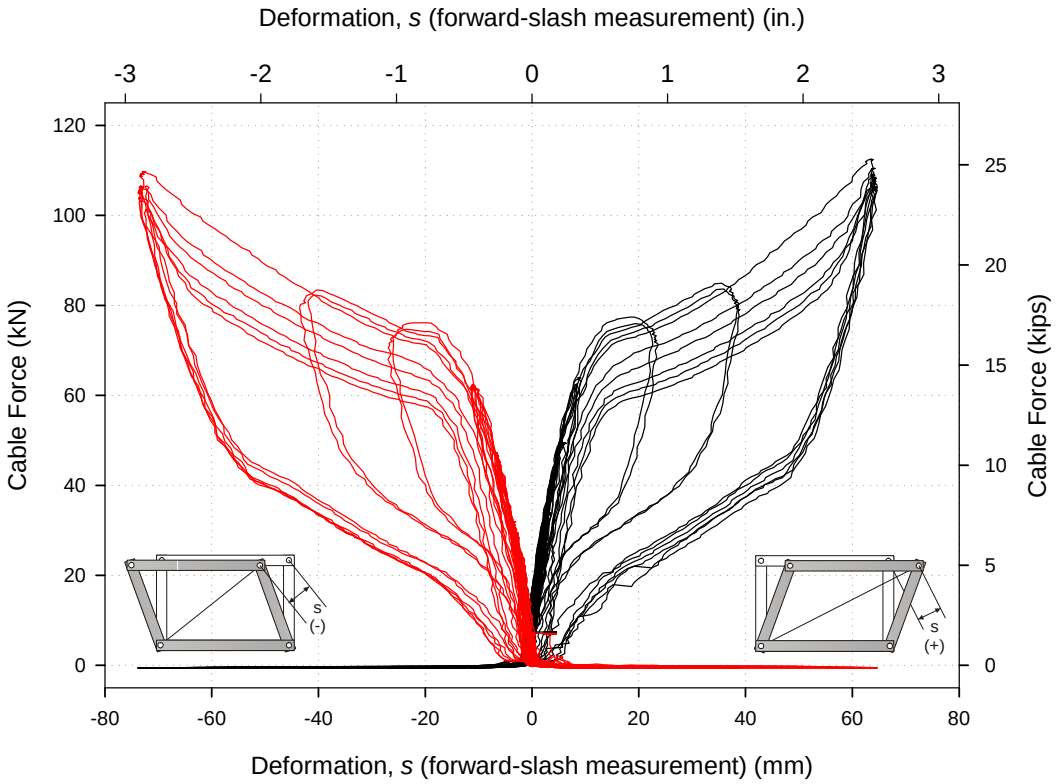

Figure 6-17: Cable force vs. AQ deformation for *Test A*.

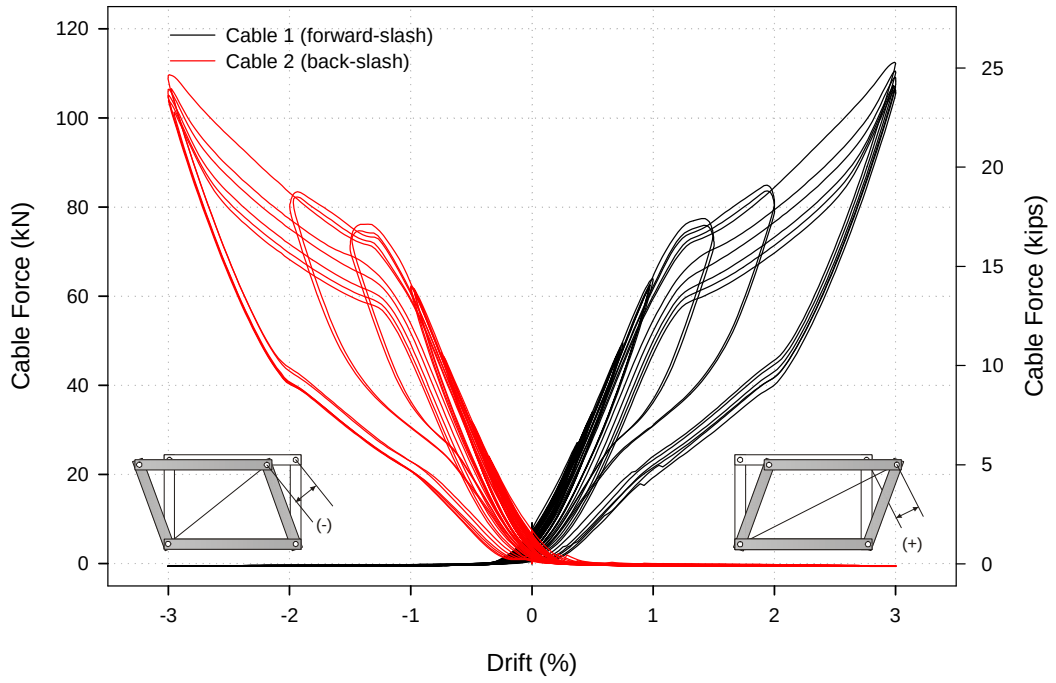

Figure 6-18: Cable force vs. drift for *Test A*.

6.6.2. Test B

In *Test B*, two c-shape dissipators were installed in the AQ. The actuator displacement time history is shown in Figure 6-19. The resulting base shear vs. story drift is shown in Figure 6-20. The brace remained essentially elastic through the 0.5% drift cycles, with only small hysteretic loops forming.

During the 0.75% and 1.0% cycles, the hysteresis grew, indicating the c-shapes were being deformed beyond their elastic limit. Figure 6-22 shows the cable force vs. AQ deformation, respectively. This plot is essentially the force-deformation plot of the c-shape element. Additionally, the cable force vs. drift is plotted in Figure 6-22.

During the 1.5% drift cycles (and beyond), the ties that connected the two c-shapes together began bearing against the AQ links. This resulted in a jump in stiffness upon further loading and eventual yielding of the AQ links. This issue was addressed and corrected in *Test C*. The deformed shape and associated interference is show in Figure 6-23.

At larger drift levels, the brace stiffened when cycled to the left (negative drift). This was the result of the tension/compression asymmetry of the c-shape. This issue is explored more in the discussion of results. Nonetheless, the brace strength and stiffness were stable and c-shape was able to deliver good hysteretic damping. The test was stopped after the first 3% cycle due to significant flexural yielding of one of the AQ links caused by bearing of the c-shape ties.

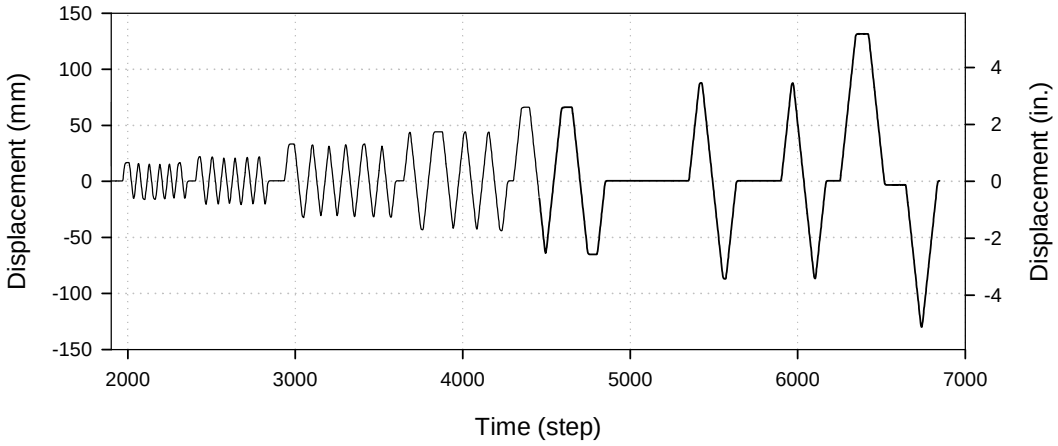

Figure 6-19: Actuator displacement time history for *Test B*.

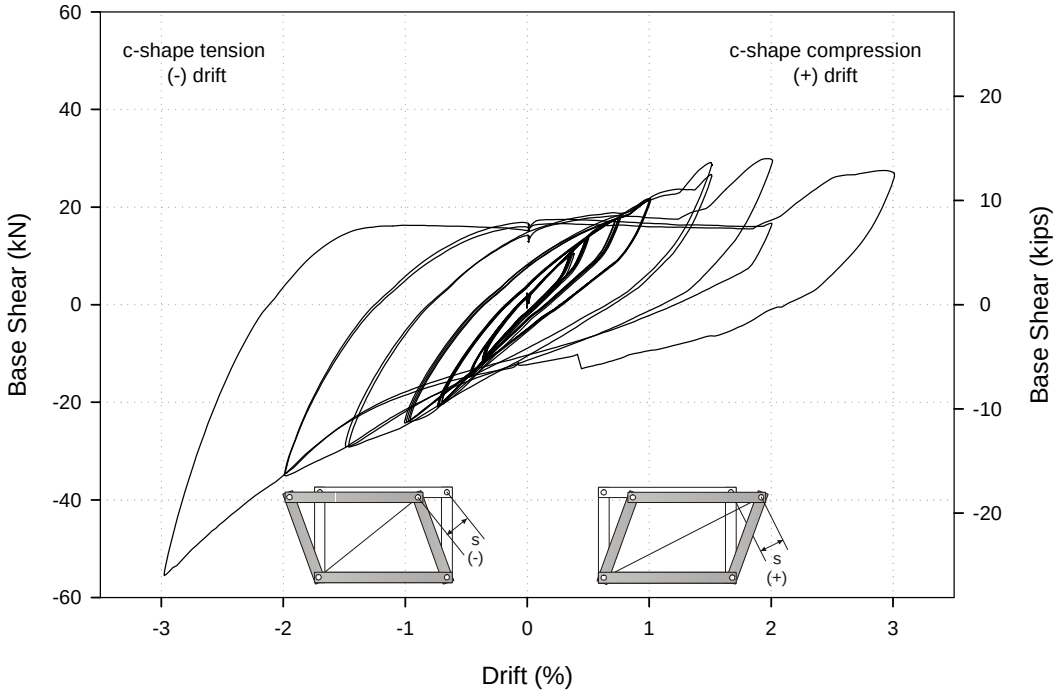

Figure 6-20: Base shear vs. story drift for *Test B*.

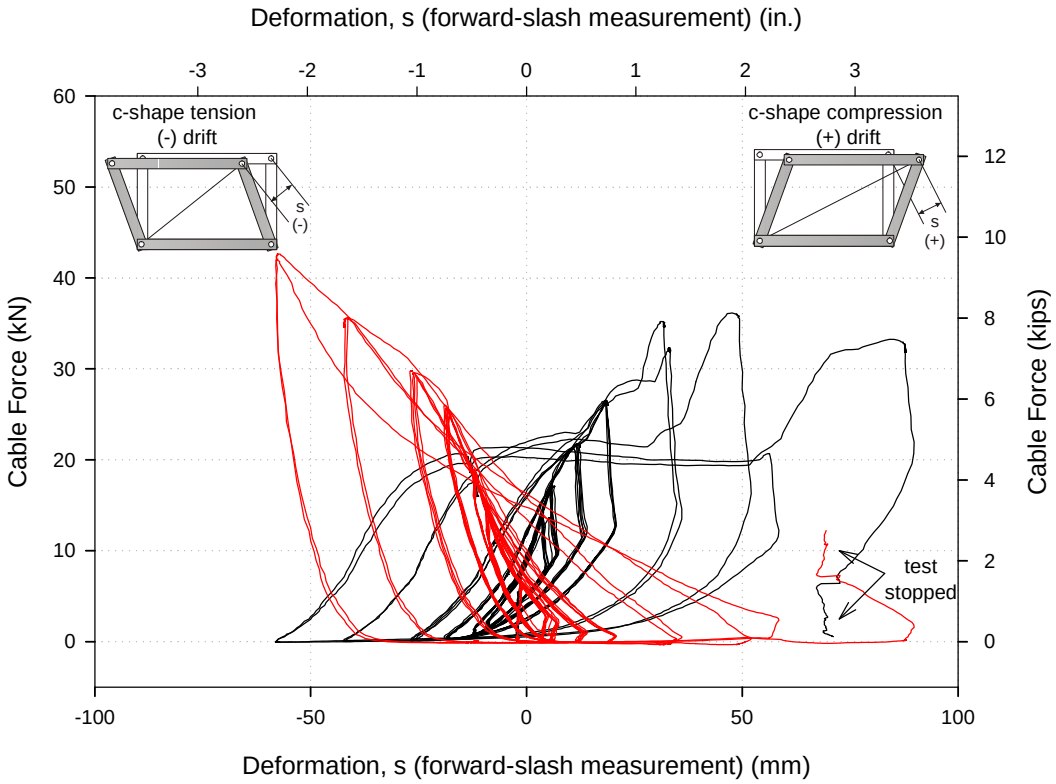

Figure 6-21: Cable force vs. AQ deformation for *Test B*.

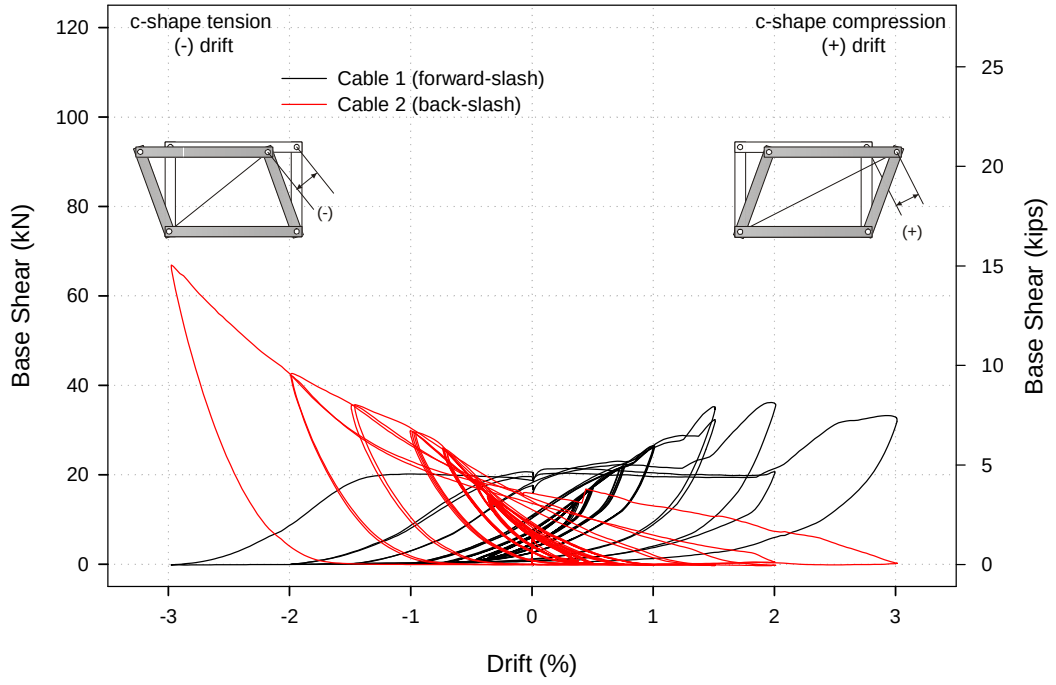

Figure 6-22: Cable force vs. drift for *Test B*.

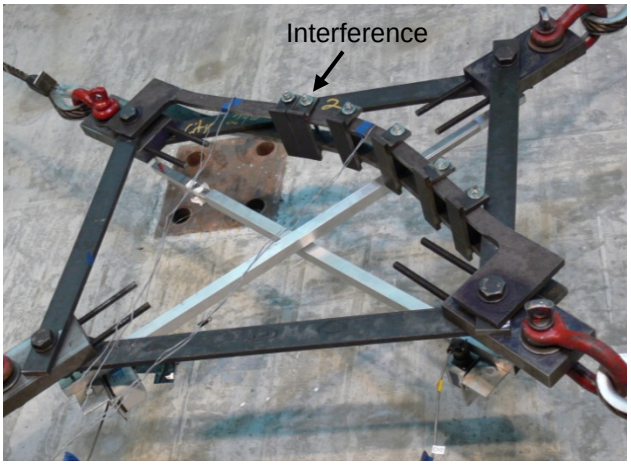

Figure 6-23: C-shape interference at 1.5% drift.

6.6.3. Test C

In *Test C*, two c-shape dissipators were combined in parallel with SMA wire bundles. The resulting base shear vs. story drift is shown in Figure 6-24 and the resulting base shear vs. story drift is shown in Figure 6-25. The brace remained mostly elastic through the 1.5% drift cycles, with good recentering at the end of each cycle.

During the 2.0% cycle, the SMA elements reached their transformation stress, as is evident by the load plateau in Figure 6-25 and Figure 6-26. Figure 6-26 plots the cable force (average from the two load cells on each diagonal) vs. the AQ deformation. This plot is essentially the force-deformation plot of the SMA element paralleled with the c-shape element. Additionally, Figure 6-27 shows the cable force vs. the drift. During the 2.5% drift cycle (added for this test), the SMA was pushed further along its loading plateau. The brace showed little strength and stiffness degradation.

To finish the test, the frame was cycled two times to 3% drift. As expected, the brace began to have some strength degradation and some residual accumulation (and therefore stiffness degradation).

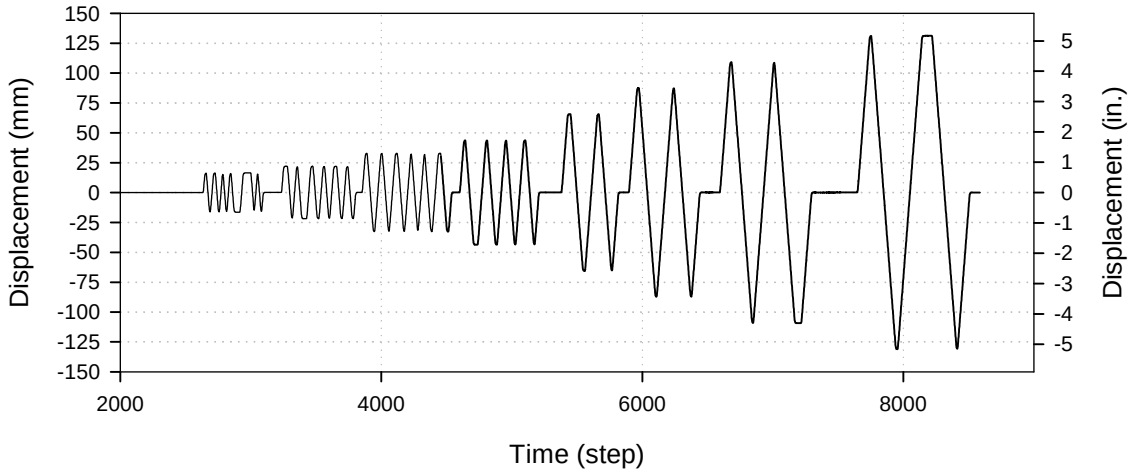

Figure 6-24: Actuator displacement time history for *Test C*.

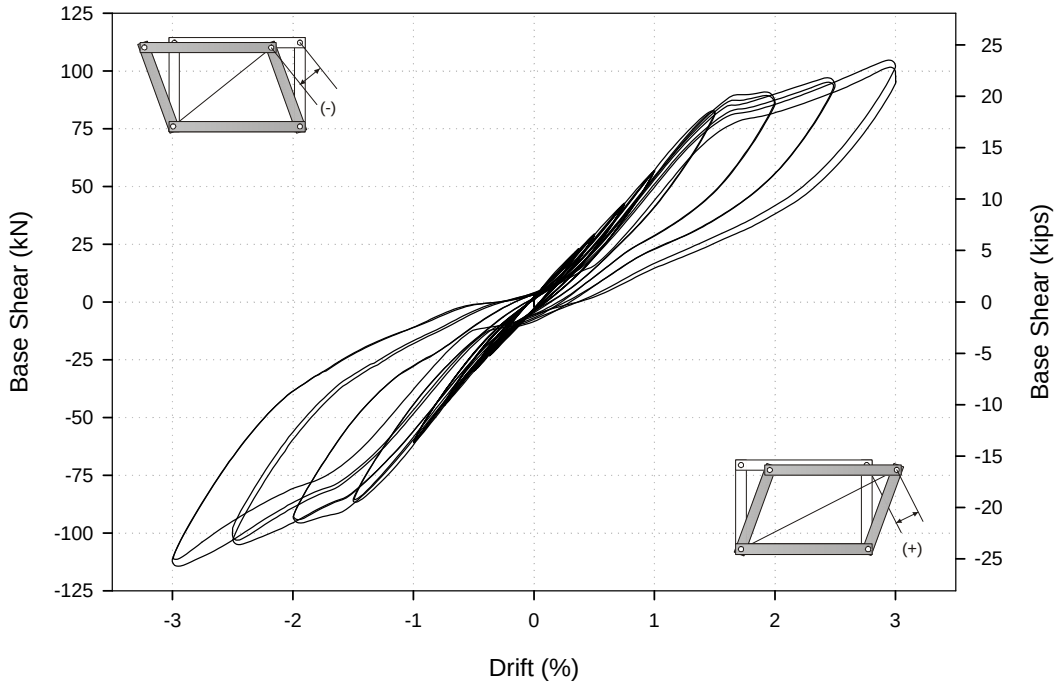

Figure 6-25: Base shear vs. story drift for *Test C*.

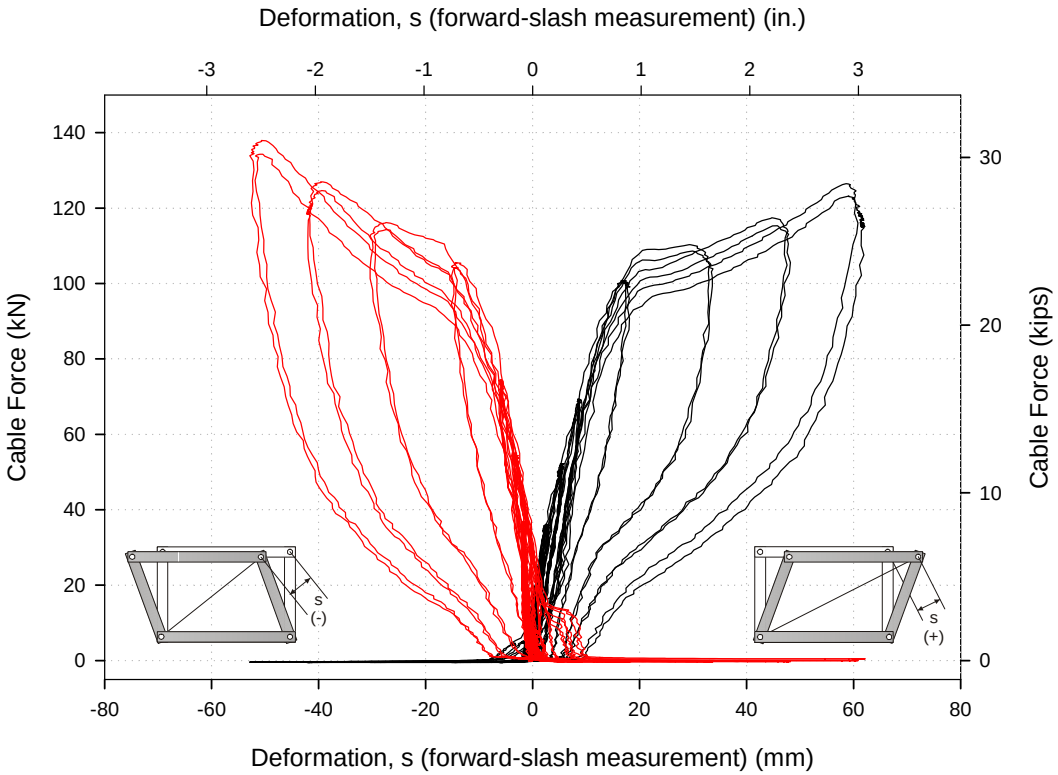

Figure 6-26: Cable force vs. AQ deformation for *Test C*.

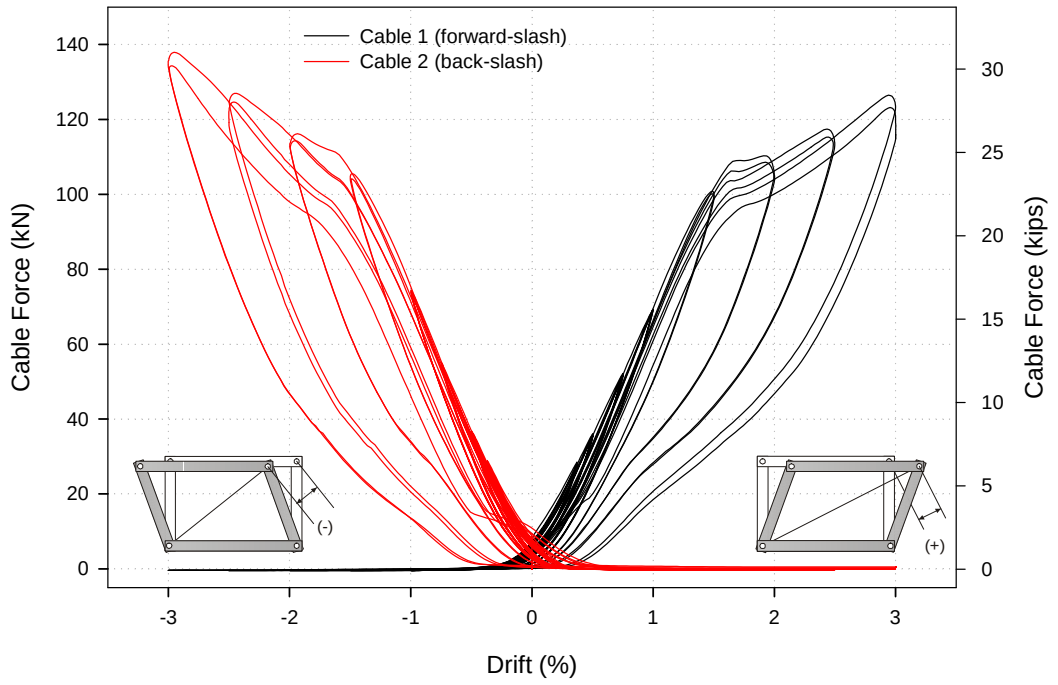

Figure 6-27: Cable force vs. drift for *Test C*.

6.7. Discussion of Results

6.7.1. General Behavior

While the previous section presented the performance of three braced frame tests, this section takes an in-depth look into these results and tries to explain the underlying behavior. The goal is to evaluate the performance of this new bracing system and assess this performance with analytical simulations. Several response parameters are investigated including changes in stiffness, strength, energy dissipation, and recentering.

Before these performance parameters are examined, the effect of the relative stiffnesses of the elements combined to make the bracing system need to be discussed. When SMA and elastic elements are combined in series, a resulting quantitative force deformation relationship will form as shown in Figure 6-28. The length of the loading plateau relative to the yield deformation (plateau ductility factor, η) will decrease as a consequence. To maximize η, the brace elements combined in series with the SMA element should be sufficiently stiff. For a perfectly rigid connecting member, a η greater than 4 can be obtained (dependent on the SMA, approximately 2.5 for this experiment). Figure 6-29, Figure 6-30, and Figure 6-31 show the contributing elements for *Tests A, B, and C*, respectively. Further studies need to be conducted to determine the full implications of this effect (further discussion in APPENDIX H).

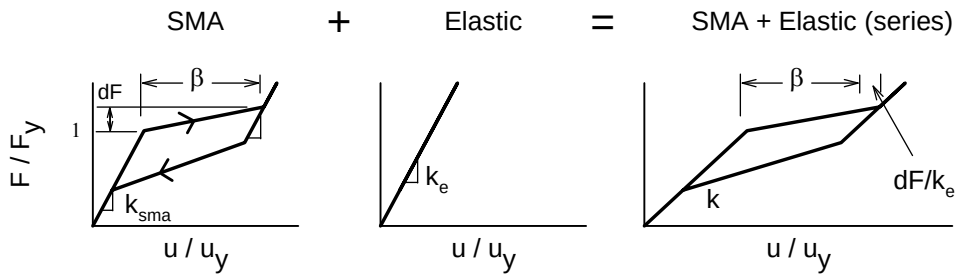

Figure 6-28: The resulting force-deformation characteristics of an SMA element combined in series with an elastic element.

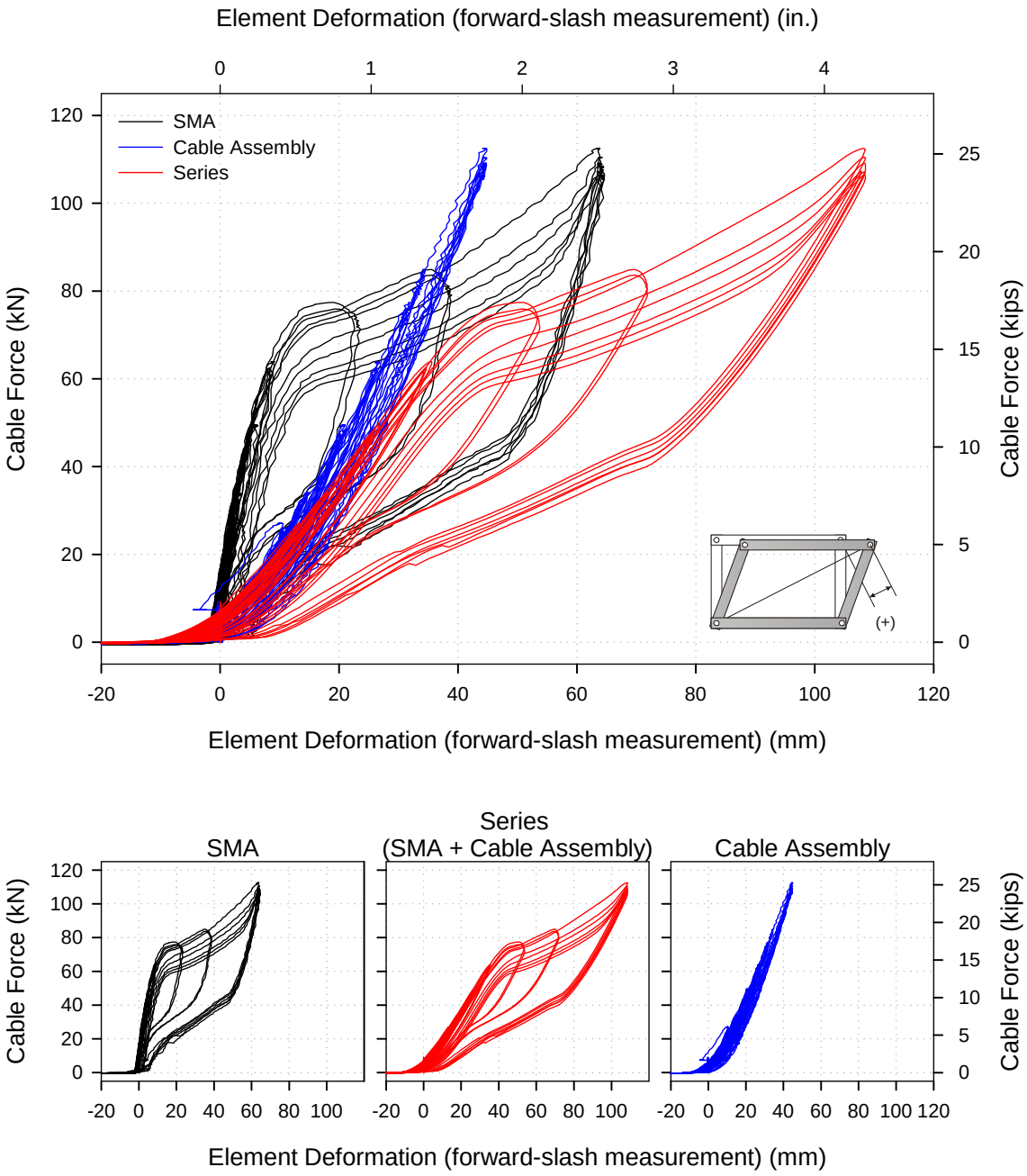

Figure 6-29: Contributions of the different brace elements in series for *Test A*.

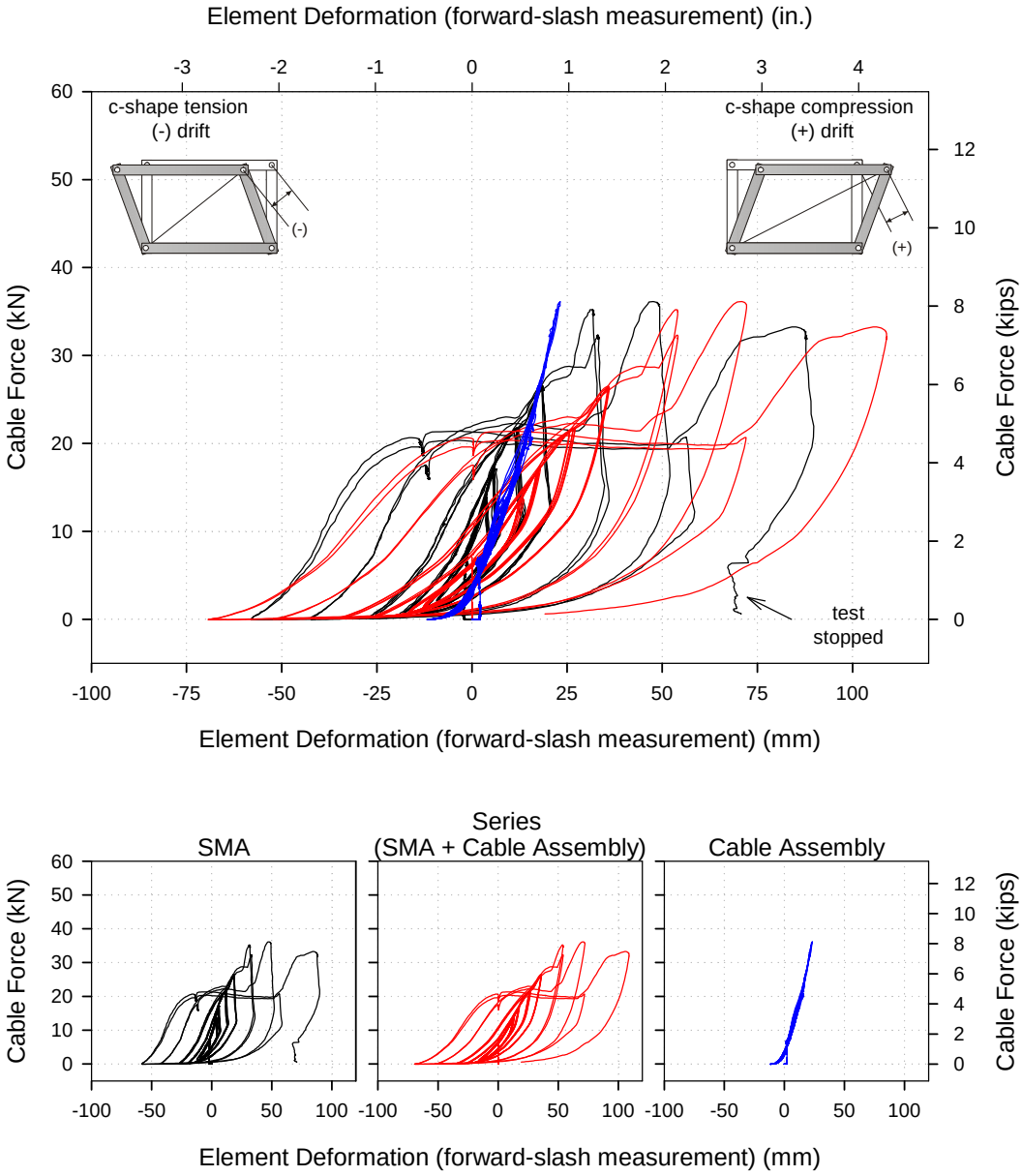

Figure 6-30: Contributions of the different brace elements in series for *Test B*.

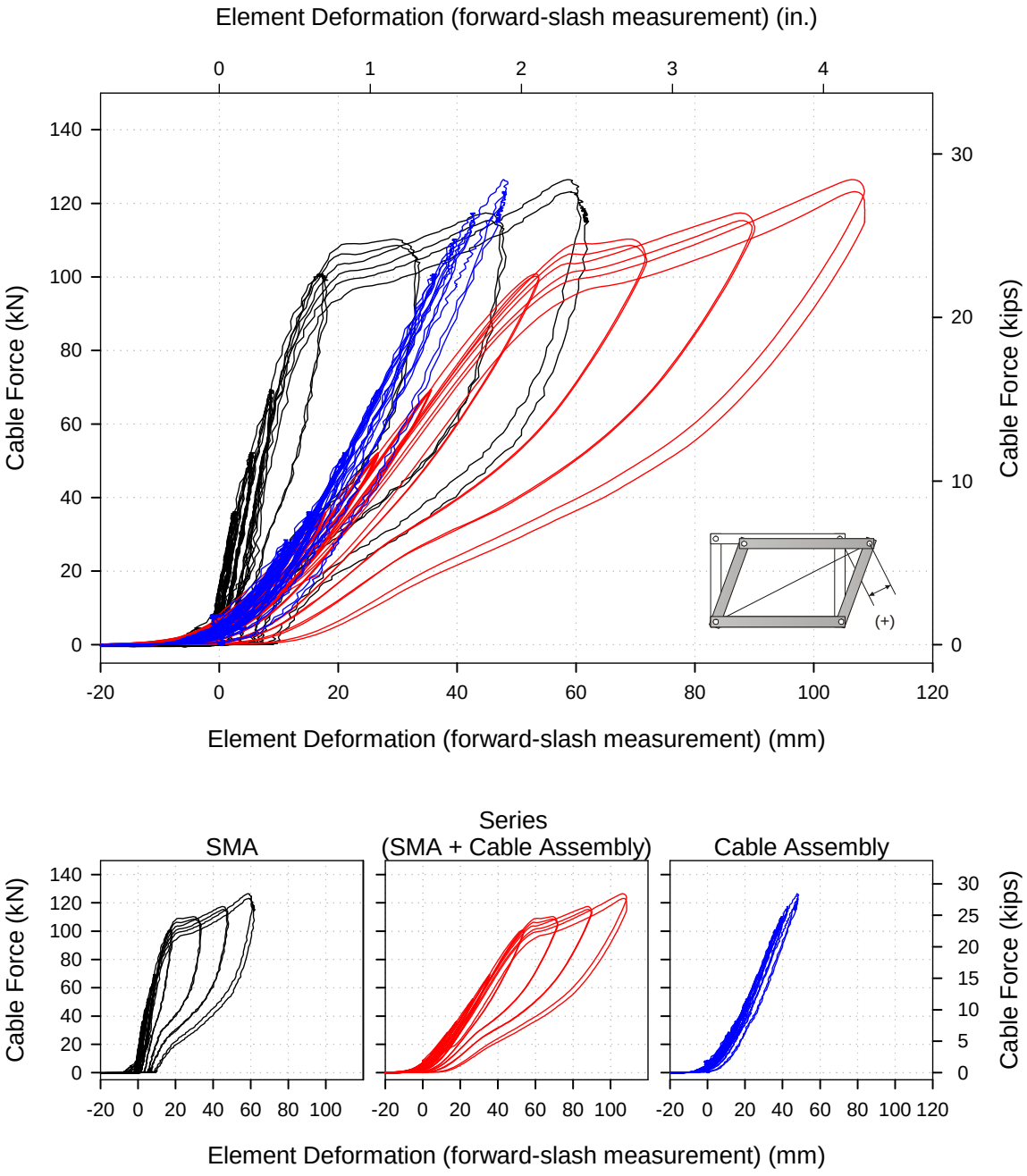

Figure 6-31: Contributions of the different brace elements in series for *Test C*.

6.7.1.1. Response Path

Before the response parameters are examined, it is helpful to look at an individual cycle of base shear vs. drift for *Tests A and C*. Figure 6-32 shows the base shear vs. drift response of the first 3% drift cycle for the SMA test (*Test A*) and the parallel test (*Test C*). The transition points (*a* through *g*) are plotted to help delineate the different phenomena that were occurring as the braces were cycled.

For both tests, the brace was prone to have some loss in stiffness at small drift levels due to accumulating residual strains in the SMA wires (plus the compression resistance of the c-shape for *Test C)*. This portion is denoted by *a* to *a'*. For *Test A* these two points were generally closer (and sometimes undistinguishable) than in *Test C*, because of the added c-shape resistance.

Moving along the response path, the brace remained linearly elastic from point *a'* to *b*. At point *b*, the SMA wires began transitioning into its plateau range (and the c-shape began to yield for *Test C*). From points *c* to *d* the SMA (and the c-shape) traversed across their loading plateaus and exhibited some slight stiffening as the response approached point *d*. At this point, the SMA wires had transformed almost entirely into martensite.

For the unloading portion, the SMA wires began transforming from martensite back into austinite at point *e*. The unloading plateau was fully reached at point *f*, in which the SMA began recentering the frame. For *Test C*, point *f'* was approximated as the point in which the c-shape was fully yielding in tension. Points *g'* and *g* were the final two points on the path. These two points, similar to *a* and *a'*, represent the level of recentering the system experienced. When *g* and *g'* occupy the same coordinates, full recentering is achieved. *Test A* generally had much better recentering, as was expected.

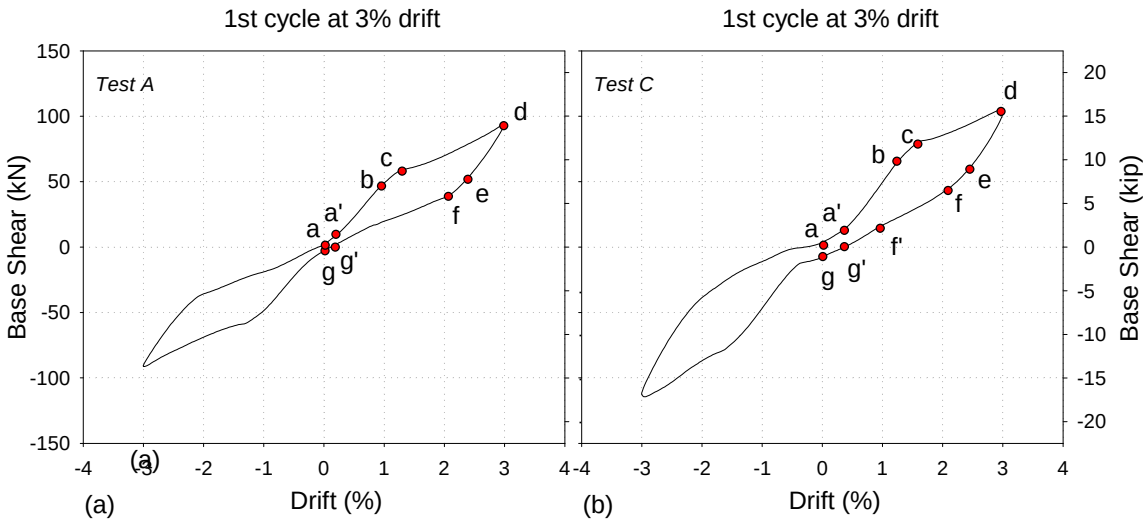

Figure 6-32: General response path of braced frame (a) *Test A* and (b) *Test C*.

6.7.1.2. C-shape Behavior: Kinematic Effects

Before moving on to the remainder of the discussion, it is helpful to look at the kinematics of the c-shape elements at large deformations. In Figure 6-33, the response of the c-shape test (*Test B*) is plotted on the top and the corresponding kinematic relationship between the hole-separation, *s*, and arm rotation angle, ϕ, is plotted at the bottom. Notes were made in Figure 6-33a to highlight the response of the c-shape in tension. Assuming the hole-separation, *s*, comes entirely from bending of the c-shape body (and the arms are rigid), the relationship between *s* and the arm rotation, ϕ, can be found as plotted in Figure 6-33b. For the holes to have further separation, the c-shape must have any combination of the following: axial elongation of its body, bearing elongation of its holes, or bending of its arms. This kinematic hardening played a significant role in the behavior of the c-shape in tension. To try to reduce this effect, the c-shapes in *Test C* were given slotted holes, providing a "fuse" for the deformations. Further discussion on this topic can be found in APPENDIX G.

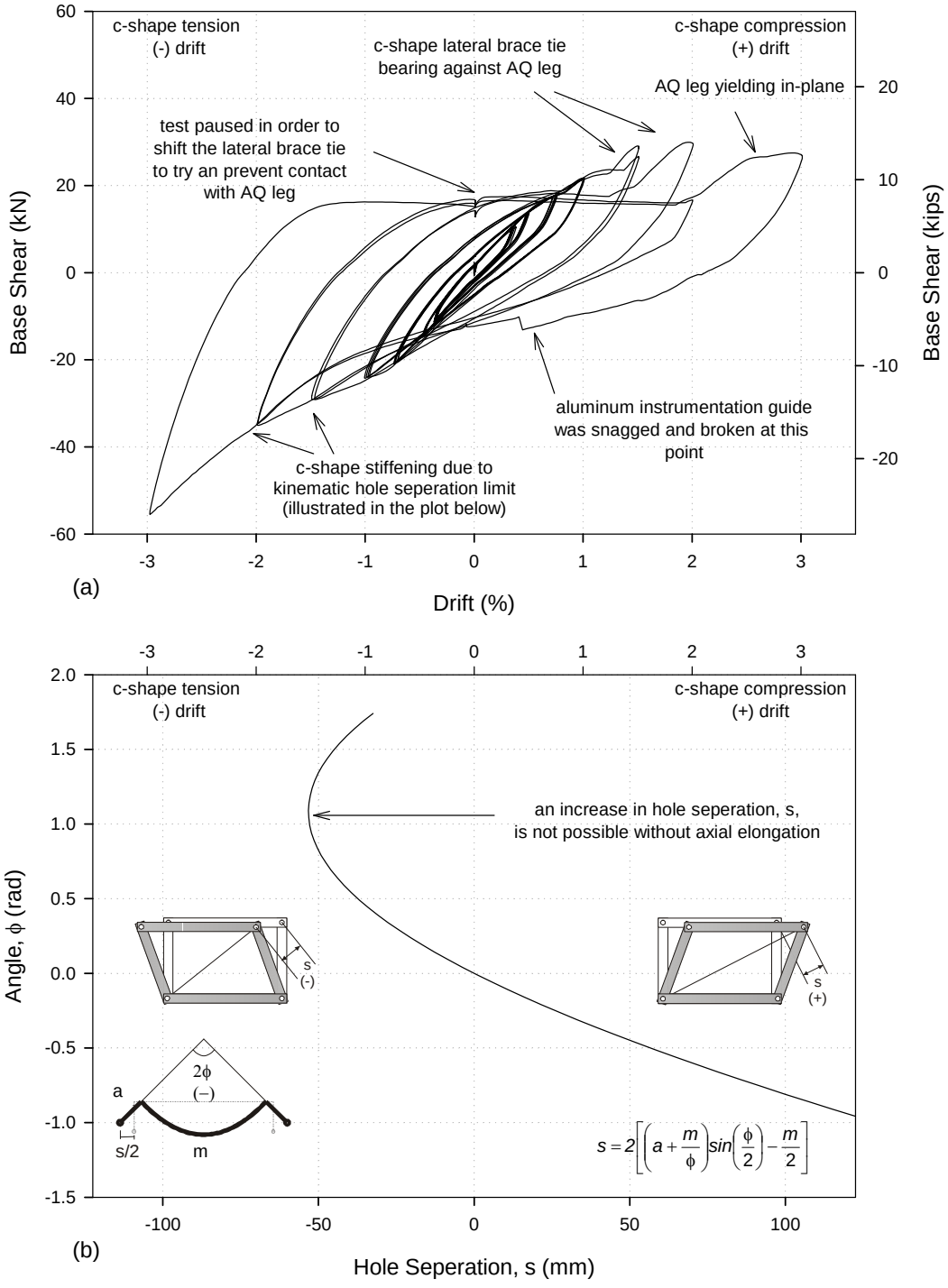

Figure 6-33: Discussion of c-shape disspator response for *Test B*.

6.7.2. *Effective Stiffness and Yield Moment*

The cyclic curves for the first cycle at 1.5% and 3.0% drift for *Test A* are shown in Figure 6-34 . Straight lines were overlaid in order to approximate the effective stiffness, K_e, and "yielding" base shear, V_{by}, of the braced frame (where "yielding" for the SMA is really a phase transformation) . The line for determining the stiffness was drawn asymptotically to the forward and reverse loading curves and runs approximately through the origin. In order to determine the "yielding" plateau, another line was drawn. The SMA did not hit its transformation stress for drift levels less than 1.0% in *Test A* and 1.5% in *Test C*.

The resulting trends for stiffness and strength are plotted in Figure 6-35 and Figure 6-36, respectively. The stiffness generally decreased with increasing drift level, though the decrease was only 15-20% at 3% drift. The strength also had a moderate decrease for both tests. *Test C* decreased at a faster rate due to more residual accumulation, which will be discussed in the next section. As expected, *Test C* had larger stiffness and strength than that of *Test A* due to the addition of the c-shape dissipators.

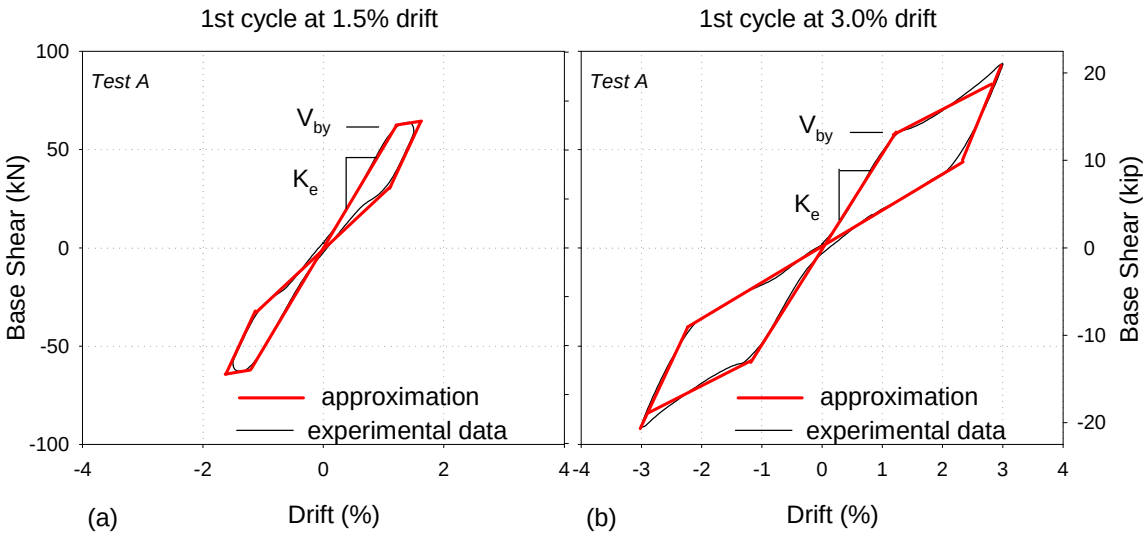

Figure 6-34: Straight line approximations of the base shear vs. drift response to obtain M_y and K_e.

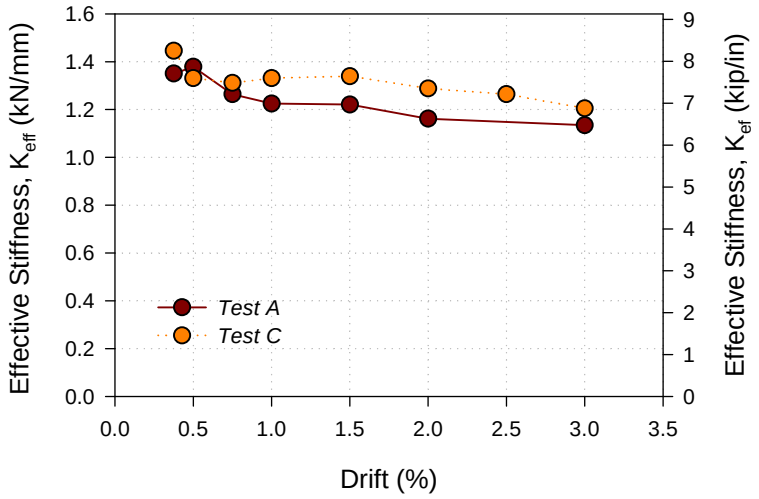

Figure 6-35: Effective stiffness, K_e, over a range of drift levels for *Tests A* and *C.*

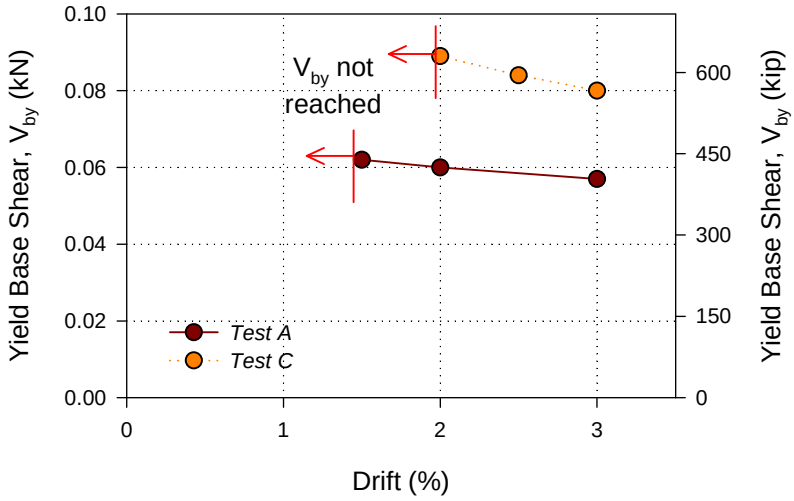

Figure 6-36: Yield base shear, V_{by}, over a range of drift levels for *Tests A* and *C.*

6.7.3. Residual Drift

The change in stiffness of the braced frame was mainly due to the accumulation of residual strains in the SMA wires. For these tests, the residual drift was set to the point in which the response path crossed the zero base shear line. The residual drifts, Δ_{res}, were manually picked from the response curves and the trend is shown in Figure 6-37.

Test A performed the best, having only 0.12% residual drift after being subjected to 3.0% drift. *Test C* had approximately four times the residual drift than *Test A*, which was mainly due to the c-shape dissipator preventing recentering. To achieve better recentering in the parallel system (*Test C*), the SMAs should be given increased pretension.

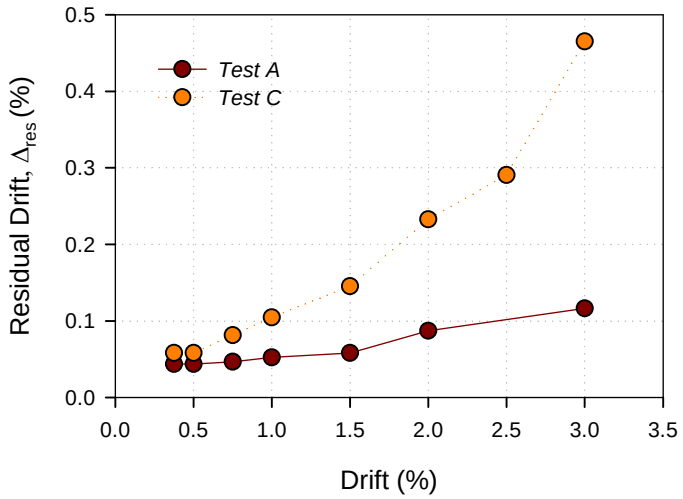

Figure 6-37: Residual drift, Δ_{res}, over a range of drift levels in *Tests A* and *B.*

6.7.4. Energy Dissipation

The energy dissipation of the brace is assessed by calculating the equivalent viscous damping, ζ, for the first and second cycles of *Tests A* and *C*. The trend in ζ is shown in Figure 6-38. The ζ varied from 3-9%, with the first cycle's ζ generally greater than that of the second cycle. At 0.375% and 0.5% drift, the ζ was greatly influenced by the friction in the system. This had less of effect at the 1.0% drift level, therefore the ζ dropped. However, at 1.5% drift and greater, the ζ rapidly increased. For 1.5-3% drift, the ζ was approximately 6-8% for *Test A* due to the hysteresis that formed in the SMA wires. For *Test C*, the ζ did not increase as quickly because a higher drift level was

needed to cause the SMAs to transform. This was due to the increased stiffness in the AQ elements which resulted in the cable assemblies taking up more of the deformations. For 2-3% drift, the ζ was approximately 7-9% for *Test C*.

Though recentering is the main focus of this bracing system, the added damping has been shown to have a positive impact on a recentering system's dynamic performance (see CHAPTER 3). The purpose of adding the c-shape damping in parallel with the SMA wire bundle was to enhance the brace's damping while maintaining good recentering. The ζ plots are slightly deceiving, in this regard, because the two systems that are compared had different "yield" drifts and "yield" strengths. This effectively shifted the response of the *Test C*'s ζ to the right by approximately 0.5% drift. With this in mind, the damping of *Test C* was enhanced by the addition of the c-shape, as would be expected. Nonetheless, the balance between recentering and energy dissipation needs further development to ensure optimized system behavior.

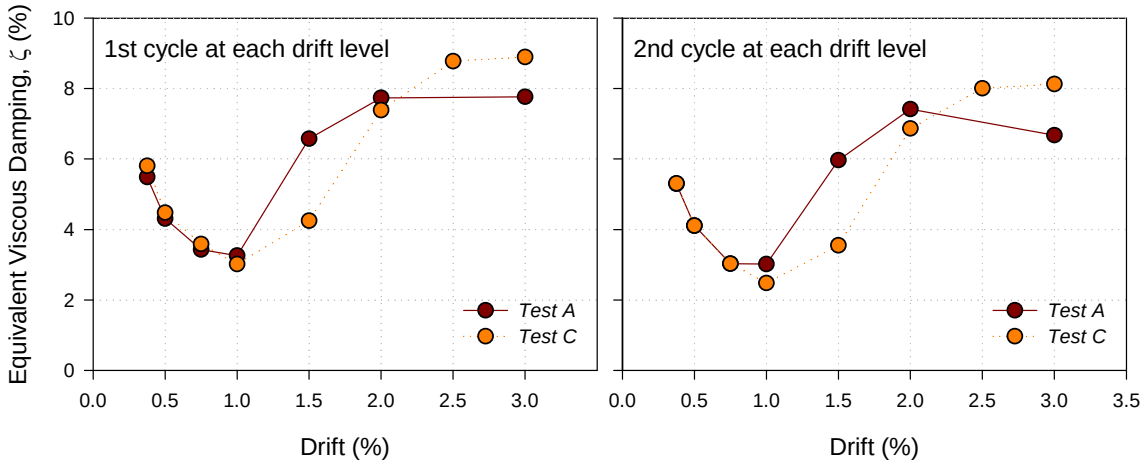

Figure 6-38: Equivalent viscous damping in the first and second cycle for *Tests A* and *C*.

6.8. Analytical Study

6.8.1. Description and Setup

In order to assess the effectiveness of the SMA-based bracing system, the response of a seven-story building outlined in the 2005 NEHRP Design Examples (FEMA 451, section 5.2, alternative B) is investigated (FEMA, 2006). The seven-story building was modeled in OpenSEES. Four different brace behaviors were investigated to assess the SMA-based system's performance. Some liberty was taken in giving the braced members several different types of force-deformation responses without further refinement of the design parameters (i.e. R, C_d, and Ω_0 factors).

6.8.1.1. Brace Models

First, the brace members were modeled as traditional moderately stocky braces (special concentrically brace frame (SCBF) as designed in the Design Examples) which are allowed to buckle in compression. This brace model is referred to as the *Brace A* model. To capture the buckling response, an initial out-of-straightness is given at the midpoint of the brace and rotational springs are applied at the end of the brace. Each brace was calibrated to buckle in compression at the nominal capacity, P_n, and have a postbuckling strength of $0.3P_n$ at 20 times the buckling deformation. This procedure was adopted from the recommendations made by Yang et al. (2008) in their study of chevron zipper frames. The qualitative response of the SCBF, *Brace A*, is shown in Figure 6-39a.

Next, the traditional braces were replaced with an SMA-based bracing system (*Brace B*) with the same strength and stiffness. The SMA brace behavior was modeled after the response of *Test A* in the experimental results of this chapter (SMA-only brace). However, in order to maximize the plateau ductility parameter, the steel cables were assumed very stiff relative to the SMA (see the discussion in APPENDIX H for further information). The constitutive model used for the SMA material was a modified one-

dimensional model implemented into OpenSEES by Fugazza (2003) and first proposed by Auricchio and Sacco (1997). The resulting qualitative brace response for the SMA, *Brace B*, is shown in Figure 6-39b. Additionally, the braces were modeled as tension/compression elements with half the strength and stiffness of each brace in the experimental system. This effectively gave the same story stiffness (since the experimental system was tension-only) and created an easy way to model the parallel brace investigated next

Third, the braces were assigned the force-deformation characteristics seen in the parallel (PARA) bracing system (c-shape plus SMA) of experimental *Test C*. Again, the brace model (*Brace C*) assumed that the cable assemblies were rigid, thus concentrating all the brace deformation into the SMA and c-shaped elements. The parallel SMA and c-shaped elements were modeled using the *Parallel* material command in OpenSEES. The parallel element was made up of 80% SMA and 20% elastoplastic behavior, set as reasonable values from the experimental results. This resulted in the qualitative response for *Brace C* as shown in Figure 6-39c.

Finally, the braces were assigned an idealized buckling restrained brace (BRB) force-deformation relationship (*Brace D*). The BRBs were modeled with the *Steel01* material in OpenSEES, which does not consider stiffness and strength degradation. Isotropic hardening was set to zero and the strain hardening was set to 0.02. The resulting qualitative response for *Brace D* is shown in Figure 6-39d.

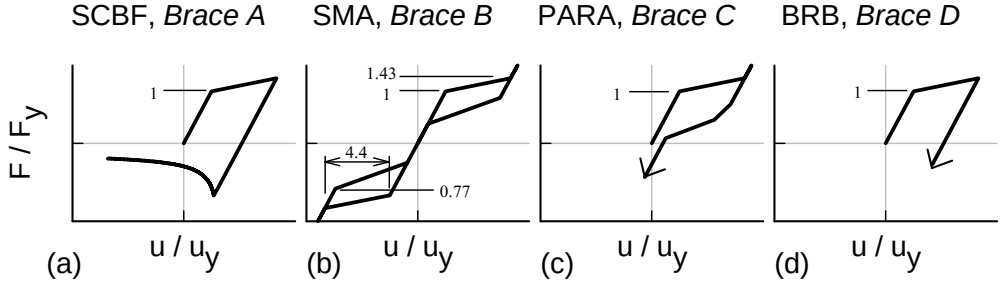

Figure 6-39: Brace models used in analysis.

6.8.1.2. Building Model

The plan view of the seven-story building is shown in Figure 6-40. The frame was designed as a special concentrically braced frame (SCBF) to be built in the Los Angeles, California area (Seismic Design Category D, Seismic Use Group I, R = 6, Ω_0 = 3, C_d = 5). Complete details of the building can be found in the FEMA 451 publication (FEMA, 2006).

To simplify the analysis, only one direction of loading was considered (N-S) and only one braced-frame section was modeled. Since the building was designed with four braces in the N-S direction, one-fourth of the mass was assigned to this frame and was lumped at each floor height (half at each intersecting beam-column node). The lateral resistance of the non-braced frames was ignored and torsion was not considered. The columns were fixed at the base and the beam-column connections were modeled as pinned, thus ignoring the stiffness that would result from the gusset plate at the end of the brace.

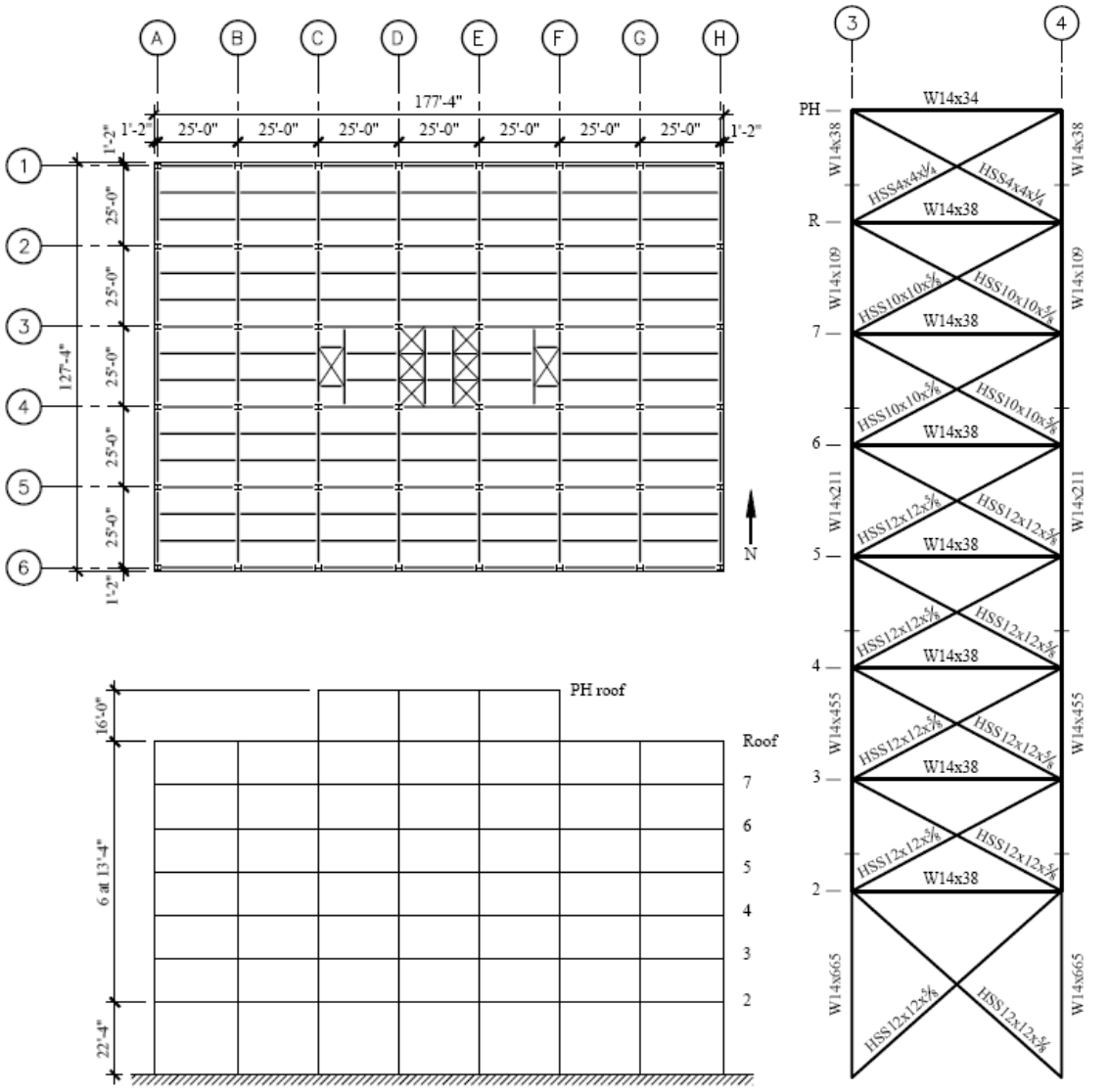

Figure 6-40: Details of the seven-story braced frame analyzed (FEMA, 2006).

6.8.1.3. Ground Motions

The braced-frame was subjected a suite of ground motion, LA21-40, with a 2% probability of exceedance in 50 years (Somerville et al., 1997). The ground motions were taken as-is from Somerville's study (i.e. no additional scaling).

6.8.2. Results and Discussion

6.8.2.1. Behavior Due to Individual Ground Motions

To highlight some of the issues that were encountered during the analysis, the behavior of the braced frames subjected to two different earthquakes is first explored. The two ground motions investigated are LA30 (1974 Tabas earthquake with a magnitude of 7.4 and PGA of 972.58 cm/sec^2 (382.9 in/sec^2)) and LA25 (1994 Northridge earthquake with a magnitude of 6.7 and a PGA of 851.62 cm/sec^2 (335.3 in/sec^2)). To get a sense of the frequency content, the response spectrum for these two earthquakes is shown in Figure 6-41. For the analyses, the fundamental period was approximately 0.85 sec and the second mode's period was approximately 0.29 sec.

For LA30, the base shear vs. first floor drift is shown in Figure 6-42a-d for the four different braced frames. Additionally, the first floor drift time histories are shown in Figure 6-42e. The maximum first story drifts for *Braces A-D* were 1.50, 1.35, 1.30, and 1.05%, respectively. The residual first story drifts for *Braces A* and *D* were 0.05 and 0.45%, respectively. *Braces B* and *C* had no residual drifts. Both systems with SMA (*Braces B* and *C*) had an approximately 10-15% reduction in maximum drift compared to the SCBF (*Brace A*), but approximately equal maximum drift compared to the BRB (*Brace D*).

For LA25, different relative performance was observed amongst the systems. The four system's base shear vs. first floor drift are shown in Figure 6-43a-d and first floor drift time histories are shown in Figure 6-43e. The maximum first story drifts for *Braces A-D* were 3.2, 1.6, 1.6, and 2.3%, respectively. The residual first story drifts for *Braces A* and *D* were 1.3 and 0.7%, respectively. Again, *Braces B* and *C* had no residual drifts. Both systems with SMA had approximately 50% reduction in drift compared to the SCBF and a 30 % reduction compared to the BRB. Furthermore, the

SCBF and the BRB both suffered from large levels of residual drift, as opposed to the SMA-based systems which displayed their recentering capabilities. The high drift demand can be related to the reduction in effective stiffness caused by the extensive yielding in the SCBF and the BRB. This effectively shifted the fundamental period of the structure and, as can be seen the LA25 response spectrum (see Figure 6-41), resulted in higher deformation demand.

It should be noted that the results from the LA25 ground must be reviewed with caution. The force levels in both SMA systems reached high up into the post-plateau stiffness region. From mechanical tests, it is clear that SMAs begin to lose superelasticity in this region. Additionally, the high forces in these elements could be problematic due to overloading of other elements that are intended to stay elastic. Clearly further analysis should be carried out to determine appropriate design procedures to limit these issues.

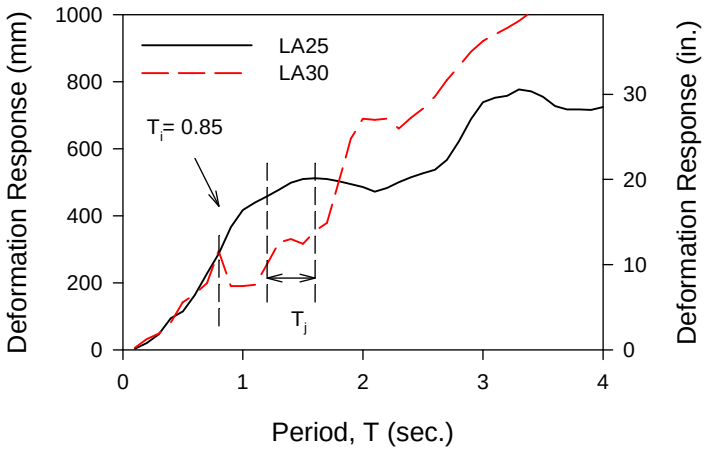

Figure 6-41: Deformation response spectrum for LA25 and LA30 with the SCBF and BRB period shift noted.

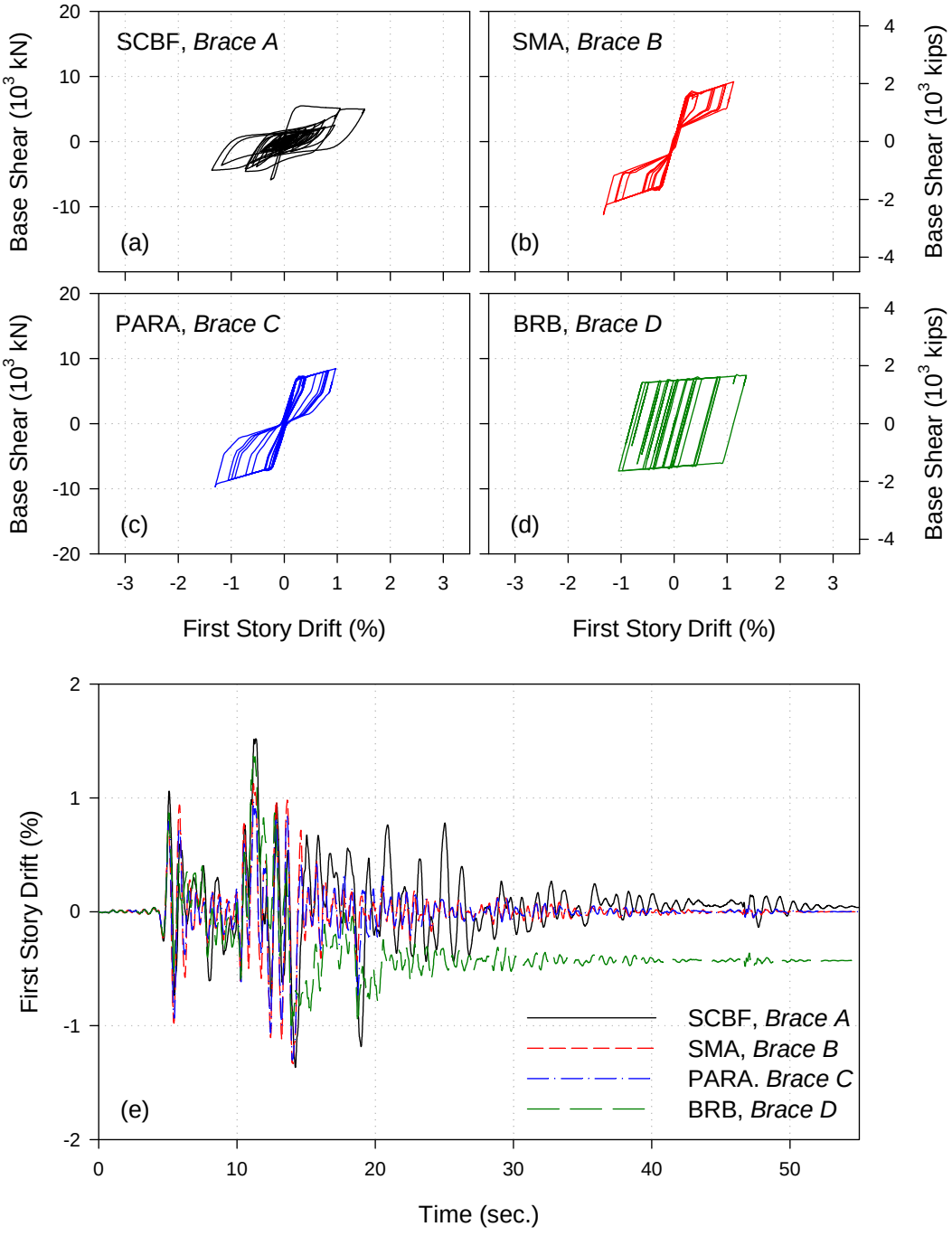

Figure 6-42: (a-d) Base Shear vs. first story drift and (e) first story drift time history for SCBF,SMA, PARA, and BRB subjected to the LA30 ground motion.

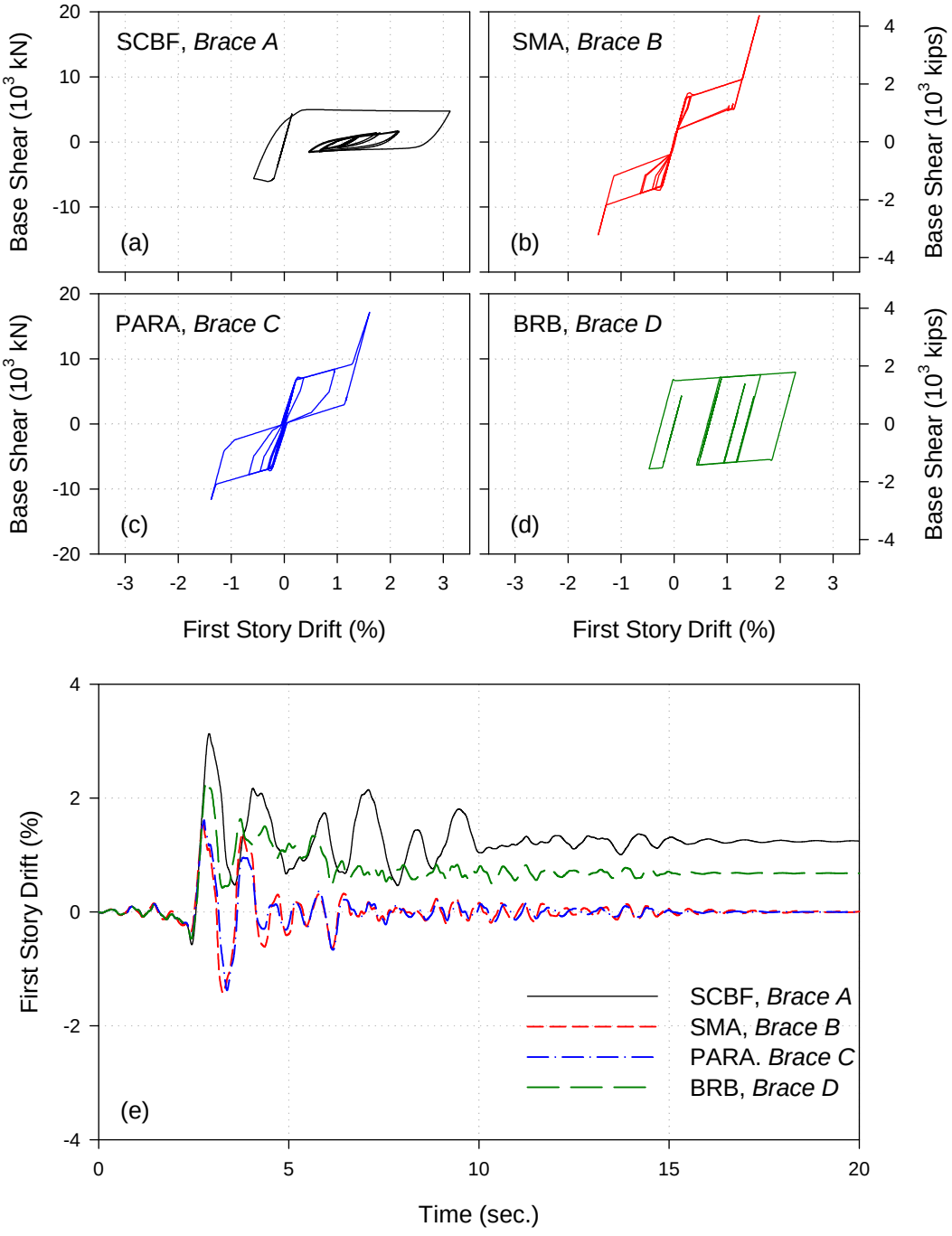

Figure 6-43: (a-d) Base Shear vs. first story drift and (e) first story drift time history for SCBF, SMA, PARA, , and BRB subjected to the LA25 ground motion.

6.8.2.2. Behavior Due to Suite of Ground Motions

Now the response is investigated over the entire suite of ground motions. Though several performance parameters exist, the performance of this braced frame was assessed by looking at the maximum displacements, interstory drifts, and residual drifts.

For the suite of earthquakes with a 2% probability of exceedance in 50 years, the results for SCBF (*Brace A*), SMA (*Brace B*), PARA (*Brace C*), and BRB (*Brace D*) are shown in Figure 6-44a-d, respectively. From these plots, the following observations can be made:

- The SCBF had large drifts forming in the first, second, and third stories. Drifts exceeded 3% in the second story for several ground motions, which would very likely result in collapse. However, collapse is not accounted for in the model.
- The SMA and PARA frames were both effective in decreasing the drifts demands in the first three stories. However, as mentioned in the analysis of the individual ground motions, care must be exercised in designing an SMA-based system to ensure the load plateau is not being greatly exceeded, otherwise forces being transferred to adjacent members could violate the capacity design method being used here.
- The SMA and PARA frames had smaller maximum interstory drifts compared to the SCBF and the BRB. This was due to the SMA and PARA frames' ability to distribute the drift demand move uniformly along the height of the structure and thus reducing undesirable soft-story behavior.
- In comparing the SMA and the PARA frames, the PARA system had a slight performance advantage in terms of maximum drifts. However, the results are not conclusive. Further investigation needs to be conducted to more fully understand the impact of a PARA system on the response of a complete structural system.

- The residual drifts were highest in the SCBF, where the bottom three stories had an average residual drift of 0.6%. The BRB frame was also prone to acquiring residual drift, though on average the residual drift was half that seen in the SCBF.

From these observations, SMA-based braces were effective in decreasing interstory drift for the suite of large earthquakes. The SMA braces did a good job of distributing the drift demands over the height of the building and thus reducing soft stories. They also have a clear advantage due to recentering.

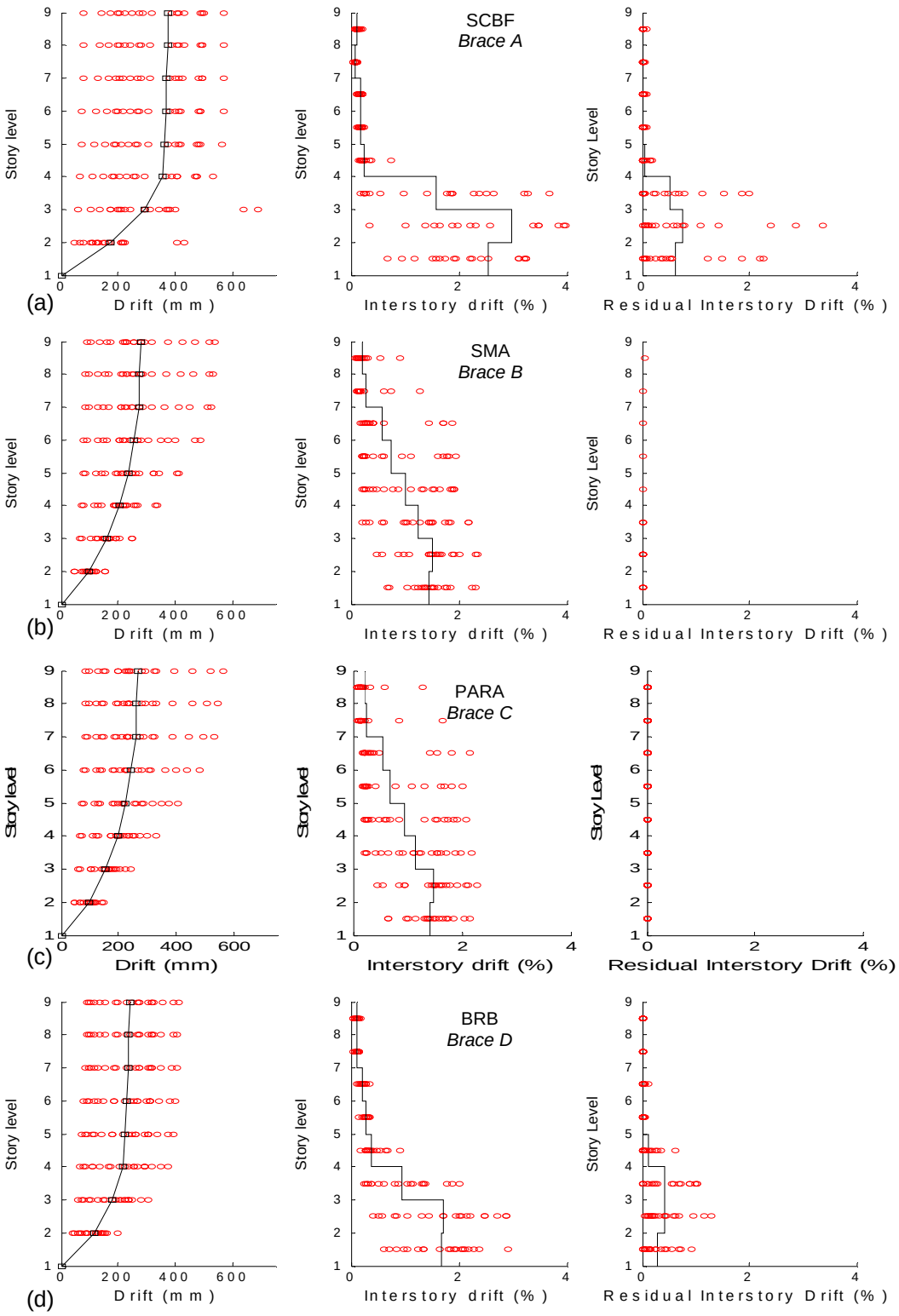

Figure 6-44: Drift, interstory dift, and residual drift for the first story of the (a) SCBF, (b) SMA, (c) PARA, and (d) BRB. Braces *A-D* (mean = black line, data point = red circles).

6.9. Summary

In this chapter, an articulated quadrilateral bracing system was proposed as a unique way to implement SMAs. The behavior of the AQ created a platform for SMAs to be combined in parallel with energy dissipating elements. If properly calibrated, it was envisioned that this bracing system would have good recentering with optimized energy dissipation. The following main conclusions are made from this experimental investigation:

- SMA wire bundles were able to recover large levels of strain (from 9-12% in this study).
- The relative stiffness of the elements combined to make the bracing assembly have an effect on the length of the loading plateau relative to the yield deformation (plateau ductility parameter). To maximize this parameter, the brace elements combined in series with the SMA element should be sufficiently stiff. In this experimental test, the brace had a ductility factor of approximately 2.5.
- C-shape dissipators are unique damping elements that display stable hysteretic behavior and can be fabricated to a variety of strength, stiffness, and deformation capacities.
- The SMA-only bracing system was the best choice when residual drifts needed to be minimized. The SMA-only system had drifts less than 0.12% after being pushed to 3% drift.
- The bracing system that incorporated both SMA and c-shape dissipators (PARA) had a larger level of damping. Recentering was sacrificed to obtain this additional damping. After being cycled to 3% drift, the frame had 0.47% residual drift.

- Both SMA-only and the PARA systems had little loss in strength and stiffness after repeated cycling, demonstrating that such a system is well suited for earthquake loading.
- In the analytical study, the SMA and PARA frames had the best performance in terms of interstory and residual drifts. These systems both tended to distribute the drifts move evenly over the height of the structure, thus reducing the likelihood of the formation of a soft-story.

This study was exploratory in nature, focusing on the effects of recentering vs. energy dissipation. It is recommended that further work be done to develop such a device and more fully determine the performance advantages. Some areas of potential future work are as follows:

- Create an AQ that allows for higher levels of SMA-pretension. This will increase the recentering ability of the system.
- Investigate different methods to supplement the SMA damping. One option that could have good potential is a friction mechanism used by Pall Dynamics.
- Further investigate the benefits of increased damping in a SMA-based system (i.e. PARA system).
- Develop system behavior factors.

CHAPTER 7

SUMMARY, CONCLUSIONS, AND RECOMMENDED FUTURE RESEARCH

7.1. Summary and Conclusions

Shape memory alloys have the unique ability to spontaneously recover up to 8% strain upon the removal of load. NiTi SMAs, known for their superb superelasticity and corrosion resistance, have only been used in a handful of applications in the civil engineering industry since their discovery over four decades ago. The potential to provide both recentering and supplemental damping is the hallmark of SMA's behavior for applications in civil engineering. In this research, it was hypothesized that enhanced structural performance can be obtained by appropriately balancing recentering and damping, thus limiting maximum displacements while maintaining reduced residual displacements. To demonstrate this fundamental idea, a single-degree-of-freedom (SDOF) study was first investigated. The SDOF study showed that a recentering system performs best when the flag-shaped hysteresis is maximized (i.e. the energy dissipation is maximized while the recentering is retained).

With this observation in mind, three different SMA-based systems were developed and tested: a tension/compression device, an interior beam-column connection, and an articulated quadrilateral (AQ) bracing system. Each system was subjected to a cyclic loading protocol to simulate deformation demands expected during an earthquake. Because these investigations were exploratory in nature, each system needs further development and refinement in order to be implemented into practice.

Nonetheless, this work was done in hopes of providing justification and motivation for this further development.

For the SMA tension/compression device, several creative forms of SMAs were implemented. NiTi helical springs inserted into a stainless steel device were subjected to compression loading. The results showed that the device has excellent recentering behavior (no residual deformations) due to the superelasticity and the precompression of the helical spring. The device's equivalent viscous damping was approximately 6% over the entire deformation range. Though the initial results were promising, work needs to be done to determine if the springs can achieve full-scale load and stiffness levels (the levels reached in this study were low for typical structural applications). Additionally, work needs to be done to better understand the effect of several design parameters (coil diameter, pitch, and thickness) on the resulting strength and stiffness values.

With regards to the SMA Belleville washers, they can be stacked in numerous different parallel and series arrangements, creating different force and deformations capacities. For the washer stacks investigated in this study, the equivalent viscous damping ranged from 4-12%. The force-deformation curve was not predictable due to the weakest washer losing load carrying capacity thus taking on high levels of deformation until it was completely flat. The maximum force levels ranged from 20 kN (4.5 kips) for the single-stacked arrangement to 35 kN (7.9 kips) for the triple-stacked arrangement. Improved behavior of an individual washer was shown through cyclic training and deformation demand reduction; when an individual washer was cycled to approximately 60% of its flat deformation, the load drop-off was eliminated and residual deformations were greatly reduced.

After the tension/compression device investigation was completed, an innovation interior SMA beam-column connection was tested. This investigation was done to evaluate the efficacy of using SMA tendons as recentering and damping elements in a

partially-restrained connection. The design consisted of four SMA tendons attached to the end of the beams via anchor brackets. When drift was imposed, the beams were forced to pivot off the face of the column flange which resulted in the SMA tendons stretching. The results demonstrated that a SMA-based connection can be developed to have good ductility, energy dissipation, and recentering. The following conclusions and significant observations are made from the experimental testing:

- SMA tendons possessed significant superelastic properties which fully recentered the connection at drift levels below 1.0% and adequately recentered the connection at drift levels above 1%. The connection was able to recover 85% of its deformation after being cycled to 5% drift.
- The SMA connection had equivalent viscous damping that varied from approximately 6 to 13% as drift levels increased from 0.375 to 5%. The energy dissipation in the connection was a direct result of NiTi's hysteretic mechanical behavior and friction in the shear tab connection.
- The equivalent viscous damping in the SMA-only (*Test D*) connection was greater than that of the SMA + aluminum (*Test E*) parallel connection. This surprising result can be explained by the following observations: 1) the same physical tendons were used in both tests, resulting in reduced material hysteresis for *Test E*; and 2) the AL tendons buckled in compression resulting in a minimal increase in hysteretic area at larger drift levels.
- For the test connection layout, a 0.5% prestrain was applied to all SMA tendons. Prestraining of the SMA tendons was effective in increasing the recentering capability, and the overall behavior of the connection.
- A simple model in OpenSEES provided a good fit to the experimental data and could account for some level of residual deformation. However, this model

tended to overestimate the strength and stiffness at small drift levels due to its inability to capture the behavior at the transition zone.

Finally, a SMA-based bracing system was developed and tested. The system consisted of a special articulated quadrilateral (AQ) arrangement that accommodated 710 mm (28 in.) long SMA wire bundles. The AQ created a convenient platform for the SMA wire bundles to be combined in parallel with energy dissipating elements. If properly calibrated, it was envisioned that this bracing system would have good recentering with optimized energy dissipation. The following main conclusions are made from this experimental investigation:

- SMA wire bundles were able to recover large levels of strain (approximately 9-12% in this study).
- C-shape dissipators are a unique damping element that display stable hysteretic behavior and can be fabricated to a variety of strength, stiffness, and deformation capacities.
- Both SMA-only and the SMA plus c-shape (PARA) systems had little loss in strength and stiffness after repeated cycling, demonstrating that such a system is well suited for earthquake loading.
- The relative stiffnesses of the SMA elements and those put in series with the SMA elements (steel cables in this case) are important. The adjacent elements should be made stiffer than that of the SMA in order to get full advantage of the SMA loading plateau.
- An analytical study showed that the SMA system and the PARA system had the best performance in terms of interstory and residual drifts. These SMA systems tended to distribute the drifts move evenly over the height of the structure, thus

reducing the likelihood of the formation of soft-stories. Additionally, the SMA systems had a clear advantage in terms of residual drifts.

7.2. Recommended Future Research

This study was exploratory in nature, focusing on the effects of recentering vs. energy dissipation and the development of innovative systems that provided both. It is recommended that further work be done to develop each system investigated in this work. Some areas of potential future work are as follows:

- Assess and improve the behavior of individual SMA Belleville washers and verify the benefits of training illustrated in CHAPTER 4. Integrate these washers into partially-restrained connections. The unique response of the SMA Belleville washer could enhance the behavior of the connection and give it some degree of recentering.
- Create a SMA-based beam-column connection that is designed with realistic, efficient, and cost effective construction details. Such a connection could involve integrating SMA tendons into other promising connection types currently being developed, such as the Kaiser Bolted Bracket connection (Adan and Gibb, 2008) or the welded T-stub connection (Kasai and Xu, 2002a; Kasai and Xu, 2002b). Additionally, new ways to impose higher levels of pretension on the SMA tendons should be investigated, since these tendons tended to twist rather than allow further pretensioning. This work should be done in collaboration with practicing engineers who have a firm grasp on the design and construction process.
- Investigate different methods to supplement the SMA hysteretic damping in the AQ arrangement. One option that could have good potential is a friction mechanism used by Pall Dynamics Limited.

- Investigate different spatial arrangements of SMA connections and braces to see how best a high level of performance can be achieved. Also investigate the uses of SMA-based systems as part of a dual system.
- Develop a design procedure for SMA-based systems (both moment-resisting and braced frames). SMA-based systems behave differently than other traditional and advance systems, therefore system design factors need to be determined (i.e. R, Ω_0, and C_d).
- Further investigation is needed to advance the performance of large bar diameter SMAs. Guidelines should be developed for controlling the properties of SMAs with regard to the properties that are important to civil/structural engineers.
- A study needs to be performed that assesses the root causes for the lack of implementation of SMAs in civil engineering. Though SMAs have shown great promise over the last several decades, limited applications have reached practice. The gap between research and practice needs to be closed.

APPENDIX A

LOADING FRAME DETAILS

This appendix gives detailed description of the lateral loading frame used throughout the experimental portion of this research. For the frame beams, two 801.4 cm (315.5 in.) long W914x224 (W36x150) members were used. These members were left over from other experimental work and had a variety of stiffeners already in place, as indicated by Figure A-1. Additional angled stiffeners were welded at the left end of the top member to transfer the actuator force without buckling the top beam web. The bottom beam was leveled by shimming and post-tensioned to the strong floor. For the frame columns, two 327.7 cm (129.0 in.) W356x216 (W14x145) members were used. These columns had 2.54 cm (1.0 in.) thick plates welded to each end which enabled them to be easily attached to pin-clevis assemblies.

For the pin-clevis assemblies, two types were installed in the frame. At the top, existing assemblies were used with Strainsert SPA-160 load sensing clevis pins. These pins have a capacity of 717 kN (160 kip) and a sensitivity of 2 mV/V at full scale. For the bottom assemblies, larger capacity assemblies were fabricated using 1479 kN (330 kip) Strainsert SPA-330 pins with a sensitivity of 2 mV/V at full scale. These bottom assemblies integrated low friction ball bearings in order to minimize the overall frame friction resistance.

For the load application, a 1000 kN (220 kip) +/- 25.4 cm (10 in.) hydraulic actuator was used. The actuator, controlled by a digital MTS 407b PIDF servo controller, was installed between two stiffened W-sections. The reaction frame was

designed to handle two actuators in parallel for a total capacity of 2000 kN (440 kips). For this research, only one actuator was used.

For the tests presented in CHAPTER 5, interior members were added to the frame to accommodate a half-scale beam-column connection specimen. Appropriate members and shim plates were installed to raise the center of the specimen connection with that of the loading frame in order to reduce kinematic issues (see discussion in APPENDIX B, Section B.2). Loading pin-clevis assemblies were designed and fabricated to transfer the load from the frame to the specimen (Figure A-2). The specimen beams have a slotted pin in order to enable the beams to move laterally during the testing. The pins at the ends of the specimen column and beams are representative of the location of inflection points in a full framing system.

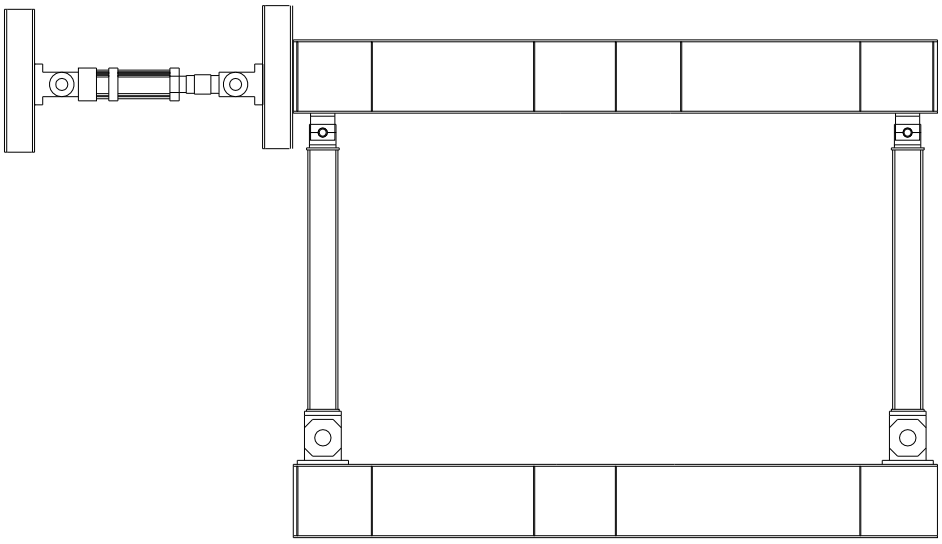

Figure A-1: Loading frame test bed.

Figure A-2: Column pins with shim plates installed.

APPENDIX B

BEAM-COLUMN CONNECTION: EXPERIMENTAL PROGRAM

This appendix gives detailed information on the mechanical tests of the various connection components and additional information on the testing scheme employed to test the connection.

B.1 COMPONENT TESTING

This section describes the setup and component tests of the beam coupons, steel tendons, NiTi tendons, and aluminum tendons.

B.1.1 Component Test Setup

Mechanical tests were carried out using an 810 MTS Universal Testing Machine as shown in Figure B-1. The MTS machine has a capacity of 250 kN (55 kip) measured by a built-in load cell and a +/-127 mm (5 in.) stroke measured by a built-in LVDT. The machine was fitted with hydraulic vee-notched wedge grips which could accommodate a bar diameter up to 19.05 mm (0.75 in.). The tests were run in displacement control using the stroke as the controlling parameter. The machine was controlled by Teststar running Testware software. During some of the tests a 25.4 mm (1.0 in.) gauge MTS extensometer and a 120-ohm strain gauge were used for additional measurements.

Figure B-1: The 810 MTS Universal Testing Machine.

B.1.2 Beam Coupons

For the connection to behave properly, the A572 Grade 50 beams were designed to remain elastic throughout the connection tests. To confirm the mechanical properties of the beam, two coupons were taken from an extra beam section, one along the edge of the flange and the other at the center of the web. The coupons were subjected to a monotonic loading protocol at a rate of 0.127 mm (0.005 in.) per min. until 0.4% strain and then 1.27 mm (0.05 in.) per min. until failure. The results are shown in Figure B-2 (a-d). The coupons yielded at 376 MPa (54.5 ksi) and 386 MPa (56.0 ksi), which both exceeded the required strengths for A572 grade 50 materials.

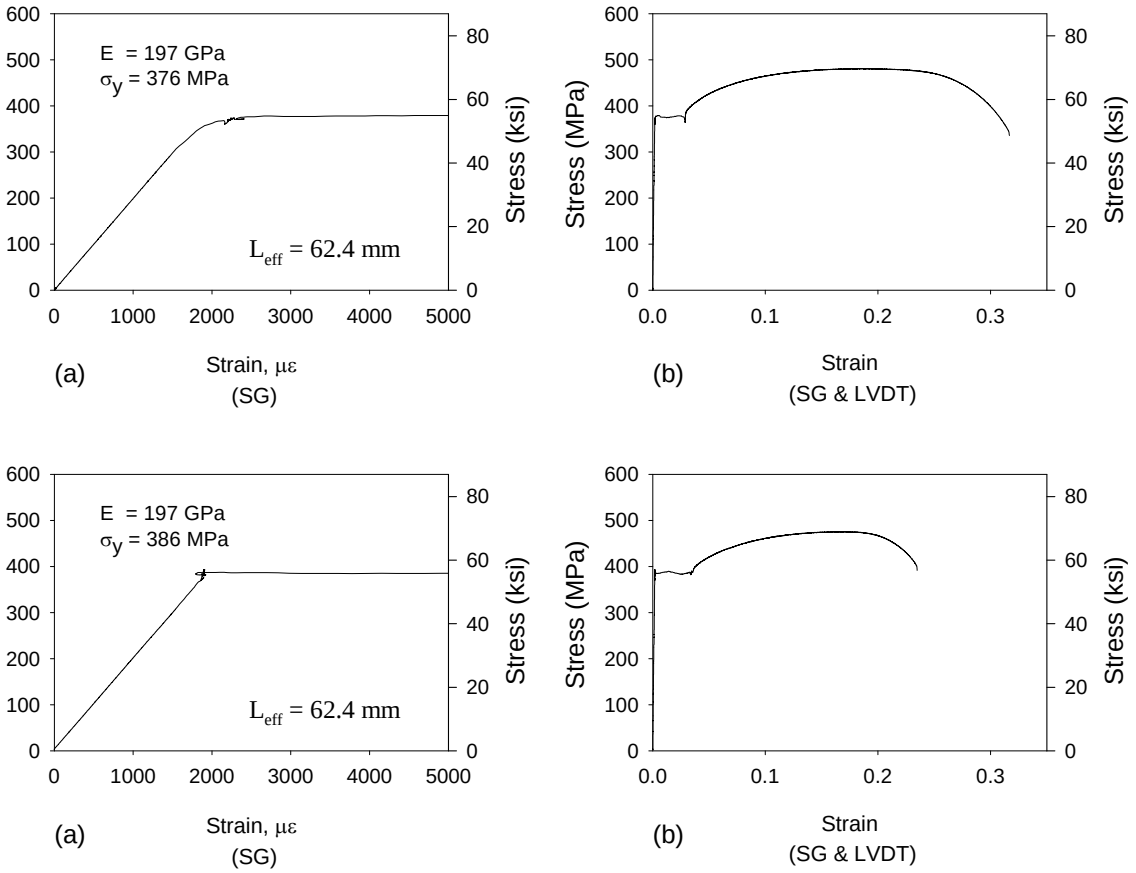

Figure B-2: Stress-strain relationship of the beam coupons.

B.1.3 Steel Bars

For beam-column *Tests A* and *B*, steel bars were used as the tendon elements. Monotonic and cyclic tests were conducted on dogbone specimens of these steel bars. The tests were run in displacement control at 2.5 mm (0.1 in.) per min. The bar dimensions for the tests are shown in Figure B-4. Each bar was machined as per the ASTM E8-03 standard for tensile testing of round bars (ASTM, 2003). Steel bars were used in the connection instead of SMA bars in order to provide a less expensive first-run test on the connection and to provide a benchmark performance comparison of a recentering connection using superelastic SMAs.

Two different types of steel bars were used. In *Test A*, plain steel threaded rod of unknown ASTM grade was purchased and machined. The stress-strain curves are shown in Figure B-5 for a) a monotonic test used to calculate the elastic modulus and the yield stress, b) the same monotonic test used to show gross strain based on the LVDT reading, and c) a cyclic test. The elastic modulus, yield stress, and ultimate stress were found to be 197 GPa (28,600 ksi), 325 MPa (47.1 ksi), and 490 MPa (71.1 ksi), respectively. During the monotonic loading, the bar fractured at approximately 32% strain. During the cyclic loading, the bar had a stable hysteretic response with the yield plateau beginning and ending at approximately 375 MPa (54.4 ksi) and 450 MPa (65.3 ksi), respectively.

In *Test B*, standard A36 steel was used. The bars were already machined from previous work (Penar, 2005) on the beam-column connection. Only one mechanical test, a cyclic loading protocol, was run on this bar and is shown in Figure B-6 . The elastic modulus and yield stress were found to be 197 GPa (28,500 ksi) and 350 MPa (50.8 ksi), respectively. The bar was not stretched until failure, therefore neither the ultimate strength nor the ultimate strain was known.

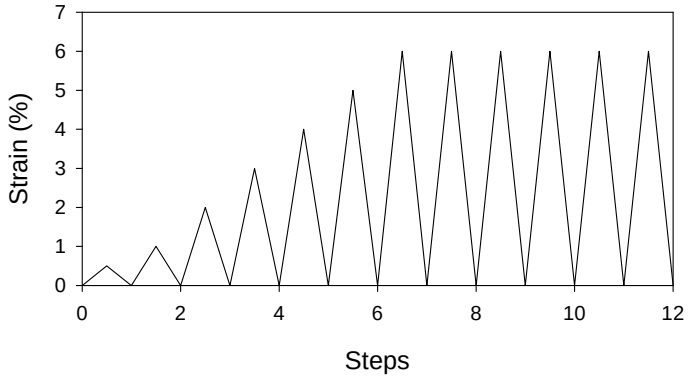

Figure B-3: Cyclic loading protocol for the mechanical testing.

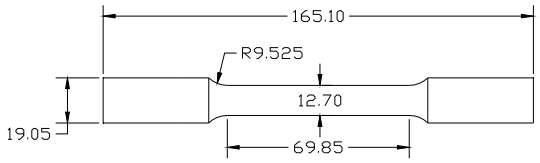

Figure B-4: Dogbone mechanical test specimen dimensions (units in mm).

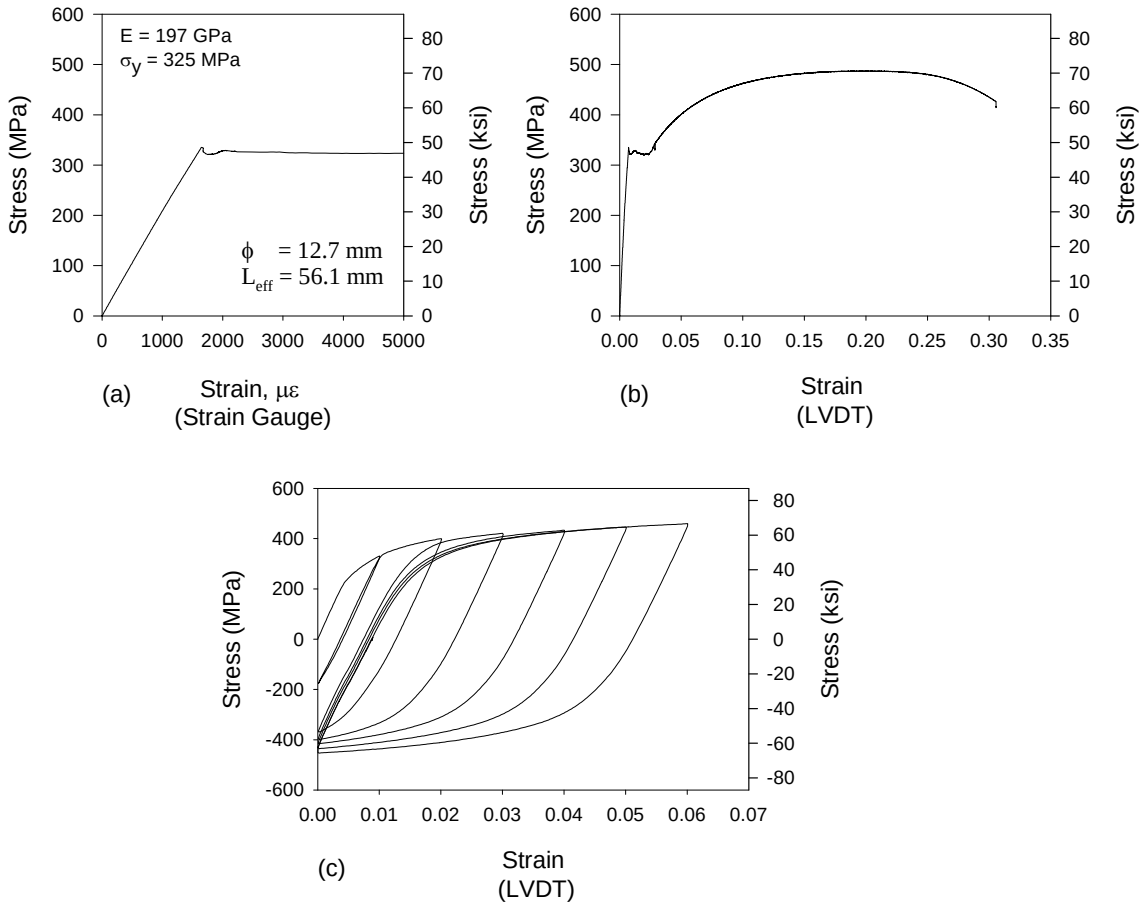

Figure B-5: Stress-strain of the steel threaded bar for *Test A.*

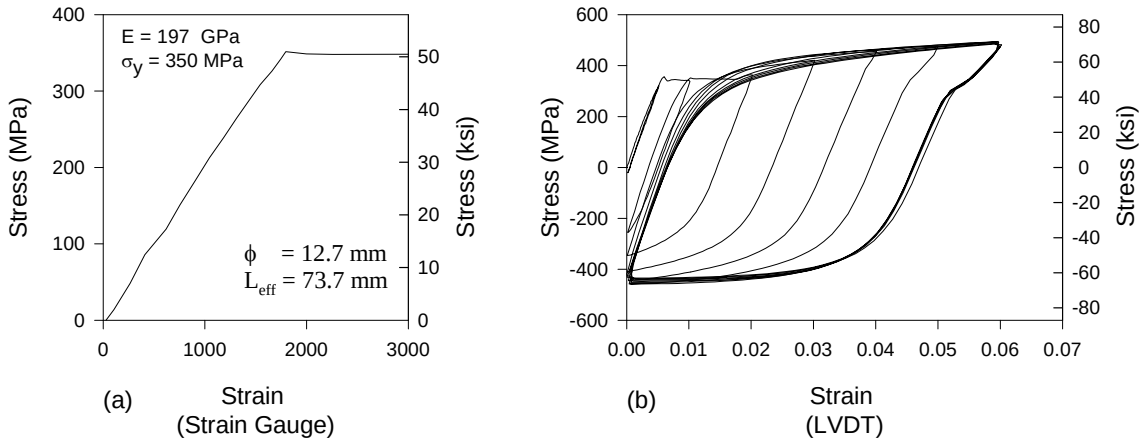

Figure B-6: Stress-strain of A36 steel bar for *Test B* (data from Penar, 2005).

B.1.4 NiTi Bars

The loading protocol followed for the SMA mechanical testing was the same as that for the steel testing as shown in Figure B-3. Again, this protocol was implemented using displacement control, with the strain calculated as the crosshead displacement divided by the effective length of the specimen (69.9 mm (2.75in.) in this case). It should be noted that this gross strain is smaller than that which is obtained from the more concentrated strain recorded from the extensometer. The NiTi bars had an elastic modulus and yield strength of approximately 23 GPa (3300 ksi) and 325 MPa (47.0 ksi), respectively. These values were both less then seen in previous research testing of similar bar specimens (McCormick 2006).

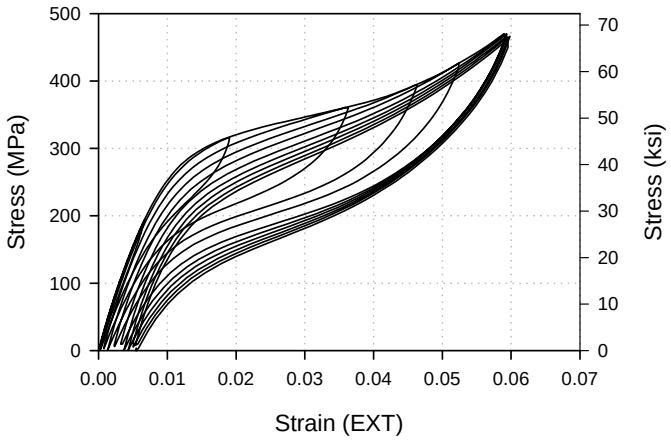

Figure B-7: Stress-strain of the NiTi dogbone.

B.1.5 Aluminum Bars

In order to create a connection with a parallel resisting system as proposed in the SDOF study of CHAPTER 3, low strength aluminum (AL) bars were used. A low strength material was needed in order to prevent the connection beam from being overloaded. Readily available 6061-T6511 AL was purchased and tested; it displayed a yield strength of approximately 414 MPa (60 ksi). Since lower strength material was desired, the AL was annealed. First the tendons were machined and threaded. Next, the tendons were heated to 425 °C for 4 hrs., then cooled 30 °C/hr. until the temperature fell below 260 °C, and then finally air-cooled (annealing procedure adopted from the *Handbook of Aluminum)* (Alcan, 1970).

The loading protocol followed for the AL mechanical testing was the same as that for the steel and SMA testing as shown in Figure B-3. The effective length of the test specimen was 71.9 mm (2.83 in.). The resulting stress-strain relationship is show in Figure B-8. The elastic modulus and yield stress were 32.4 GPa (4700 ksi) and 117 MPa (17 ksi), respectively. The low strength was a direct result of the annealing process.

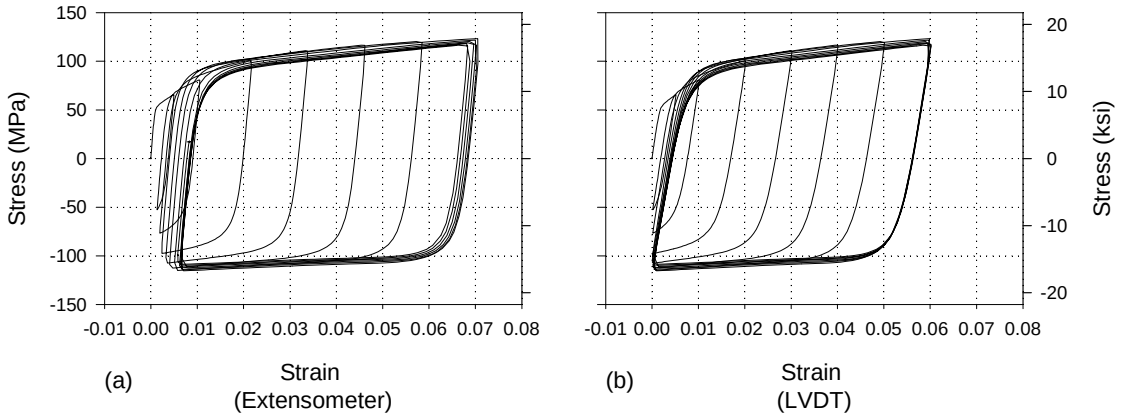

Figure B-8: Stress-strain for the annealed aluminum bar.

B.2 LOADING FRAME AND SPECIMEN INTERACTION

When the loading frame deflects laterally, the frame's top beam translates downward (vertical) due to the arc traced by the top of the frame's column. The amount of vertical translation is a function of the height of the frame column. The larger the height of the column, the less this vertical translation is per unit horizontal movement. Since the installed specimen column does not have the same height as that of the frame column, tension is induced in the specimen column by lateral movement of the loading frame. In order to reduce this unwanted kinematic effect, steel plates were used as shims to provide some precompression to the specimen column. The column was installed with the frame displaced 120 mm (4.7 in.) to the right. When the frame was moved back to center, the kinematics described above resulted in precompression of the column. During the testing the specimen column must first give up the precompression before it can go into tension, thus reducing the magnitude of the tension that is ultimately induced.

Another kinematic issue identified is the tendency for specimen's lateral dimension to grow as the frame is cycled. This is caused by the beams pivoting off the

face of the column. During traditional testing of an interior beam-column connection, the beams are not restrained from elongation in the axial direction. Therefore, in order to relieve the unwanted axial load that this would cause, the end beams were fitted with slotted pins that allow beam ends to slide in the horizontal direction. Additionally, the specimen was installed at mid-height of the frame because the beam ends will travel approximately half that of the top of the specimen columns.

B.3 INSTRUMENTATION

A detailed schedule of the instrumentation is given in Table B-1. Figure B-9 and Figure B-10 show a detailed layout of where the instrumentation was placed.

Table B-1: Instrumentation Schedule for the Beam-Column Tests.

#	Type	Details	Location	SCXI Block	SCXI Card	Comments
1	LVDT		Actuator	1303	1100	10 in.
2	LC		Actuator	1303	1100	220 kips
3	SG	FLA-5-11-5L	CF-left-up-mid	1317	1520B	120 ohm
4	SG	FLA-5-11-5L	CF-left-up-side	1317	1520B	120 ohm
5	SG	FLA-5-11-5L	CF-right-up-mid	1317	1520B	120 ohm
6	SG	FLA-5-11-5L	CF-right-up-side	1317	1520B	120 ohm
7	SG	FLA-5-11-5L	CF-left-down-mid	1317	1520B	120 ohm
8	SG	FLA-5-11-5L	CF-left-down-side	1317	1520B	120 ohm
9	SG	FLA-5-11-5L	CF-right-down-mid	1317	1520B	120 ohm
10	SG	FLA-5-11-5L	CF-right-down-side	1317	1520B	120 ohm
11	SG	FLA-5-11-5L	BF-left-up-mid	1317	1520B	120 ohm
12	SG	FLA-5-11-5L	BF-left-up-side	1317	1520B	120 ohm
13	SG	FLA-5-11-5L	BF-left-down-mid	1317	1520B	120 ohm
14	SG	FLA-5-11-5L	BF-left-down-side	1317	1520B	120 ohm
15	SG	FLA-5-11-5L	BF-right-up-mid	1317	1520B	120 ohm
16	SG	FLA-5-11-5L	BF-right-up-side	1317	1520B	120 ohm
17	SG	FLA-5-11-5L	BF-right-down-mid	1317	1520B	120 ohm
18	SG	FLA-5-11-5L	BF-right-down-side	1317	1520B	120 ohm
19	SP	PA-10-35090455	B-left	1303	1100	10 in.
20	SP	PA-10-35090456	B-right	1303	1100	10 in.
21	SP	PA-20-35090457	C-bottom	1303	1100	20 in.
22	SP	PA-20-35090460	C-top	1303	1100	20 in.
23	EXT	3545-0200-020-ST	T-top-front	1314	1520	Epsilon
24	EXT	3545-0200-025-ST	T-top-back	1314	1520	Epsilon
25	EXT	3545-0200-020-ST	T-bottom-front	1314	1520	Satec

26	EXT	545-0100-025-ST	T-bottom-back	1314	1520	Epsilon
27	LVDT	DCTH500-42979	top-left	1303	1100	+/- 0.5"
28	LVDT	DCTH500-42976	top-right	1303	1100	+/- 0.5"
29	LVDT	DCTH500-42978	bottom-left	1303	1100	+/- 0.5"
30	LVDT	DCTH500-42966	bottom-right	1303	1100	+/- 0.5"
31	Pin LC	SPA-160	top-left	1303	1100	Strainsert
32	Pin LC	SPA-160	top-right	1303	1100	Strainsert
33	Pin LC	SPA-330	bottom-left	1303	1100	Strainsert
34	Pin LC	SPA-330	bottom-right	1303	1100	Strainsert
35	SG	FRA-5-11-5L	PZ-upper-left 1	1317	1520B	rosette, 120 ohm
36	SG	FRA-5-11-5L	PZ-upper-left 2	1317	1520B	rosette, 120 ohm
37	SG	FRA-5-11-5L	PZ-upper-left 3	1317	1520B	rosette, 120 ohm
38	SG	FRA-5-11-5L	PZ-middle 1	1317	1520B	rosette, 120 ohm
39	SG	FRA-5-11-5L	PZ-middle 2	1317	1520B	rosette, 120 ohm
40	SG	FRA-5-11-5L	PZ-middle 3	1317	1520B	rosette, 120 ohm
41	SP	PA-20-35090459	Frame-top	1303	1100	20"
42	SG	FLA-5-11-5L	B-left-top-mid	1317	1520B	120 ohm
43	SG	FLA-5-11-5L	B-right-top-mid	1317	1520B	120 ohm
44	SG	YEFLA-5-11-5LT	T-top-front	1314	1520	high elongation, 120 ohm
45	SG	YEFLA-5-11-5LT	T-top-back	1314	1520	high elongation, 120 ohm
46	SG	YEFLA-5-11-5LT	T-bottom-front	1314	1520	high elongation, 120 ohm
47	SG	YEFLA-5-11-5LT	T-bottom-back	1314	1520	high elongation, 120 ohm

SG = strain gauge, LC = load cell, LVDT = linear variable displacement transducer, EXT = extensometer, SP = string potentiometer, C(F) = column (flange), B(F) = beam (flange), PZ = panel zone

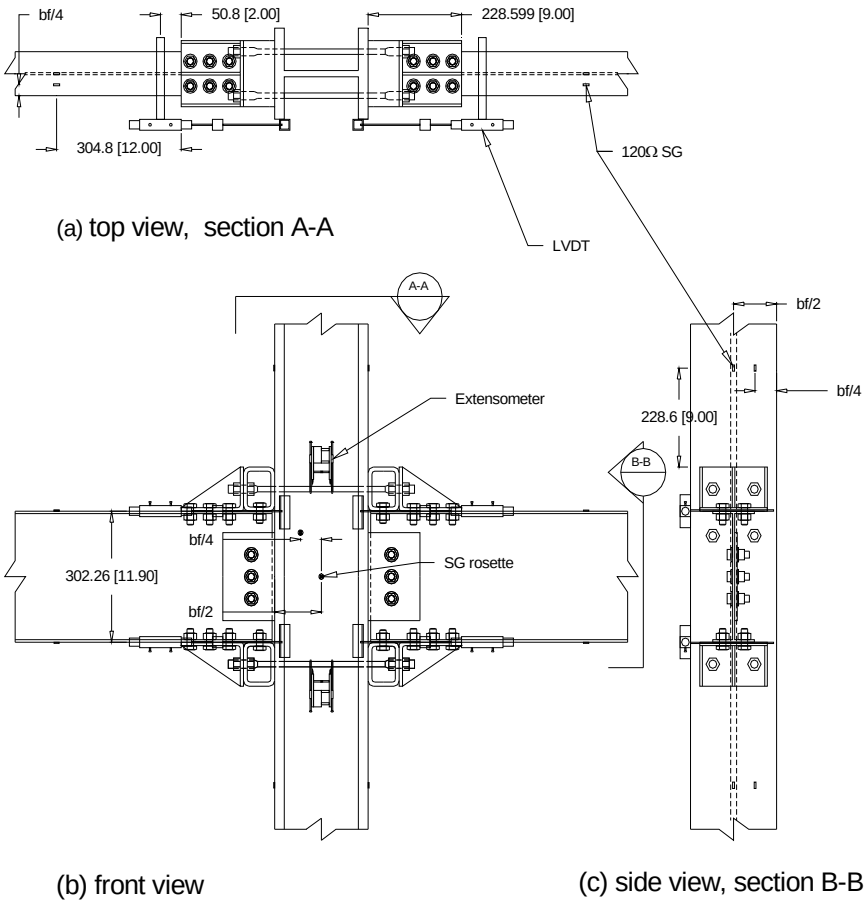

Figure B-9: Instrumentation of specimen connection (units in cm).

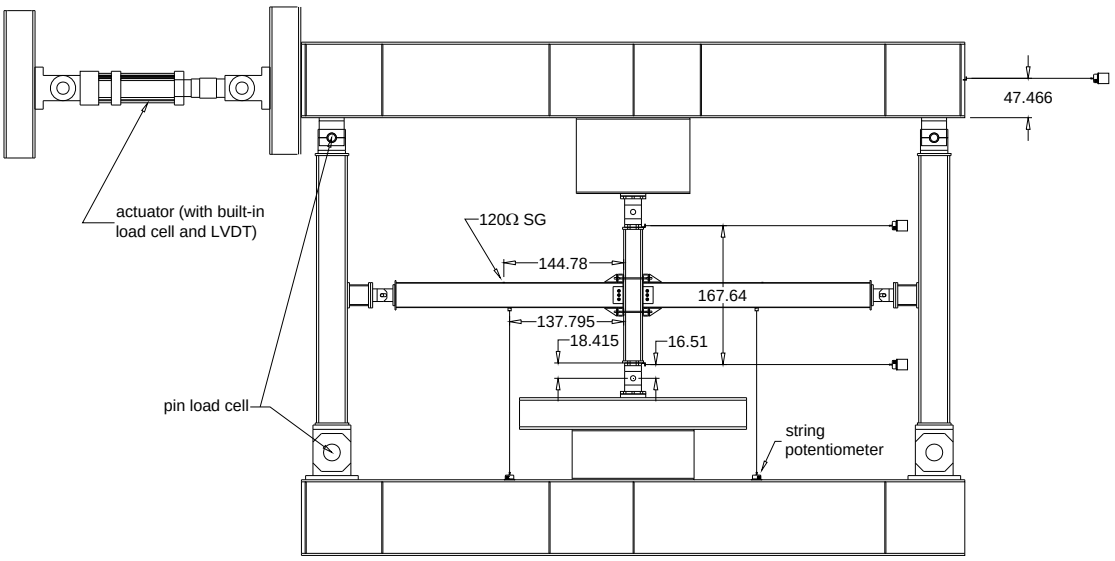

Figure B-10: Instrumentation of frame and specimen (units in cm).

B.4 DATA ACQUISITION

Data from the appropriate sensors was collected using a National Instruments SCXI-1001 chassis fitted with the following module cards and terminal blocks:

- Slot 1: (a) SCXI-1520 8-channel Wheatstone bridge module card (b) SCXI-1314 universal strain terminal block
- Slot 2: (a) SCXI-1521 350 Ω 24-channel quarter bridge module card (b) SCXI-1317 terminal block
- Slot 3: (a) SCXI-1521B 120 Ω 24-channel quarter bridge module card (b) SCXI-1317 terminal block
- Slot 4: (a) SCXI-1100 module card (b) SCXI-1303 32-channel thermocouple terminal block

This chassis was connected to a Dell computer running National Instruments Labview version 8.0. A virtual instrument was designed within Labview to excite sensors and

collect the corresponding data. Data was sampled at 100 readings per second. In order to smooth out some of the existing noise, 50 readings were collected (per ½ second), averaged, and then recorded as the value for the corresponding channel. This effectively gives recording rate of 2 average readings per second. However, due to the DAQ's speed limitations, the actual recording rate was reduced to approximately every 0.9 seconds.

APPENDIX C

BEAM-COLUMN CONNECTION: DATA REDUCTION

C.1 DEFINITIONS

General

ε Strain

d Distance

δ Displacement

δ_{LV1} LVDT displacement at top of left beam

δ_{LV2} LVDT displacement at top of right beam

δ_{LV3} LVDT displacement at bottom of left beam

δ_{LV4} LVDT displacement at bottom of right beam

E Elastic modulus

I Section moment of inertia

M Moment

θ Rotation

σ Stress

Sign Convention

The sign convention followed for the moment and rotations are illustrated in Figure C-1.

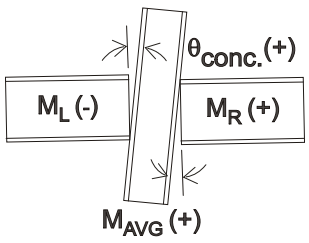

Figure C-1: Sign convention for the M-θ plots.

C.2 MOMENT

The moments in the specimen beams and the specimen column were calculated based on the strain gauge readings mounted at a distance *d* from the respective connection bracket. It is assumed herein, and experimentally verified for all tests that the beams and the column remained elastic; therefore Hooke's Law applies:

$$\sigma = E\varepsilon \tag{C.1}$$

In order to get the stress at the outside flange surface, the middle and quarter strain gauges are averaged as follows:

$$\sigma_t = \frac{\left(\sigma_{tm} + \sigma_{tq}\right)}{2} \tag{C.2}$$

$$\sigma_b = \frac{\left(\sigma_{bm} + \sigma_{bq}\right)}{2} \tag{C.3}$$

$$\sigma_a = \frac{\left(\sigma_t + \sigma_b\right)}{2} \tag{C.4}$$

$$\sigma_M = \frac{\left(\sigma_b - \sigma_t\right)}{2} \tag{C.5}$$

where σ_t, σ_b, σ_a, and σ_m are the top flange stress, bottom flange stress, axial stress component, and bending stress component, respectively.

The moment can be calculated by the flexure formula:

$$M = \int_A y\sigma \cdot dA \Rightarrow M = \frac{\sigma_M I}{(d/2)} \tag{C.6}$$

where *d* is the depth of the beam.

C.3 ROTATIONS

C.3.1 Concentrated rotations

The concentrated rotation calculated from the LVDT readings for the right (concR) and left (concL) beam are:

$$\theta_{concR} = \frac{(\delta_{LV2} - \delta_{LV4})}{d'} \quad \text{(C.7)}$$

$$\theta_{concL} = \frac{(\delta_{LV1} - \delta_{LV3})}{d'} \quad \text{(C.8)}$$

where *d'* is the distance between the LVDTs and δ_{LV1}, δ_{LV2}, δ_{LV3}, and δ_{LV4} are the readings from the top-left, top-right, bottom-left, and bottom-right LVDTs, respectively.

C.3.2 Total Rotation

The total rotation is defined as:

$$\theta_{total} = \frac{\delta_{col}}{L_c} \quad \text{(C.9)}$$

where δ_{col} is the displacement at the top of the column (at centerline of the pin)

C.4 PRINCIPLE STRAINS

The three gauge rosettes provided means to calculate the principle strains in the panel zone. The three readings in each gauge are denoted by ε_A, ε_B, and ε_C as depicted in Figure C-2. Knowing the strain gauges are 45° apart, the strain in each gauge can be written in terms of the principle strains, ε_1 and ε_2, as follows:

$$\varepsilon_A = \frac{\varepsilon_1 + \varepsilon_2}{2} + \frac{\varepsilon_1 - \varepsilon_2}{2}\cos(2\phi) \quad \text{(C.10)}$$

$$\varepsilon_B = \frac{\varepsilon_1 + \varepsilon_2}{2} + \frac{\varepsilon_1 - \varepsilon_2}{2}\cos(2\phi + 45°) \quad \text{(C.11)}$$

$$\varepsilon_C = \frac{\varepsilon_1 + \varepsilon_2}{2} + \frac{\varepsilon_1 - \varepsilon_2}{2}\cos(2\phi + 90°) \quad \text{(C.12)}$$

With three equations and three unknowns (ε_1, ε_2, and ϕ), the principle strains are solved for giving:

$$\varepsilon_{1,2} = \frac{\varepsilon_A + \varepsilon_C}{2} + \frac{1}{\sqrt{2}}\sqrt{(\varepsilon_A - \varepsilon_B)^2 + (\varepsilon_B - \varepsilon_C)^2} \quad \text{(C.13)}$$

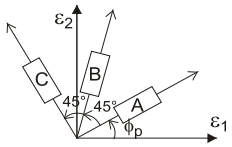

Figure C-2: Strain gauge rosette orientation for principle strain calculations.

C.5 DRIFT CONTRIBUTION CALCULATIONS

In the following calculations, small angles are assumed which affords the following approximations:

$$\sin(\theta) \cong \theta \qquad \cos(\theta) \cong 1 \qquad 1-\cos(\theta) \cong \frac{\theta^2}{2} \tag{C.14}$$

C.5.1 Drift contribution due to beam and column elastic flexure

General Formulation

Starting with the established relationship between curvature, ϕ, and moment, *M*,

$$\frac{d\theta}{dx} = \phi = \frac{M}{EI} \tag{C.15}$$

Solving for the rotation, θ

$$\theta = \int \frac{M}{EI} dx \tag{C.16}$$

The moment is linearly changing along the length, therefore

$$M = mx \tag{C.17}$$

Where *m* is the slope of *M* and *x* is the distance along the member as illustrate in Figure C-3. Solving for θ yields

$$\theta = \frac{mx^2}{2EI} + c \tag{C.18}$$

Accounting for the boundary conditions to solve for the constant *c* (i.e. θ = 0 at *x* = *L*) gives

$$c = -\frac{mL^2}{2EI} \tag{C.19}$$

Now, solving for the deflection δ in terms of x

$$\delta = \frac{m}{2EI}\int\left(x^2 - L^2\right)\cdot dx \tag{C.20}$$

$$\delta = \frac{m}{2EI}\left(\frac{x^3}{3} - xL^2\right) \tag{C.21}$$

Beam Calculations

The various variables are defined in Figure C-3. Solve for θ_{a0}

$$\theta_{a0} = \frac{\delta_{a0}}{L_{b'}} \tag{C.22}$$

where

$$L_{b'} = L_b + \frac{d_c}{2} \tag{C.23}$$

$$\delta_{a0} = -\frac{m_b {L_b}^3}{3EI_b} \tag{C.24}$$

Column Calculations

The various variables are defined in Figure C-3. Solve for θ_{a1}

$$\theta_{a1} = \frac{\delta_{a1}}{L_{c'}} \tag{C.25}$$

where

$$L_{c'} = \frac{L_c - d_{c'}}{2} \tag{C.26}$$

$$\delta_{a1} = -\frac{m_c {L_{c'}}^3}{3EI_c} \tag{C.27}$$

Also,

$$\delta_{a3} = \theta_{a0} d_{b'} \tag{C.28}$$

Overall frame

The overall drift contribution due to flexure can be calculated by first finding δ_{a2} then summing the appropriate δ's.

$$\delta_{a2} = \left(\theta_{a0} + \theta_{a1}\right) \cdot L_{c'} \tag{C.29}$$

Finally, the drift contribution due to elastic bending of the beam and column is:

$$\delta_a = 2\delta_{a2} + \delta_{a3} \tag{C.30}$$

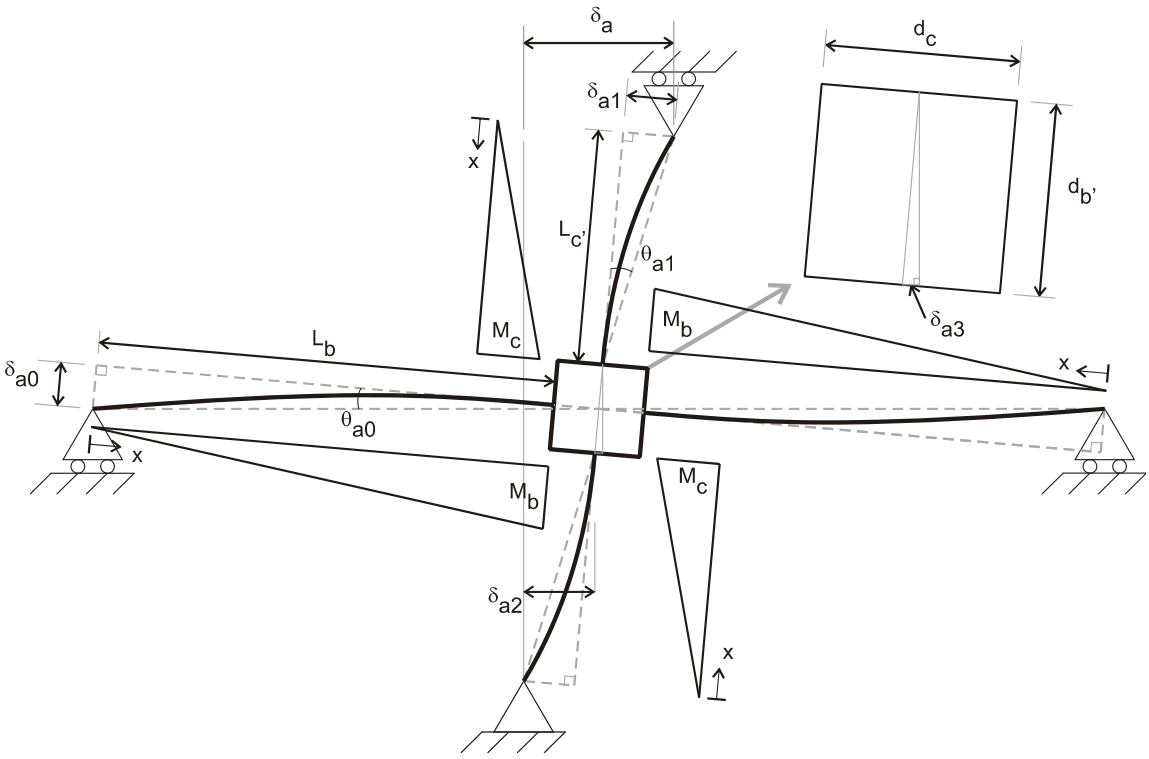

Figure C-3: Schematic defining parameters in order to calculate the drift from beam and column flexure.

C.5.2 Drift Contribution Based on Column Joint Shear

The drift contribution due to panel zone shear is:

$$\delta_b = \frac{\left(L_c - d_{b'}\right)\left(\frac{L_c}{d_{b'}} - 1\right)}{G t_p d_c} V_c \qquad \text{(C.31)}$$

Where V_c is the shear force in the column calculated from the strain gauges in the column by the following formula

$$V_c = \frac{M_c L_{c'}}{d_{b'}} \qquad \text{(C.32)}$$

$$G = \frac{E}{2(1+\nu)} \qquad \text{(C.33)}$$

where ν = 0.3, M_c is the moment in the column at the outside face of the connection, $L_{c'}$ is the length of the column as show in Figure C-3.

C.5.3 Drift contribution Based on Beam Concentrated (Inelastic) Rotation

The following equations first relate the concentrated rotation, $\theta_{conc.}$, to the column rotation, θ_{c1}. Once this relation is known, the equation for the drift contribution, δ, based on $\theta_{conc.}$ is found. Figure C-4 and Figure C-5 define the parameters used to make these calculations.

Right Beam

When the imposed drift is to the right, the right beam is governed by the following equations which ultimately relate the θ_{concR} to the θ_{c1R} (where the "*R*" denotes the right beam).

$$\theta_{concR} = \frac{\left(\delta_{LV2} - \delta_{LV4}\right)}{d'} \qquad \text{(C.34)}$$

Where δ_{LV2} and δ_{LV2} are defined in Section A.3.1. The variable d' is the depth of the beam plus the mounting brackets.

From geometry, the following equations can be written

$$\delta_{cR0} = \delta_{cR1} + \delta_{cR2} \tag{C.35}$$

$$\delta_{cR1} = \frac{L_c}{2}\theta_{cR1} \tag{C.36}$$

$$\delta_{cR2} = \frac{d_c}{2}\theta_{cR1} \tag{C.37}$$

Therefore

$$\delta_{cR1} = \frac{L_c}{d_c}\delta_{cR2} \tag{C.38}$$

Substituting (C.37) into (C.35) gives

$$\delta_{cR0} = \left(\frac{L_c}{d_c} + 1\right)\delta_{cR2} \tag{C.39}$$

Getting θ_{cR2} in terms of θ_{cR1} yields

$$\theta_{cR2} = \frac{\delta_{cR0}}{L_b} = \frac{(L_c + d_c)\cdot\theta_{cR1}}{2L_b} \tag{C.40}$$

$$\theta_{concR} = \theta_{cR1} + \theta_{cR2} = \left[\frac{(L_c + d_c)}{2L_b} + 1\right]\theta_{cR1} \tag{C.41}$$

Therefore

$$\theta_{cR1} = \frac{1}{\left[\frac{(L_c + d_c)}{2L_b} + 1\right]}\theta_{concR} \tag{C.42}$$

Equation (C.42) is the rotation of the specimen column with respect to the ground in terms of the right beam's concentrated rotation.

Finally, the drift contribution is

$$\delta_{cR} = L_c\theta_{cR1} \tag{C.43}$$

Left Beam

In contrast to the right beam, the left beam is governed by different equations when the imposed drift is to the right (due to the kinematics of the setup). The following equations give the relation between θ_{concL} to the θ_{cL1}, where the "*L*" denotes the left beam.

$$\theta_{concL} = \frac{\left(\delta_{LV1} - \delta_{LV3}\right)}{d'} \tag{C.44}$$

Where δ_{LV1} and δ_{LV3} are defined in section A.2.1

$$\delta_{cL0} = \delta_{cL1} + \delta_{cL2} \tag{C.45}$$

Where

$$\delta_{cL2} = \left(1 - \cos\left(\theta_{cL1}\right)\right)\frac{L_c}{2} \tag{C.46}$$

$$\delta_{cL2} = \left(1 - \cos\left(\theta_{cL1}\right)\right)\frac{L_c}{2} \tag{C.47}$$

Substituting in (A.7c)

$$\delta_{cL2} = \frac{L_c}{4}\theta_{cL1}^{\ 2} \tag{C.48}$$

Concurrently

$$\delta_{cL2} = L_b\left(\theta_{cL1} - \theta_{concL}\right) + \frac{d_c}{2}\theta_{cL1} \tag{C.49}$$

Setting (A.20) equal to (A.21), and solving the quadratic equation for θ_{cL1} gives

$$\theta_{cL1} = \frac{\left(L_b + d_c/2\right) \pm \sqrt{\left(L_b + d_c/2\right)^2 - L_c L_b \theta_{concL}}}{L_c/2} \tag{C.50}$$

When θ_{concL}= 0 then θ_{cL1} = 0. Only the negative root satisfies this condition, therefore

$$\theta_{cL1} = \frac{\left(L_b + d_c/2\right) - \sqrt{\left(L_b + d_c/2\right)^2 - L_c L_b \theta_{concL}}}{L_c/2} \tag{C.51}$$

Finally, the drift contribution is

$$\delta_{cL} = L_c\theta_{cL1} \tag{C.52}$$

Both Beams

In theory the δ_{cR} and the δ_{cL} should be equal. Therefore, the average is taken as the drift contribution, δ_c, due to concentrated inelastic beam rotation.

$$\delta_c = \frac{\delta_{cR} + \delta_{cL}}{2} \qquad \text{(C.53)}$$

Note that when the imposed drift is to the left, the equations are switched for the right and left beams. This is programmed into the script when the data reduction is carried out.

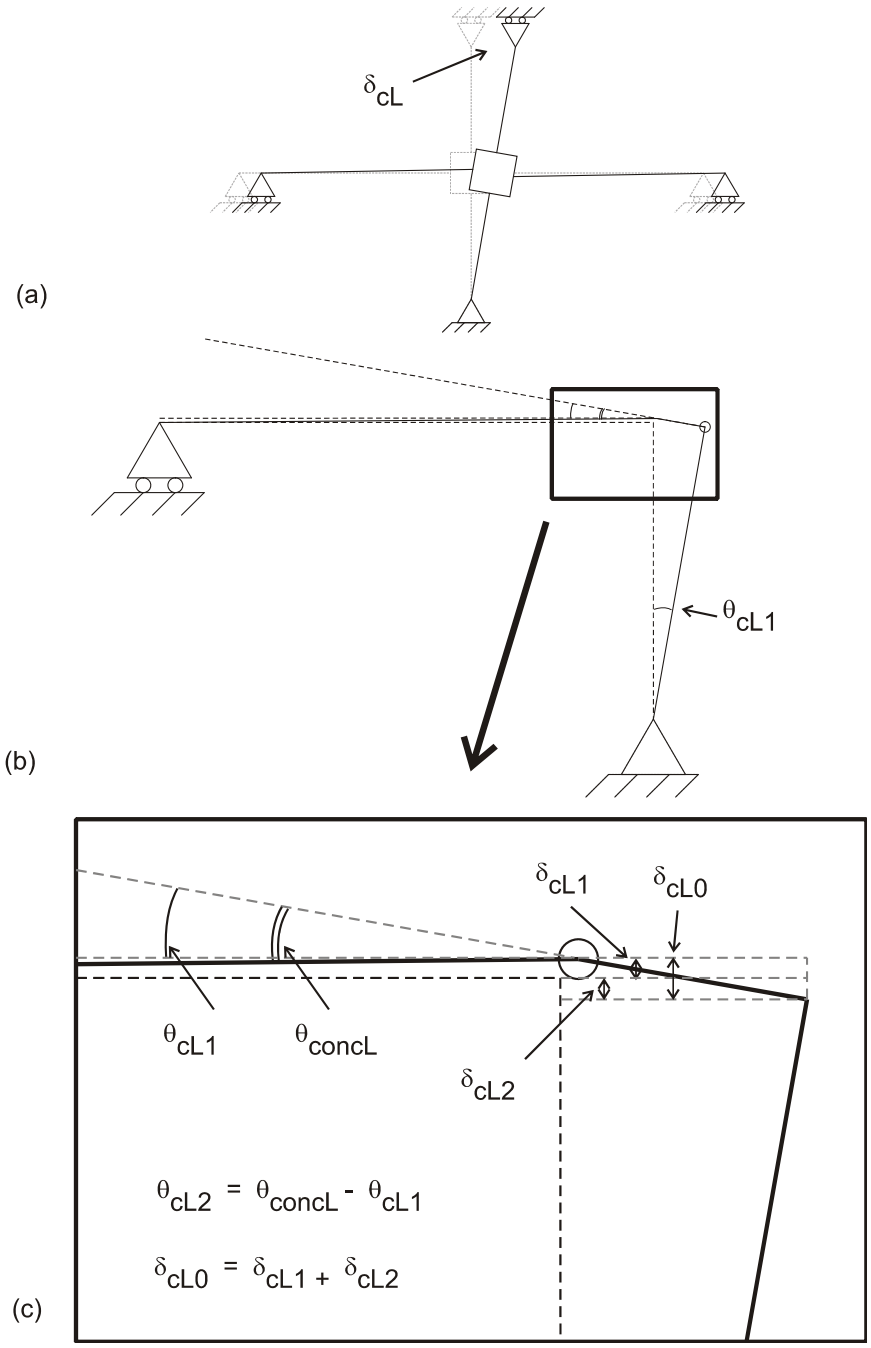

Figure C-4: Schematic defining parameters in order to calculate the drift per the left beam instrumentation.

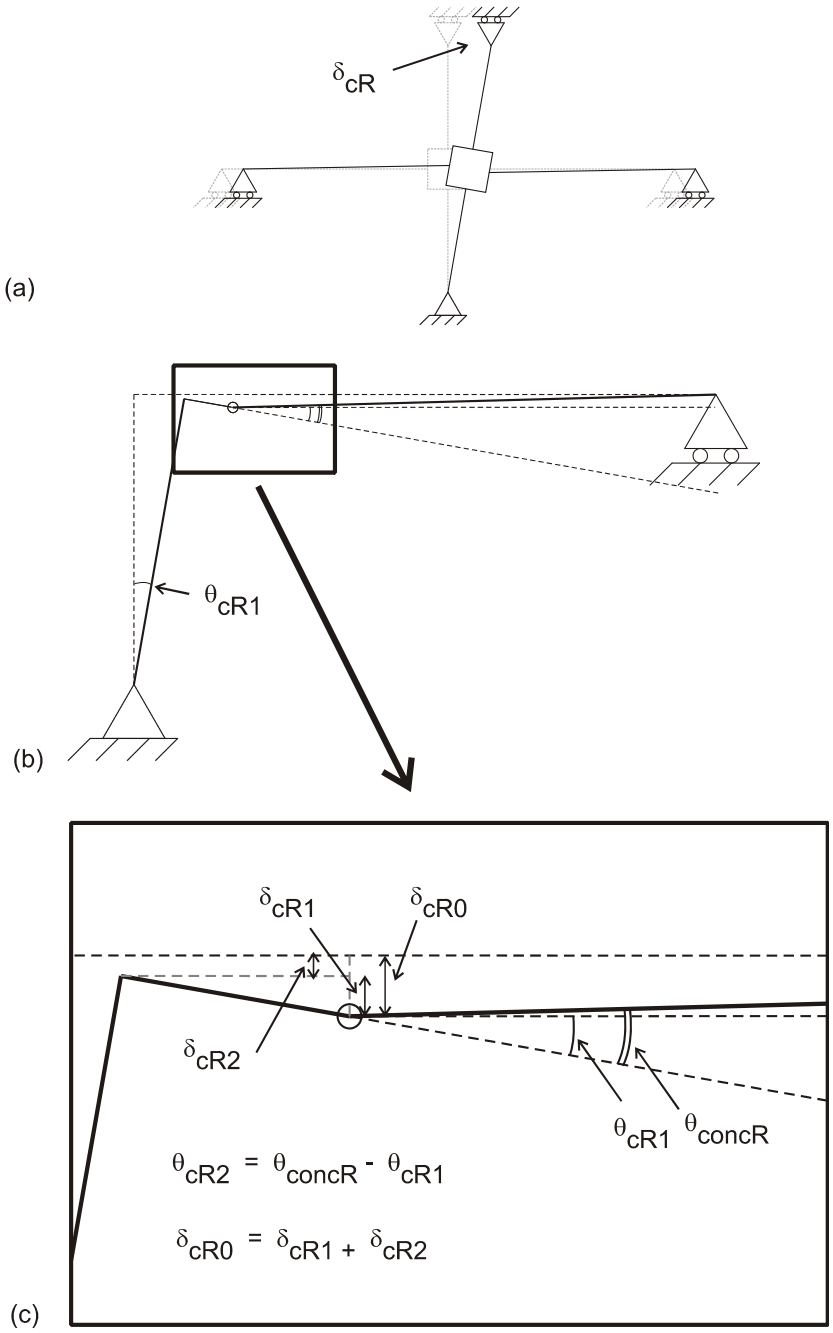

Figure C-5: Schematic defining parameters in order to calculate the drift per the right beam instrumentation.

APPENDIX D

BEAM-COLUMN CONNECTION: VALIDATION

This appendix walks through selected experimental data obtained from each test, with the intent to lend validity to the results. The calculations made in the data reduction of each beam-column test assumed the beams and column remained elastic.

To confirm this assumption, the strain time histories as recorded from the SGs attached at a distance *d* from the L-shape bracket termination (see Figure B-9) are shown in Figure D-1. Additionally, a dashed line is plotted by extrapolating this SG reading to get the strain at the face of the column. This extrapolated value is conservative because the majority of the forces have already been transferred into the bracket elements before the column face is reached. Nevertheless, this extrapolated value is assumed to be the largest strain present in the member. From the coupon tests, the yield strain, ε_y, is calculated to be approximately 2000 microstrain. The SG readings (both real and extrapolated) are well below the ε_y, confirming the assumption of the beams remaining elastic.

The panel zone elasticity also needs to be verified. Plots of principal strains calculated from the strain gage rosettes are shown in Figure D-2. The strain levels in the panel zone never exceed 1000 microstrain, which is well below the yielding value.

To further validate the results, the drift contributions are calculated as described in APPENDIX C. The contributions are schematically illustrated in Figure D-3 and include the elastic action of the beam and column, δ_a; the shear deformation action in the panel zone, δ_b; and the inelastic action of the beam at the column face, δ_c. No

contribution from the column inelastic action was calculated because the column remains fully elastic at the joint interface.

On the left side of Figure D-4, the sum of these three contributions, $\delta = \delta_a + \delta_b + \delta_c$, and the drift as measured by the mounted sensors (SP), δ_{sensor}, are plotted vs. time for each test. On the right side of Figure D-4, the difference between these drift values, $\delta - \delta_{sensor}$, is plotted and the maximum absolute value of this difference is noted for each test. Since these values should be equal, the difference is a measure of error in the experimental calculations. This error ranged in between 5-10%, which was determined to be satisfactory.

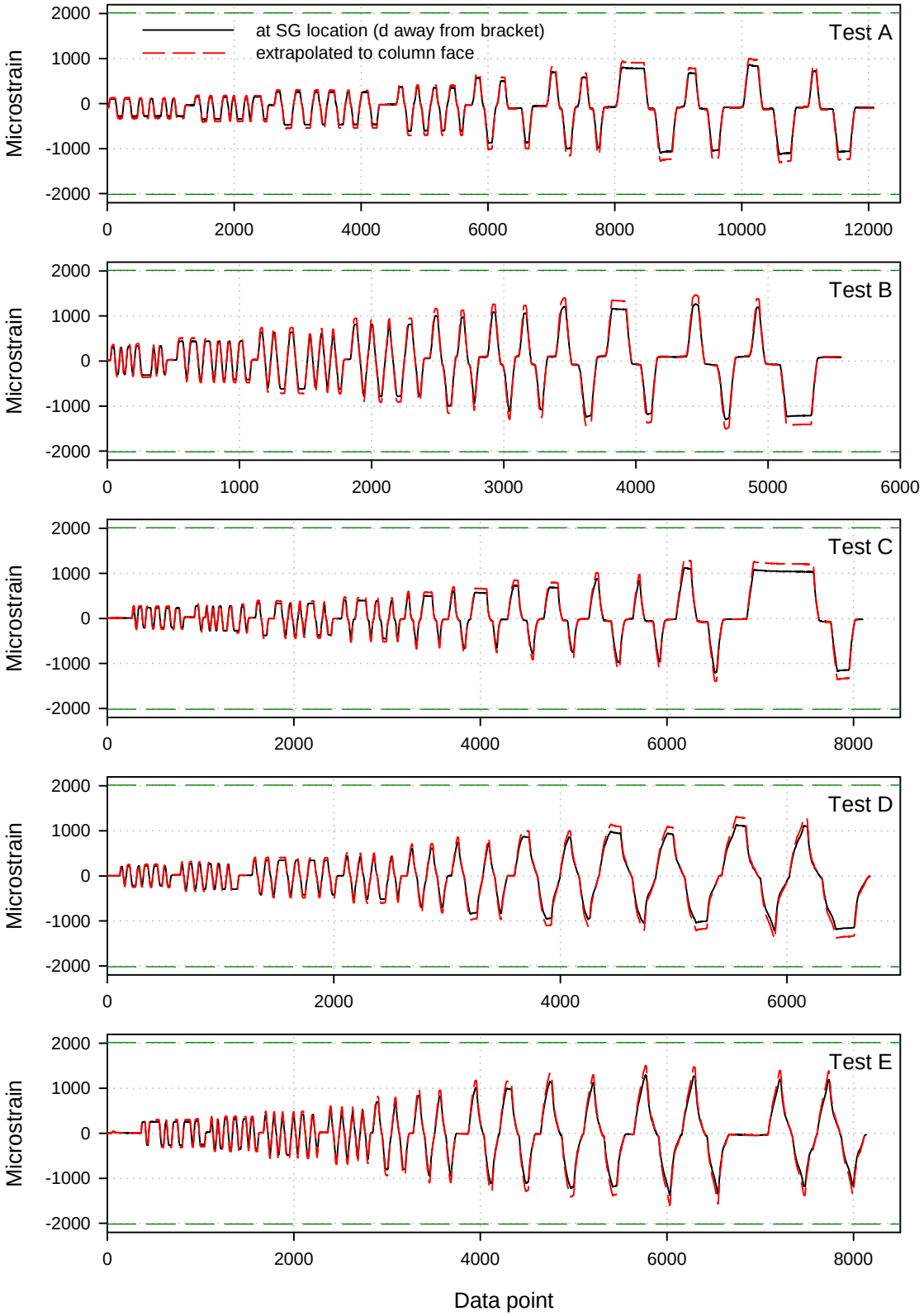

Figure D-1: Strain time history of top-mid SG on left beam for each test.

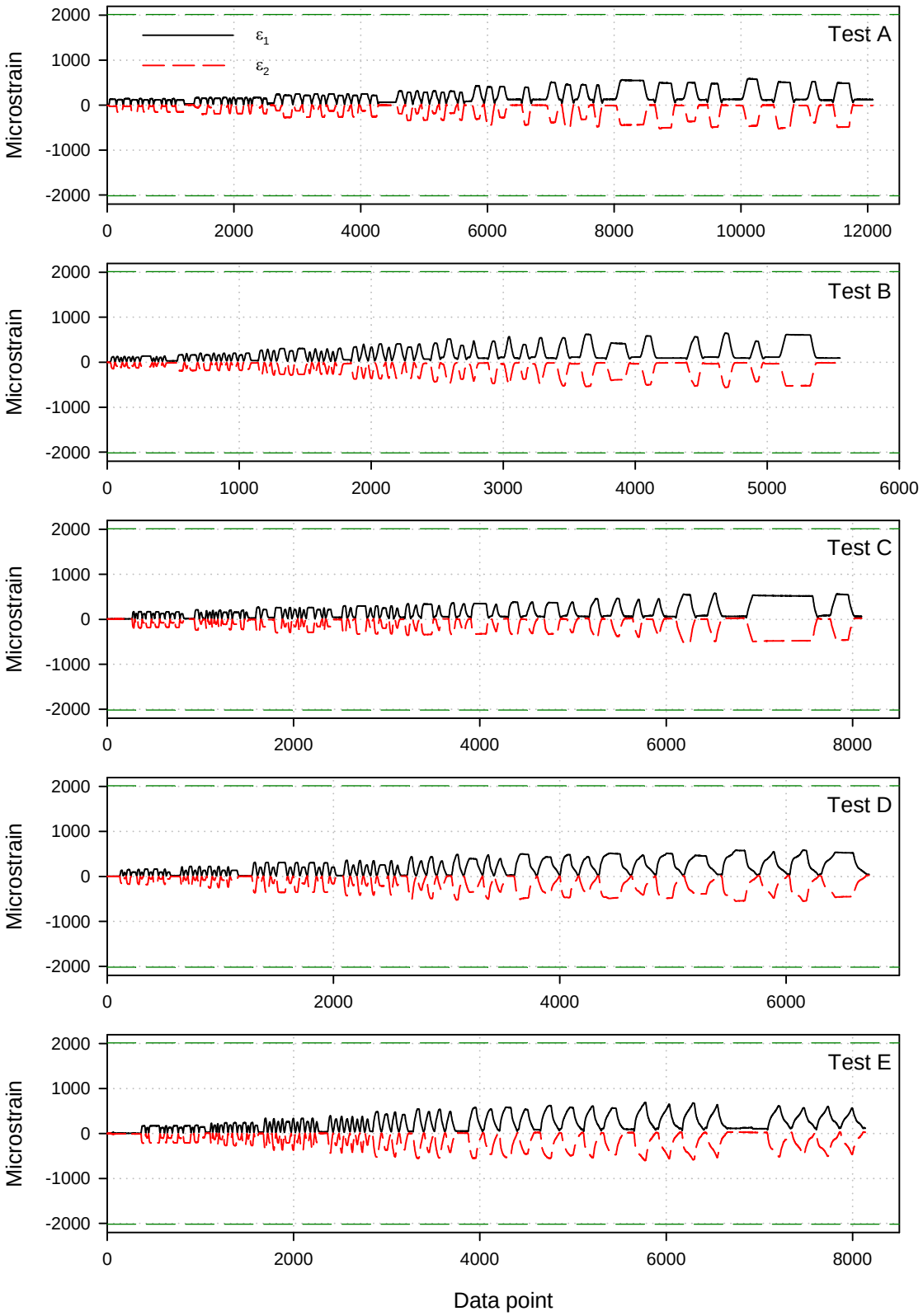

Figure D-2: Principle strain time history at center of the panel zone for each test.

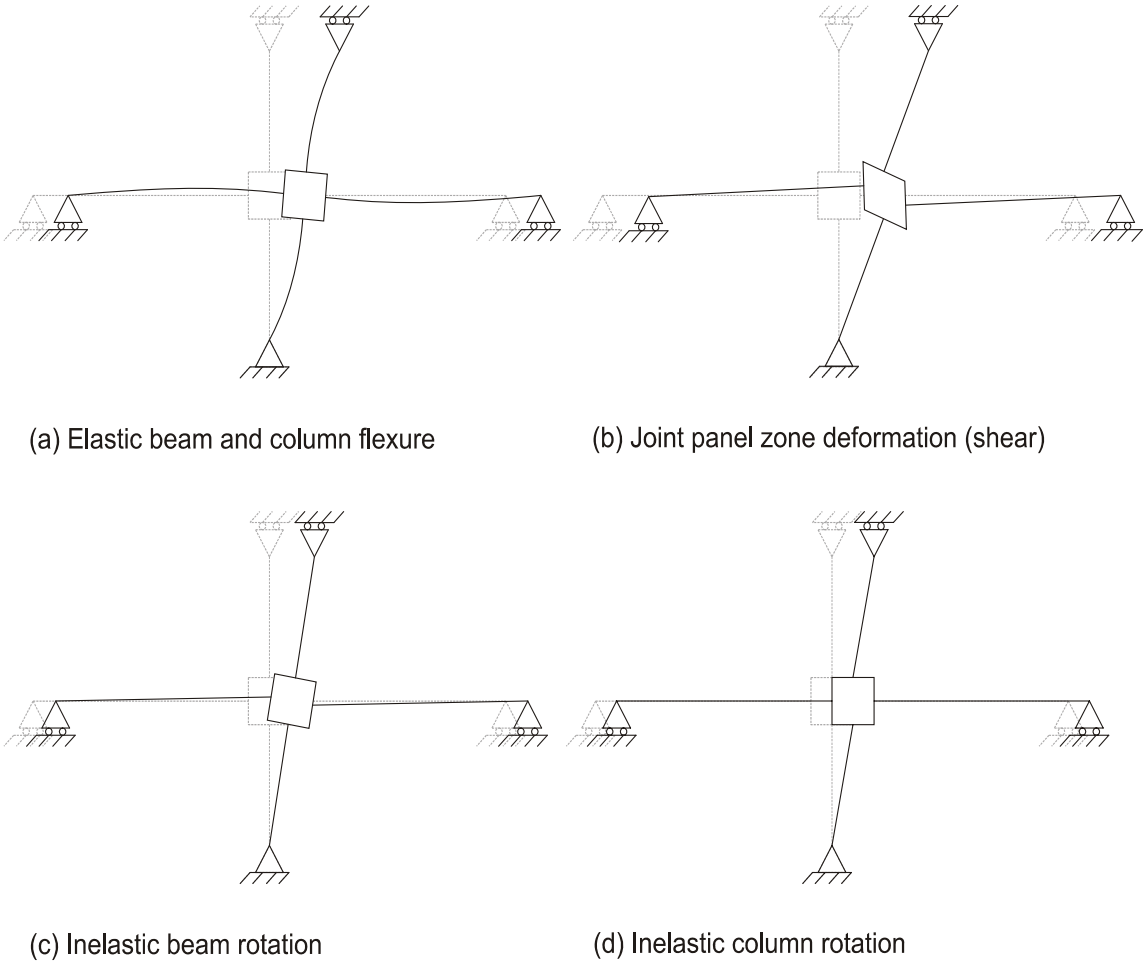

Figure D-3: Description of the drift contributions.

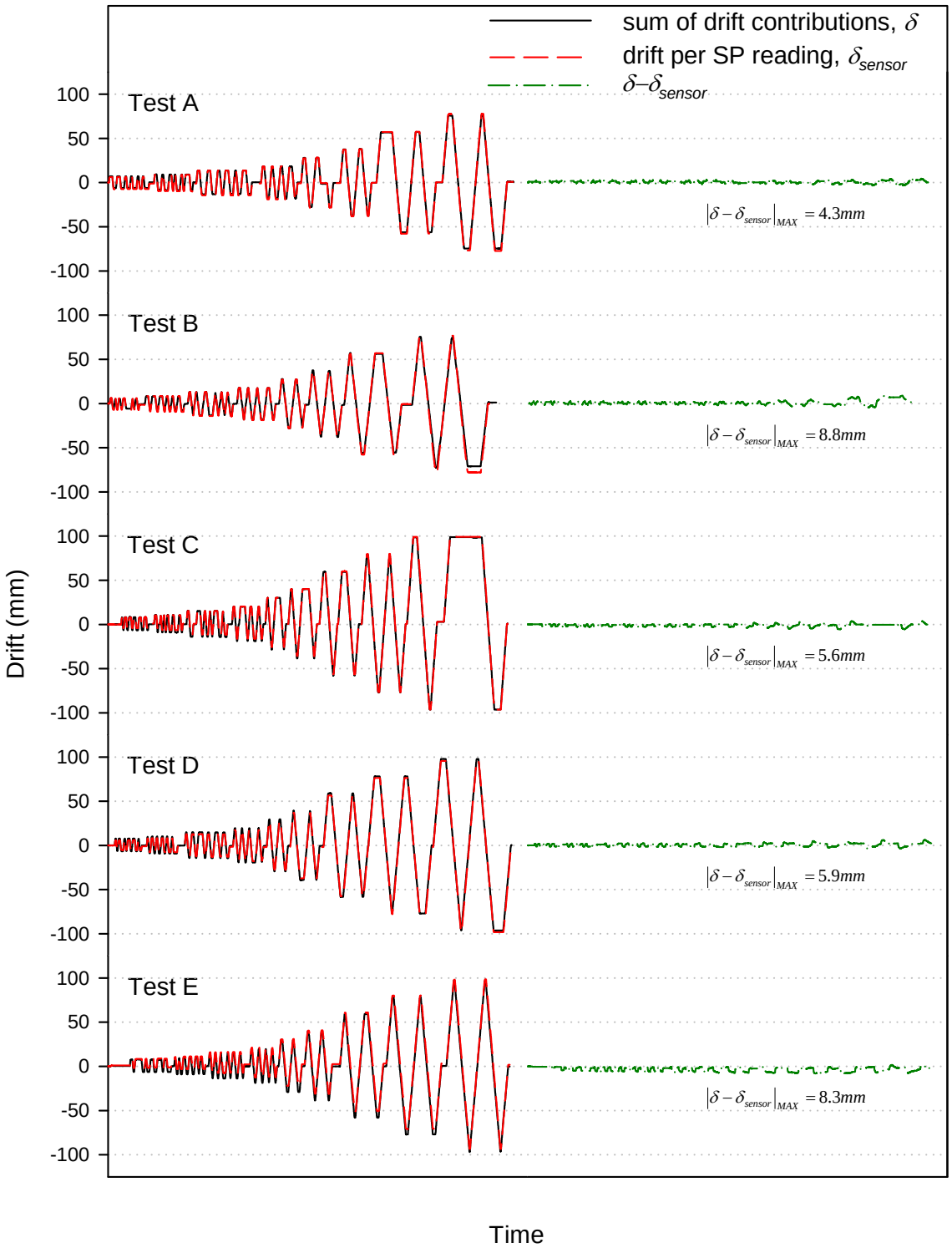

Figure D-4: Drift time histories as calculated by the (1) sum of the drift contributions, (2) the SP sensor, and (3) the difference these two values.

APPENDIX E

BEAM-COLUMN CONNECTION: DATA

E.1 TEST A

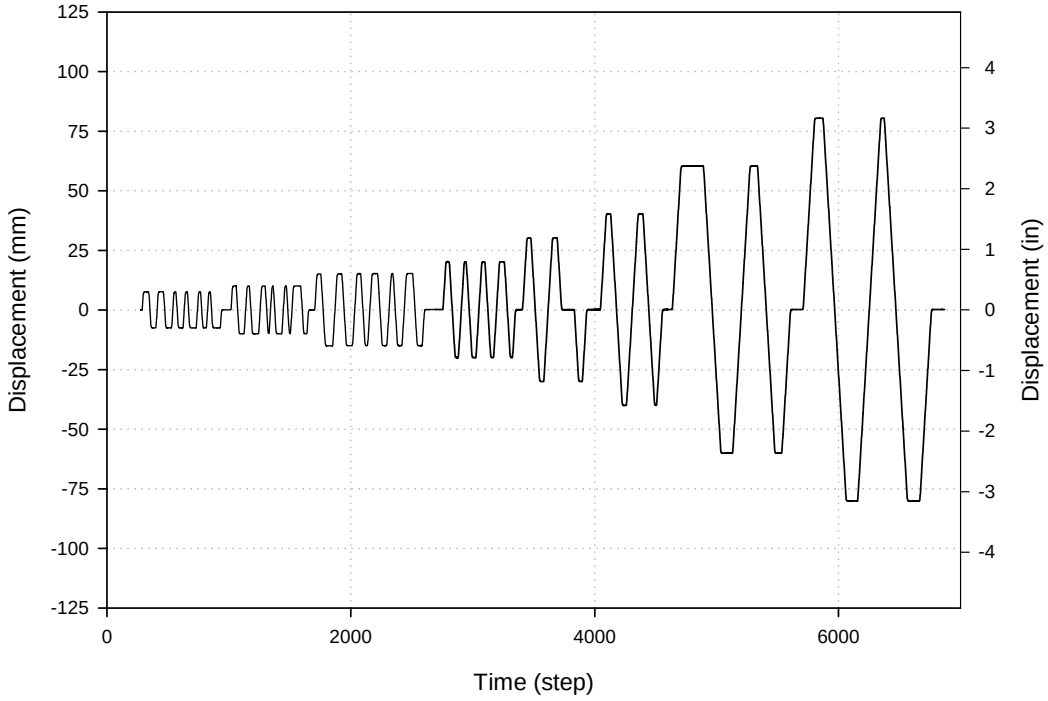

Figure E-1: Actuator displacement time history for *Test A.*

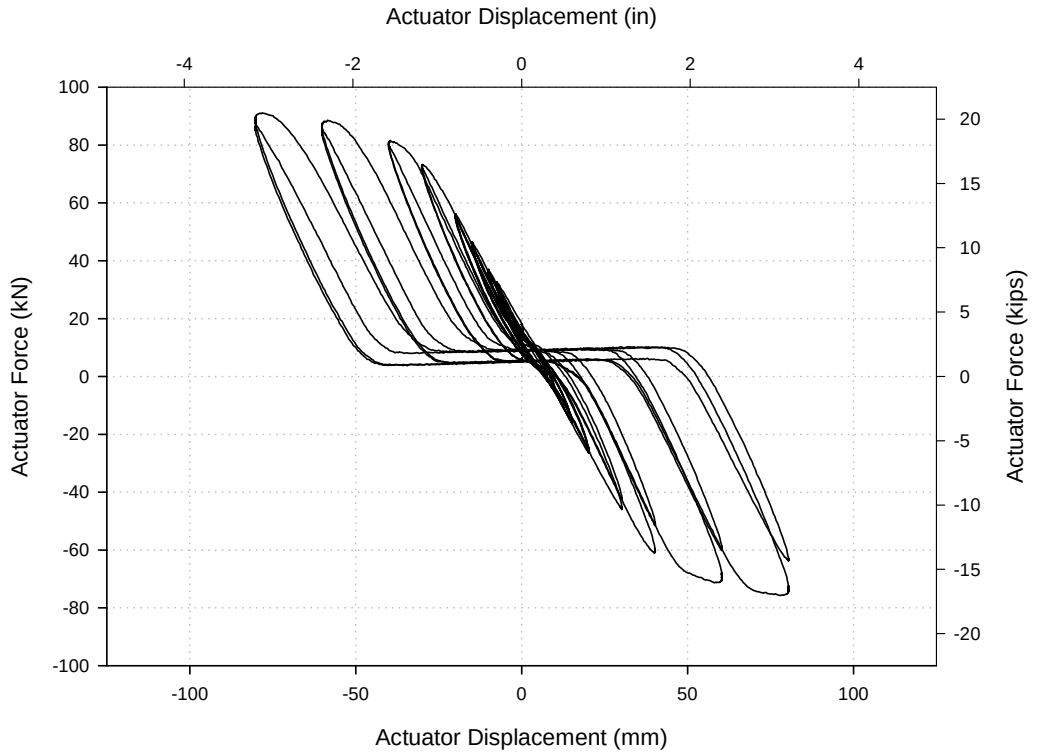

Figure E-2: Actuator force-displacement for *Test A.*

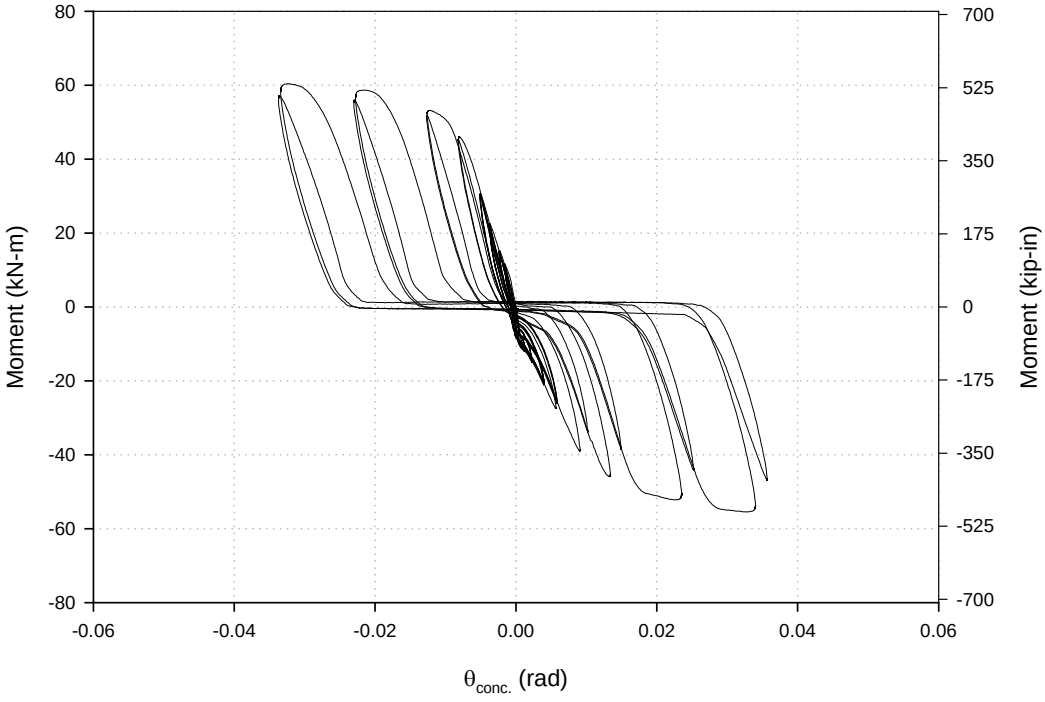

Figure E-3: M-θ at the column face of the left beam for *Test A.*

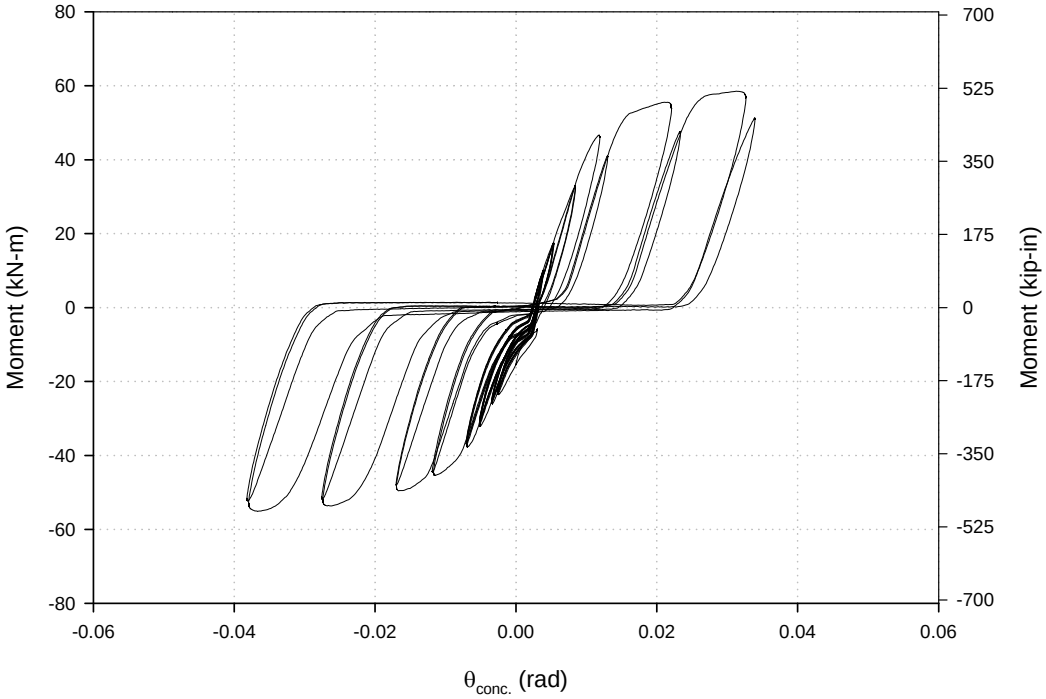

Figure E-4: M-θ at the column face of the right beam for *Test A.*

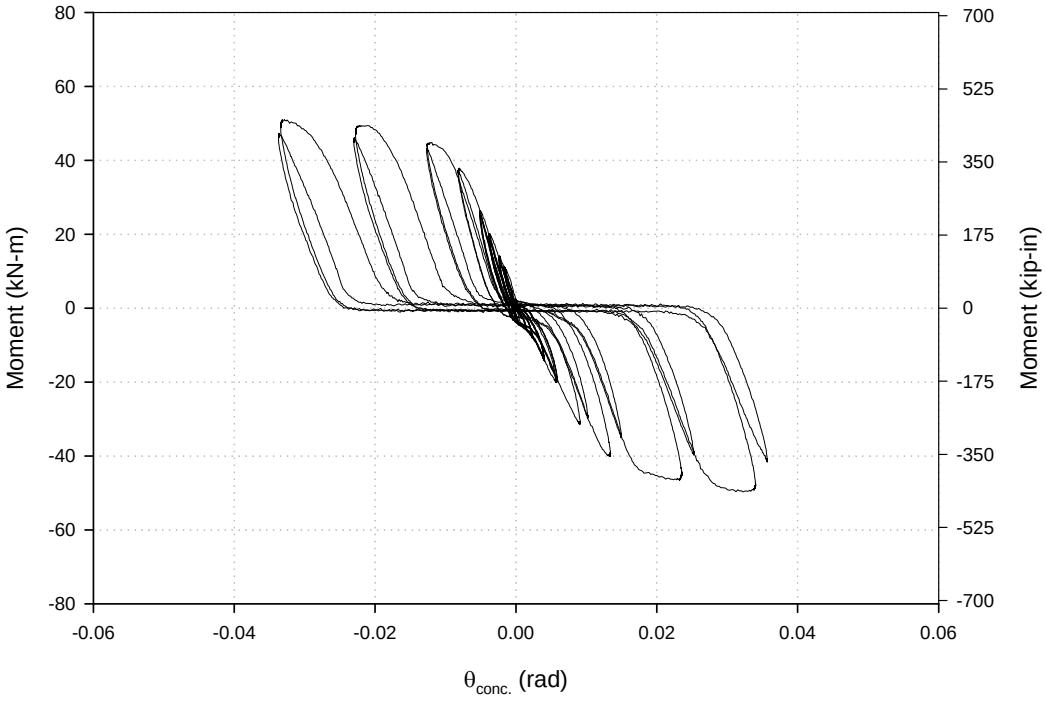

Figure E-5: M-θ at outside L-shape for column per top strain gauges for *Test A.*

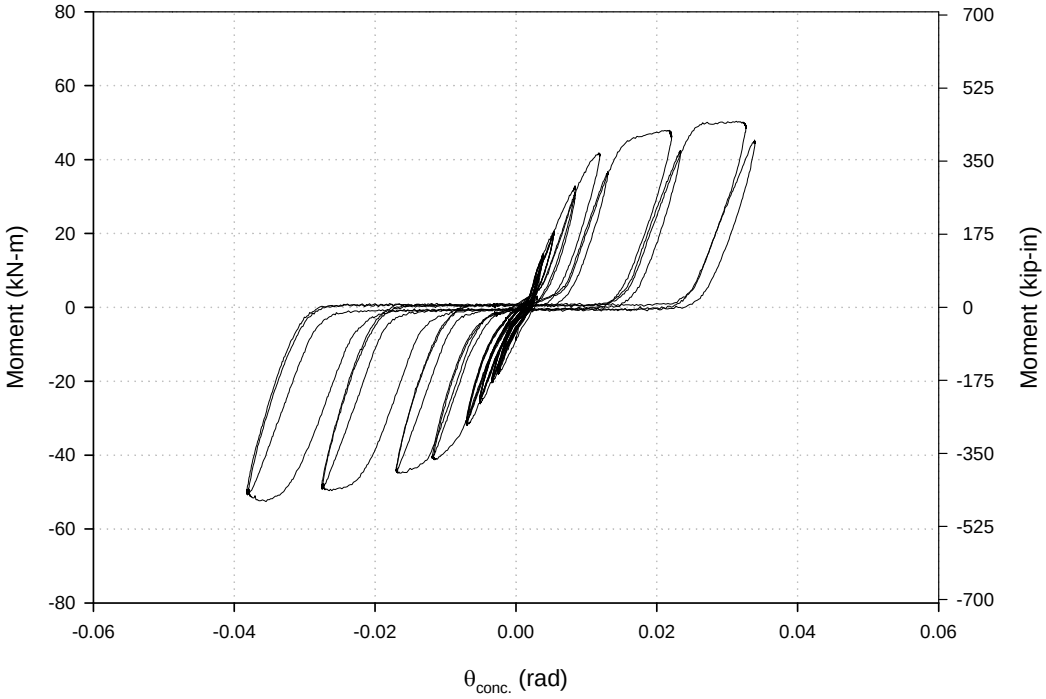

Figure E-6: M-θ at outside L-shape for column per bottom strain gauges for *Test A.*

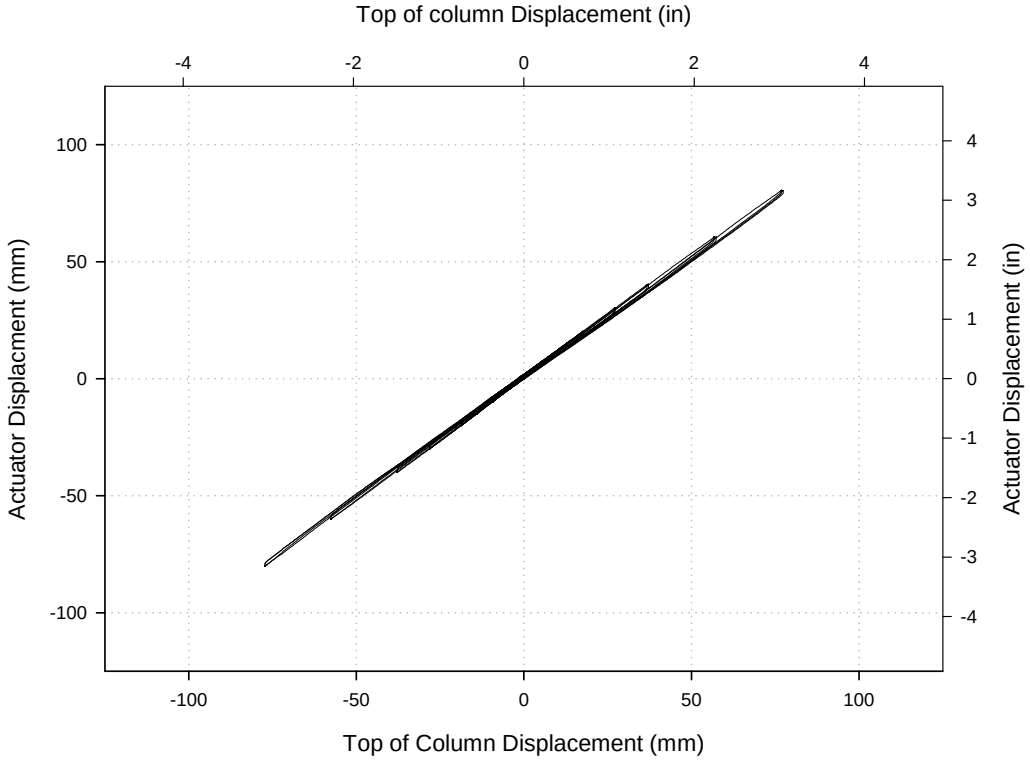

Figure E-7: Displacements at the top of the column vs. at the actuator for *Test A.*

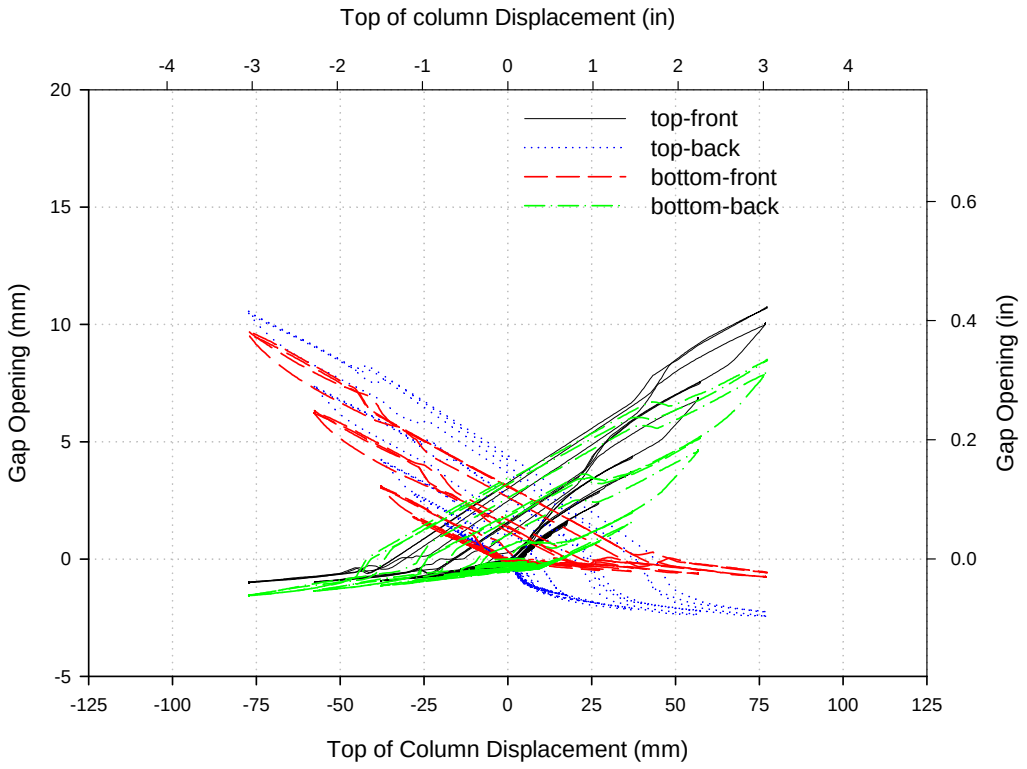

Figure E-8: Gap openings (LVDT) vs. top of column displacement for *Test A.*

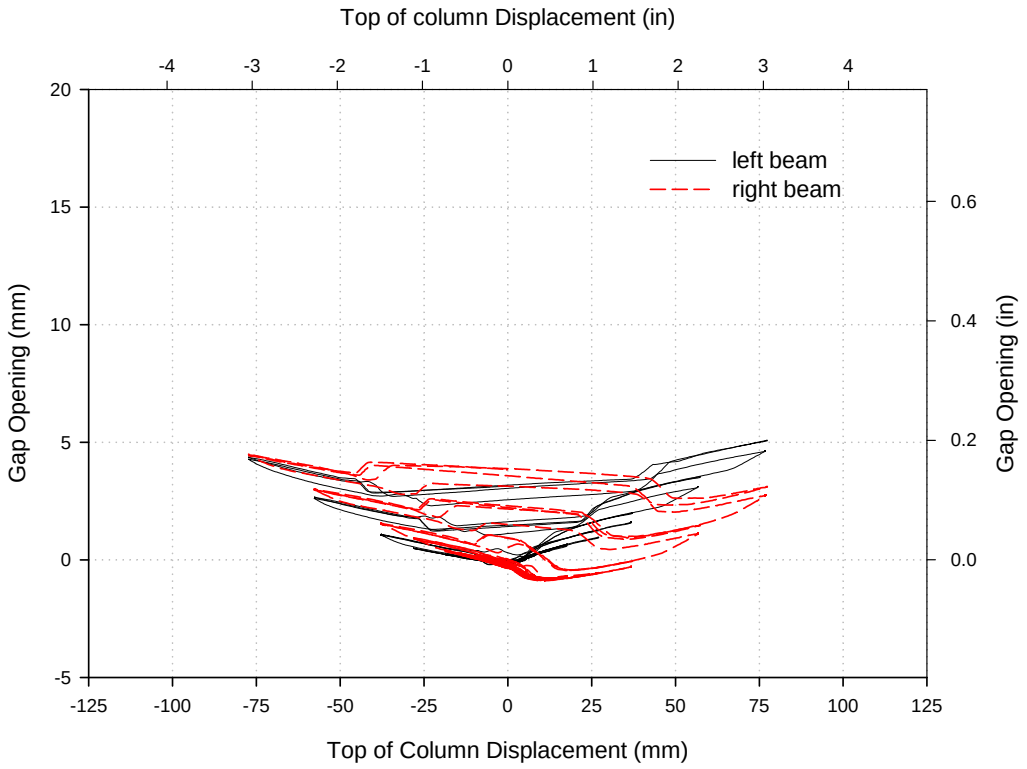

Figure E-9: Average gap opening (LVDT) vs. top of column displacement for *Test A.*

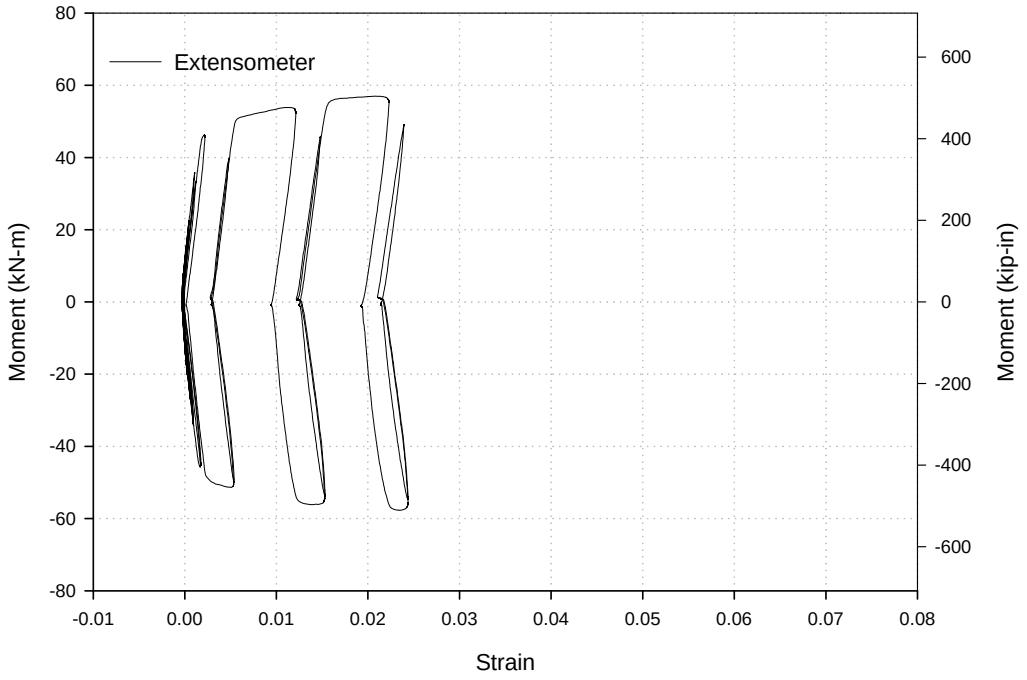

Figure E-10: Strain in the top-front tendon vs. $M_{beam,avg}$ for *Test A.*

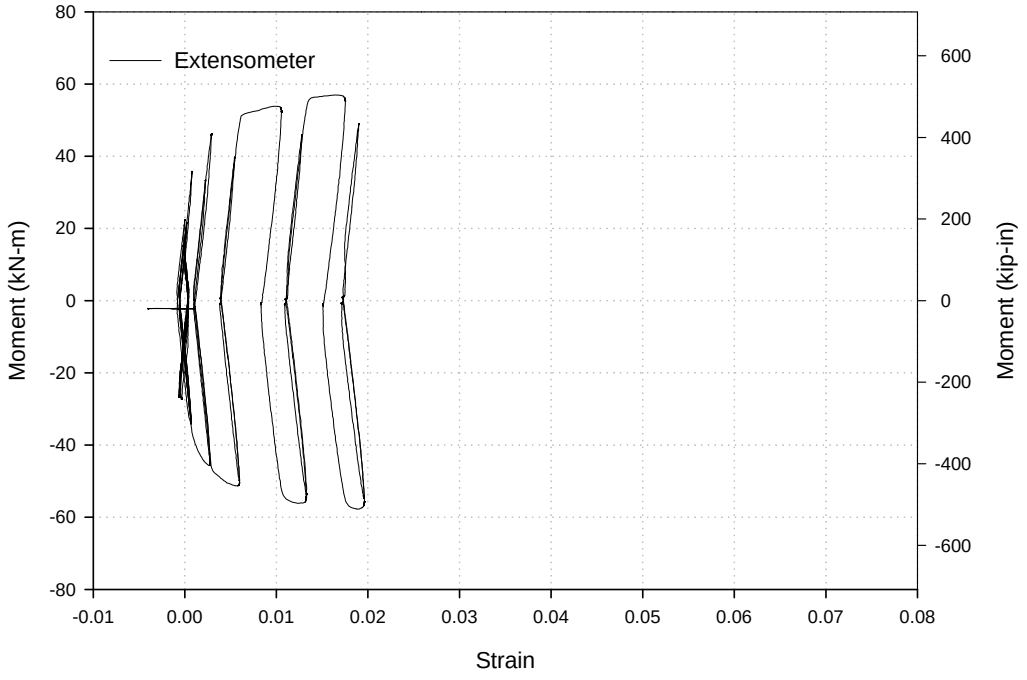

Figure E-11: Strain of the top-back tendon vs. $M_{beam,avg}$ for *Test A.*

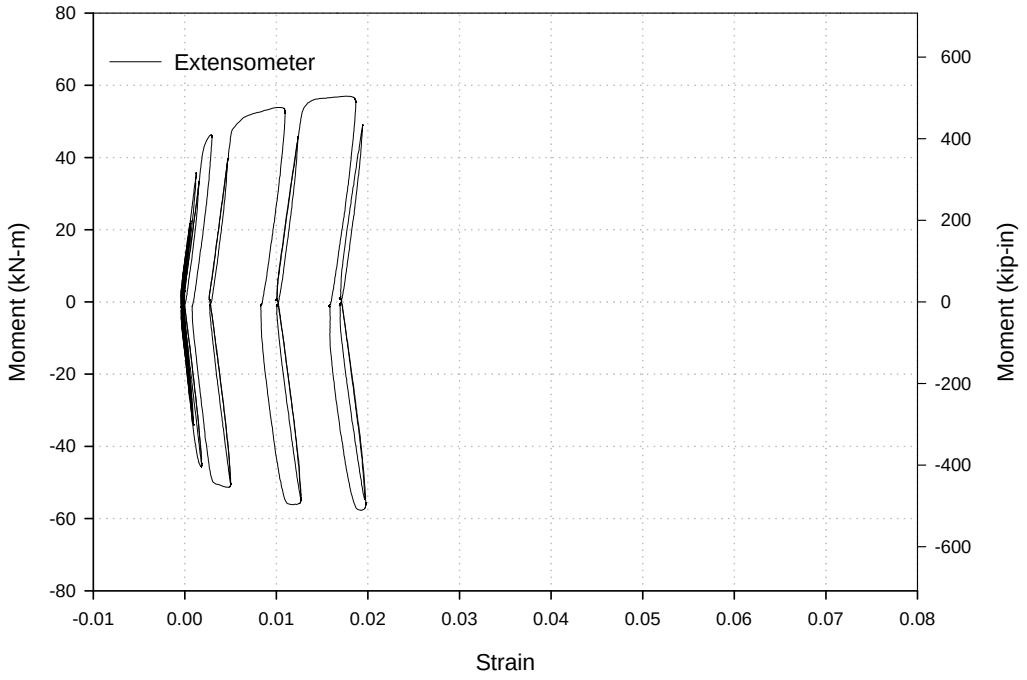

Figure E-12: Strain of the bottom-front tendon vs. $M_{beam,avg}$ for *Test A.*

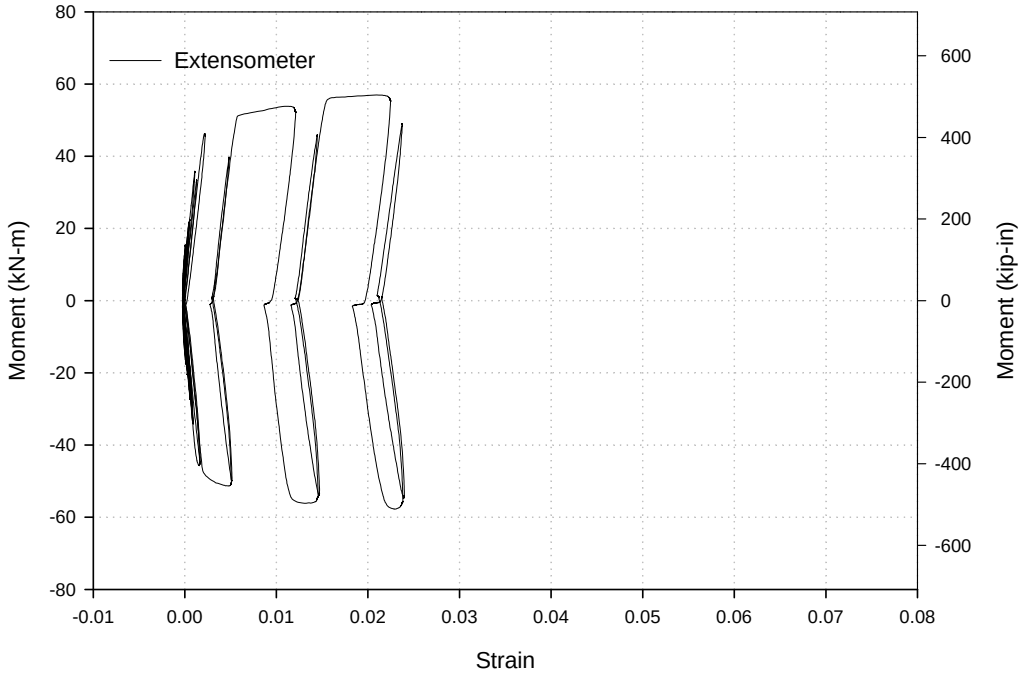

Figure E-13: Strain in the bottom-back tendon vs. $M_{beam,avg}$ for *Test A.*

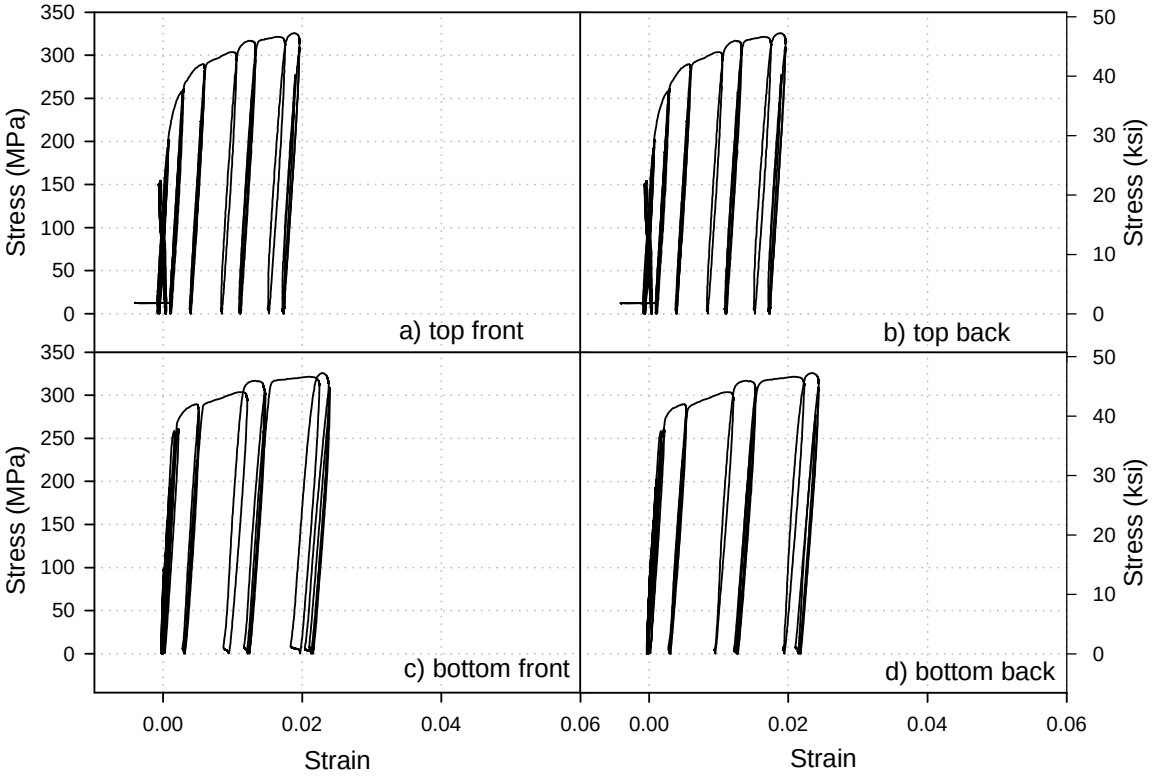

Figure E-14: Stress (assuming tensile force is transferring through the tendon, thus neglecting the shear-tab contribution) vs. strain (EXT) of each tendon element for *Test A.*

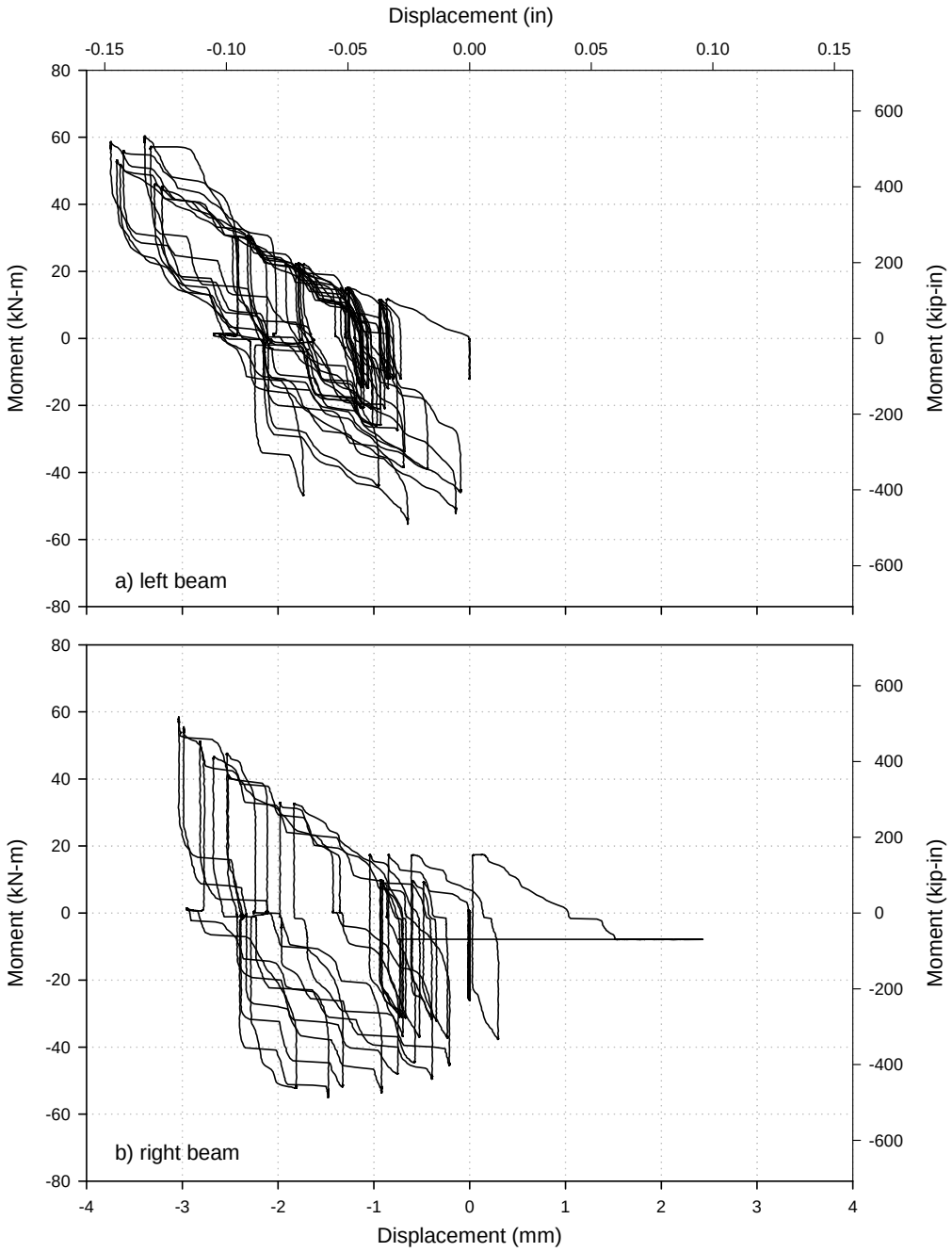

Figure E-15: Averaged moment vs. vertical beam displacement for a) left and b) right beams measured by stringpot at 137.8 cm (54.25 in.) from the outer face of the column flange for *Test A.*

E.2 TEST B

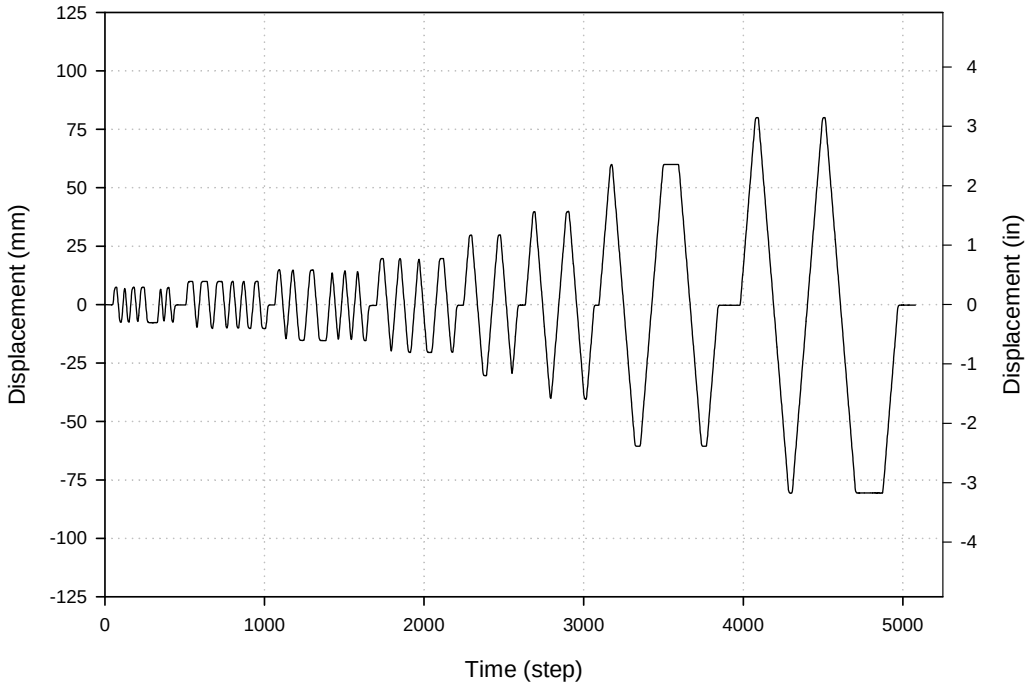

Figure E-16: Actuator displacement time history for *Test B.*

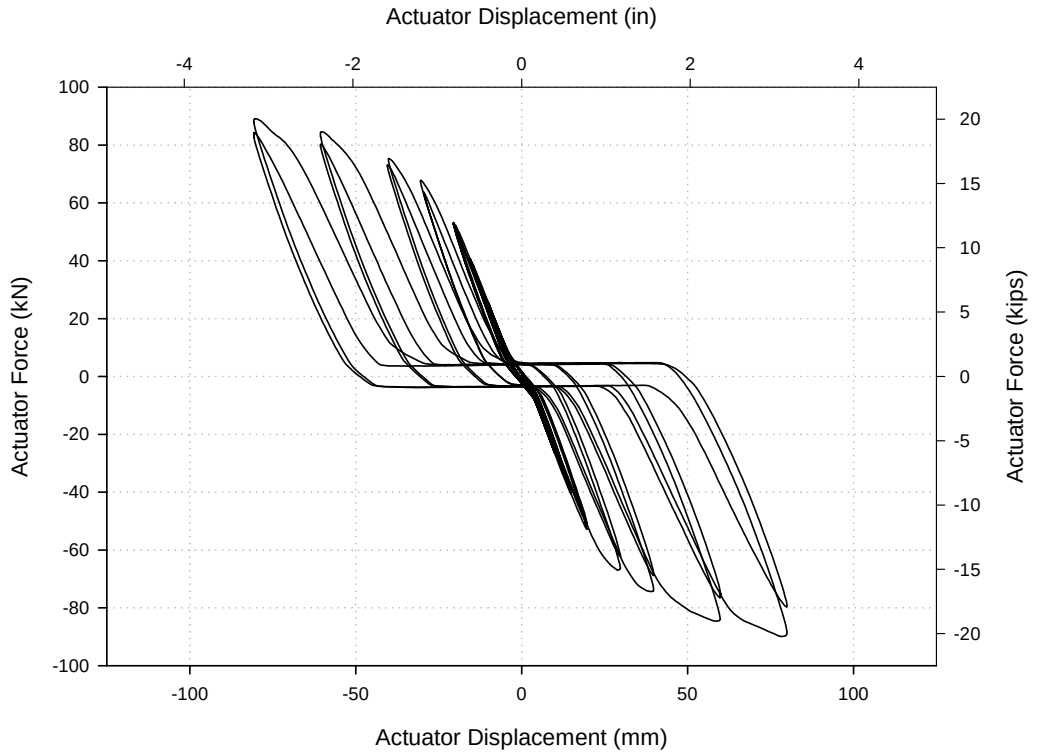

Figure E-17: Actuator force-displacement for *Test B.*

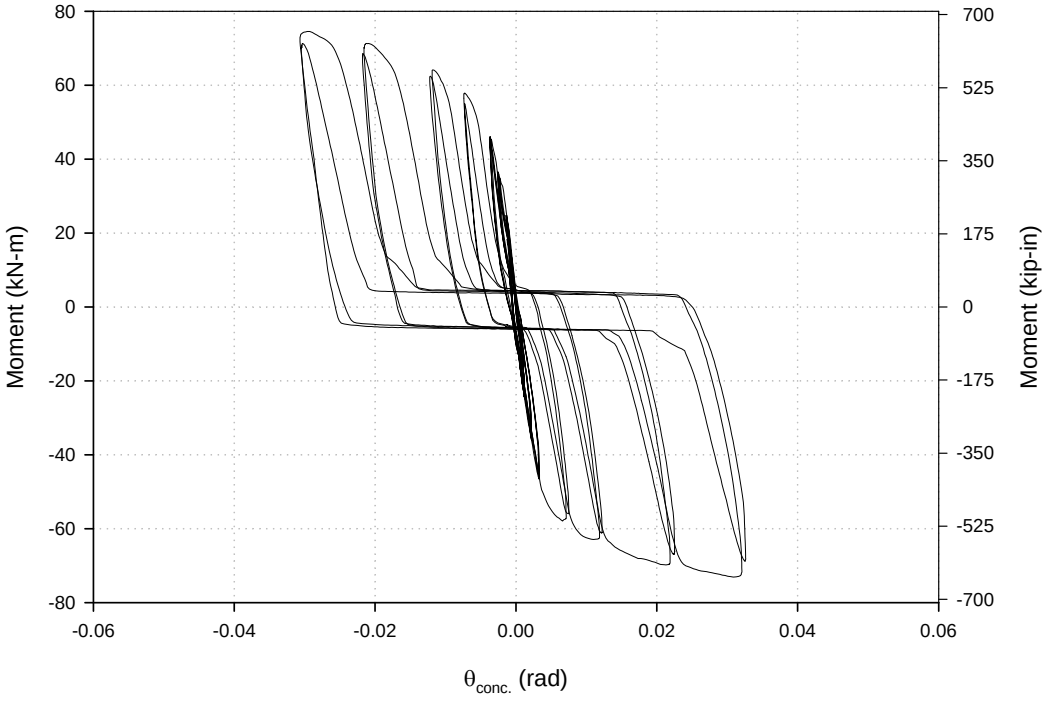

Figure E-18: M-θ at the column face of the left beam for *Test B.*

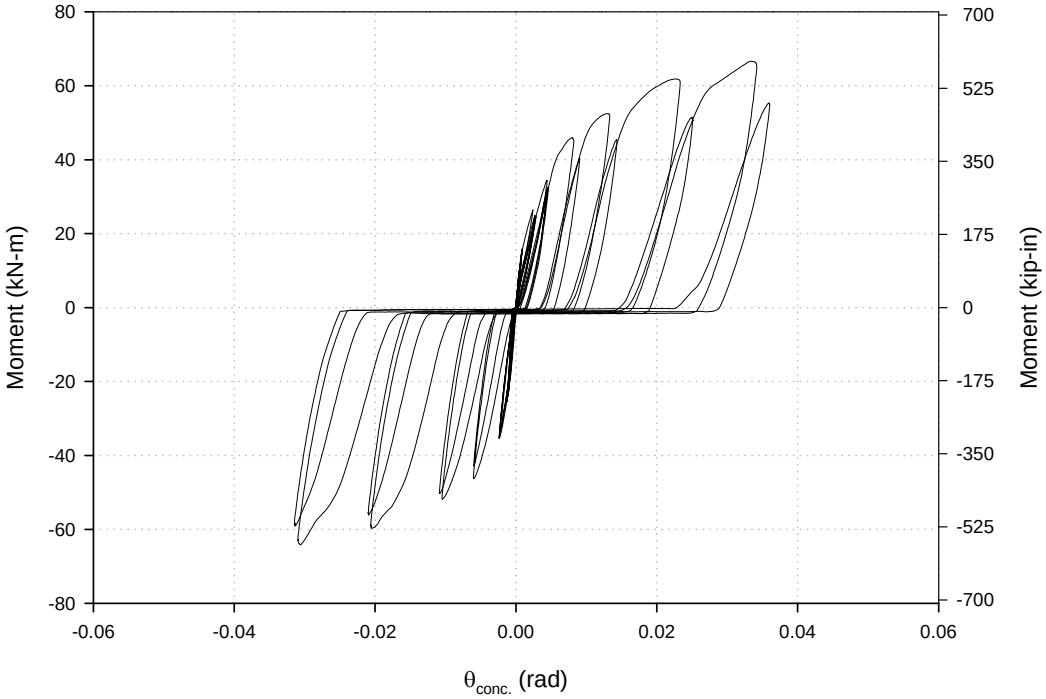

Figure E-19: M-θ at the column face of the right beam for *Test B.*

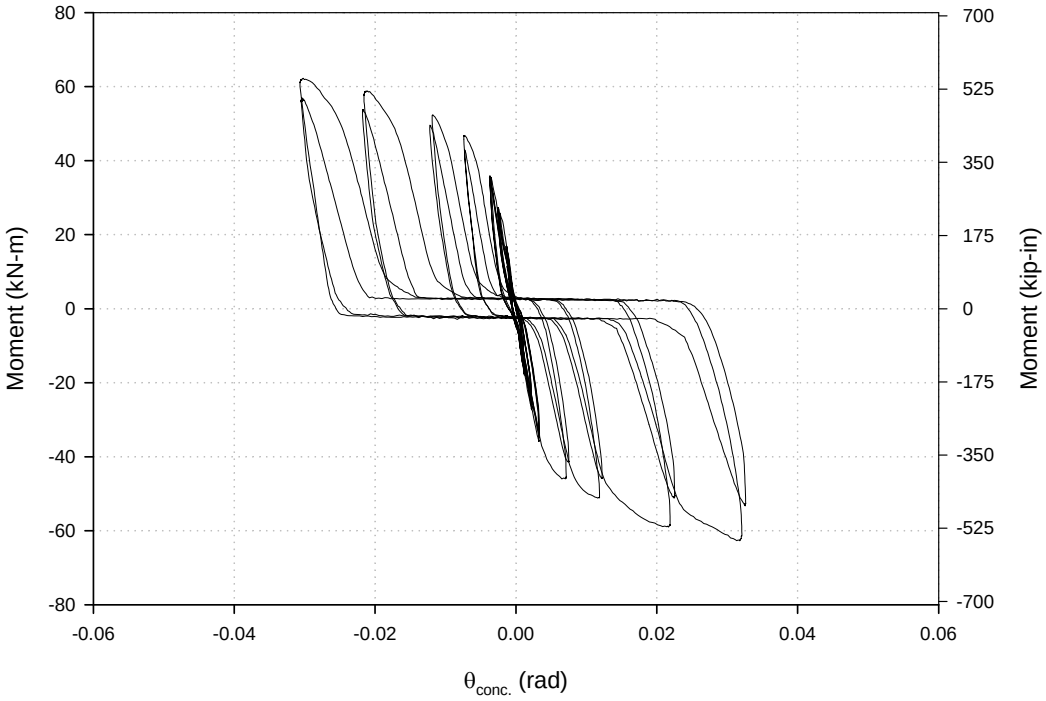

Figure E-20: M-θ at outside of the HSS for column per top strain gauges for *Test B.*

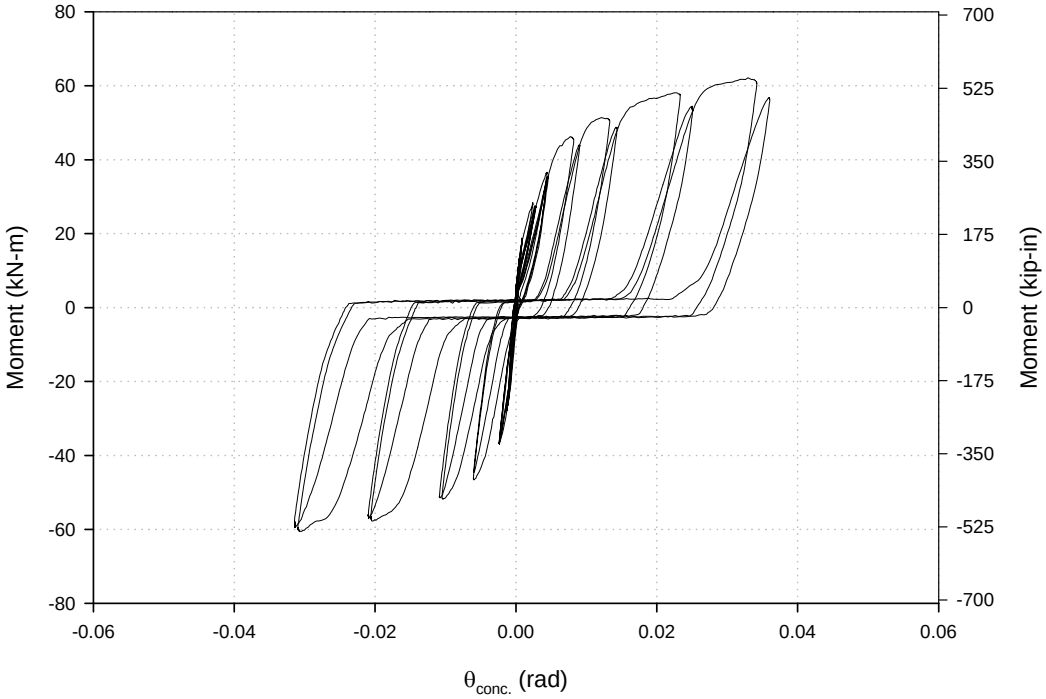

Figure E-21: M-θ at outside of the HSS for column per bottom strain gauges for *Test B.*

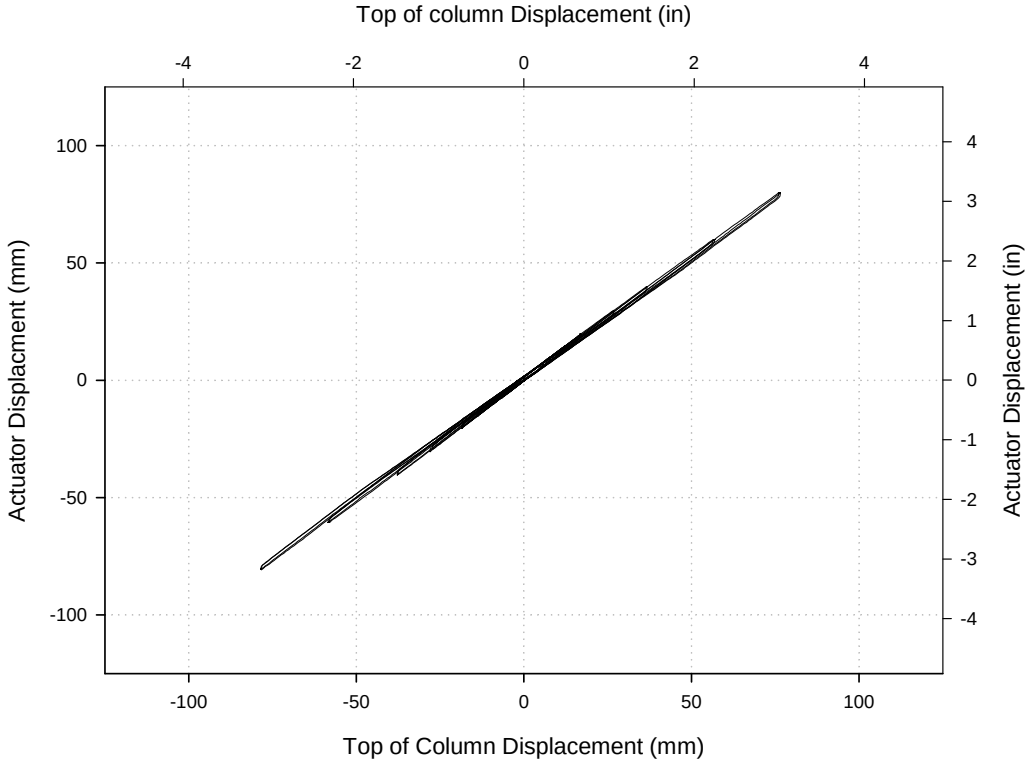

Figure E-22: Displacements at the top of the column vs. at the actuator for *Test B.*

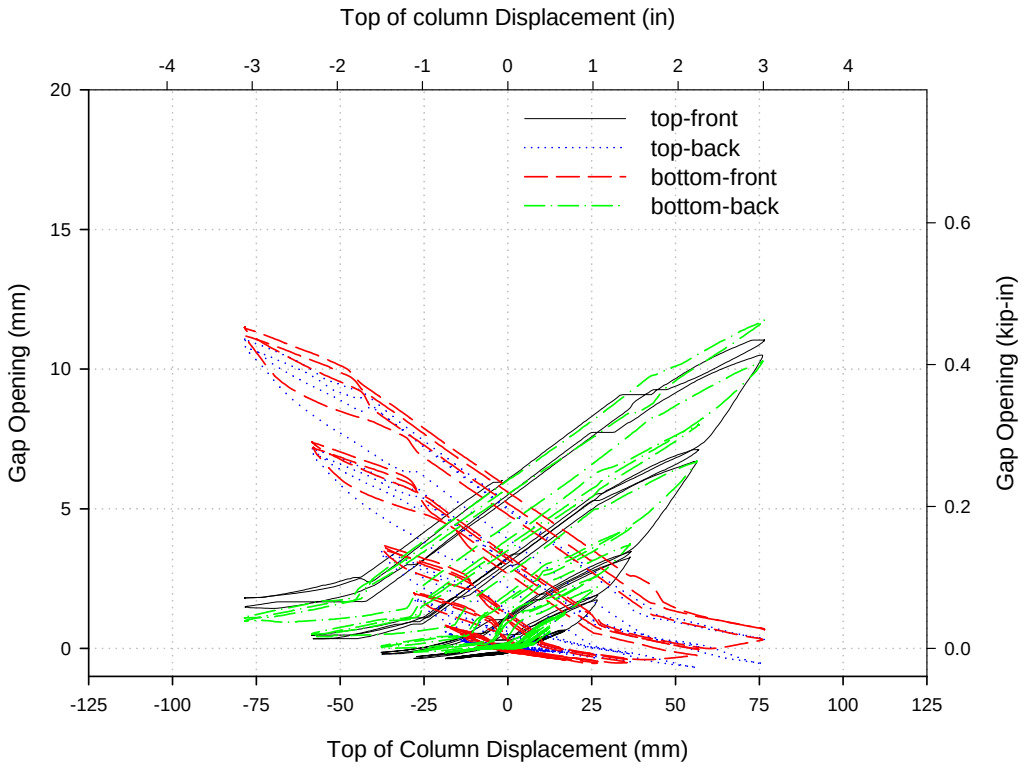

Figure E-23: Gap openings (LVDT) vs. top of column displacement for *Test B.*

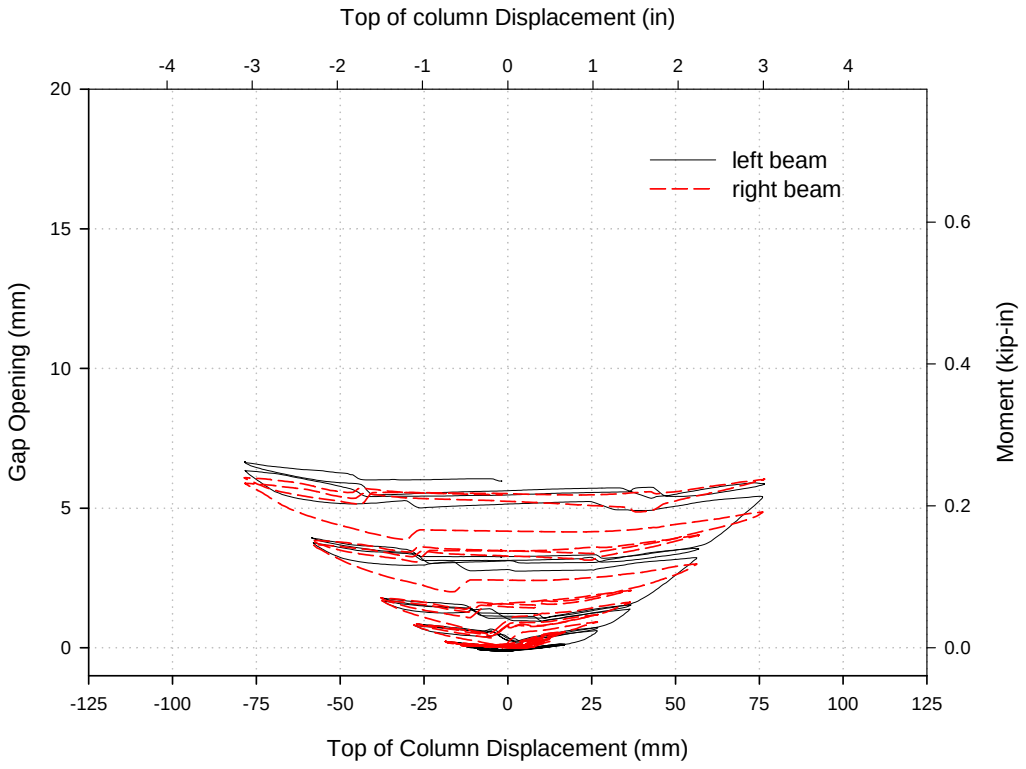

Figure E-24: Average gap opening (LVDT) vs. top of column displacement for *Test B.*

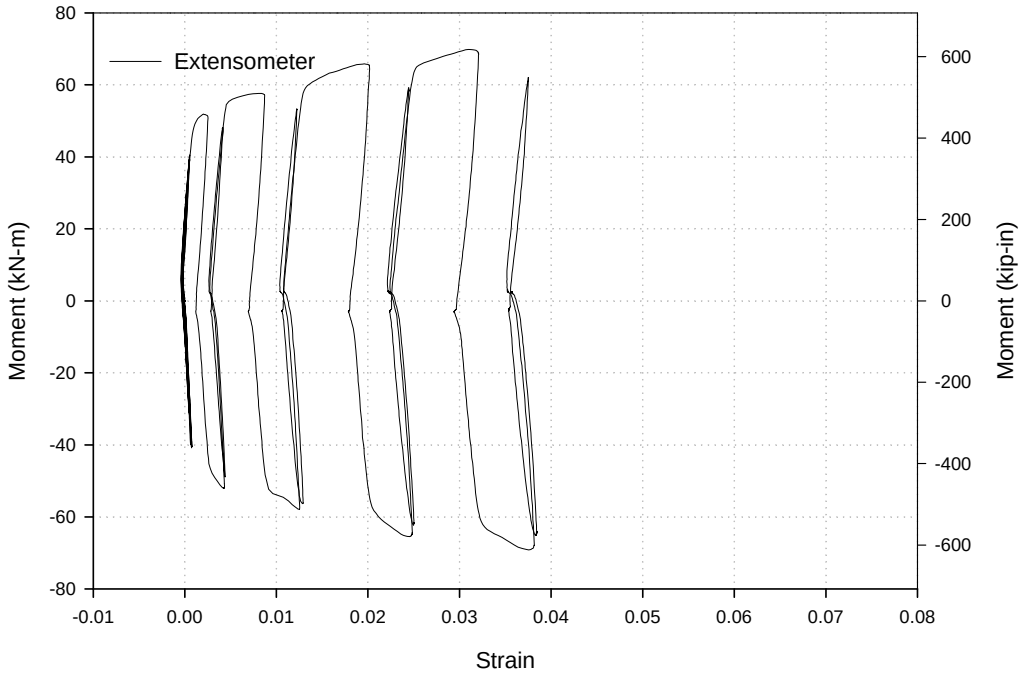

Figure E-25: Strain in the top-front tendon vs. $M_{beam,avg}$ for *Test B.*

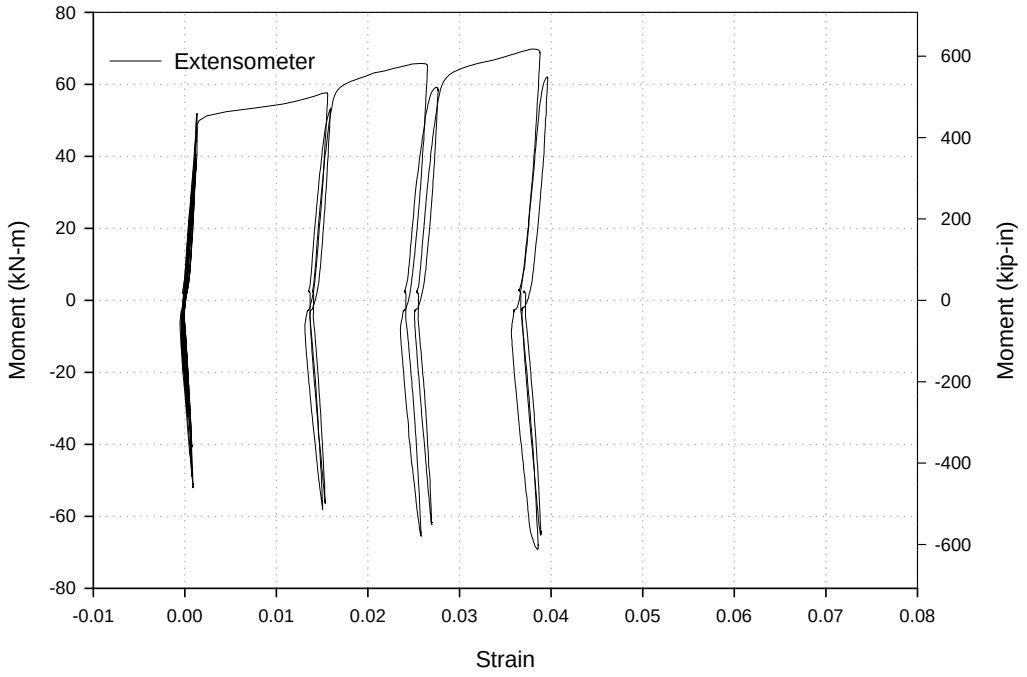

Figure E-26: Strain in the top-back tendon vs. $M_{beam,avg}$ for *Test B.*

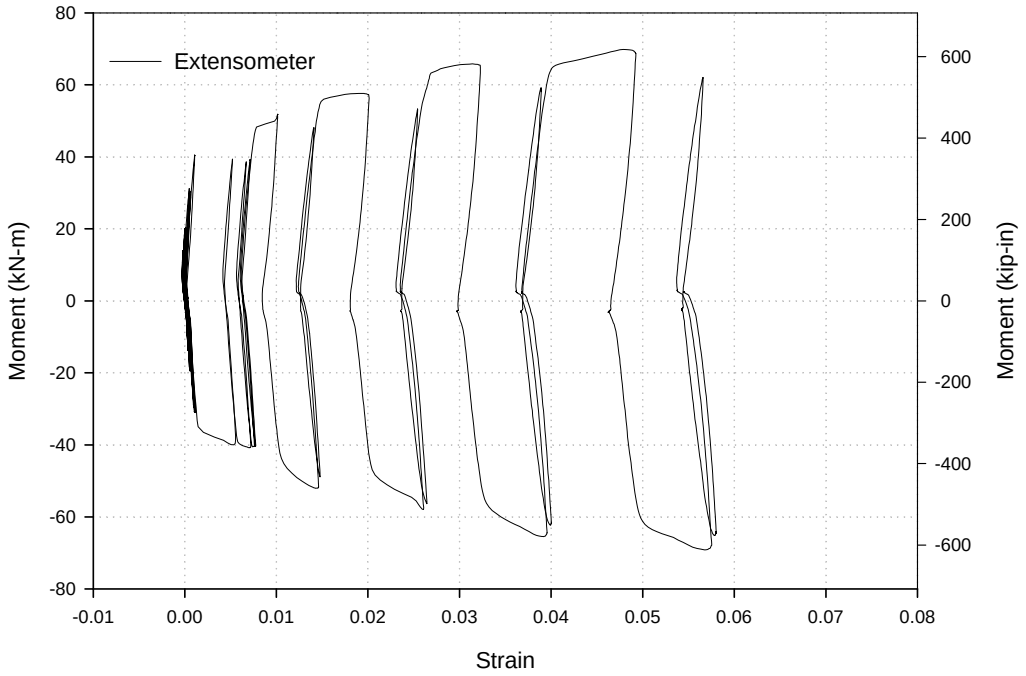

Figure E-27: Strain in the bottom-front tendon vs. $M_{beam,avg}$ for *Test B.*

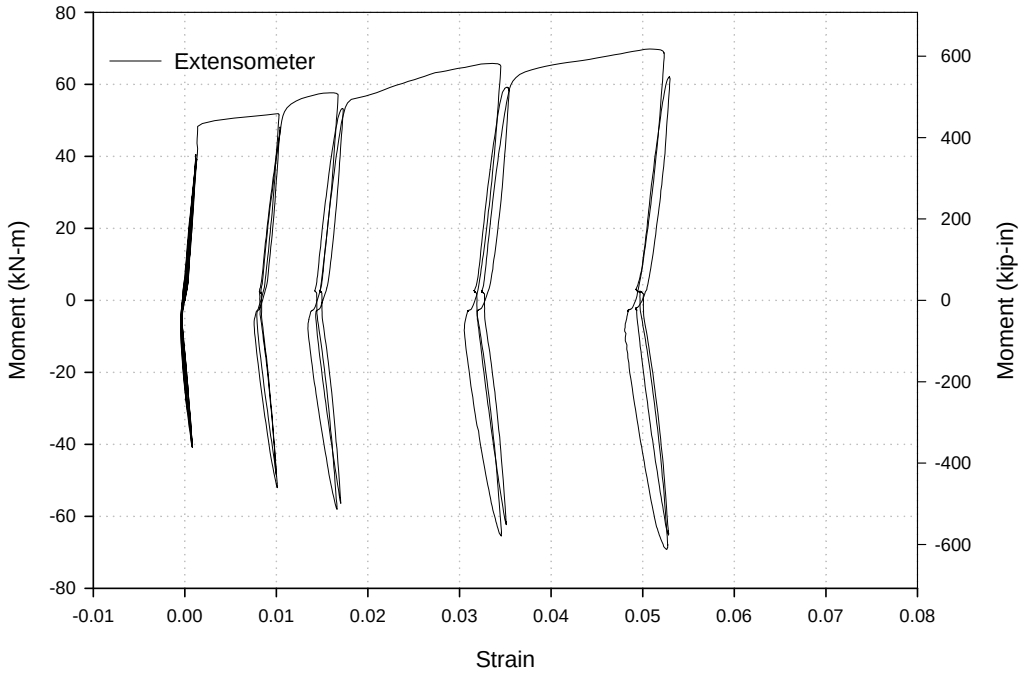

Figure E-28: Strain in the bottom-back tendon vs. $M_{beam,avg}$ for *Test B.*

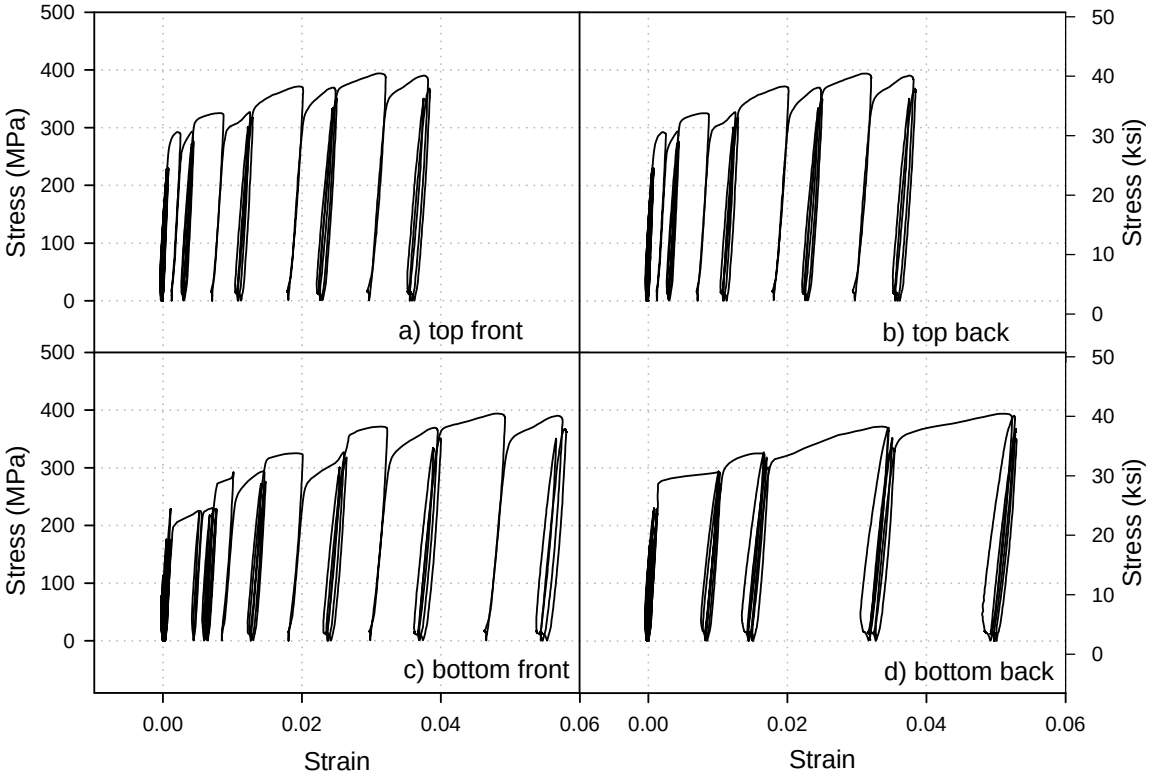

Figure E-29: Stress (assuming tensile force is transferring through the tendon, thus neglecting the shear-tab contribution) vs. strain (EXT) of each tendon element for *Test B.*

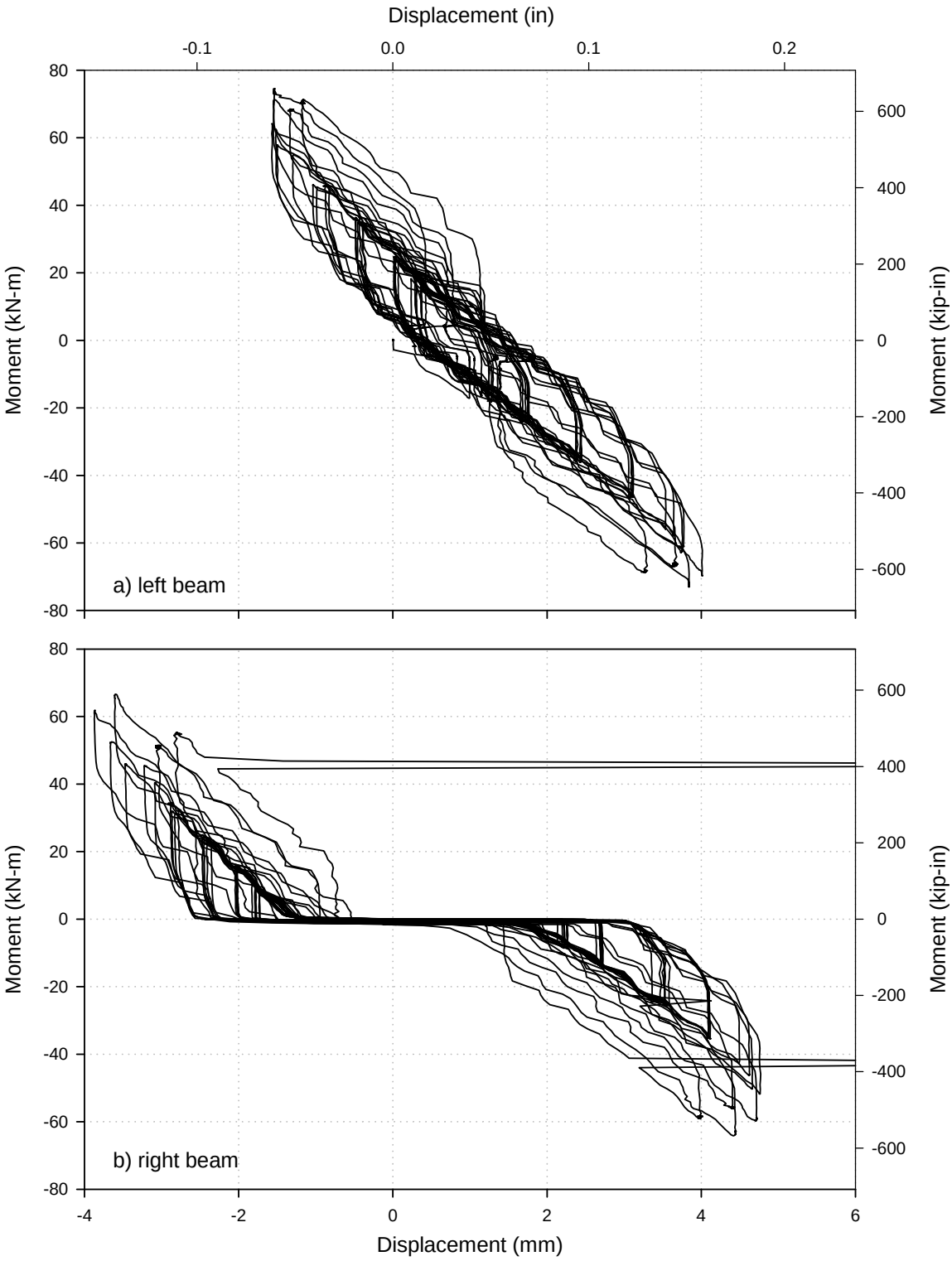

Figure E-30: Averaged moment vs. vertical beam displacement for a) left and b) right beams measured by stringpot at 137.8 cm (54.25 in.) from the outer face of the column flange for *Test B.*

E.3 TEST C

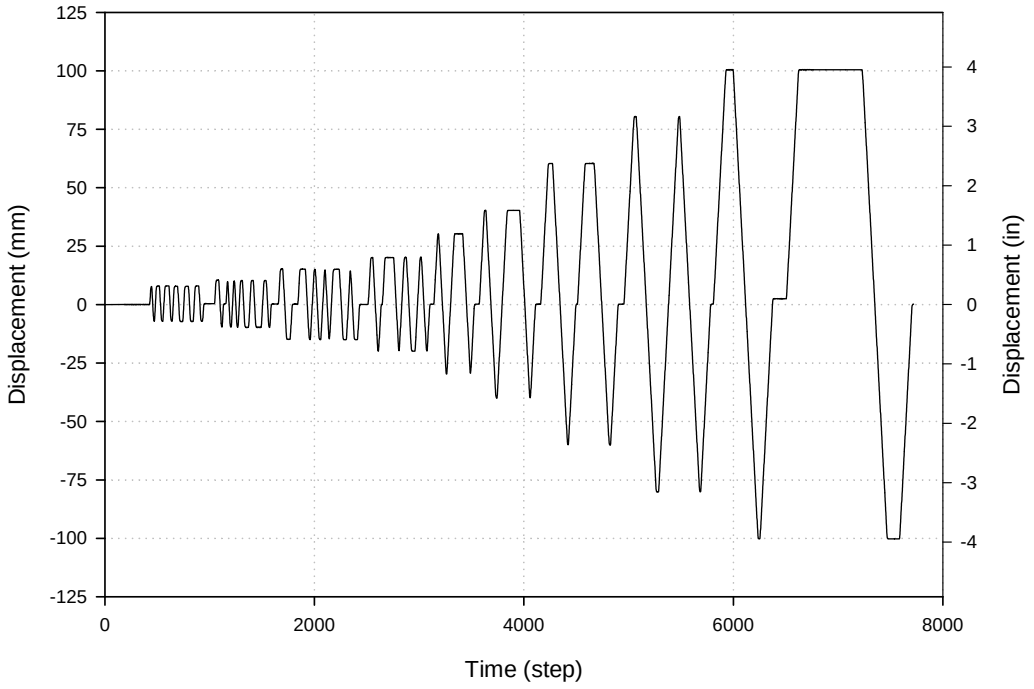

Figure E-31: Actuator displacement time history for *Test C.*

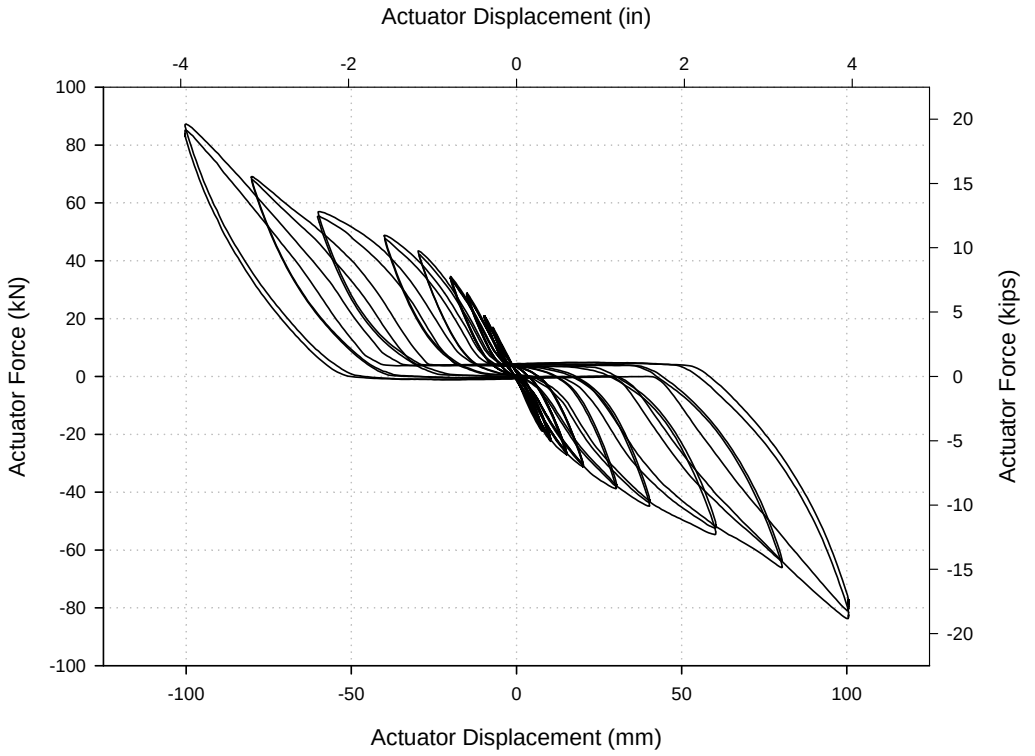

Figure E-32: Actuator force-displacement for *Test C.*

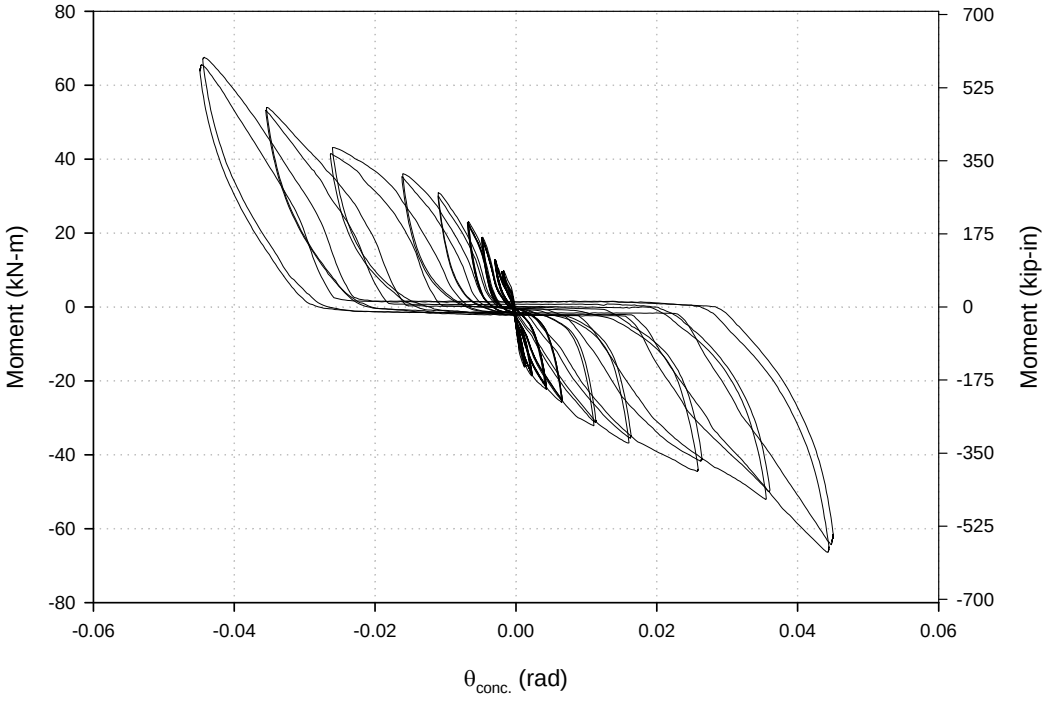

Figure E-33: M-θ at the column face of the left beam for *Test C.*

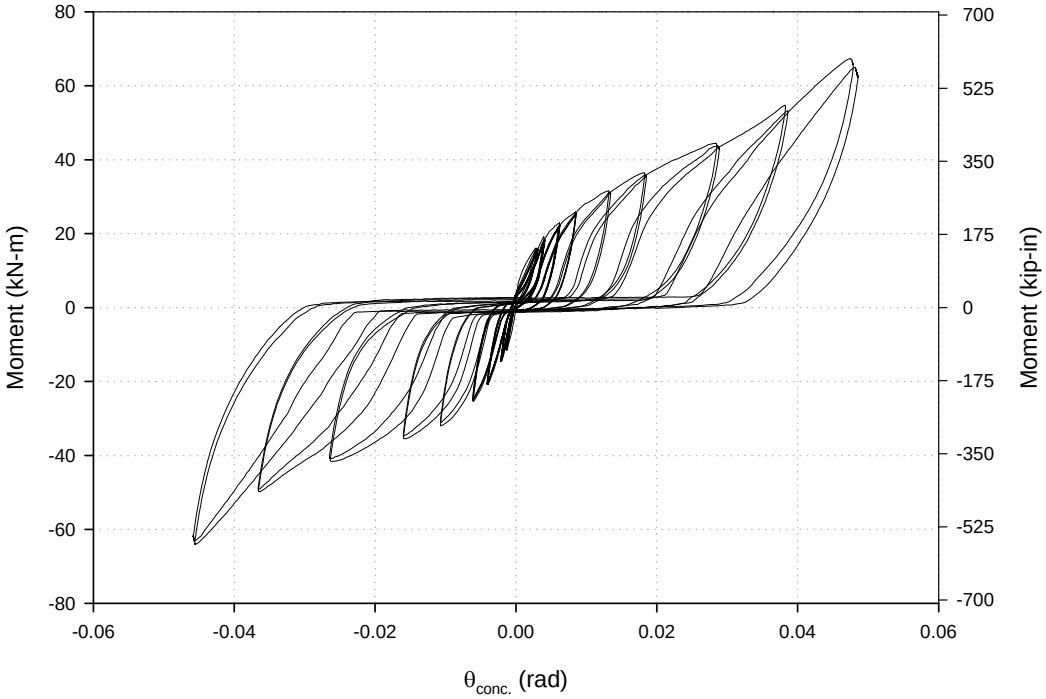

Figure E-34: M-θ at the column face of the right beam for *Test C.*

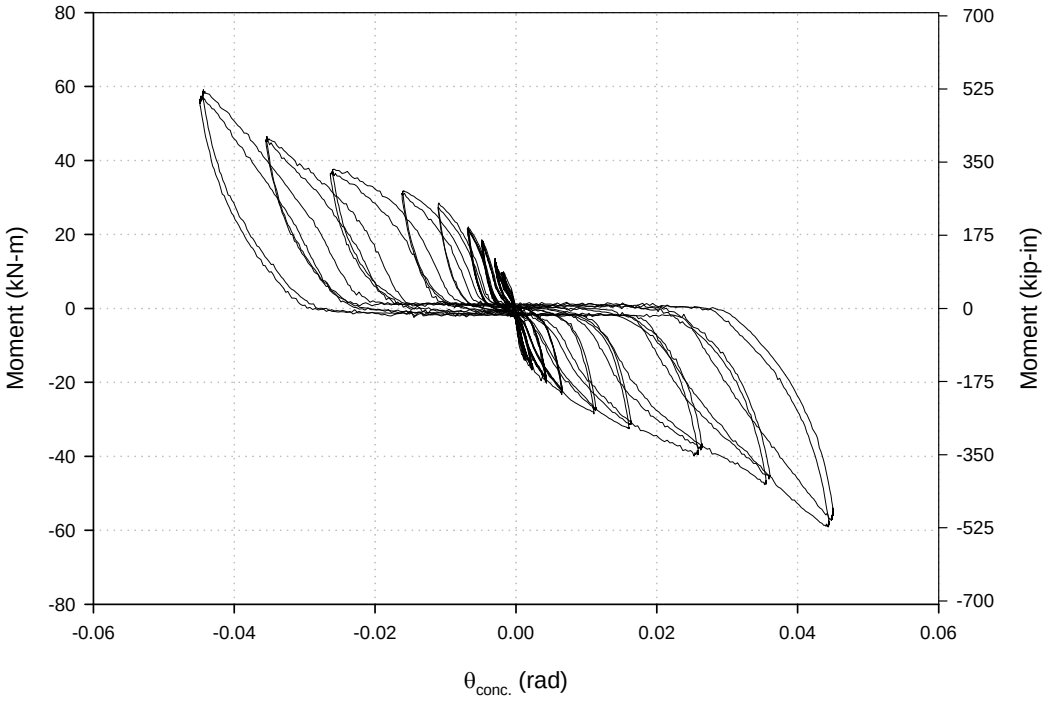

Figure E-35: M-θ at outside of the HSS for column per top strain gauges for *Test C.*

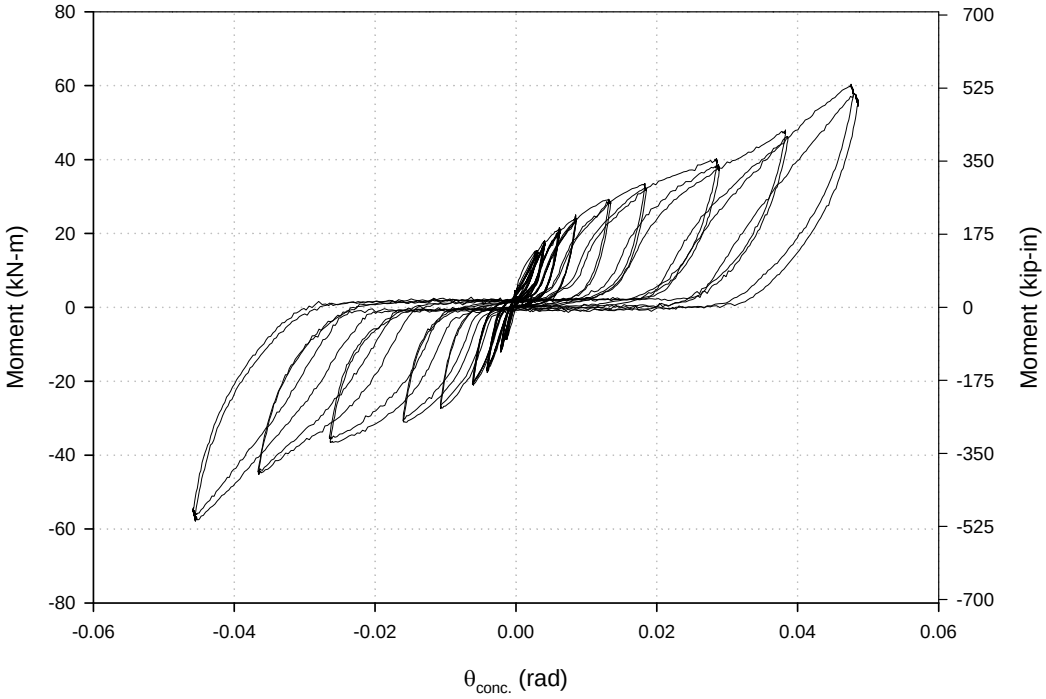

Figure E-36: M-θ at outside of the HSS for column per bottom strain gauges for *Test C.*

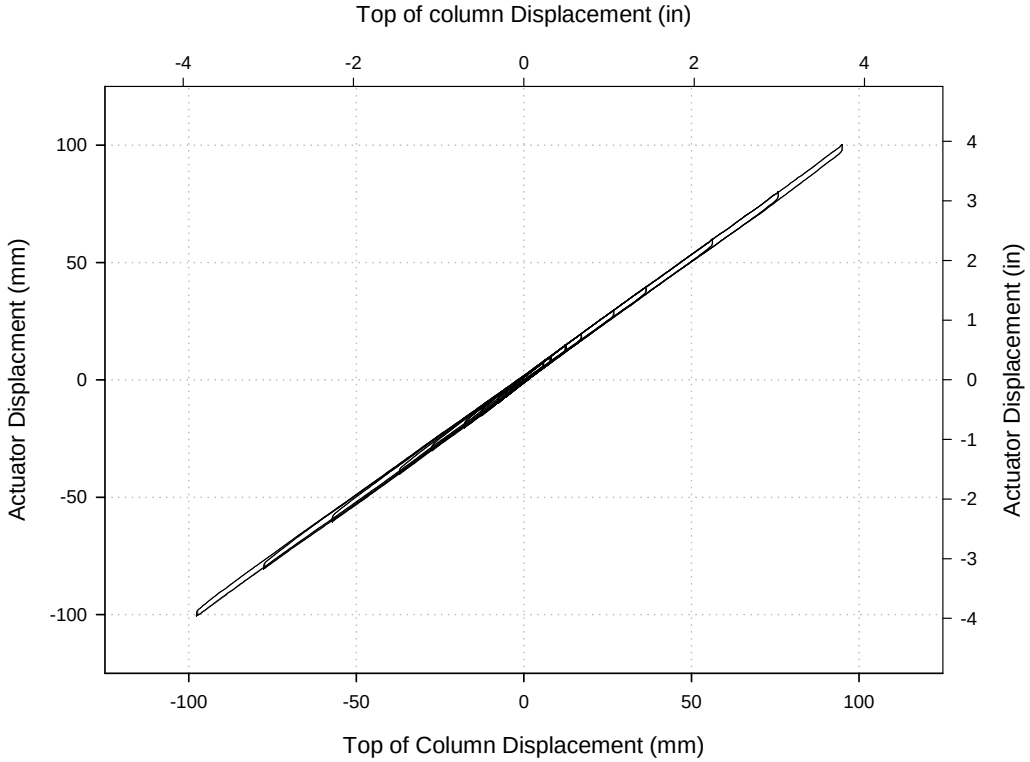

Figure E-37: Displacements at the top of the column vs. at the actuator for *Test C.*

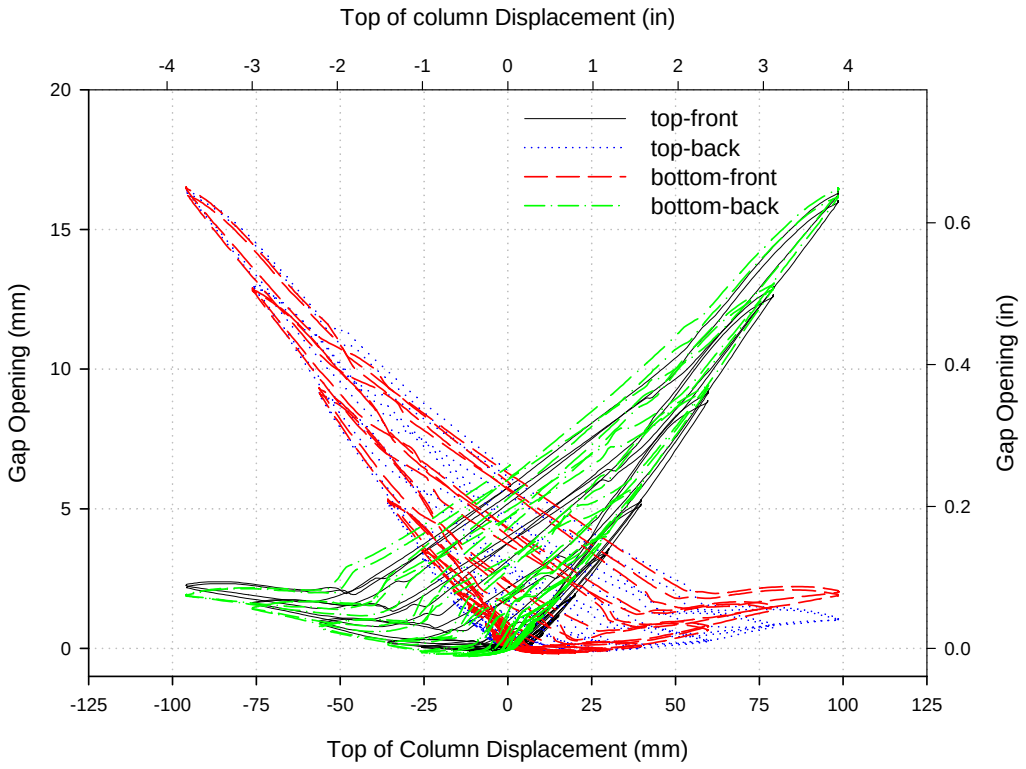

Figure E-38: Gap openings (LVDT) vs. top of column displacement for *Test C*

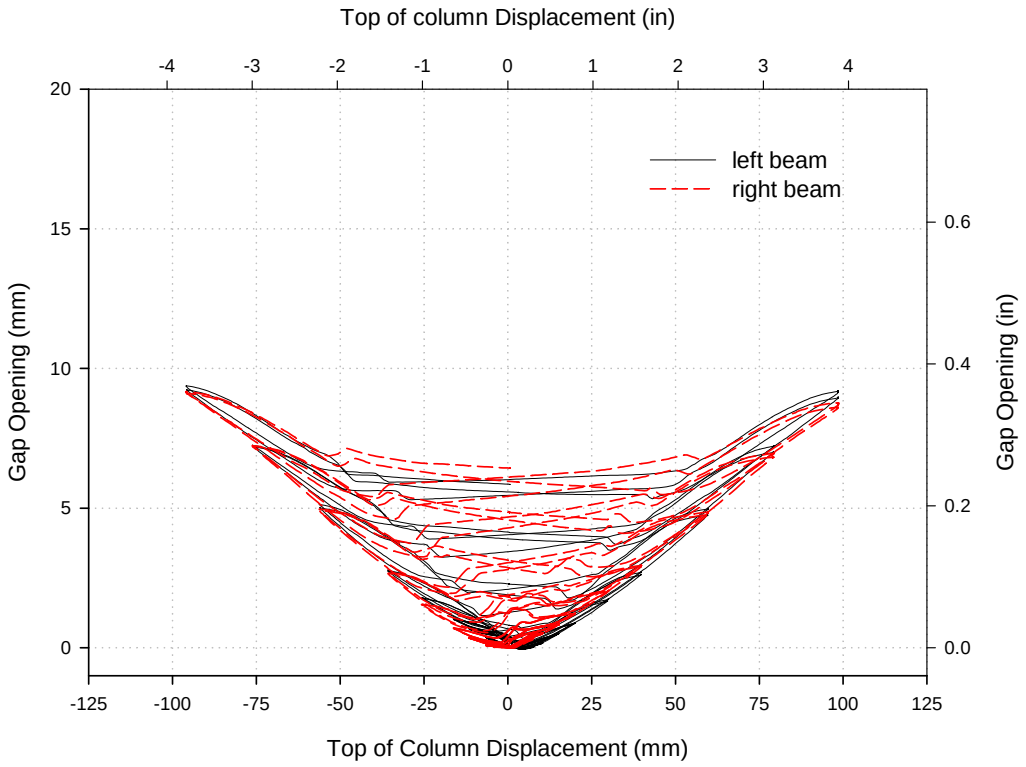

Figure E-39: Average gap opening (LVDT) vs. top of column displacement for *Test C*

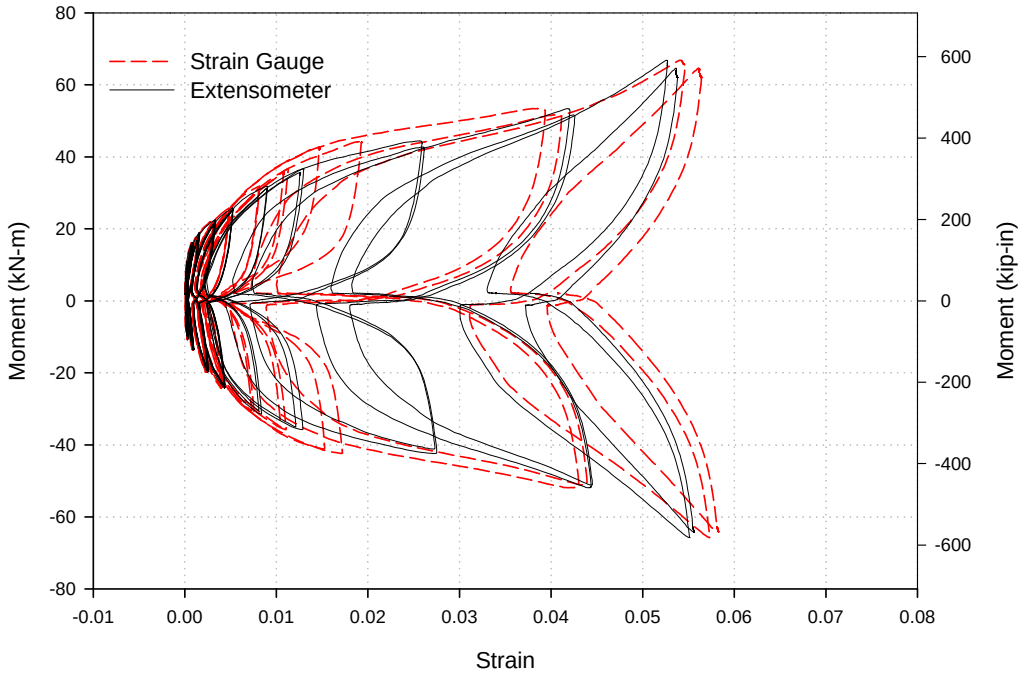

Figure E-40: Strain in the top-front tendon vs. $M_{beam,avg}$ for *Test C*

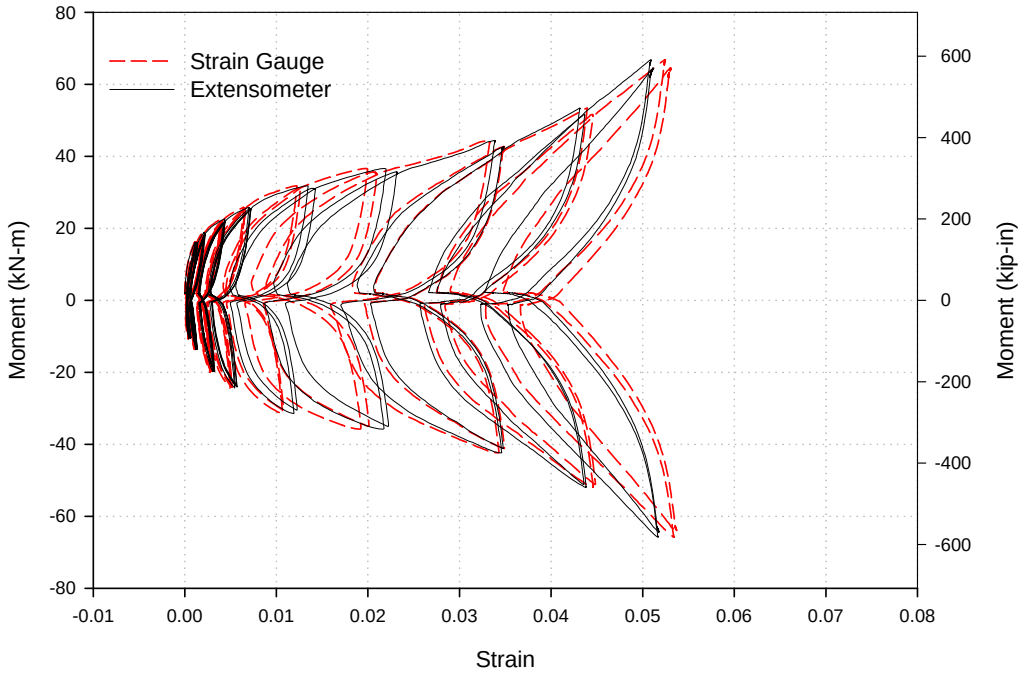

Figure E-41: Strain in the top-back tendon vs. $M_{beam,avg}$ for *Test C*

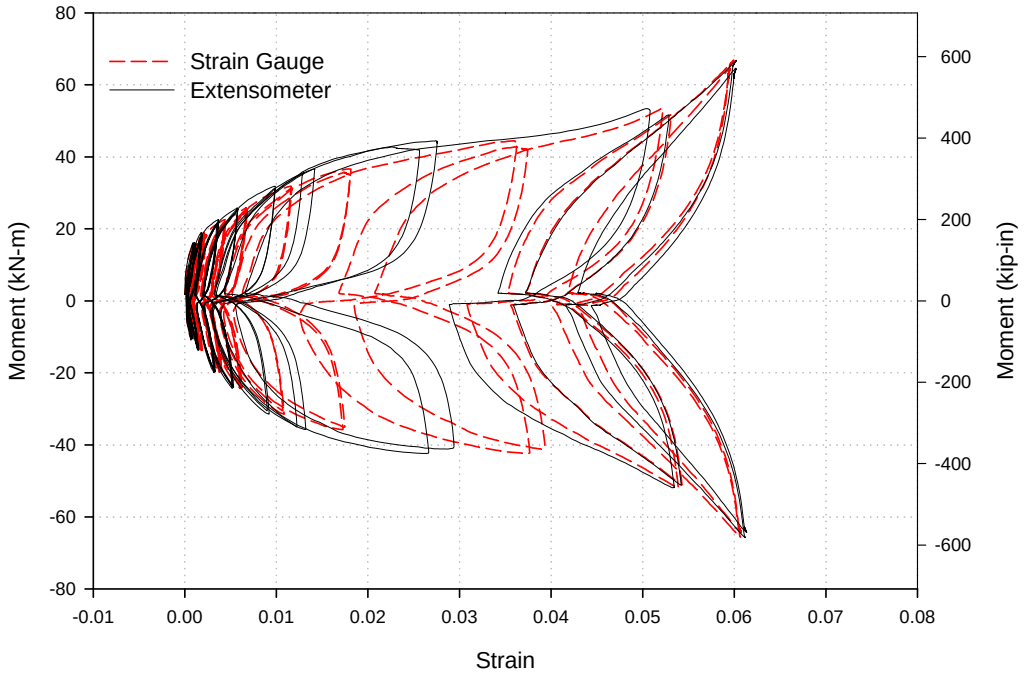

Figure E-42: Strain in the bottom-front tendon vs. $M_{beam,avg}$ for *Test C*

Figure E-43: Strain in the bottom-back tendon vs. $M_{beam,avg}$ for *Test C*

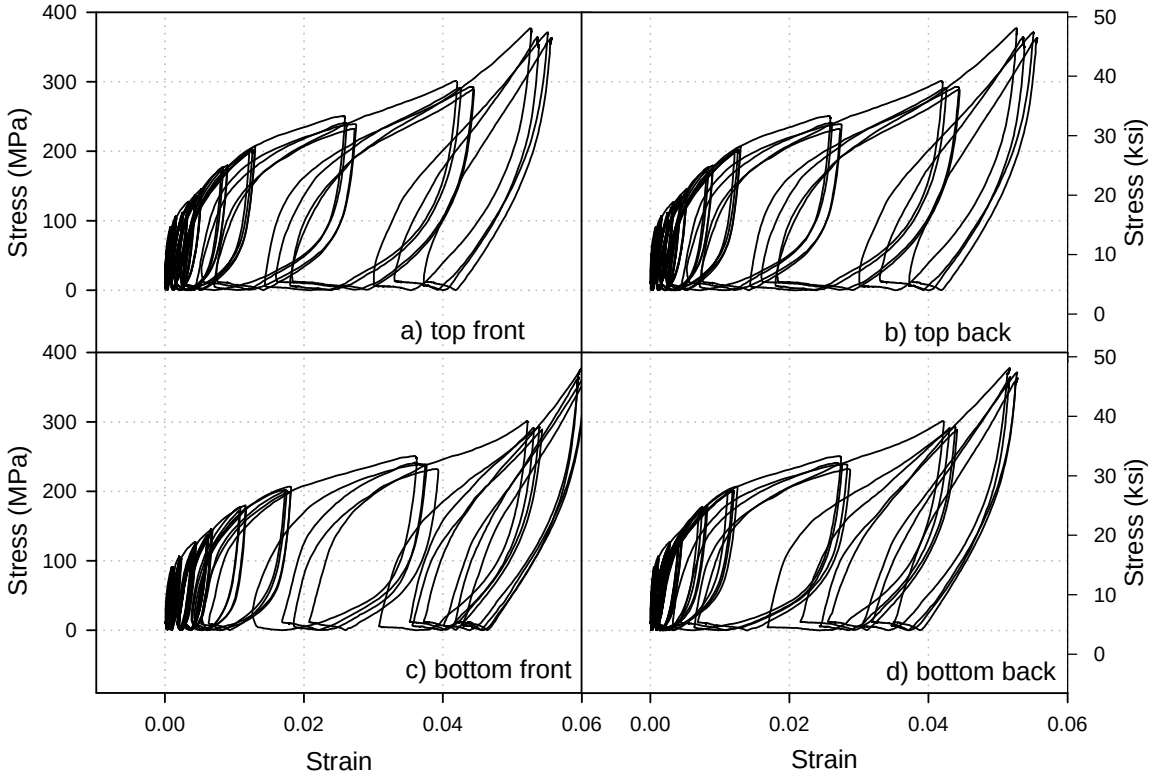

Figure E-44: Stress (assuming tensile force is transferring through the tendon, thus neglecting the shear-tab contribution) vs. strain (EXT) of each tendon element for *Test C.*

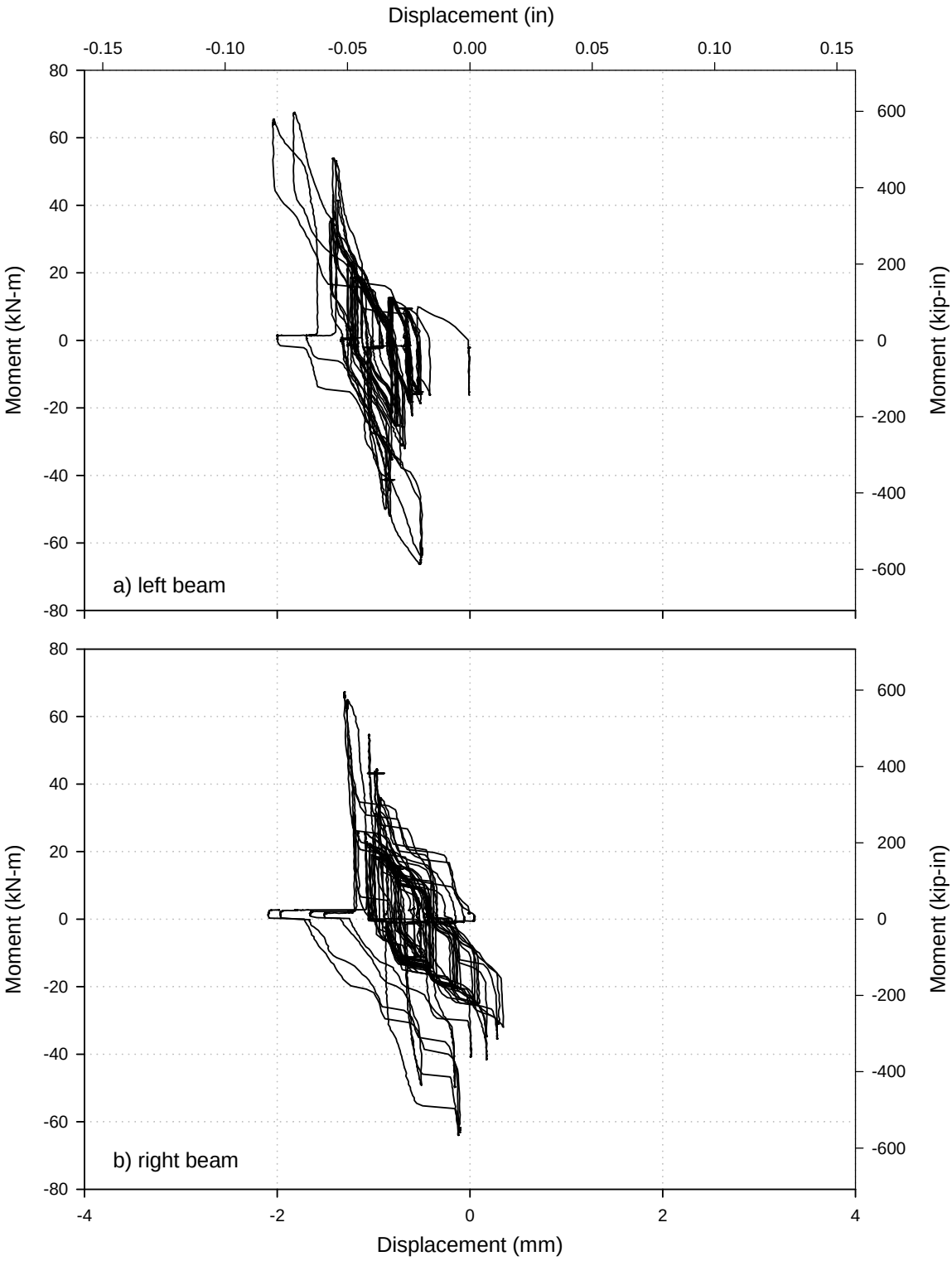

Figure E-45: Averaged moment vs. vertical beam displacement for a) left and b) right beams measured by stringpot at 137.8 cm (54.25 in.) from the outer face of the column flange for *Test C.*

E.4 TEST D

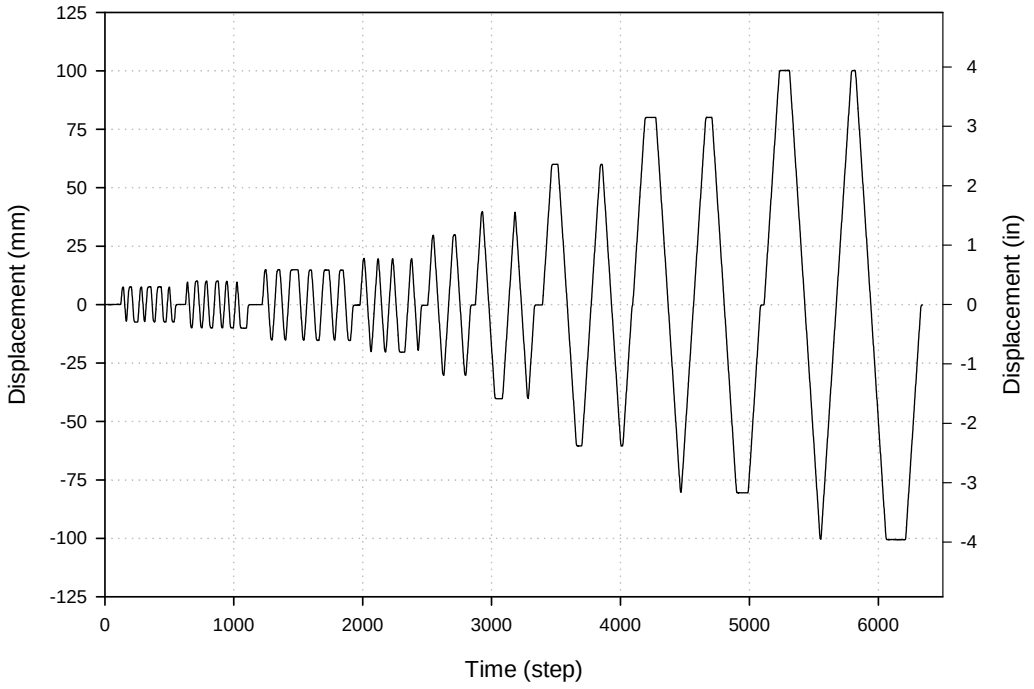

Figure E-46: Actuator displacement time history for *Test D.*

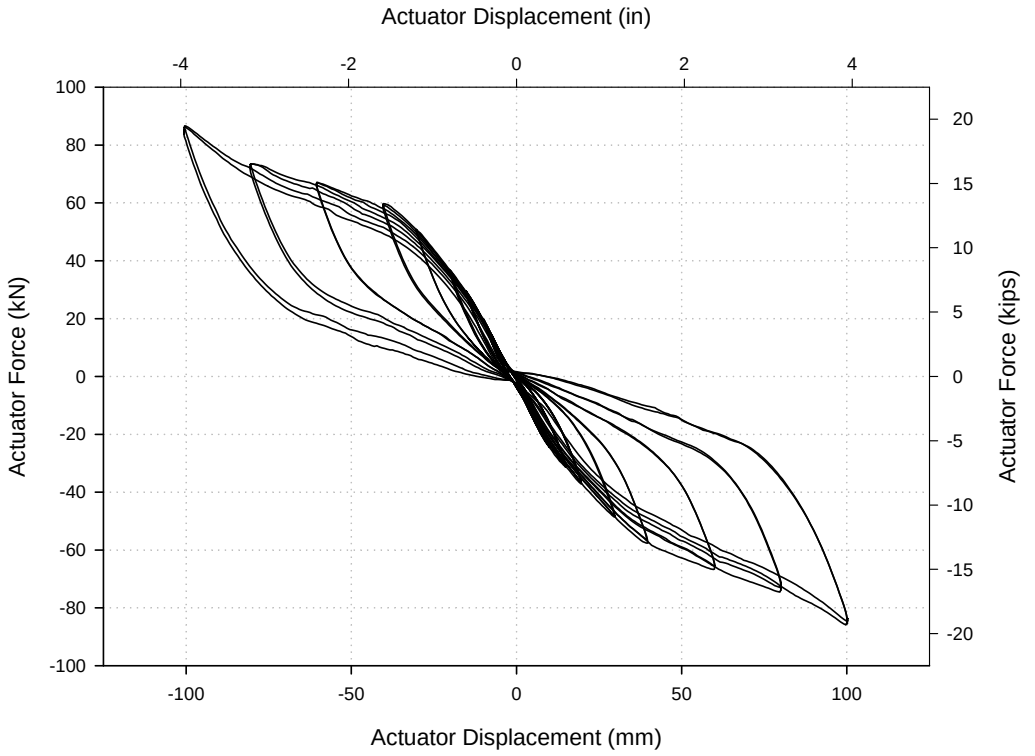

Figure E-47: Actuator force-displacement for *Test D.*

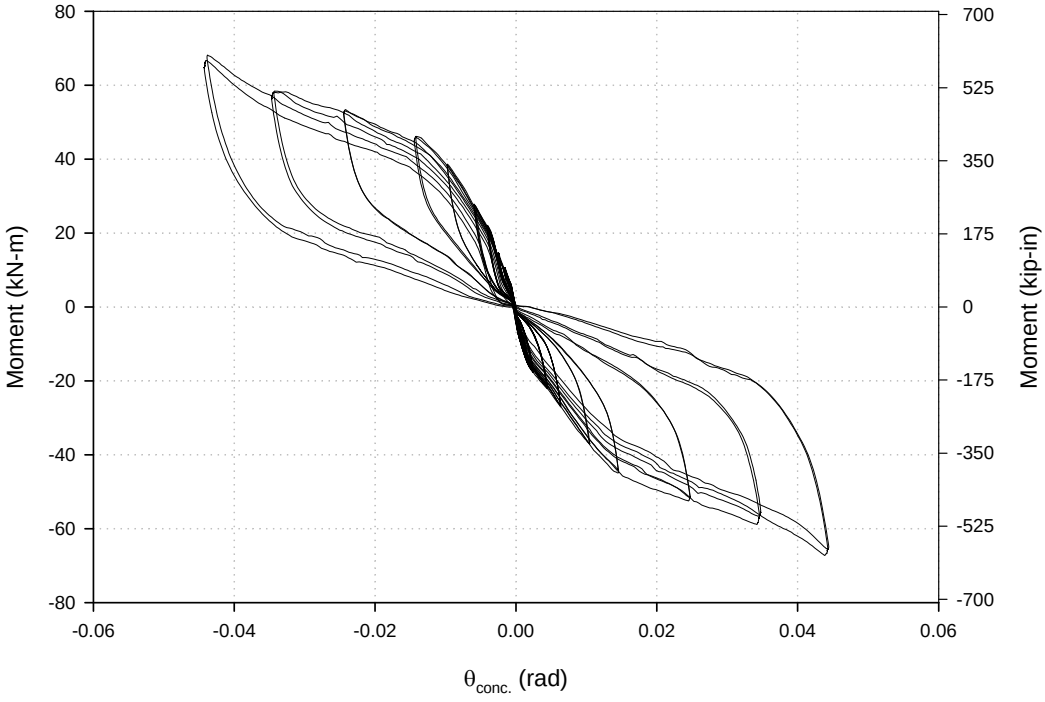

Figure E-48: M-θ at the column face of the left beam for *Test D.*

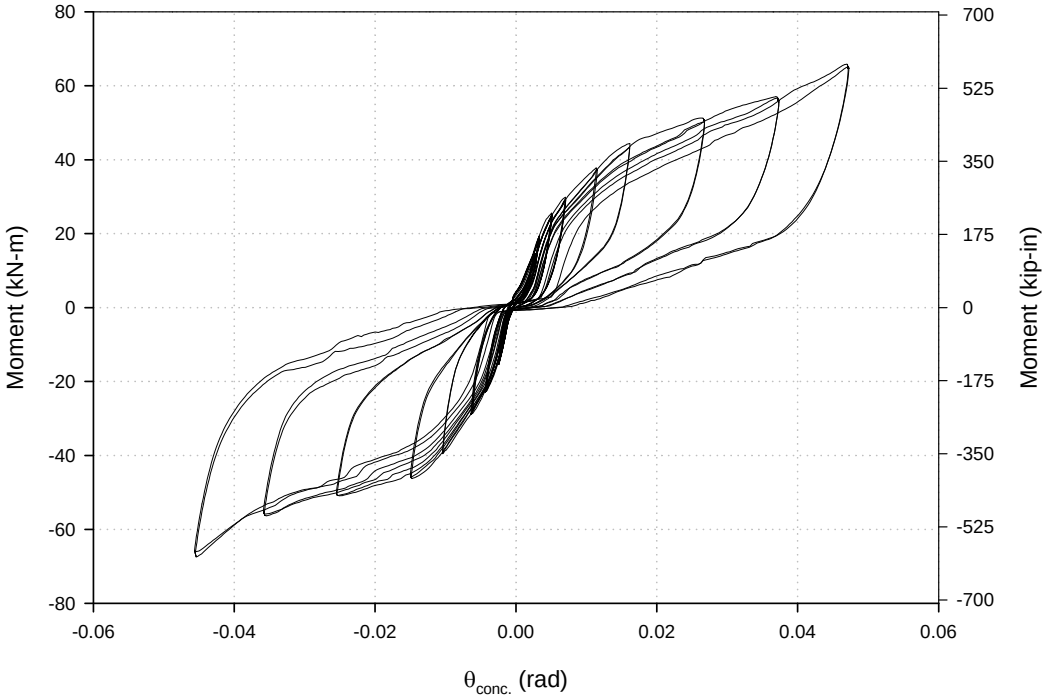

Figure E-49: M-θ at the column face of the right beam for *Test D.*

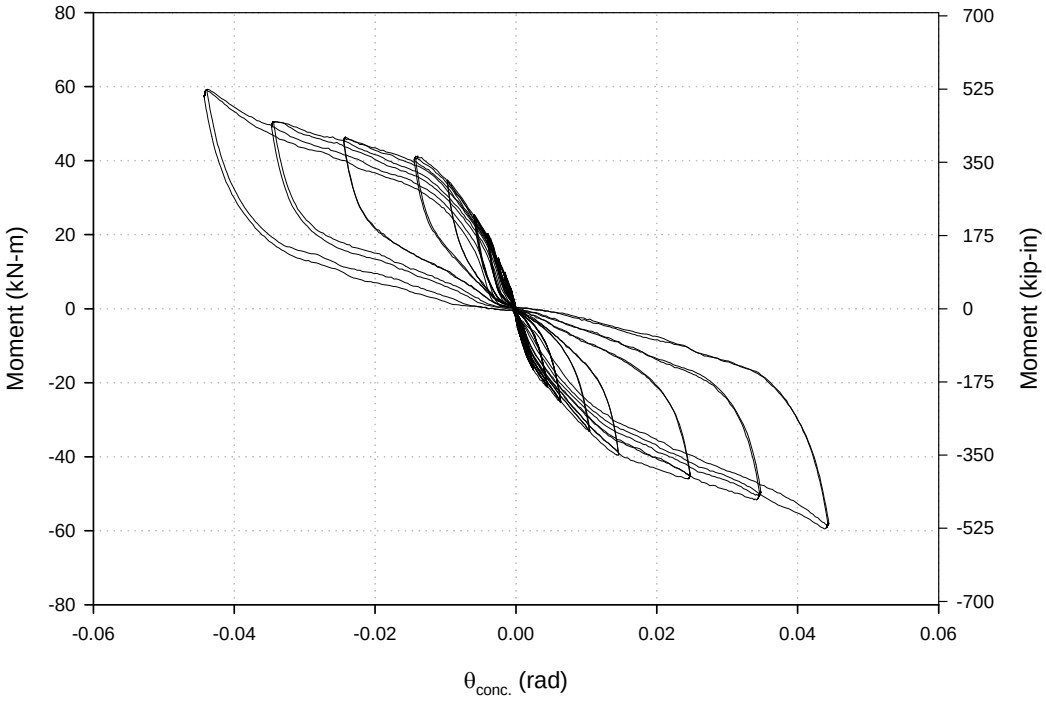

Figure E-50: M-θ at outside of the HSS for column per top strain gauges for *Test D.*

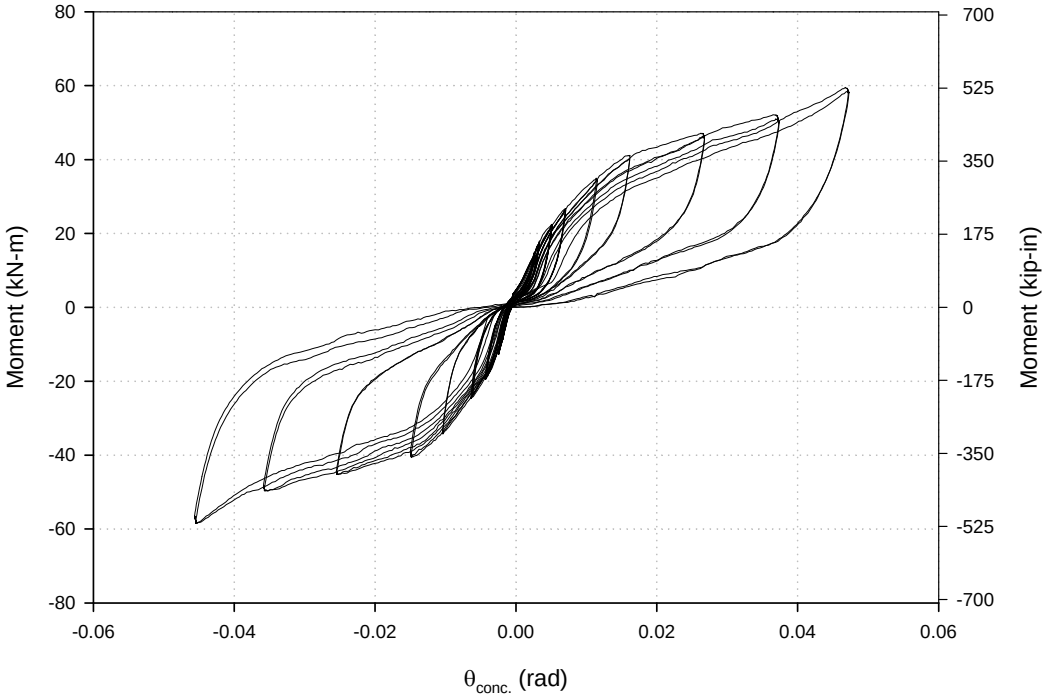

Figure E-51: M-θ at outside of the HSS for column per bottom strain gauges for *Test D.*

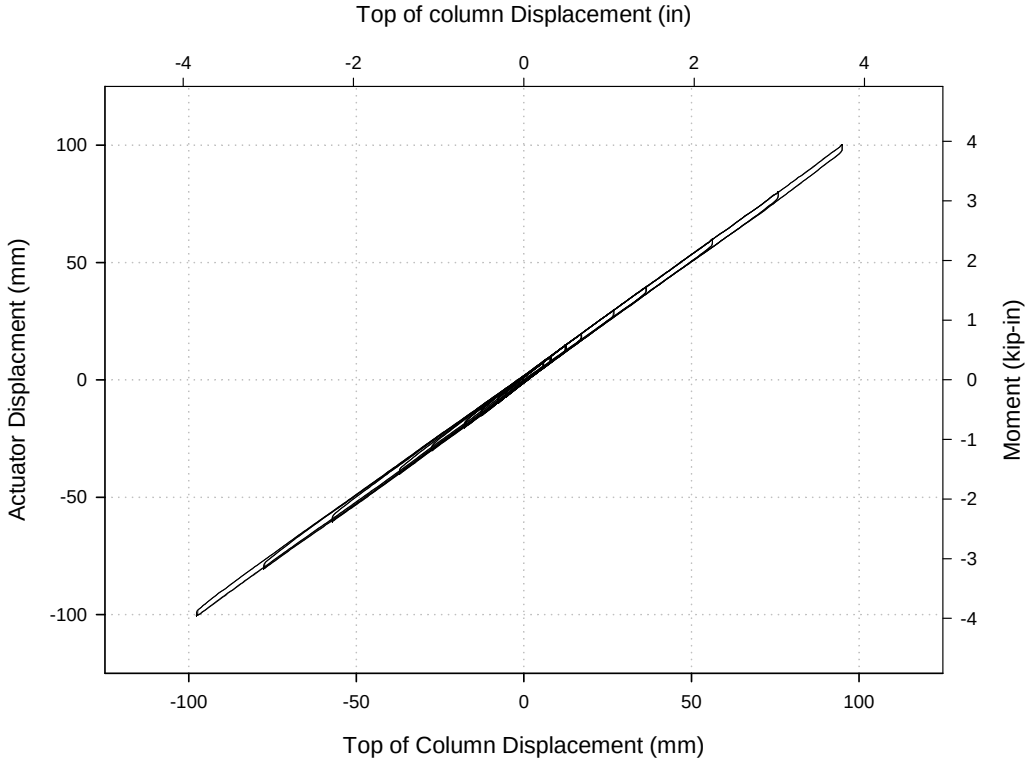

Figure E-52: Displacements at the top of the column vs. at the actuator for *Test D.*

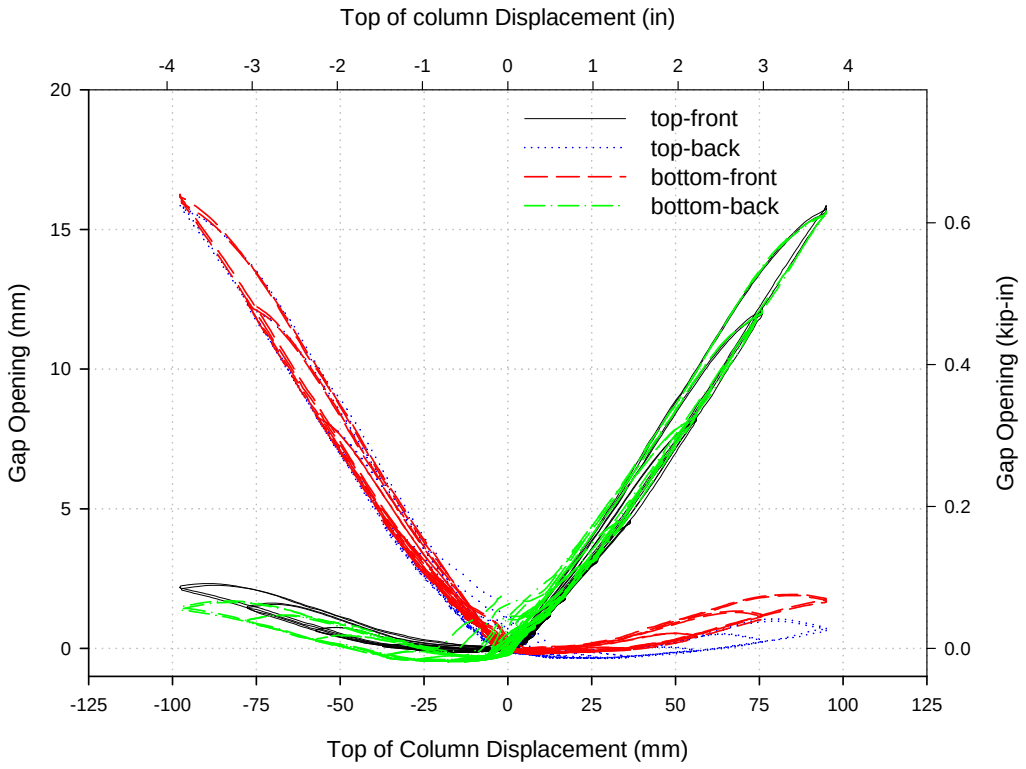

Figure E-53: Gap openings (LVDT) vs. top of column displacement for *Test D.*

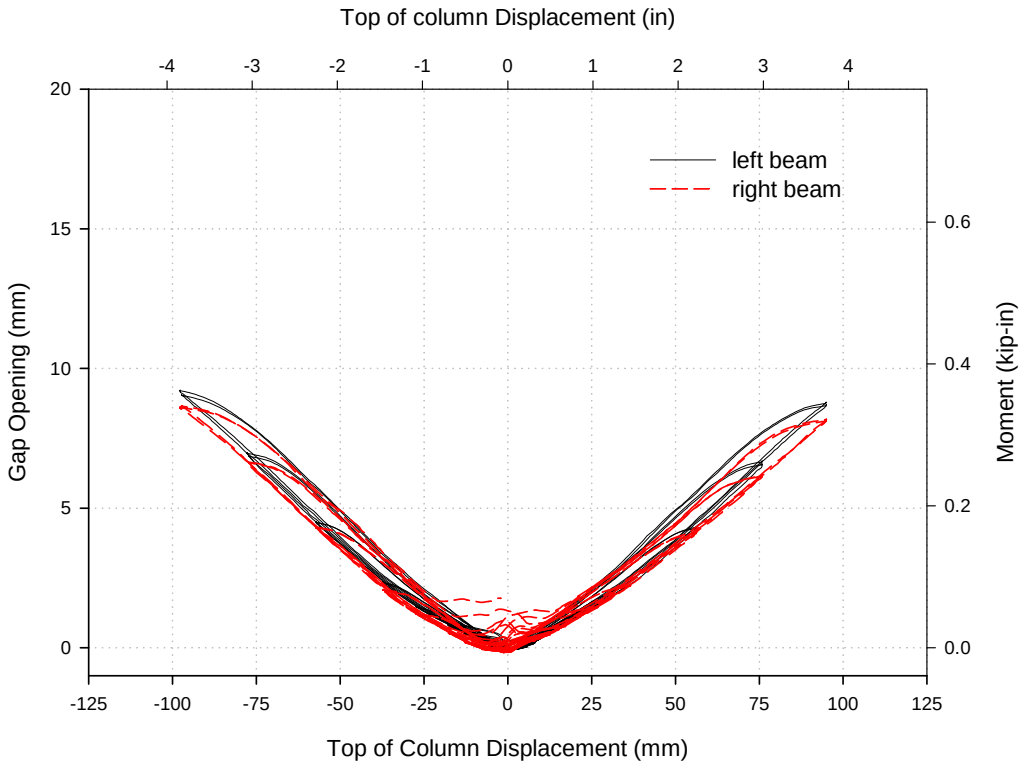

Figure E-54: Average gap opening (LVDT) vs. top of column displacement for *Test D.*

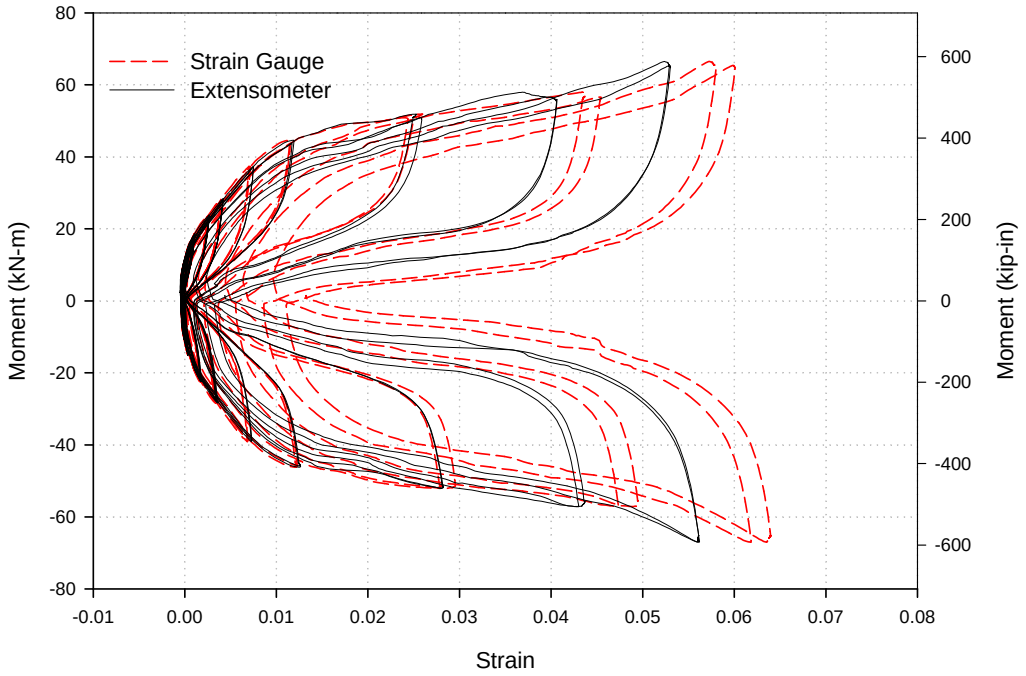

Figure E-55: Strain in the top-front tendon vs. $M_{beam,avg}$ for *Test D.*

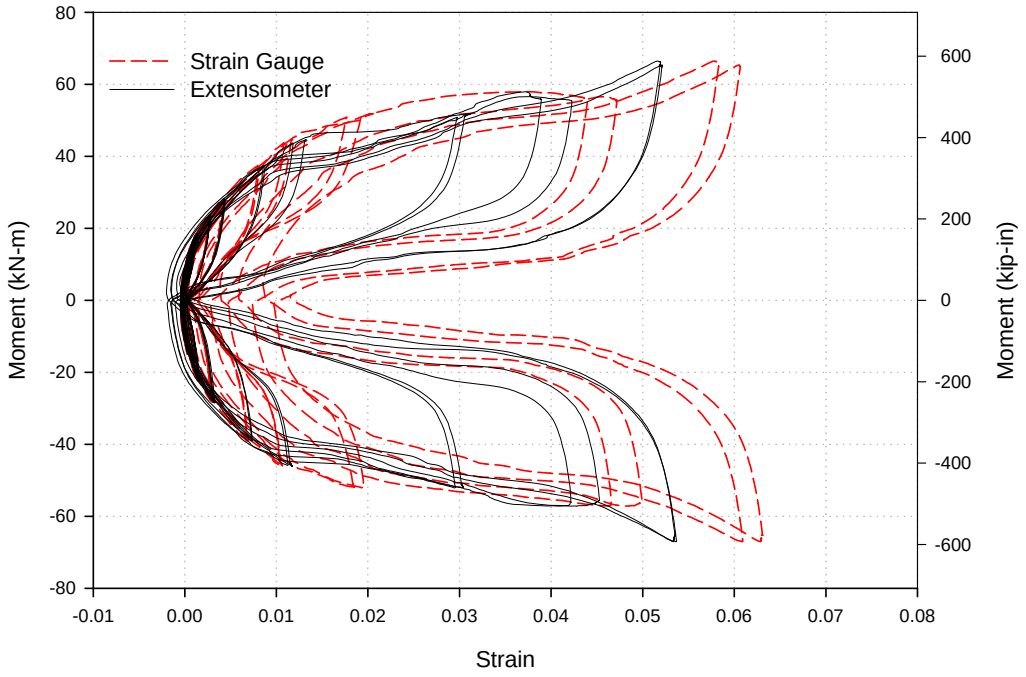

Figure E-56: Strain in the top-back tendon vs. $M_{beam,avg}$ for *Test D.*

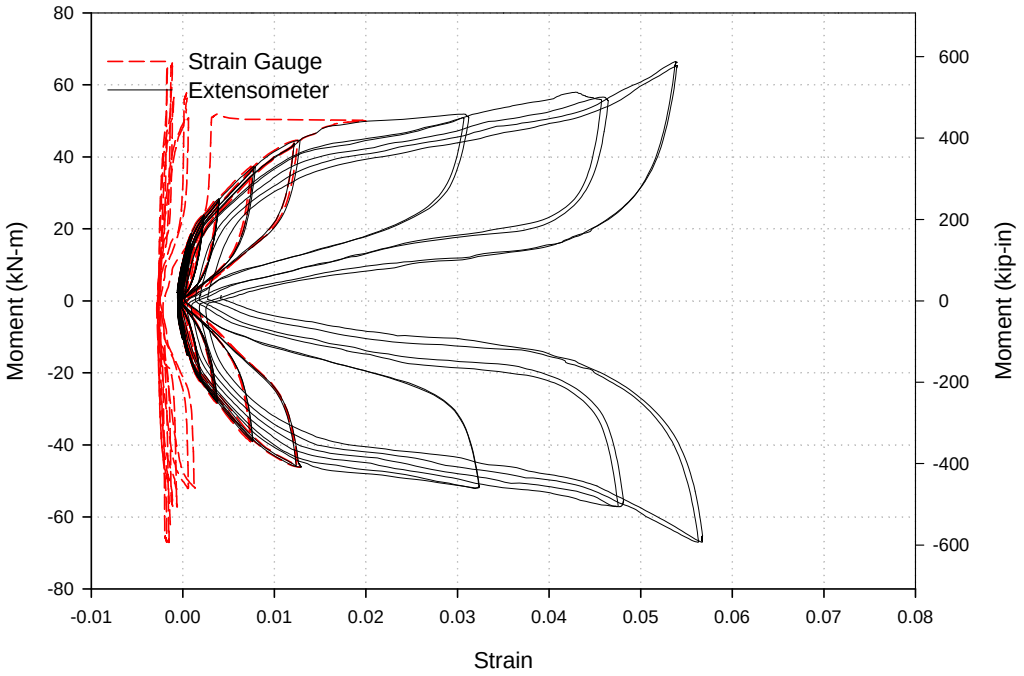

Figure E-57: Strain (EXT) in the bottom-front tendon vs. $M_{beam,avg}$ for *Test D.*

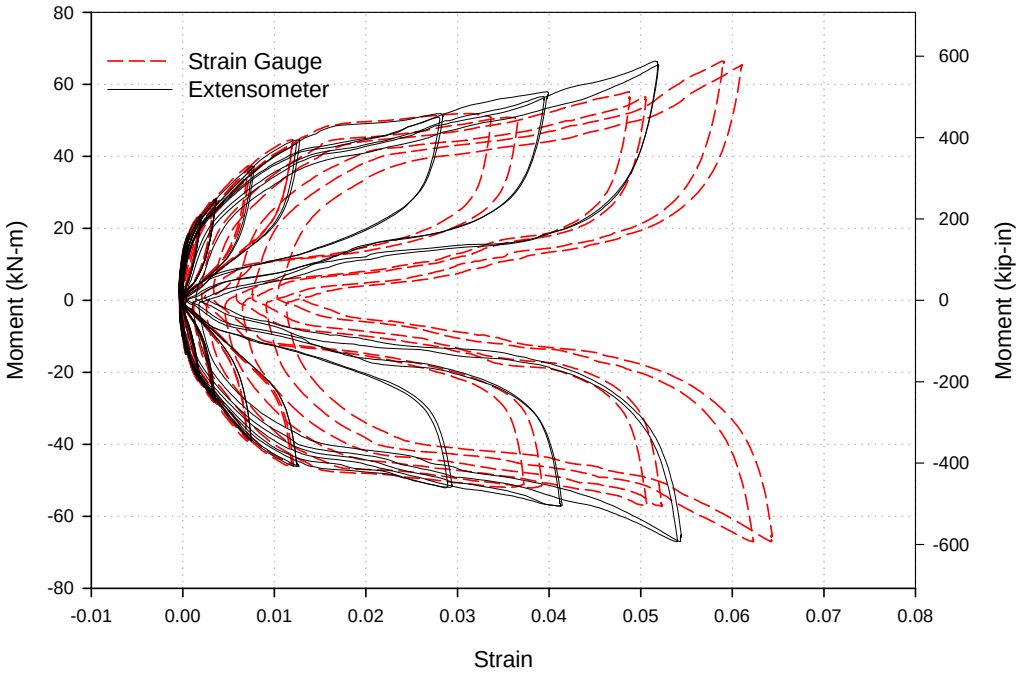

Figure E-58: Strain (EXT) in the bottom-back tendon vs. $M_{beam,avg}$ for *Test D.*

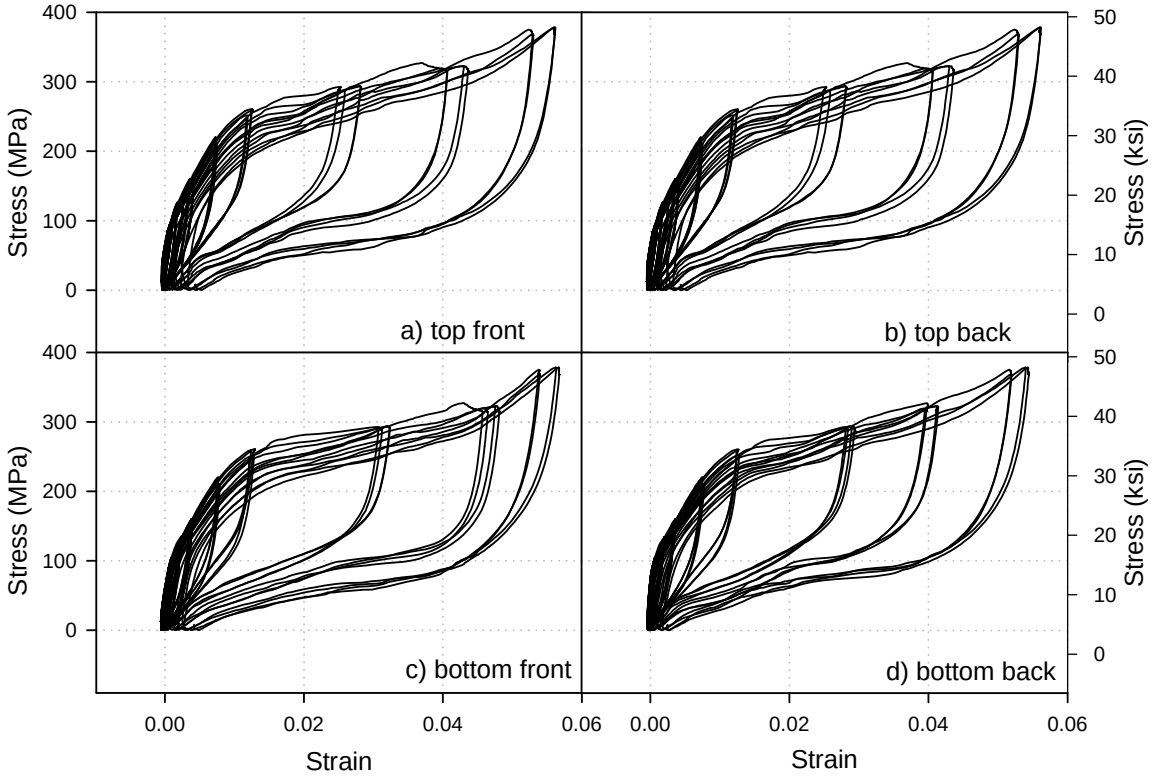

Figure E-59: Stress (assuming tensile force is transferring through the tendon, thus neglecting the shear-tab contribution) vs. strain (EXT) of each tendon element for *Test D.*

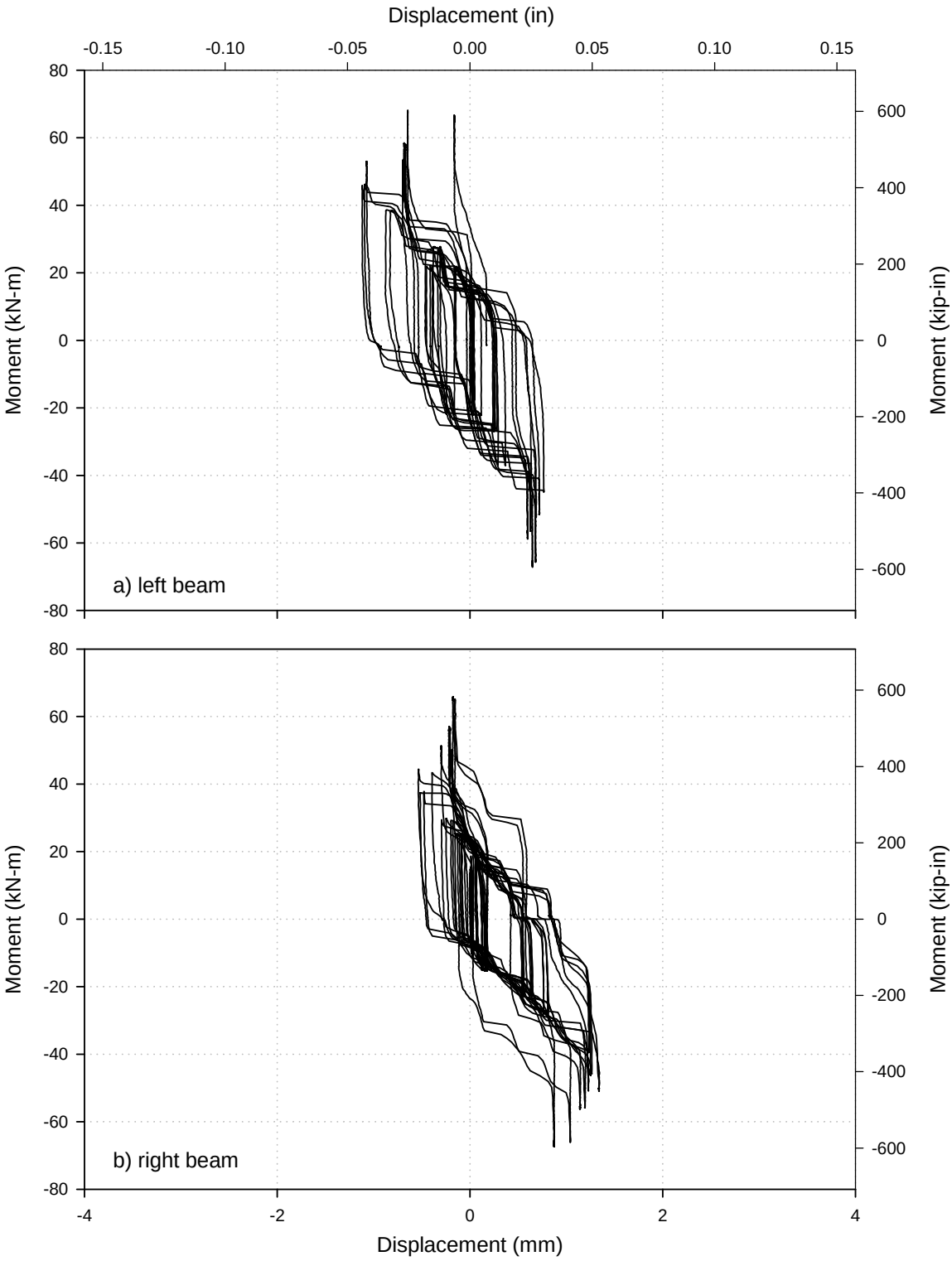

Figure E-60: Averaged moment vs. vertical beam displacement for a) left and b) right beams measured by stringpot at 137.8 cm (54.25 in.) from the outer face of the column flange for *Test D.*

E.5 TEST E

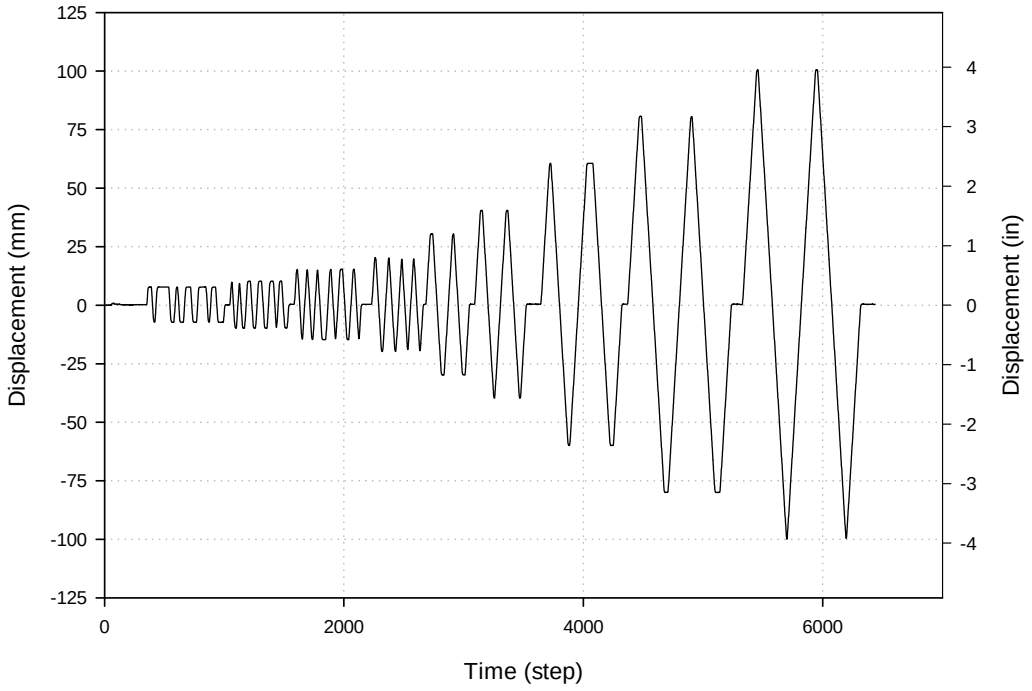

Figure E-61: Actuator displacement time history for *Test E.*

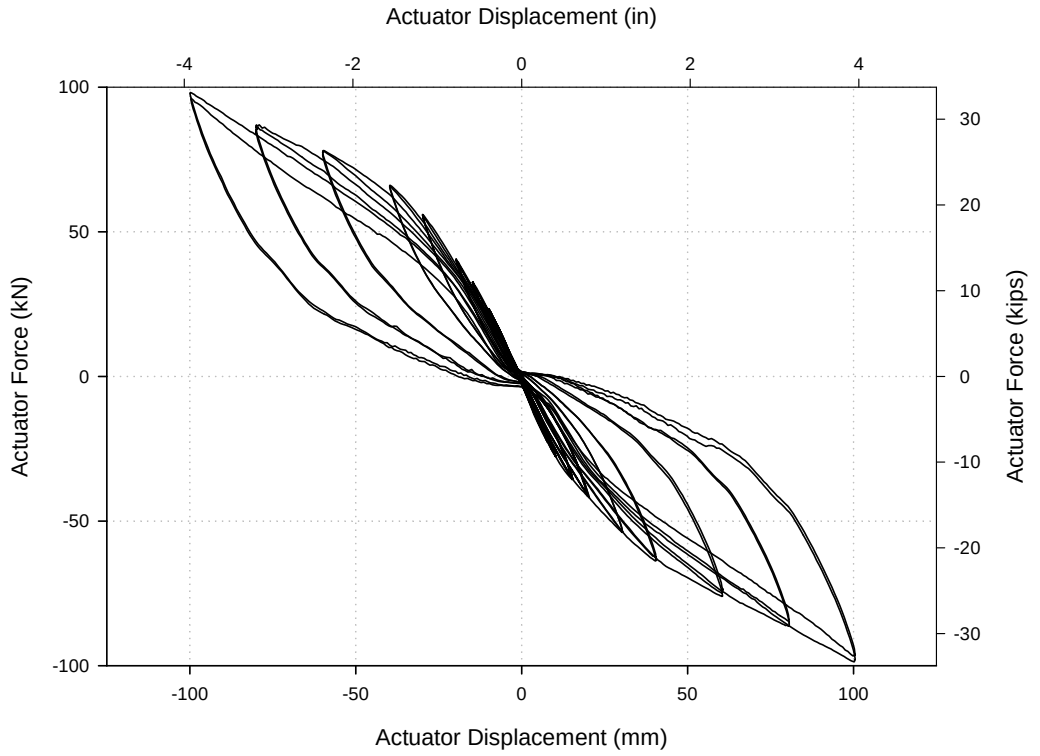

Figure E-62: Actuator force-displacement for *Test E.*

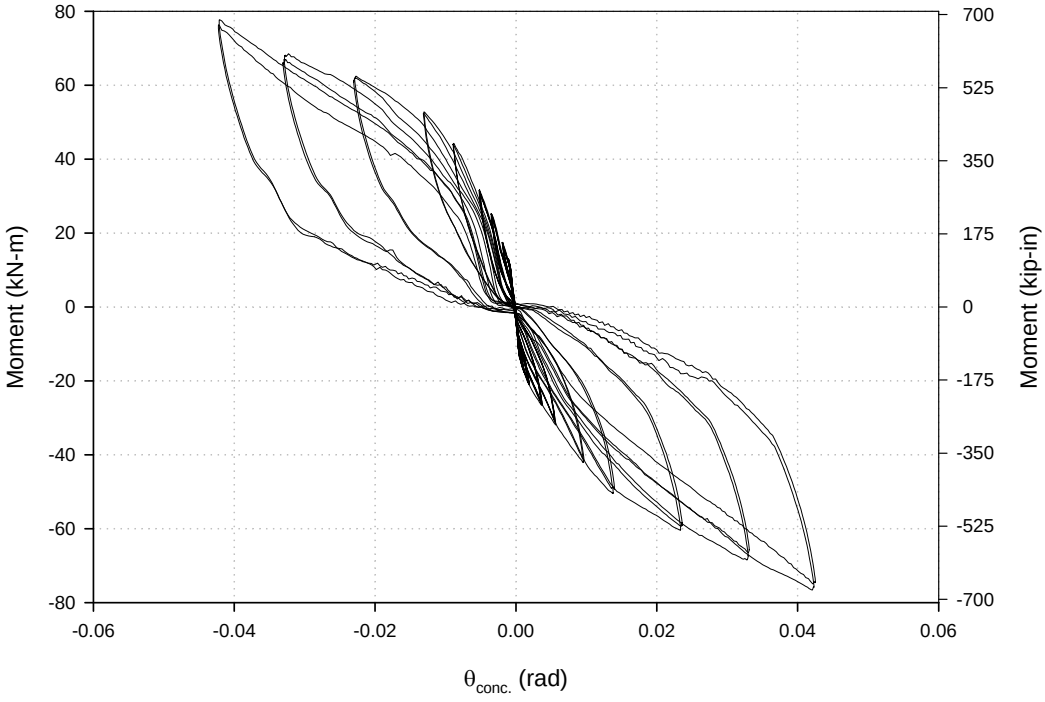

Figure E-63: M-θ at the column face of the left beam for *Test E.*

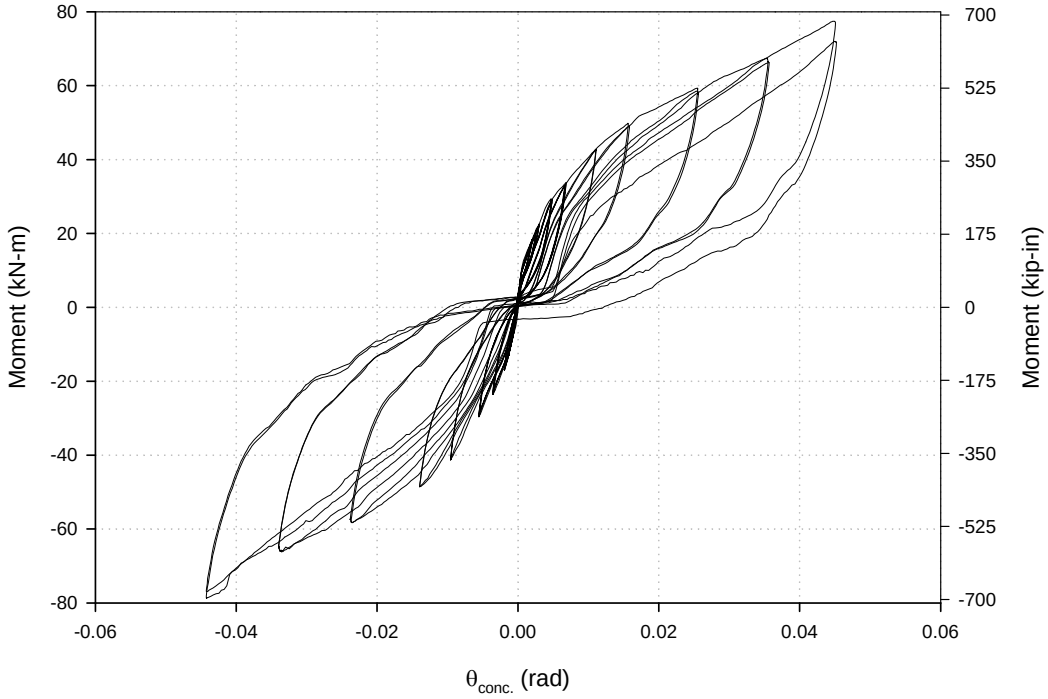

Figure E-64: M-θ at the column face of the right beam for *Test E.*

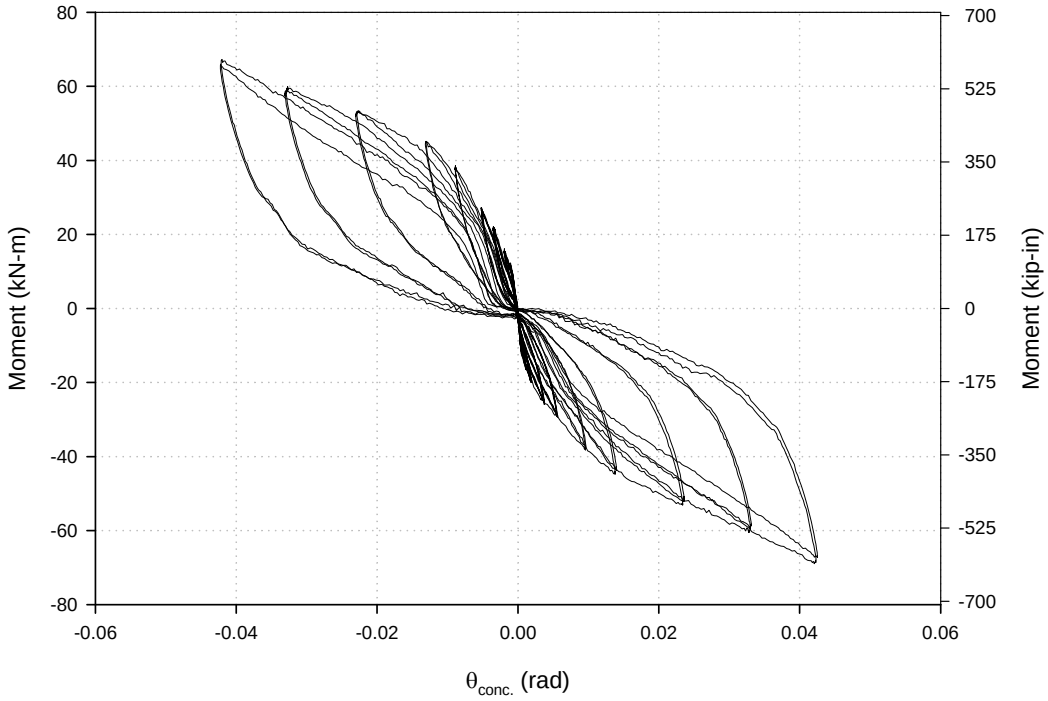

Figure E-65: M-θ at outside of the HSS for column per top strain gauges for *Test E.*

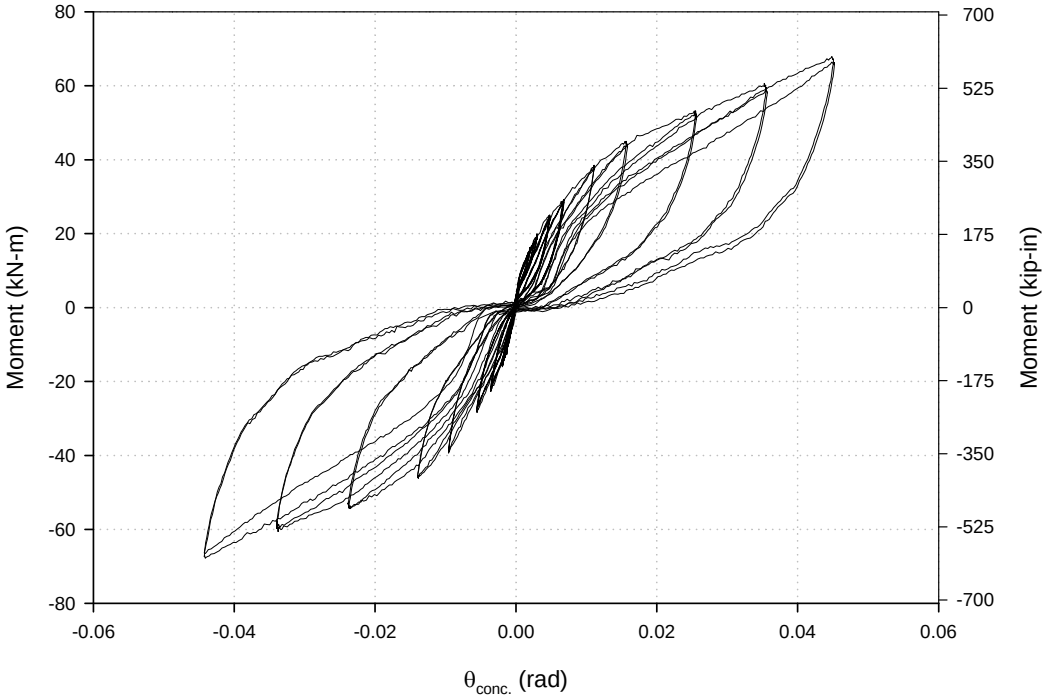

Figure E-66: M-θ at outside of the HSS for column per bottom strain gauges for *Test E.*

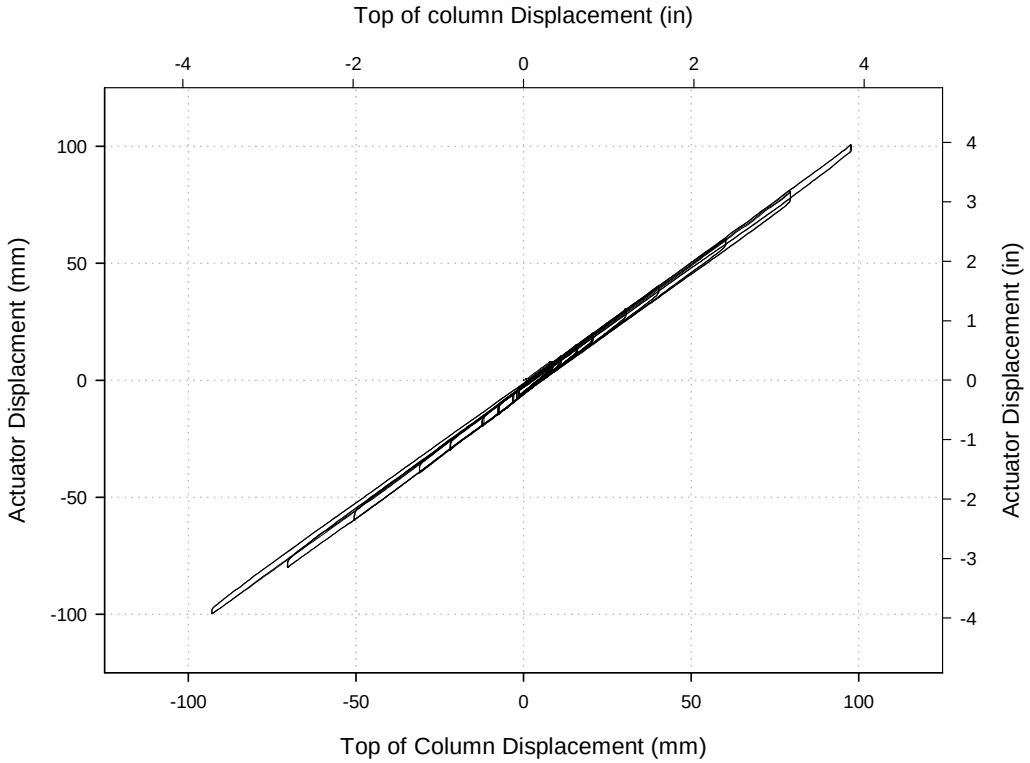

Figure E-67: Displacements at the top of the column vs. at the actuator for *Test E.*

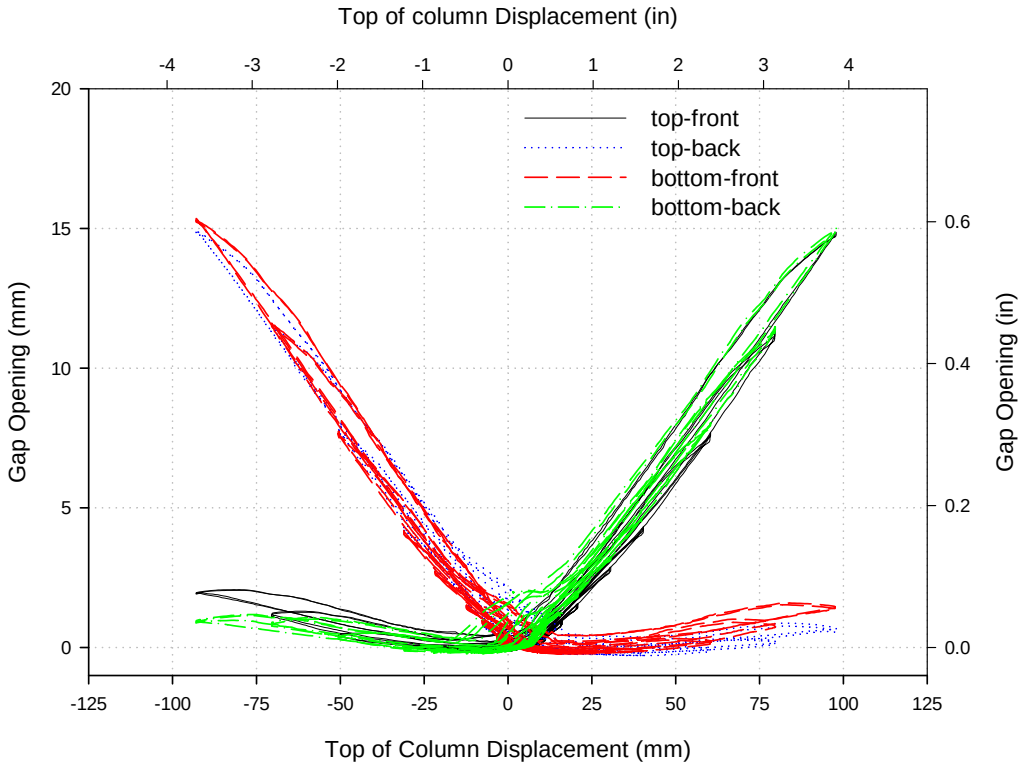

Figure E-68: Gap openings (LVDT) vs. top of column displacement for *Test E.*

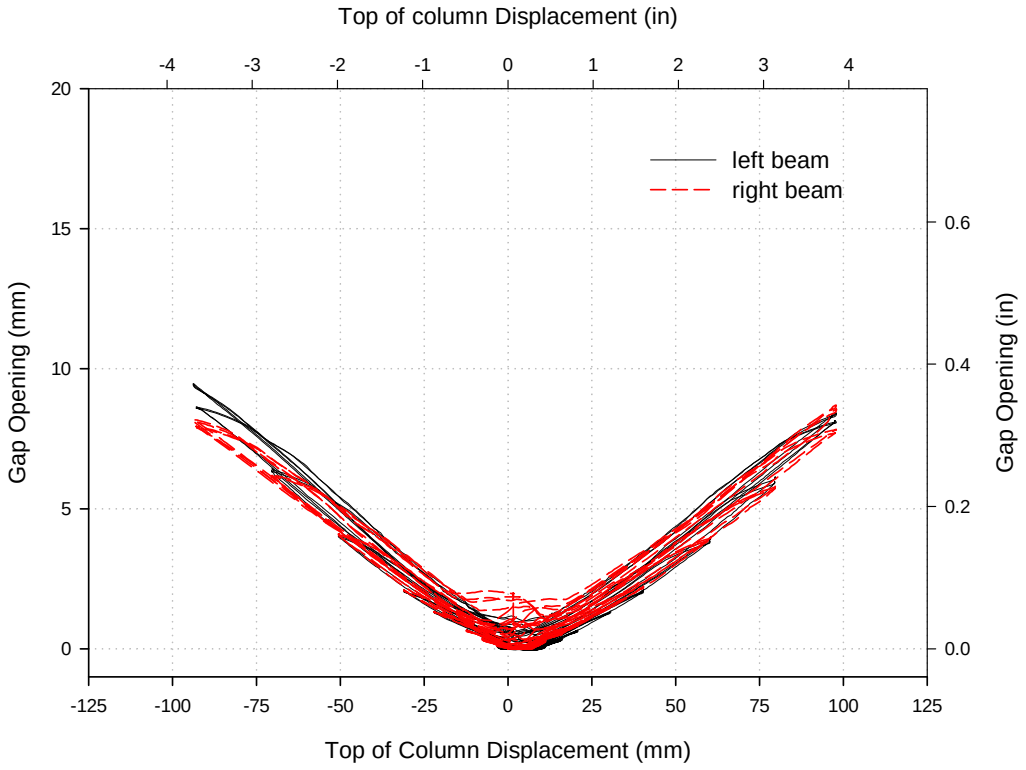

Figure E-69: Average gap opening (LVDT) vs. top of column displacement for *Test E.*

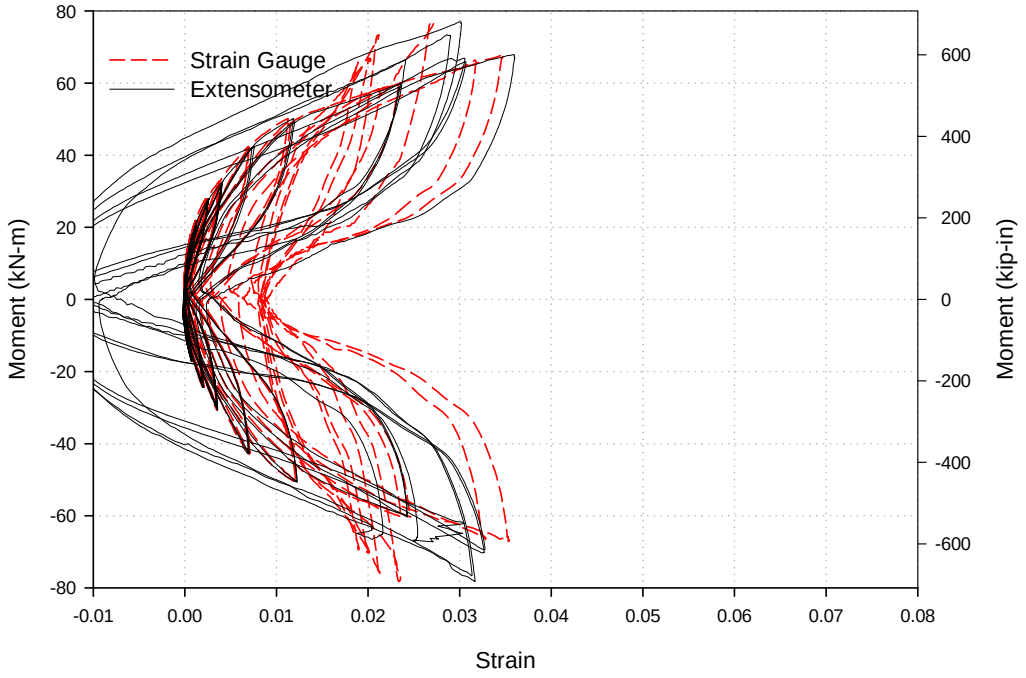

Figure E-70: Strain (EXT) in the top-front tendon vs. $M_{beam,avg}$ for *Test E.*

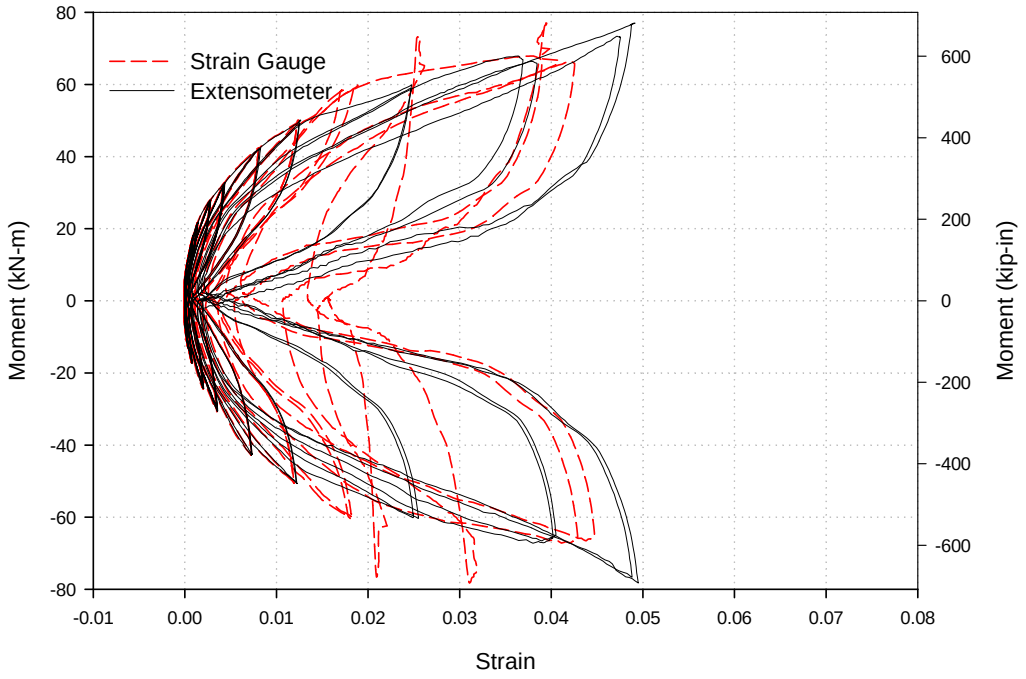

Figure E-71: Strain (EXT) in the top-back tendon vs. $M_{beam,avg}$ for *Test E.*

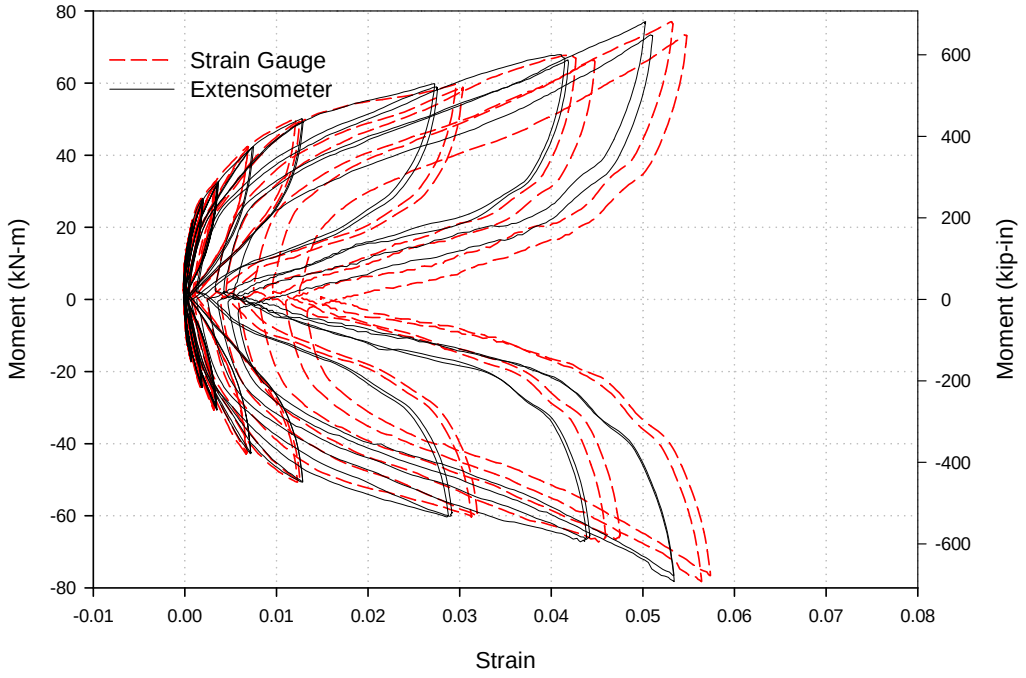

Figure E-72: Strain (EXT) in the bottom-front tendon vs. $M_{beam,avg}$ for *Test E.*

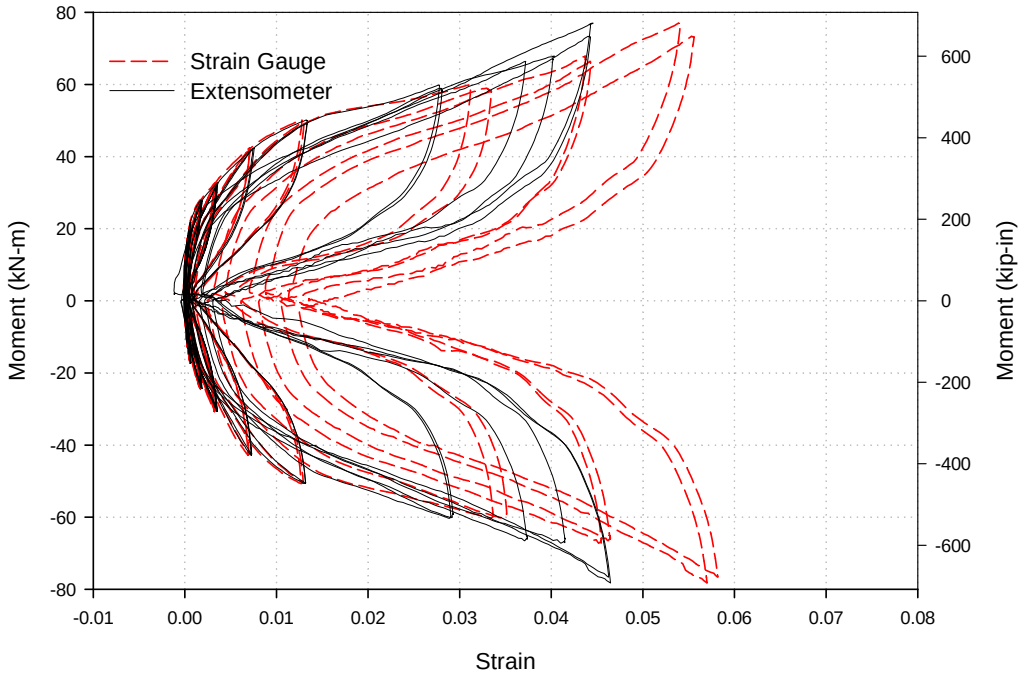

Figure E-73: Strain (EXT) in the bottom-back tendon vs. $M_{beam,avg}$ for *Test E.*

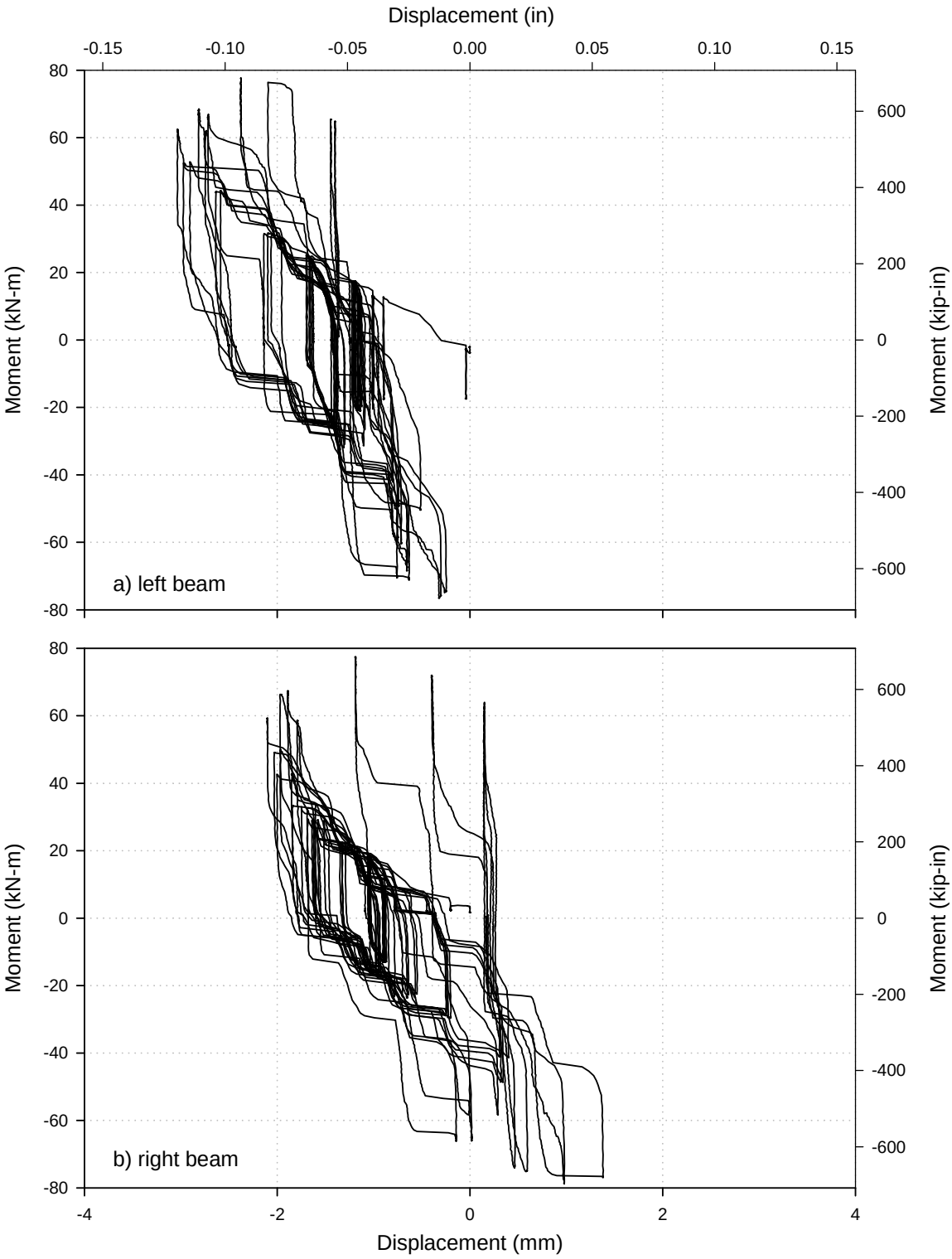

Figure E-74: Averaged moment vs. vertical beam displacement for a) left and b) right beams measured by stringpot at 137.8 cm (54.25 in.) from the outer face of the column flange for *Test E.*

APPENDIX F

BEAM COLUMN CONNECTION: PHOTOGRAPHS

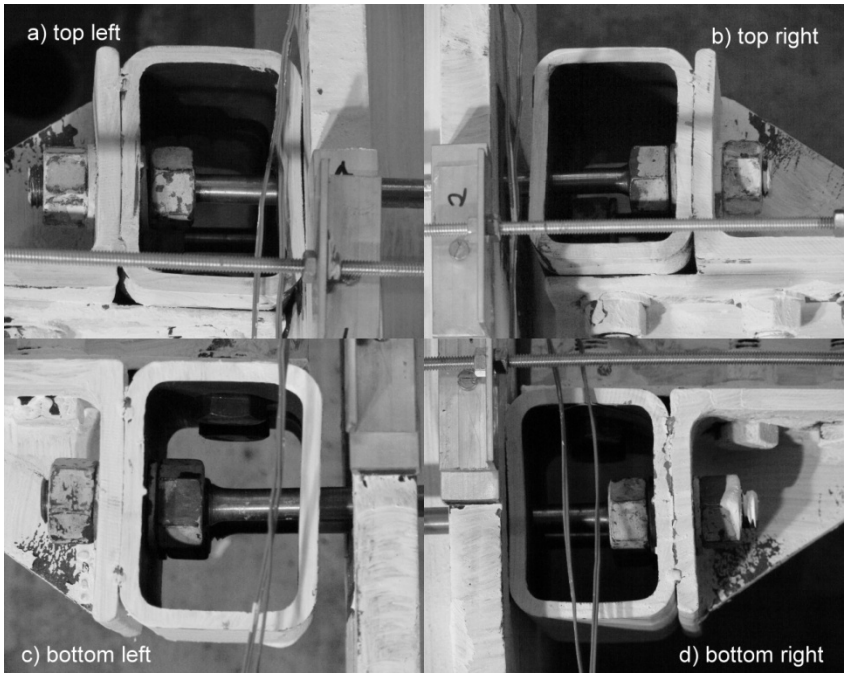

Figure F-1: Deformation of HSS transfer elements after the completion of *Test A.*

Figure F-2: Experimental test setup with beam-column installed.

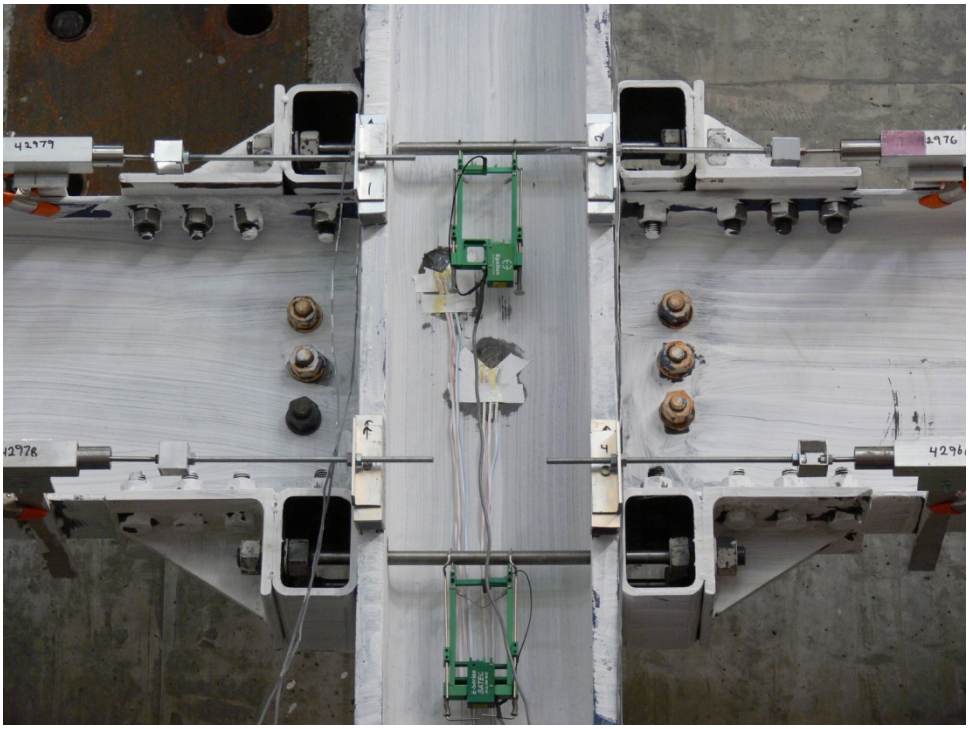

Figure F-3: Profile view of *Test A*.

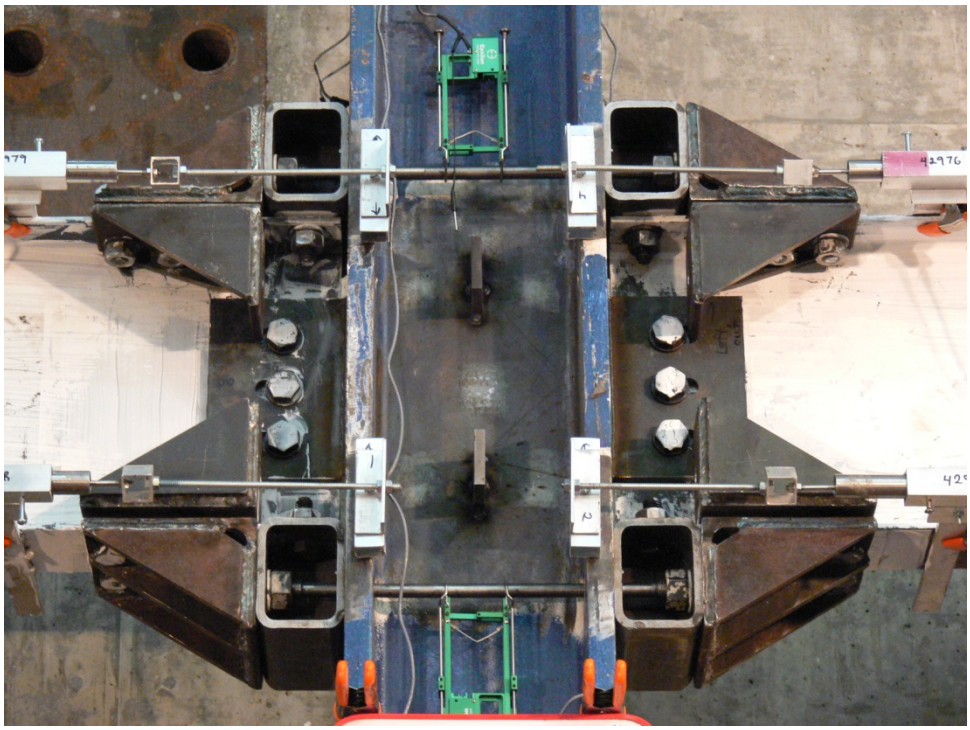

Figure F-4: Profile view of *Test B*.

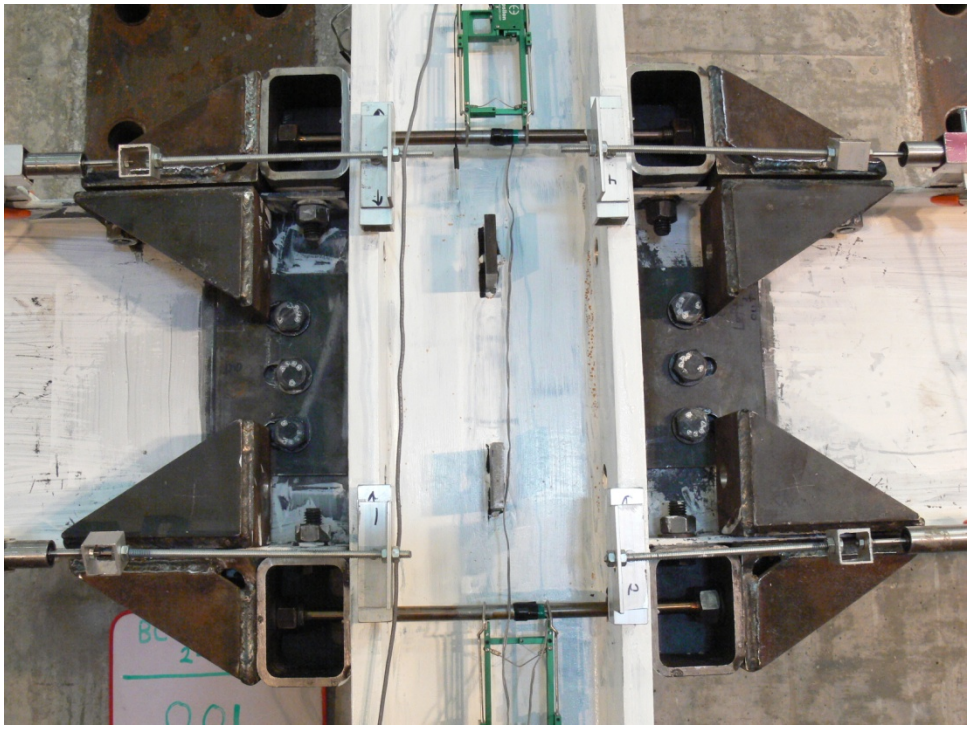

Figure F-5: Profile view of *Test C*.

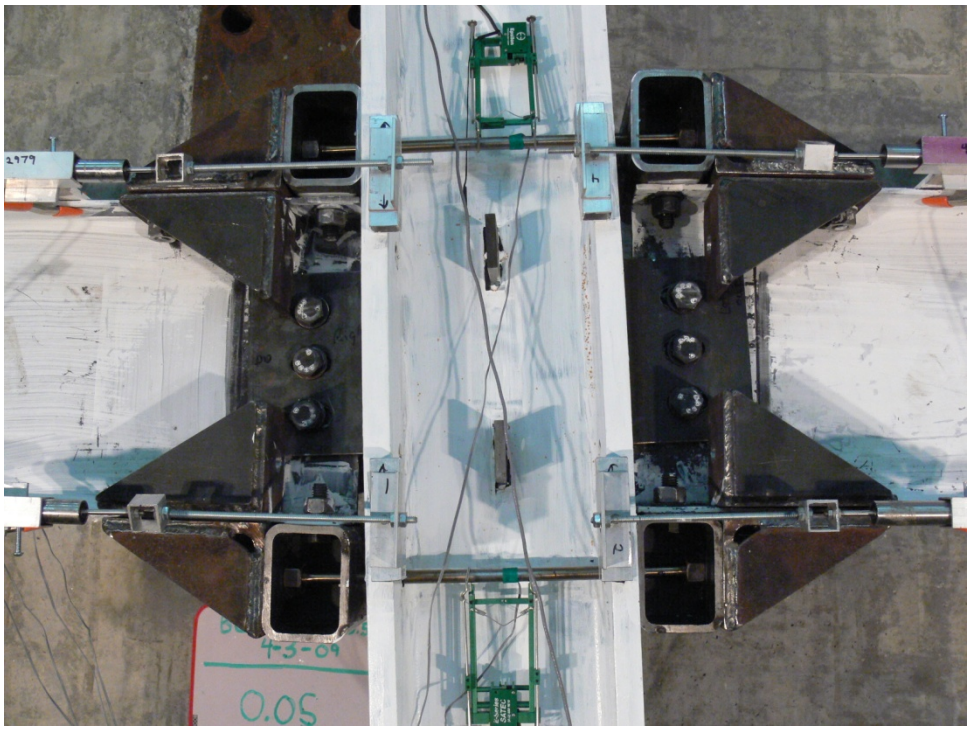

Figure F-6: Profile view of *Test D*.

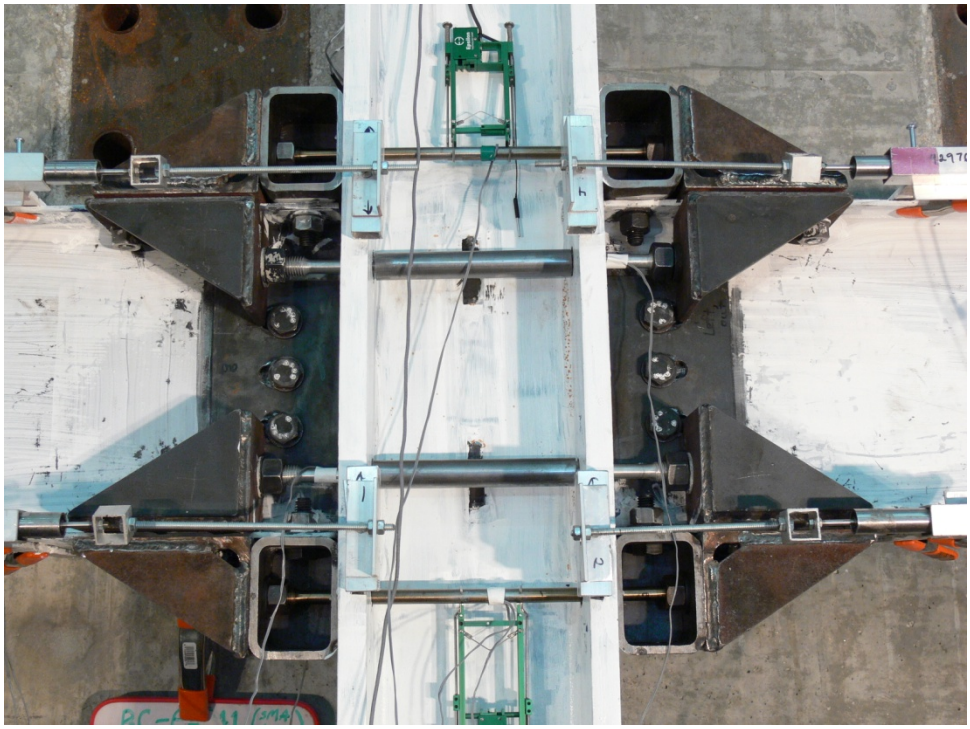

Figure F-7: Profile view of *Test E*.

APPENDIX G

ARTICULATED QUADRILATERAL CONCEPTION AND DEVELOPMENT

One of the main goals of this bracing system is to create an effective way to combine SMA elements in parallel with supplemental energy dissipating elements. This idea is rooted in the following result observed in the SDOF Study chapter: a recentering system with a maximized hysteretic loop will produce the best performance. To dissipate energy by yielding or by friction, the dissipating element must be subjected to load reversal (i.e. tension and compression). For a cable bracing system, this is difficult to obtain without a special arrangement. The AQ configuration accomplishes this requirement in a unique way and facilitates the use of a variety of dissipating elements.

Several options for dissipating elements have been identified including torsional dissipators (either friction or yielding) at the AQ joints, frictional dissipators on the diagonals (Pall and Marsh, 1982), flexural yielding of the AQ members (Tyler, 1983), and c-shaped dissipators on the diagonals (Renzi et al., 2007). The c-shape dissipator was chosen for this research because of the predictable results shown in experimental work by Renzi. Nevertheless, the other methods of providing energy dissipation should not be discounted and have been found to be very successful in research and application.

The options for loading the SMA elements include torsion at the joints and tension across the diagonal. The latter option was chosen because tension is the most efficient use of the material. Additionally, superelastic NiTi wires have been shown to have excellent performance in terms of inherent energy dissipation and recentering. A

bundle of NiTi wires was fabricated by Nitinol Technologies Inc. The full details of the NiTi bundles are described in the component test section of this chapter.

Figure G-1a-b shows a schematic of the complete AQ setup. The SMA bundles cross in the middle and are anchored to square steel bars at the ends. This steel bar is then mounted to threaded bars which are inserted into a steel transfer block. This setup enables tightening of the SMA bundles to either remove slack or to instill some initial pretension while maintain a configuration that is as compact as possible. The c-shape members are attached at the corner joints with a large diameter bolt functioning as a pin.

Two c-shaped dissipators were used in the same direction but on opposite faces of the AQ. Due to the geometry implemented, out-of-plane ties were attached to the c-shape along the length. These ties effectively braced the two dissipators together and forced flexure yielding to occur before lateral torsional buckling.

The dimensions and the material properties of the c-shape determine its strength and stiffness. When selecting the dimensions, the following criteria were adhered to:

- The thickness of the c-shape should be minimized to ensure the AQ's compactness (12.7 mm (0.5 in.) was selected in this study).
- The yield strength should be the fraction of the SMA element yield that creates increased system damping while maintaining good recentering. The yield strength was selected to be 22 kN (5 kips), the approximate end of the unloading plateau seen in mechanical testing of the SMA wire bundle.
- The stiffness of the c-shape should be greater than or equal to the stiffness that results in the c-shape yielding at the same deformation as the SMA. This criterion ensures the c-shape is pushed beyond its elastic range.

To show the effects of length change, Figure G-1c provides a graphical illustration of how the dimensions of a c-shape change when thickness, stiffness, and yield force are held constant and length is varied.

For this research, the length is predetermined by the length of the SMA wire bundles. Because of the length, strength, and stiffness requirements, the c-shape is rather long. In Figure G-2 the relationship between hole separation, *s*, and arm rotation, *f*, is plotted for a range of *m/a* ratios (defined on the plot) and the governing equation is:

$$s = 2\left(a + \frac{m}{\phi}\right)\sin\left(\frac{\phi}{2}\right) - m \qquad \text{(G.1)}$$

This equation and corresponding plot assume that the c-shape body (*m* portion) is axially inextensible and that arms (*a* portions) are rigid. The maximum hole separation for each *m/a* gives the limitation of each c-shape geometry. If further hole separation is induced, the deformation mode will be axial extension rather than flexural bending. Slotted holes were implemented in the experimental specimen to work-around this constraint.

To further understand the selection of the AQ setup as the ideal platform of implementing SMAs in a bracing system, the following benefits are identified:

- The SMA bundles can be factory installed to a prescribed pretension, thus reducing or eliminating field installation errors. However, the AQ ties would have to be designed to prevent buckling from compression due to this pretensioning.
- The SMA bundles can be combined in parallel with a variety of possible energy dissipation elements such as torsion elements at the AQ joints, c-shape dissipators, AQ element deformation dissipator, or friction dissipators across the diagonal.
- Shock loading will be minimized because the c-shape dissipator is instantly activated upon reversal of drift demand.
- The dimension of the AQ can be adjusted to create a system with a wide range of force-deformation characteristics.

The dimension and further description of the AQ setup tested in this research are given in the Section 6.3.4 of the main text.

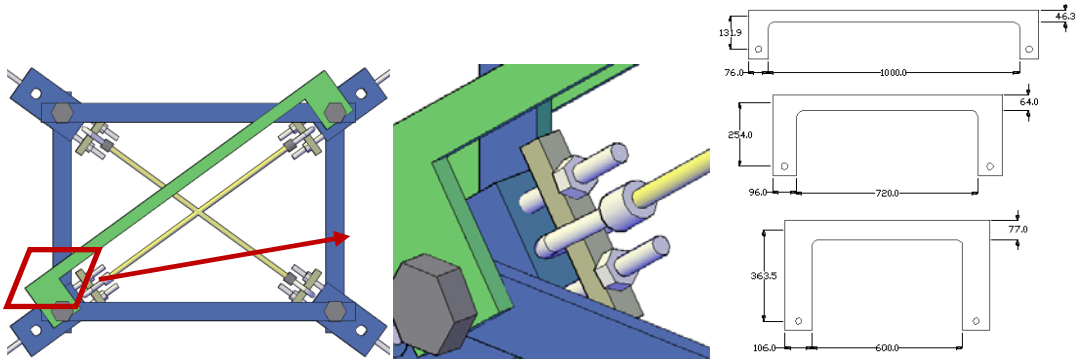

(a) (b) (c)

Figure G-1: (a) AQ with SMA bundles and c-shape dissipaters, (b) 3D view of SMA attachment, and (c) c-shape dimension variation for constant thickness, stiffness, and yield force.

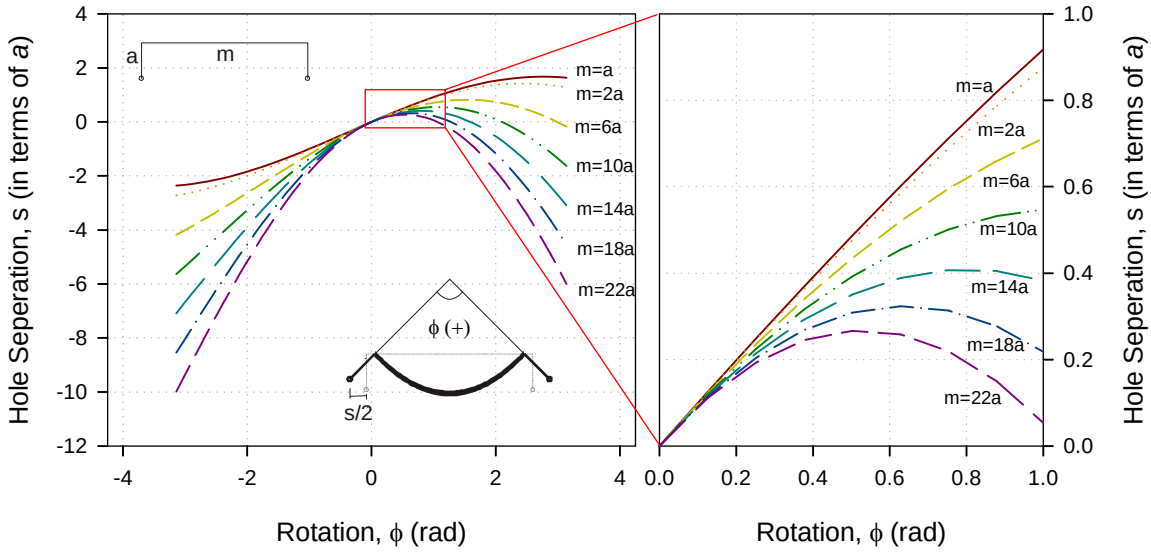

Figure G-2: C-shape kinematic behavior assuming the center of c-shape is axially inextensible and the arms are completely rigid.

APPENDIX H

SMA-BASED BRACING DESIGN

The behavior of a SMA-based bracing system is largely governed by the stiffness of the attributing parts. The general strategy is to concentrate the inelastic deformations into the SMA only: thus the remainder of the brace should remain completely elastic. To illustrate this point, the force-deformation of a SMA element and an elastic element are combined in series (deformations are additive while the forces are equal) as shown in Figure H-1. The following observations can be made from the resulting element's behavior:

1) The stiffness of the series spring is:

$$k_s = \frac{1}{1/k_e + 1/k_{SMA}} \tag{H.1}$$

which is always less then k_{SMA} unless $k_e \to \infty$.

2) The length of the loading plateau for the series element, β_s, is defined as:

$$\beta_s = \beta_{SMA} + \Delta F / k_e \tag{H.2}$$

where β_{SMA} is the length of the SMA loading plateau and ΔF is the change in force in the series system ($F_{SMA} = F_e = F_s$).

3) A plateau ductility parameter, η, is defined as:

$$\eta = \beta / \Delta_y \tag{H.3}$$

where β is the length of the loading plateau Δ_y is the yield displacement. The η value is a measure of the ductility in the element available until the end of the loading plateau.

4) Assuming η_{SMA} to be predetermined by strength and stiffness requirements, it is desirable to create a system with a η_s value approaching η_{SMA}, which is the upper bound. This is done by making the relative stiffness ratio, ρ, as large as possible. ρ is defined as:

$$\rho = k_{SMA}/k_e \quad \text{(H.4)}$$

5) For the experimental tests, the ρ was much lower than anticipated (0.4). Parametric studies need to be conducted to determine an appropriate target ρ.

The "series" arrangement effectively shortens the plateau ductility parameter as defined in this appendix. The designer of an SMA-base system must pay special attention to these phenomena. In this experimental work, though the elastic elements were large relative to the SMA elements, the ρ factor was much smaller than anticipated. For the analytical study, the general behavior is taken from the experimental results, and the effect of the relative stiffness is briefly explored.

In terms of practicality, there remain issues with providing the appropriate amount of SMA at the appropriate length. For example, in the analysis section of this study, the *SMA1* area is defined by the target brace yield force. The SMA length is then calculated by setting the SMA stiffness equal to the target stiffness while assuming rigidity in the attaching members. This results in the SMA needing to have a very large area over a short length (the bottom floor brace is 914 mm (36 in.) long but has an area of 11900 mm^2 (18.45 in^2)). The practicality of attaching this amount of SMA to the bracing elements is challenging.

One potential solution is to spread the SMA braces over more frame lines. For example, if there were four SMA braces for every one steel brace in the corresponding design, then the area of the SMA would be much more manageable for the analytical

study example's numbers. However, cost should be factored into the viability of this option. For the sake of this study, these issues are noted but ignored.

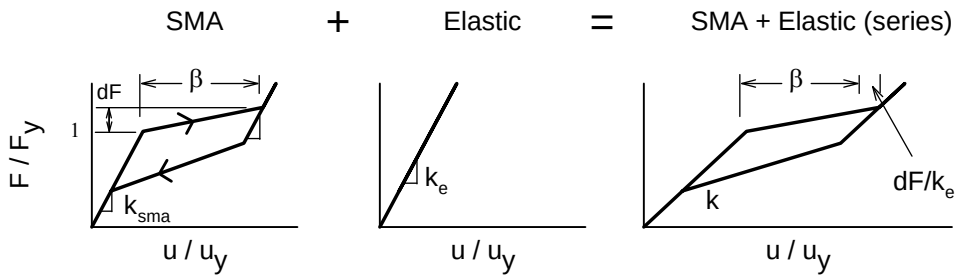

Figure H-1: The resulting force-deformation characteristics of an SMA element combined in series with an elastic element.

REFERENCES

Adachi, Y., and Unjoh, S.(1999). "Development of shape memory alloy damper for intelligent bridge systems." *SPIE Conference on Smart Systems for Bridges, Structures, and Highways*, Newport Beach, CA, 31-42.

Adan, S. M., and Gibb, W.(2008). "Inelastic cyclic testing of the kaiser bolted bracket moment connection." *2008 Structures Congress - Structures Congress 2008: Crossing the Borders, April 24, 2008 - April 26, 2008*, Vancouver, BC, Canada.

Aiken, I. D., Nims, D. K., Whittaker, A. S., and Kelly, J. M. (1993). "Testing of passive energy dissipation systems." *Earthquake Spectra*, 9(3), 335.

AISC. (2005a). "Seismic provisions for structural steel buildings." American Institure of Steel Constructions, Chicago, IL.

AISC. (2005b). *Specification for Structural Steel Buildings*, Chicago, IL.

Andrawes, B., and DesRoches, R. (2005). "Unseating prevention for multiple frame bridges using superelastic devices." *Smart Materials and Structures*, 14(3), 60-7.

Andrawes, B., and DesRoches, R. (2008). "Sensitivity of seismic applications to different shape memory alloy models." *Journal of Engineering Mechanics*, 134(2), 173-183.

Asai, M., and Suzuki, Y. (2000). "Applications of shape memory alloys in Japan." *Materials Science Forum*, 327, 17-22.

ASTM. (2003). "Standard test methods for tension testing of metallic materials E8-03." 1-23.

Auricchio, F., and Sacco, E. (1997). "A one-dimensional model for superelastic shape-memory alloys with different elastic properties between austenite and martensite." *International Journal of Non-Linear Mechanics*, 32(6), 1101-14.

Beauchamp, C. H., Nadolink, R. H., Dickinson, S. C., and Dean, L. M.(1992). "Shape memory alloy adjustable camber (SMAAC) control surface." *Proceedings of the First European Conference on Smart Structures and Materials*, Glasgow, Scotland.

Callister, W. D. (2000). *Materials science and engineering : an introduction*, Wiley.

Cardone, D., and Dolce, M. (2009). "SMA-based tension control block for metallic tendons." *International Journal of Mechanical Sciences*, 51(2), 159-165.

Castellano, M. G., Indirli, M., and Martelli, A.(2001). "Progress of application, research and development and design guidelines for shape memory alloy devices for

cultural heritage structures in italy." *Smart Systems for Bridges, Structures, and Highways-Smart Structures and Materials 2001-, Mar 5-7 2001*, Newport Beach, CA, 250-261.

Chandra, R. (2001). "Active shape control of composite blades using shape memory actuation." *Smart Materials and Structures*, 10(5), 1018-1024.

Cheok, G. S., and Lew, H. S. (1990). "Seismic performance of 1/3 scale post-tensioned precast beam-column connections." *Proceedings of the 4th US National Conference on Earthquake Engineering, May 20-24 1990*, 757.

Cheok, G. S., and Lew, H. S. (1991). "Performance of precast concrete beam-to-column connections subject to cyclic loading." *PCI Journal*, 36(3), 56-67.

Cheok, G. S., Stone, W. C., and Lew, H. S.(1993). "Seismic performance behavior of precast concrete beam-column joints." *Proceedings of the Symposium on Structural Engineering in Natural Hazards Mitigation, Apr 19-21 1993*, Irvine, CA, USA, 83-88.

Christopoulos, C., Filiatrault, A., and Folz, B. (2002a). "Seismic response of self-centring hysteretic SDOF systems." *Earthquake Engineering and Structural Dynamics*, 31(5), 1131-1150.

Christopoulos, C., Filiatrault, A., Uang, C.-M., and Folz, B. (2002b). "Posttensioned energy dissipating connections for moment-resisting steel frames." *Journal of Structural Engineering*, 128(9), 1111-1120.

Christopoulos, C., Tremblay, R., Kim, H.-J., and Lacerte, M. (2008). "Self-centering energy dissipative bracing system for the seismic resistance of structures: Development and validation." *Journal of Structural Engineering*, 134(1), 96-107.

Ciampi, V., De Angelis, M., and Paolacci, F. (1995). "Design of yielding or friction-based dissipative bracings for seismic protection of buildings." *Engineering Structures: Recent Developments in Seismic Resistant Structural Systems and Components*, 17(5), 381-391.

Clark, P. W., Aiken, I. D., Kelly, J. M., Higashino, M., and Krumme, R. C.(1995). "Experimental and analytical studies of shape memory alloy dampers for structural control." *Proceedings of Passive Damping*, San Diego, CA.

Cross, H. (1952). *Engineers and Ivory Towers*, McGraw-Hill, New York.

DesRoches, R., and Delemont, M. (2002). "Seismic retrofit of simply supported bridges using shape memory alloys." *Engineering Structures*, 24(3), 325-332.

DesRoches, R., McCormick, J., and Delemont, M. (2004). "Cyclic properties of superelastic shape memory alloy wires and bars." *ASCE Journal of Structural Engineering*, 130(1), 38-46.

Di Sarno, L., and Elnashai, A. S. (2003). "Special metals for seismic retrofitting of steel buildings." *Progress in Structural Engineering and Materials*, 5.

Dolce, M., and Cardone, D. (2001). "Mechanical behaviour of shape memory alloys for seismic applications 2. Austenite NiTi wires subjected to tension." *International Journal of Mechanical Sciences*, 43(11), 2657-2677.

Dolce, M., and Cardone, D. (2006). "Theoretical and experimental studies for the application of shape memory alloys in civil engineering." *Journal of Engineering Materials and Technology, Transactions of the ASME*, 128(3), 302-311.

Dolce, M., Cardone, D., and Marnetto, R. (2000). "Implementation and testing of passive control devices based on shape memory alloys." *Earthquake Engineering and Structural Dynamics*, 29(7), 945-968.

Dolce, M., Cardone, D., and Marnetto, R.(2001). "SMA Re-centering devices for seismic isolation of civil structures." *Smart Systems for Bridges, Structures, and Highways-Smart Structures and Materials 2001-, Mar 5-7 2001*, Newport Beach, CA, 238-249.

Dolce, M., Cardone, D., Marnetto, R., Mucciarelli, M., Nigro, D., Ponzo, F. C., and Santasiero, G.(2004). "Experimental static and dynamic response of a real R/C frame upgraded with SMA re-centering and dissipating braces." *13th World Conference on Earthquake Engineering*, Vancouver, B.C., Canada.

Dolce, M., Cardone, D., Ponzo, F. C., and Valente, C. (2005). "Shaking table tests on reinforced concrete frames without and with passive control systems." *Earthquake Engineering and Structural Dynamics*, 34(14), 1687-1717.

Dolce, M., and Marnetto, R. (1999). "Seismic devices based on shape memory alloys." *Manside Project, II105-134*, Italian Dept. for National Technical Services, Rome.

Duerig, T. W., Melton, K. N., Stöckel, D., and Wayman, C. M. (1990). *Engineering Aspects of Shape Memory Alloys*, Butterworth-Heinemann Ltd, Boston, MA.

Duval, L., Noori, M. N., Hou, Z., Davoodi, H., and Seelecke, S.(2000). "Random vibration studies of an SDOF system with shape memory restoring force." *Proceedings of the 1999 2nd International Symposium on Hysteresis Modeling and Micromagnets (HMM'99), Jun 7-Jun 9 1999, Physica B: Condensed Matter*, Perugia, Italy, 138-141.

Eatherton, M., Hajjar, J. F., Deierlein, G. G., Ma, X., Billington, S., and Krawinkler, H.(2009). "Steel-framed rocking structural systems for moderate seismic zones." Austin, TX, United states, 804-812.

FEMA. (2006). "NEHRP recommended provisions: design examples." *Rep. No. FEMA 451*, Washington, D.C.

Frick, C. P., Ortega, A. M., Tyber, J., Maksound, A. E. M., Maier, H. J., Liu, Y., and Gall, K. (2005). "Thermal processing of polycrystalline NiTi shape memory alloys." *Materials Science & Engineering A (Structural Materials: Properties, Microstructure and Processing)*, 405(1-2), 34-49.

Fromm, E., and Kleiner, W. (2003). *Handbook for Disc Springs*, Schnorr Corporation.

Fugazza, D. (2003). "Shape-Memory alloy devices in earthquake engineering: Mechanical properties, constitutive modeling and numerical simulations," Master's Thesis, University of Pavia, Pavia, Italy.

Gall, K., Sehitoglu, H., Chumlyakov, Y. I., Kireeva, I. V., and Maier, H. J. (1999c). "The influence of aging on critical transformation stress levels and martensite start temperatures in NiTi: Part I - aged microstructure and micro-mechancal modeling." *Journal of Engineering Materials and Technology*, 121(1), 19-27.

Gall, K., Sehitoglu, H., Chumlyakov, Y. I., Kireeva, I. V., and Maier, H. J. (1999d). "The influence of aging on critical transformation stress levels and martensite start temperatures in NiTi: Part II - Discussion of experimental results." *Journal of Engineering Materials and Technology*, 121(1), 28-37.

Gong, J. M., Tobushi, H., Takata, K., Okumura, K., and Endo, M. (2002). "Cyclic superelastic deformation of TiNi shape-memory alloy." *Materials Science Forum*, 394-395, 245-248.

Graesser, E. J., and Cozzarelli, F. A. (1991). "Shape-Memory alloys as new materials for aseismic isolation." *Journal of Engineering Mechanics*, 117(11), 2590-2608.

Hane, K. F., and Shield, T. W. (1999). "Microstructure in the cubic to monoclinic transition in titanium-nickel shape memory alloys." *Acta Materialia*, 47(9), 2603-2617.

Higashino, M., Aizawa, S., Clark, P. W., Whittaker, A. S., Aiken, I. D., and Kelly, J. M.(1996). "Experimental and analytical studies of structural control system using shape memory alloy." *Second International Workshop on Structural Control*, Hong Kong.

Hsu, S. E., Yeh, M. T., Hsu, I. C., Chang, S. K., Dai, Y. C., and Wang, J. Y. (2000). "Pseudo-elasticity and shape memory effect on the TiNiCoV alloy." *Materials Science Forum*, 327, 119-122.

Indirli, M., Castellano, M. G., Clemente, P., and Martelli, A.(2001). "Demo-application of shape memory alloy devices: The rehabilitation of the S. Giorgio Church Bell-Tower." *Smart Systems for Bridges, Structures, and Highways-Smart Structures and Materials 2001-, Mar 5-7 2001*, Newport Beach, CA, 262-272.

Jackson, C., Wagner, H., and Wasilewski, R. (1972). "55-Nitinol - The Alloy With a Memory: Its Physical Metallurgy, Properties, and Applications." *Report NASA-SP 5110*, National Aeronautics and Space Administration.

Kasai, K., and Xu, Y. (2002a). "Experimental parameter study on cyclic inelastic behavior of bolted angle connections." *Journal of Construction Engineering, AIJ*, 560(October), 169-179.

Kasai, K., and Xu, Y. (2002b). "Experimental study on cyclic inelastic behavior and low-cycle fatigue of bolted t-stub connections." *Journal of Construction Engineering, AIJ*, 561(November), 227-235.

Kawaguchi, M., Ohashi, Y., and Tobushi, H. (1991). "Cyclic characteristics of pseudoelasticity of Ti-Ni alloys (Effect of maximum strain, test temperature and shape memory processing temperature)." *JSME International Journal*, 34(1), 76-82.

Lafortune, P., McCormick, J., Desroches, R., and Terriault, P. (2007). "Testing of superelastic recentering pre-strained braces for seismic resistant design." *Journal of Earthquake Engineering*, 11(3), 383-399.

MANSIDE. (1998). "Memory alloys for new structural vibrations isolating devices." *Manside Third Twelve Monthly Progress Rep.*, Italian Dept. for National Technical Services, Rome.

Masuda, A., and Noori, M. (2002). "Optimization of hysteretic characteristics of damping devices based on pseudoelastic shape memory alloys." *International Journal of Non-Linear Mechanics*, 37(8), 1375-86.

McCormick, J., Barbero, L., and DesRoches, R.(2005). "Effect of mechanical training on the properties of superelastic shape memory alloys for seismic applications." *Smart Structures and Materials 2005: Smart Structures and Integrated Systems, 10 March 2005, Proceedings of the SPIE - The International Society for Optical Engineering*, San Diego, CA, USA, 430-9.

McCormick, J., and DesRoches, D. R.(2006). "The Effect of Training, Pre-Straining, and Loading History on the Properties of NiTi Shape Memory Alloys for Protective Systems in Civil Structures." *Structures Congress*.

McCormick, J., and DesRoches, R. (2004). "Behavior of large diameter Niti SMAs for seismic applications." *5th International PhD Symposium in Civil Engineering*.

McCormick, J., DesRoches, R., Fugazza, D., and Auricchio, F. (2007a). "Seismic Assessment of Concentrically Braced Steel Frames with Shape Memory Alloy Braces." *Journal of Structural Engineering*, 133(6), 862-870.

McCormick, J., Tyber, J., DesRoches, R., Gall, K., and Maier, H. J. (2007b). "Structural engineering with NiTi. II: Mechanical behavior and scaling." *Journal of Engineering Mechanics*, 133(9), 1019-1029.

McKenna, F., and Fenves, G. L. (2004). "OpenSees command language manual. Version 1.5.2." Pacific Earthquake Engineering Research Center, Berkeley, CA.

McMaster-Carr. (2009). <http://www.mcmaster.com/#spherical-washers/=48cm0h>.

Miyazaki, S. (1990). "Thermal and stress cycling effects and fatigue properties of Ni-Ti alloys." Engineering aspects of shape memory alloys, T. W. Duerig, K. N. Melton, D. Stöckel, and C. M. Wayman, eds., Butterworth-Heinemann, Boston, MA, 394-413.

Miyazaki, S., Imai, T., Igo, Y., and Otsuka, K. (1986). "Effect of cyclic deformation on the pseudoelasticity characteristics of Ti-Ni." *Metallurgical Transactions A*, 17A, 115-120.

Murray, T. M. (1988). "Recent developments for the design of moment end-plate connections." *Journal of Constructional Steel Research*, 10, 133-162.

Ocel, J., DesRoches, R., Leon, R. T., Hess, W. G., Krumme, R., Hayes, J. R., and Sweeney, S. (2004). "Steel beam-column connections using shape memory alloys." *Journal of Structural Engineering*, 130(5), 732-740.

Otsuka, K., and Shimizu, K. (1986). "Pseudoelasticity and shape memory effects in alloys." *International Metals Reviews*, 31(3), 93-114.

Otsuka, K., and Wayman, C. M. (1998). *Shape memory materials*, Cambridge University Press, New York.

Pall, A. S., and Marsh, C. (1982). "Response of Friction Damped Braced Frames." *Journal of the Structural Division (ASCE)*, 108(ST6), 1313-1323.

Penar, B. (2005). "Recentering Beam-Column Connections Using Shape Memory Alloys," Masters Thesis, Georgia Institute of Technology, Atlanta, GA.

Perkins, J. (1981). "Ti-Ni and Ti-Ni-X shape memory alloys." *Metals Forum*, 4(3), 153-163.

Priestley, M. J. N., and MacRae, G. A. (1996). "Seismic tests of precast beam-to-column joint subassemblages with unbonded tendons." *PCI Journal*, 41(1), 64-80.

Renzi, E., Perno, S., Pantanella, S., and Ciampi, V. (2007). "Design, test and analysis of a light-weight dissipative bracing system for seismic protection of structures." *Earthquake Engineering & Structural Dynamics*, 36(4), 519-539.

Renzi, E., Ranieri, N., and DeCanio, G.(2004). "Experimental verifications of seismic protection of steel and R.C. structures at Enea-Casaccia shaking tables." *13th World Conference on Earthquake Engineering*, Vancouver, B.C., Canada, Paper No. 846.

Ricles, J. M., Sause, R., Garlock, M. M., and Zhao, C. (2001). "Posttensioned seismic-resistant connections for steel frames." *Journal of Structural Engineering*, 127(2), 113-121.

SAC. (1997). "Protocol for fabrication, inspection, testing and documentation of beam-column connection test and other experimental specimens." SAC Joint Venture, SAC Rep. SAC/BD-97/02, Sacramento, CA.

Seelecke, S.(2000). "Dynamics of a SDOF system with shape memory element." *Smart Structures and Materials 2000: Active Materials: Behavior and Mechanics*, Newport Beach, CA, USA, 474-481.

Sepulveda, J., Boroschek, R., Herrera, R., Moroni, O., and Sarrazin, M. (2008). "Steel beam-column connection using copper-based shape memory alloy dampers." *Journal of Constructional Steel Research*, 64(4), 429-435.

Somerville, P., Smith, N., Punyamurthula, S., and Sun, J. (1997). "Development of ground motion time histories for Phase 2." *SAC-BD-97-04*, SAC Joint Venture, Sacramento, CA.

Speicher, M., Hodgson, D. E., Desroches, R., and Leon, R. T. (2009). "Shape memory alloy tension/compression device for seismic retrofit of buildings." *Journal of Materials Engineering and Performance*, 18(5-6), 746-753.

Strnadel, B., Ohashi, S., Ohtsuka, H., Ishihara, T., and Miyazaki, S. (1995a). "Cyclic stress-strain characteristics of Ti-Ni and Ti-Ni-Cu shape memory alloys." *Materials Science and Engineering A*, 202(1-2), 148-156.

Strnadel, B., Ohashi, S., Ohtsuka, H., Miyazaki, S., and Ishihara, T. (1995b). "Effect of mechanical cycling on the pseudoelasticity characteristics of Ti-Ni and Ti-Ni-Cu alloys." *Materials Science Engineering A (Structural Materials: Properties, Microstructure and Processing)*, A203(1-2), 187-96.

Swanson, J. A., and Leon, R. T. (2000). "Bolted steel connections: Tests on T-stub components." *Journal of structural engineering New York, N.Y.*, 126(1), 50-56.

Tadaki, T., Otsuka, K., and Shimizu, K. (1988). "Shape memory alloys." *Ann. Rev. Mater. Sci.*, 18, 25-45.

Taftali, B. (2007). "Probalistic seismic demand assessment of steel frames with shape memory alloy connections," Doctoral Thesis, Georgia Institute of Technology, Atlanta, GA.

Tobushi, H., Shimeno, Y., Hachisuka, T., and Tanaka, K. (1998). "Influence of strain rate on superelastic properties of TiNi shape memory alloy." *Mechanics of Materials*, 30, 141-150.

Tremblay, R., Lacerte, M., and Christopoulos, C. (2008). "Seismic Response of Multistory Buildings with Self-Centering Energy Dissipative Steel Braces." *Journal of Structural Engineering*, 134(1), 108-120.

Tyber, J., McCormick, J., Gall, K., DesRoches, R., Maier, J. H., and Abdel Maksoud, A. E. (2007). "Structural engineering with NiTi. I: Basic materials characterization." *Journal of Engineering Mechanics*, 133(9), 1009-1018.

Tyler, R. G. (1983). "PRELIMINARY TESTS ON AN ENERGY ABSORBING ELEMENT FOR BRACED STRUCTURES UNDER EARTHQUAKE LOADING." *Bulletin of the New Zealand National Society for Earthquake Engineering*, 16(3), 201-212.

Tyler, R. G. (1985a). "FURTHER NOTES ON A STEEL ENERGY-ABSORBING ELEMENT FOR BRACED FRAMEWORKS." *Bulletin of the New Zealand National Society for Earthquake Engineering*, 18(3), 270-279.

Tyler, R. G. (1985b). "TEST ON A BRAKE LINING DAMPER FOR STRUCTURES." *Bulletin of the New Zealand National Society for Earthquake Engineering*, 18(3), 280-288.

Wang, D., and Filiatrault, A. (2008). "Numerical and experimental studies of self-centering post-tensioned steel frames." *MCEER-08-0017* Buffalo, NY.

Wang, Z. G., Zu, X. T., Dai, J. Y., Fu, P., and Feng, X. D. (2003). "Effect of thermomechanical training temperature on the two-way shape memory effect of TiNi and TiNiCu shape memory alloys springs." *Materials Letters*, 57, 1501-1507.

Wayman, C. M., and Duerig, T. W. (1990). "An introduction to martensite and shape memory." Engineering aspects of shape memory alloys, T. W. Duerig, K. N. Melton, D. Stöckel, and C. M. Wayman, eds., Butterworth-Heinemann, Boston, MA, 3-20.

Weinert, K., and Petzoldt, V.(2004). "Machining of NiTi based shape memory alloys." *European Symposium on Martensitic Transformation and Shape-Memory, 17-22 Aug. 2003*

Materials Science & Engineering A (Structural Materials: Properties, Microstructure and Processing), Cirencester, UK, 180-4.

Wilson, J. C., and Wesolowsky, M. J. (2005). "Shape memory alloys for seismic response modification: A state-of-the-art review." *Earthquake Spectra*, 21(2), 569-601.

Wu, K., Yang, F., Pu, Z., and Shi, J. (1996). "The effect of strain rate on detwinning and superelastic behavior of NiTi shape memory alloys." *Journal of Intelligent Material Systems and Structures*, 7(3), 138-144.

Yan, S., Song, G., Huo, L., and Gu, H.(2007). "Seismic response control of frame structure braced with SMA tendons." *Sensors and Smart Structures Technologies for Civil, Mechanical, and Aerospace Systems 2007, 19 March 2007, Proceedings of the SPIE - The International Society for Optical Engineering*, USA, 65292H (9 pp.).

Yang, C.-S., Leon, R. T., and DesRoches, R. (2008). "Design and behavior of zipper-braced frames." *Engineering Structures*, 30(4), 1092-1100.

Zhang, Y., and Zhu, S. (2008). "Seismic response control of building structures with superelastic shape memory alloy wire dampers." *Journal of Engineering Mechanics*, 134(3), 240-251.

Zhu, S., and Zhang, Y. (2008). "Seismic Analysis of Concentrically Braced Frame Systems with Self-Centering Friction Damping Braces." *Journal of Structural Engineering*, 134(1), 121-131.